INVESTIGATIONS ON SELECTED BIOACTIVE GLASSES AND GLASS-CERAMICS CONTAINING IRON OXIDE

By

Rajendra Kumar Singh

Department of Physics
Indian Institute of Technology Guwahati,
Guwahati-781039, INDIA

March, 2009

INVESTIGATIONS ON SELECTED BIOACTIVE GLASSES AND GLASS-CERAMICS CONTAINING IRON OXIDE

A thesis submitted

by

Rajendra Kumar Singh

to

Indian Institute of Technology Guwahati

in

partial fulfillment of the requirement for the award of the degree of
Doctor of Philosophy in Physics

Department of Physics
Indian Institute of Technology Guwahati
Guwahati – 781039, Assam, India

March 2009

Statement

The work contained in the thesis entitled "Investigations on selected bioactive glasses and glass-ceramics containing iron oxide" has been carried out by me under the supervision of Prof. A. Srinivasan at Department of Physics, Indian Institute of Technology Guwahati. This work has not been submitted elsewhere for the award of any degree.

30 March 2009

(Rajendra Kumar Singh)
Roll No: 05612106
Department of Physics
Indian Institute of Technology Guwahati
Guwahati - 781039
Assam
India

Certificate

This is to certify that the work contained in the thesis entitled "Investigations on selected bioactive glasses and glass-ceramics containing iron oxide" submitted by Mr. Rajendra Kumar Singh in the partial fulfillment of the requirement for the award of the degree of Doctor of Philosophy in Department of Physics, Indian Institute of Technology Guwahati, is a record of the candidate's own work carried out by him under my supervision and guidance. The matter embodied in this report has not been submitted in part or full to any other university or institute for the award of any degree.

30 March 2009

(Dr. A. Srinivasan)
Professor
Department of Physics
Indian Institute of Technology Guwahati
Guwahati - 781039
Assam
India

Dedicated

to

my parents

Acknowledgements

At this momentous occasion of compiling my thesis work, I would like to acknowledge the contribution of all those benevolent people, I have been blessed to associate with.

My first and foremost offering of thanks goes to the architect who shaped my dreams into reality, my guide and mentor Prof. A. Srinivasan. Perseverance, exuberance and positive approaches are just some of the traits he imprinted on my personality. He steered me through this journey through his invaluable advice, positive criticism, stimulating discussion and consistent encouragement. His meticulous attention towards my progress, his devoted time and his ideas has enabled me to make the project a success. His faith in me has always made me more confident. His blessing always made me optimistic. If I stand proud of my achievements, then undeniably he is the main contributor. It had been my privilege to work under his tutelage.

I would like to express my sincere thanks to Dr. A. Perumal Department of Physics, Indian Institute of Technology Guwahati for his help in improving my dissertation. I am grateful to him for sharing his time and expertise. His comments and views were very insightful and helpful.

I am grateful to my doctoral committee members, Dr. S. Ravi, Dr. A. Perumal, Dr. S. B. Santra and Dr. G. Das for reviewing my research work regularly and for all their valuable suggestions for my doctoral research. I am thankful to the Head of the Department, Prof. A. Khare and all the members of the Department of Physics for their support. My thanks are due to all faculty members of our Department for their help and suggestions.

I express my sincere thanks to the staff members of Physics Department, Mr. Sidananda Sarma, Mr. Lokesh Chakraborty, Mr. Atul Deka, Mr. Bimal K. Sarma, Mr. Pankaj Goswami and Mr. Modan Deka for helping me during my research work.

My sincere thanks are due to Prof. P. S. Robi, and Mr. Rituraj Saikia for extending their help in the microhardness measurements. During my work, I have benefited from the mechanical workshop in the fabrication of the instrumental set up. I would like to thank all the members in the workshop for their help.

I am very fortunate to have Sida da and Manos da as my seniors. Their expertise in the field of XRD and magnetic properties has been a great help to me. I thank them for many discussions I had with him. It has been a great pleasure sharing knowledge, time and small talk with all my colleagues in the department of Physics, Chemistry and Center of Nanotechnology.

Mr. Chandan Borgohain and Mr. Kula Senapati, Scientific Officers of CIF have patiently and enthusiastically extended their expertise in EPR spectroscopy, SEM-EDS work and in fabrication of essential components required for my research work.

I am fortunate to have Debabrata, Sida da and Manos as my fellow researchers in the same group. Thanks to them for providing an amiable ambience in the lab. Sandeep, Anto, Purabi, P. Nandi, Poulumi, Bishwanath, Gaurav, Meera, Veena, Samantray, Sunita, Arpita, Satchi, Himanshu, and all the research scholars of Physics Department will always be remembered for the wonderful time we shared together.

I thank Dilip, Akhilesh, Amardeep, Ravi, Pramod and all my friends for the memorable life in IITG campus.

I am deeply indebted to my parents, brother and sisters for their constant encouragement and moral support.

I profusely thank IIT Guwahati for the financial, material and infrastructure support provided to me as a research scholar.

Finally, I express my sincere thanks to all who helped me in whatever form during my stay at IIT Guwahati and who I may have inadvertently forgotten to mention in this acknowledgement.

Rajendra Kumar Singh

PREFACE

Magnetism and magnetic materials have a strong role to play in health care and biological application such as cell separation, drug delivery and magnetic intracellular hyperthermia treatment of cancer. Magnetic bioglass ceramics (MBC) are complex and multiphase biocompatible materials, usually fabricated from the original bioglass with the addition of Fe_2O_3 in the basic bioglass composition. MBCs exhibit bioactivity as well as magnetic properties. This Ph. D thesis work is focussed on the preparation and characterization of CaO, MgO and ZnO based glasses containing variable amounts of iron oxide and MBC derived from them. These investigations are aimed at (i) optimization of preparative conditions of the MBC, (ii) magnetic hysteresis loss and physical property evaluation of MBC, and (iii) evaluation of biocompatibility of the MBCs by treating them with SBF. Since preparation of bioactive glasses is the first stage in the preparation of the bioglass-ceramics, optimization and evaluation of the properties of the base glasses are also required in order to fully comprehend the MBCs derived from them.

After a careful study of the bioactive based glass containing Fe_2O_3 and magnetic glass-ceramics obtained by controlled crystallization of the respective parent glasses, three glass systems, *viz*., 41CaO(52-*x*)$SiO_2$4P_2O_5*x*$Fe_2O_3$3Na_2O, (*x* = 0, 2, 4, 6, 8 and 10 mole %), 4.5MgO(45-*x*)CaO34$SiO_2$16$P_2O_5$0.5CaF_2*x* Fe_2O_3 (*x* = 0, 5, 10, 15 and 20 wt.%) and *x*(ZnO,Fe_2O_3)(65-*x*)SiO_2 20(CaO,P_2O_5)15Na_2O (*x* = 6, 9, 12, 15, 18 and 21 mole %) with Ca/P = 1.67 and Fe/Zn = 6.5 were identified for the present investigations.

Bulk glass samples belonging to the three glass systems were prepared by melt quenching technique. Powder X-ray diffraction technique was used to verify the

amorphous nature of the glasses and to record the X-ray diffraction (XRD) pattern of heat treated glasses. Differential scanning calorimeter (DSC) was employed to determine the glass transition temperature (T_g) and the crystallization temperature (T_c) of the glasses. Density of the glass samples was measured using Archimedes' principle. A microhardness tester equipped with a Vickers pyramidal indenter was used for micro hardness measurements. Electron Paramagnetic Resonance (EPR) spectra were recorded at room temperature on powder samples using a Spectrometer in the X band for understanding the valence states and local structure of iron ions as a function of composition. Magnetization versus Temperature (M-T) curves and magnetic hysteresis (M-H) loops of the samples would be obtained using a Vibrating Sample Magnetometer (VSM) to elucidate the magnetic properties of the samples. In vitro bioactivity test was performed on the samples by immersion of bulk samples in SBF (Kokubo's solution) for different periods of time and monitoring the changes in the structure of the glasses / glass-ceramics by grazing incidence XRD, reflectance FT-IR spectroscopy and Scanning Electron Microscopy (SEM) . All the experimental data were analysed using existing theoretical formalisms. The thesis is arranged in six chapters.

The first chapter serves as a brief introduction to bioglasses and glass-ceramics, the materials of interest to this thesis work. The motivation behind the thesis work is briefly stated at the end of this chapter.

The second chapter discusses the experimental techniques used in the present investigations. The basic principle and the theory behind the experiments, the experimental set up and the measurement/estimation procedure leading to the determination of the physical properties are discussed at length here.

In the third chapter, experimental studies on $CaO\text{-}SiO_2\text{-}P_2O_5\text{-}Fe_2O_3\text{-}Na_2O$ glasses and glass-ceramics are presented. Variations in the EPR spectral features, hardness, density, molar volume, magnetic susceptibility and T_g of $CaO\text{-}SiO_2\text{-}P_2O_5\text{-}Fe_2O_3\text{-}Na_2O$ glasses with Fe_2O_3 content are interpreted and correlated with changes occurring in the glass structure with change in composition. The glasses immersed in SBF were taken out at regular time intervals and the surface structural are changes were evaluated by examining apatite layer formation. *In vitro* bioactivity studies showed that the apatite forming ability in glasses increased as a function of iron oxide content. The as-quenched glasses were heat-treated at elevated temperatures in order to crystallize useful phases. The evolution of magnetic properties in the glass-ceramics samples as a function of iron oxide molar concentration is correlated with magnetization, coercivity and crystallite size of magnetite phase present in them. M-T data indicates ferrimagnetic behavior in these samples below the transition temperature. The EPR absorption lines near $g \approx 2.0$ and $g \approx 4.3$ were observed in samples with lower concentration of iron oxide. The latter absorption line $g \approx 4.3$ was not observed in the EPR spectra of samples with higher iron oxide content. *In vitro* bioactivity studies showed an increased apatite forming ability in glass-ceramics when the iron oxide content is increased.

In four and five chapter are devoted to the study on MgO and ZnO bioactive glass and glass-ceramics systems, respectively. The investigations undertaken in the third chapter are similar to the ones discussed above.

Conclusions and scope of future work on these bioactive glass and glass-ceramics are presented in the last chapter. The similarities and the differences observed in the three systems are discussed. The references cited in the thesis are listed in the end of the thesis.

Contents

Chapter 1

Introduction

One of the most exciting and rewarding research areas of materials science involves the applications of materials to health care, and especially to reconstructive surgery. The importance of biomaterials can be well realized from the economical aspect, *i.e*. in terms of an estimate of total health care expenditure around the world. The use of synthetic materials to replace parts of human body dates back to thousands of years ago. Nevertheless, until the 19th century, these synthetic biomaterials continued to be the most frequently used to make implants. During the 1970s and 1980s, a new class of biomaterial called bioactive glasses was obtained by melting and rapid cooling of multi component oxides. Two main aspects dominate the current research on this special category of glasses, *viz*., improvement of the mechanical properties without decreasing the bioactivity, which is generally achieved by the preparation of glass-ceramics [1-2], and studying the influence of the composition on the bioactivity [3].

Bioactive glasses and glass-ceramics have another application *viz*., as thermoseeds in hyperthermia treatment of cancerous cells [4-7]. This therapy consists of

controlled heating of local regions of the living tissues and bones by magnetic implants. When an alternating magnetic field is applied in the vicinity of a magnetic implant (thermoseed), heat is generated in the material due to hysteresis loss. This heat is dissipated to the tissues over a localized region. When heated above 43 ºC, the cancerous cells are the first one to die. If the heat treatment is selective, *i.e.*, just above 43 ºC, and the application time controlled, it is possible to selectively damage the cancerous cells without affecting the healthy ones. Thermoseeds can be prepared by creating magnetic aggregates in a bioactive glass or glass-ceramic material. The amorphous nature of glass permits addition of iron oxide as a constituent and thus provides a means to obtain Fe containing glasses. These glasses can be given adequate heat treatment to induce magnetic nuclei in the material or to precipitate a magnetic phase. Thus, this material could be used as a glass or, after appropriate heat treatment, as a magnetic glass-ceramic. However, obtaining glass-ceramics which combine excellent bioactivity and magnetic properties (in the range suitable for efficient hyperthermia treatment) is a challenge.

1.1. General theory of Biomaterials

A biomaterial is a synthetic material to be used in intimate contact with living tissue. A more precise definition of a biomaterial was given in 1986, at the consensus conference of the European Society for Biomaterials, when a biomaterial was defined [8] as “a nonviable material used in a medical device, intended to interact with biological system”.

A general theory of biomaterials was proposed by Hench and Ethridge in 1982 [9]. Its salient features are

(a) An ideal implant material performs as if it were equivalent to the host tissue.

(b) Axiom 1. The tissue at the interface should be equivalent to the normal host tissue.

(c) Axiom 2. The response of the material to physical stimuli should be like that of the tissue it replaces.

These axioms are interdependent. A stable interfacial bond between tissue and implant must be achieved in order to obtain an equivalent physical response, and controlled physical stimuli are necessary for a stable interface to be produced. This general theory requires that a biomaterial should have both biochemical compatibility and biomechanical compatibility. Hence, besides bioactivity, a match in physical and mechanical properties is also essential for an implant to replace bone.

1.2. Types of tissue attachment of biomaterials

For many years, it was thought that interactions between body and implants could cause only undesirable reactions, such as tissue irritation, damage, and finally death. This was due to the observation that if a toxic material is put in contact with a tissue, the tissue will die. For this reason, the guiding principle used in biomaterials development at the beginning was that they should be as chemically inert as possible. Biomaterials for clinical applications are categorized according to the type of implant-tissue attachment into four types, which are summarized in Table 1.2 with examples [3]. The most inert material (bioinert) elicits a reaction of the body once implanted [3, 10]. A thin non-adherent fibrous capsule is developed on bioinert materials after they remain in contact with body environment for some time. This prevents further interactions with the tissues. The thickness of the protective fibrous layer developed depends on the type of bioinert material, and on the motion and fit at the interface [11]. This type of interface cannot last

for long time. Eventually, deterioration occurs, and the material has to be surgically removed. This led to the development of materials that could interact with the body inducing a desirable response from the host tissue.

Porous materials can achieve biological fixation. In this case, a mechanical bond is obtained by in-growth of bone into the pores, which have diameters > 100 μm [11]. The increased interfacial area between the implant and the tissue increases the resistance to movement of the device in the tissue. However, porous materials too do not last long once implanted. Their mechanical strength is not as high as bulk materials, and the corrosion due to the exposure of a large surface area to body fluids further decreases their strength.

Resorbable bioceramics represent an alternative solution to the problem of long term implant failure. These materials are supposed to exploit and increase the body capacity of self repairing. This happens as these materials degrade gradually over a period of time, and are replaced by the natural host tissue. An important issue related to this class of biomaterials is the biocompatibility of the products of resorption. Moreover, resorption should occur at a rate similar to cellular metabolism. Yet another requirement is the matching of the resorption rate with the repair rate of body tissues [12]. These requirements are very difficult to be fulfilled, and for this reason not many resorbable biomaterials have been clinically applied so far.

A very valuable solution to the problem of achieving a stable implant tissue interface is bioactive fixation. When a bioactive material is implanted in the body, a series of biophysical and biochemical reactions occur at the implant-tissue interface.

These reactions eventually result in a mechanically strong chemical interfacial bonding between the two [3, 8-9, 11, 13].

Table 1.2: Types of tissue attachment of biomaterials

Type of implant	Type of attachment	Example
Nearly inert	Mechanical interlock (morphological fixation)	Metals, alumina, zirconia, polyethylene (PE)
Porous	In-growth of tissues into pores (biological fixation)	Hydroxyapatite (HA), HA coated porous metals
Bioactive	Interfacial bonding with tissues (bioactive fixation)	Bioactive glasses, HA, bioactive glass-ceramics
Resorbable	Replacement with tissues	Tricalcium phosphate, polylactic acid (PLA)

In 1969, the concept of a bioactive material was discovered [14]. In the early 1970s, bio-ceramics began to be used in certain implant applications, which depended on the fact that a smooth oxide ceramics surface, especially Al_2O_3, elicited very little tissue reaction and provided good wear characteristics for a bearing surface. Since then, the field of ceramics has expanded enormously to include many new compositions of glass, glass-ceramics and ceramics [3, 15]. The concept of bioactivity was defined as "a bioactive material is one that elicits a specific biological response at the interface of the material which results in the formation of a bond between the tissues and the material" [14]. It is

intermediate between resorbable and bioinert [9, 13, 15]. A bioactive material creates an environment compatible with osteogenesis (bone growth), with the mineralizing interface developing as a natural bonding junction between living and non-living materials. This concept has now been expanded to include a large number of bioactive materials with a wide range of rates of bonding and thickness of interfacial bonding layers. They includes bioactive glasses such as Bioglass®, bioactive glass-ceramics such as Ceravital®, A/W glass-ceramics, dense calcium phosphate ceramics such as synthetic hydroxyapatite (HA), bioactive composites such as PE-HA mixtures, and a series of bioactive coating materials. The mechanism of bonding, the time dependence of bonding, the strength of the bonding and the thickness of bonding zone are different differ for each type of bioactive material is different. Large differences in the rate of bone bonding to bioactive implants indicate that different biochemical factors influence the implant-tissue interface. In 1994, a new hypothesis was proposed [10], in which bioactive materials are classified into two types, *viz.*,

1. *Class A*, osteoproductive materials. Osteoproduction has been defined by Wilson [16] as "the process whereby a bioactive surface is colonized by osteogenic stems cells free in the defect environment as results of surgical intervention". Class A bioactivity occurs when a material elicits both an intracellular and an extracellular response at its interface. Class A bioactive glass can bond with both bone and soft tissue.
2. *Class B*, osteoconductive materials. The osteoconductive implant simply provides a biocompatible interface along which bone migrates. Osteoconductive bioactivity occurs when a material elicits only an extracellular response at its interface [8].

Synthetic HA implants are osteoconductive; i.e. they have Class B bioactivity. 45S5 bioglass®, which is a Class A bioactive material, is both osteoproductive and osteoconductive.

1.3. Bioactive materials

"A bioactive material is one that elicits a specific biological response at the interface of the material which results in the formation of a bond between the tissues and the material". This definition was give by L. L. Hench, who initiated this subject of research with his colleagues in the early 1969s [14]. Certain compositions of glasses, ceramics, glass-ceramics and composites have been shown to bond to bone [8-9, 11, 13, 15, 17-18]. These materials have become known as bioactive ceramics [13, 15]. Some even more specialized compositions of bioactive glasses will bond to soft tissues as well as bone [19-20]. A common characteristic of bioactive glasses and bioactive ceramics is a time dependent, kinetic modification of the surface that occurs upon implantation [13, 15]. The surface forms a biologically active hydroxycarbonate apatite (HCA) layer which provides the bonding interface with tissues. The implants are equivalent chemically and structurally to the mineral phase in bone. It is that equivalent which is responsible for interfacial bonding.

1.3.1. Bioglasses

In 1969, Prof. L.L. Hench from the University of Florida, discovered that some compositions of glass can bond chemically with bone. These glasses are called bioactive glasses and have been used mostly as a reconstructive material for damaged hard tissues

such as the bone. The advantage of this material is that it is possible to design the glass for example in order to get a controlled rate of degradation and bonding to the tissue. The rapid reaction at the surface leads to a fast bonding with the living tissue. But, due to the mostly two-dimension structure of the glass network, the mechanical properties are relatively low. It is important to note that small changes in the composition can lead to very different properties and this gives the opportunity to use a bioglass in contact with different tissues, since one can tailor a range of properties depending on the implantation site of the prosthesis.

Hench *et al*. [3] showed that certain compositions of glasses containing SiO_2, CaO, Na_2O and P_2O_5 were able to form a bond with bone once they are implanted. In fact, when these glasses were put in contact with biological fluids, a layer of HCA analogue to the mineral phase of bones was deposited on their surface. Collagen molecules were incorporated into this layer, and a biological bond could be formed. Later work by Wilson and Nolletti [20] showed that a bond with soft tissue could also be achieved, if the speed of apatite formation was high enough.

The rate of bonding of bioactive glasses with bone depends on many factors. One of them is the bulk composition. The most rapid rates of bonding for bioactive glasses composed of SiO_2, CaO, Na_2O and P_2O_5 are obtained with SiO_2 content of 45-52 wt.% . In this compositional range, a bonding both to soft and hard connective tissues has been found to occur within 5-10 days. Bioactive glasses or glass-ceramics containing 55-60 wt.% SiO_2 require a longer time to form a bond with bones, and do not bond to soft tissues. Glass compositions with more than 60 % SiO_2 do not bond either to bone or to soft tissue, and elicit formation of a non adherent fibrous interfacial capsule [21]. These

concepts are summarized in Fig. 1.3.1, where Na_2O-CaO-SiO_2 ternary phase diagram is shown, in which the P_2O_5 % wt. is maintained at a constant value.

Glass and glass-ceramics that have a composition falling inside region A develop HA both *in vitro* and *in vivo* conditions. Compositions inside the dashed line bind also to soft tissues. The material in region B is inert, and those in region C are resorbable. Region D is a non-glass forming and nonbonding region [3]. The boundary between region A and C depends upon the ratio of surface area of the glass to the effective solution volume of the tissue, as well as the glass composition.

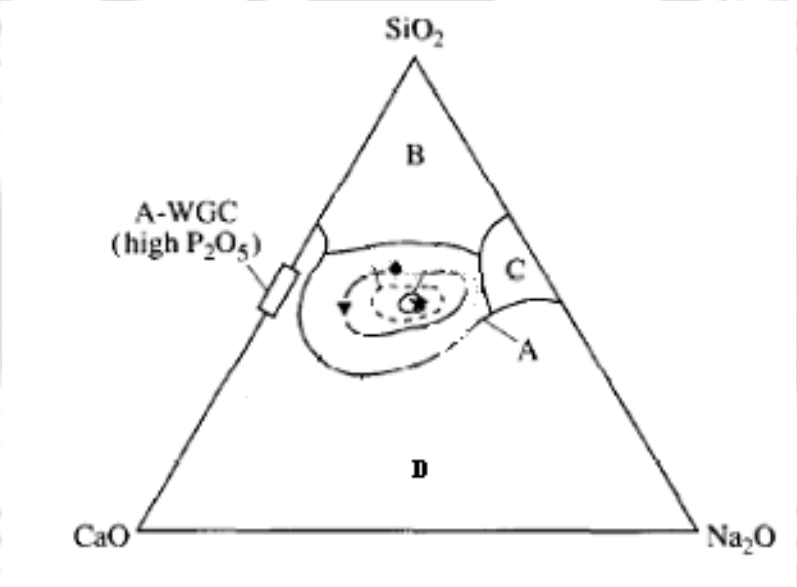

Fig. 1.3.1: Bioactive regions in the Na_2O-CaO-SiO_2 system [3].

Bioglass®, which has the following composition, 45 % SiO_2, 24.5 % Na_2O, 24.5 % CaO and 6 % P_2O_5 in weight percent, also popularly referred to as the "45S5 bioglass" was the first bioactive material discovered in 1969 by Hench [14]. This material has found many applications in orthopedic and dental fields, and is one of the most used bioceramics.

1.3.2. Bone minerals

Bone is a natural composite material, which by weight contains about 60 % mineral, 30 % matrix and 10 % water [22]. Bone is also a living tissue, with about 15 % of its weight being due to the cellular content [23]. The matrix of bone is comprised primarily of Type I collagen that is highly aligned, yielding a very anisotropic structure. This organic component of bone is predominantly responsible for its tensile strength. The mineral component of bone is a form of calcium phosphate known as HA. Stoichiometric HA has the formula $Ca_{10}(PO_4)(OH)_2$, and adopts a hexagonal geometry with the unit cell dimensions being 9.42 Å in the *a* and *b* directions, and 6.88 Å along the *c*-axis [24]. However, bone mineral is rarely stoichiometric, and usually contains many substitutions such as magnesium, sodium, potassium, fluorine, chlorine, and carbonate ions [25]. Calcium phosphate has been used in the form of artificial bone. Recently, this material has been synthesized and used for the manufacture of various forms of implants as well as solid or porous coating on implants. Calcium phosphate can be crystallized into salts, hydroxyapatite and *β*-whitelockite depending on the Ca/P ratio, presence of water, impurities and temperature. In a wet environment and at lower temperature (< 900 ºC), it is more likely that the (hydroxyl or hydroxyl) apatite will form, whereas in a dry atmosphere and at higher temperature the *β*-whitelockite will be formed. Both forms are very tissue compatible and are used as bone substitute in a granular or solid block forms. However, the mineral part of bone and teeth is made of a crystalline form of calcium phosphate similar to HA $\{Ca_{10}(PO_4)_6(OH)_2\}$ or carbonate apatite $\{Ca_{10}(PO_4)_6(OH)_{2-2x}(CO_3)_x\}$ [3]. The mineral phase of calcified tissues (enamel, dentine and bone) is biological apatite, which is hydroxy carbonate apatite (HCA). Biological apatites are

usually calcium-deficient and are always carbonate substituted. Biological apatite contains 3.2-5.8 wt.% carbonate. Consequently, biological apatites are referred to as carbonate apatites [26-27]. Biological apatites also contain other minor and trace elements as described below: $(Ca,M)_{10}(PO_4,CO_3,Y)_6(OH, F, Cl)_2$, where M represents Mg, Na, K and trace elements Sr, Pb, Ba *etc*. Y represents acid phosphate, HPO_4, sulfates, borates etc. These elements will change the lattice parameters and the crystal properties of apatite [8, 28]. The ideal Ca/P ratio of hydroxyapatite is 10:6 , the calculated density is 3.219 g/cm^3 and hardness [Vickers Hardness Number (VHN)] is 3.43 GPa. Among the most interesting properties of apatite as a biomaterial is its excellent biocompatibility. Apatite appears to form a direct chemical bond with hard tissues.

1.3.3. Bioglass ceramics

Thousand of years ago, humans discovered a new class of materials, made by firing clay and transforming this into ceramics. This discovery was fundamental in the transformation of the society from a nomadic style of life toward an agricultural society. Nowadays, we are assisting a new revolution, as in the last twenty years, the development of glass-ceramics suitable for application as biomaterials has opened new possibilities in medicine. Actually glass-ceramics have been widely used as health device but their use as implants inside the body is relatively new. With these bioceramics, we can tailor the composition for obtaining different properties [29]. The main use of these is to repair bones, joints or teeth. There are also some other applications such as for tumour treatments or to replace some parts of heart valves. The low strength of a monophase bioactive glass restricts its clinical application to non-load bearing situations. A way to

attempt to solve this problem is to prepare a glass-ceramics by a process of crystallization of glass [15, 30-31].

Several kinds of bioactive glass-ceramics have been developed, including bioactive A/W glass-ceramics, ceravital glass-ceramics and machineable glass-ceramics. These glass-ceramics also show bioactivity by bonding to bone [32]. Machineable glass-ceramics have high levels of machineability because of a mica phase crystallized during heat treating [18]. Glass-ceramics and glasses are commonly used in wide range of medical related applications, as one can easily imagine: eye glasses, chemical and chirurgical glassware, analysis instruments, etc. Moreover, ceramics have been widely used in dentistry: e.g., gold or porcelain has been used to substitute crowns, and glass cements are used as fillers [33]. Nowadays, bioceramics are used for a wide variety of applications inside human body, as can be seen in Fig. 1.3.3 [34].

A wide range of ceramics materials are used for biomedical applications: glasses (45S5 Bioglass), polycrystalline ceramics (HA, tricalcium phosphate), Polycrystalline glass-ceramics (Ceravital), vitrified ceramics (glass-HA), sintered ceramics (alumina, zirconia), hot pressed ceramics or glass-ceramics (Cerabone® A/W glass-ceramics), bioactive sol-gel glasses or ceramics compositions [29]. The first total hip replacement with alumina dates back to 1971 [34]. Hench`s paper concerning the mechanism of bonding of biomaterials to host tissue [14] opened up the research activities on bioactive materials. Shortly after this paper was published, Ceravital was patented [35]. Ceravital refers to a number of different glass compositions that have been used for the replacement of the ossicular chain in the middle ear. In the mid seventies, three

independent groups commercialized a synthetic form of HA for orthopedic applications [8, 36-38].

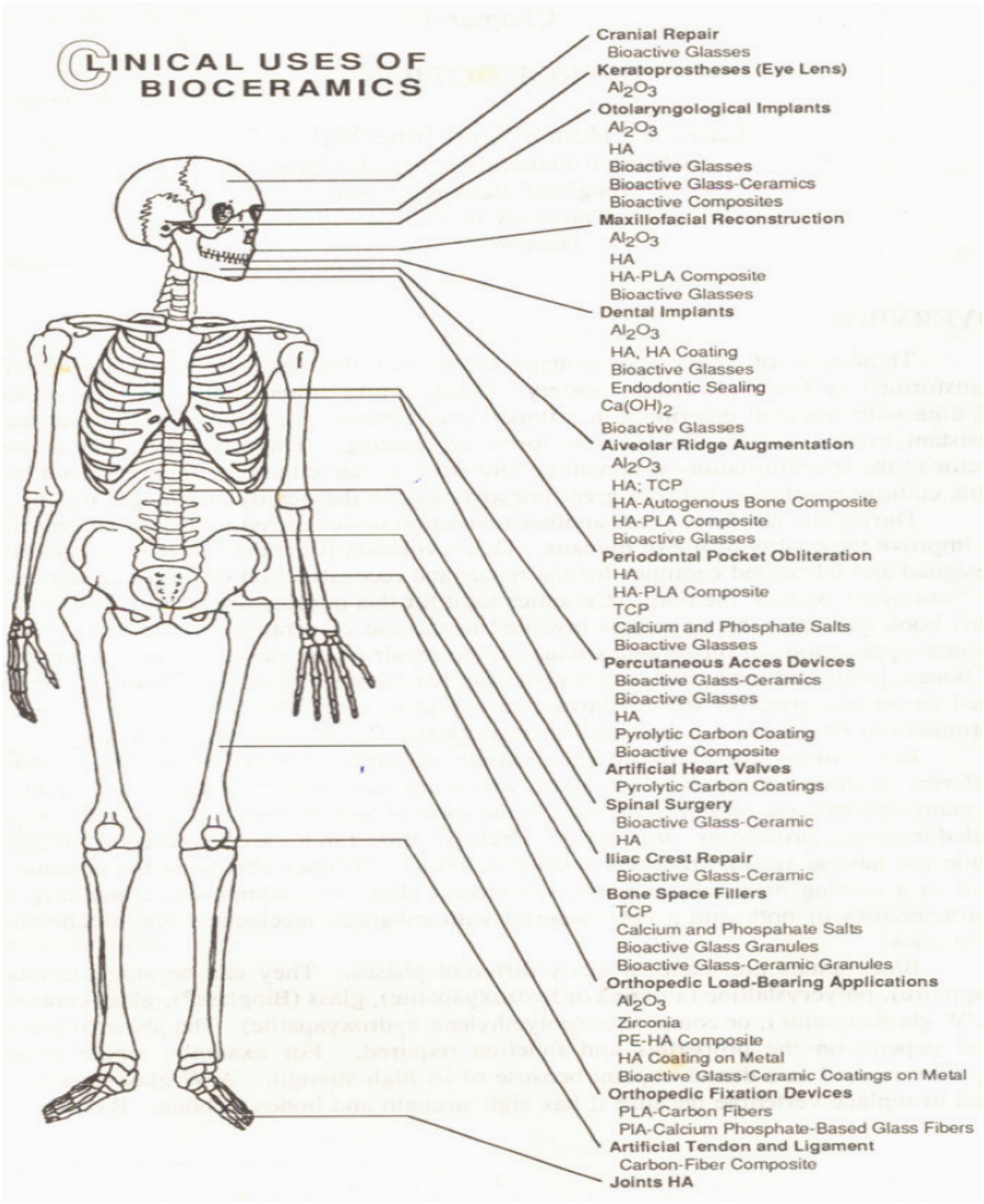

Fig. 1.3.3. Clinical uses of bioceramics [34]

HA can be used either as dense or as porous material. Tricalcium phosphate has also been used to make resorbable implants [39]. A/W glass-ceramics in the MgO-CaO-SiO_2-P_2O_5 system, containing apatite and wollastonite phases, were introduced by Kokubo *et al.* in 1982 [40]. They have been used for vertebral replacement, iliac crest prostheses and as bone defect fillers. Subsequently, composites made of a variety of bioceramics and other materials have been prepared and investigated. A few examples are stainless steel fiber reinforced bioglass, titanium fiber reinforced bioglass, tricalcium phosphate (TCP) or HA reinforced polyethylene [29]. Bioceramics can be used in granular or bulk form, depending on the need: bulk samples for tissue replacement or augmentation, whereas powders for space-filling, therapeutic treatment, tissue regeneration, or coatings [14].

1.4. Tests for biocompatibility

The fundamental requirement of any biomaterial is its biocompatibility or the ability of the material to perform with an appropriate host response for the desired application i.e. the material and the tissue environment of body should coexist without having any undesirable or inappropriate effect on each other. From biological point of view, biocompatibility arises from the acceptability of non-living materials (synthetic biomaterial) in living body (mammals/humans). The material may be a natural or synthetic polymer, a metal, a ceramic or a combination of these and it may carry a surface treatment to provide a specific chemistry or biological signal that is intended to improve the overall performance of the material. Biocompatibility testing and evaluation involves both *in vitro* and *in vivo* assessments.

1.4.1. *In vivo* test

In vivo assays use animal models to test the biological response to biomaterials in living animals with active fully integrated systems. This response provides a dual evaluation based on acquiring clinical data during the trial period and histological data from examination of sections of post-mortem tissue to assess the tissue response to the implanted materials. *In vivo* testing of biomaterials involves small animal models such as mouse, rat and/or rabbit. *In vivo* tests also provide interactions with extracellular matrix, blood-borne cells, protein and molecules.

1.4.2. *In vitro* test

The importance of analyzing bioactivity *in vitro* prior to *in vivo* analysis is obvious. *In vivo* studies require animal sacrifices, are more costly and less easily reproducible, and involve ethical issues. For these reasons, before testing bioactivity of the materials *in vivo*, screening carried out in biological labs *in vitro* is necessary. The choice of the solution used to simulate *in vitro* the reactions occurring on the surface of biomaterial is very important: simple solutions that mimic only the inorganic composition of human body fluids, or more complex solutions that also contain some biological moieties such as proteins can be used. Moreover, cell-containing solutions can be employed, thus increasing both the similarity to real body fluids and the complexity of the test.

1.4.2.1. Simulated body fluid (SBF)

In 1980, Hench *et al.* showed [41] that a SiO_2-rich layer and calcium phosphate film form on the surface of bioglass when implanted in body environment, which allows bonding to

living bone. They also demonstrated that the *in vivo* formation of calcium phosphate film can be reproduced in buffer solution consisting of tris hydroxymethylaminomethane and hydrochloric acid (tris buffer solution) at a pH of 7.4. Kitsugi *et al.* showed [42] that the SiO_2-rich layer does not form on glass-ceramics A/W, but a calcium phosphate layer forms on its surface in the living body, allowing bonding to living bone. Subsequently, Kokubo *et al.* [43], using micro X-ray diffraction, identified this calcium phosphate layer as crystalline apatite. In addition, in 1990, they showed that the *in vivo* apatite formation on the surface of glass-ceramics A/W can be reproduced in an acellular SBF with ion concentrations nearly equals to those of the human blood plasma, but not in a tris buffer solution [44-45]. Kokubo *et al.* [44] and Hench *et al.* [46] also independently confirmed the formation of apatite on the surface of Bioglass 45S5-type glass treated in SBF.

Detailed analysis of the surface apatite formed in SBF, by means of thin film X-ray diffraction (TF-XRD), Fourier transform infrared spectroscopy, scanning electron microscopy (SEM) and transmission electron microscopy (TEM), showed [44-45, 47] that it was similar to bone mineral in its composition and structure. As a result, it was speculated that osteoblasts might preferentially proliferate and differentiate to produce apatite and collagen on its surface. Thus formed apatite might bond to the surface apatite as well as to the surrounding bone. Consequently, a tight chemical bond is formed between the material and the living bone through the apatite layer. In contrast, glass-ceramic A/W (Al), (which also contains apatite and wollastonite, but in a glassy matrix containing Al_2O_3, and hence does not bond to living bone) did not have apatite formation on its surface, both *in vivo* and in SBF [45, 48]. Based on these results, it was proposed in 1991 that the essential requirement for a material to bond to living bone is the formation

of bone-like apatite on its surface in the living body and that this *in vivo* apatite formation can be reproduced *in vitro* in SBF. It is now widely accepted that *in vivo* bone bioactivity of a material can be predicted by examining apatite formation on its surface in SBF [49]. It should be noted here that the original SBF used by Kokubo *et al.* [44] and Hench *et al.* [46] lacks the SO_4^{2+} ions contained in human blood plasma [50], as shown in Table 1.4.2.1. This was corrected by Kokubo *et al.* in 1991 in papers [49, 51].

Table 1.4.2.1: Ion concentrations of SBFs and human blood plasma

Solution	**Ion concentration (mM)**							
	Na^+	K^+	Mg^{2+}	Ca^{2+}	Cl^-	HCO_3^-	HPO_4^{2-}	SO_4^{2-}
Human blood plasma	142.0	5.0	1.5	2.5	103.0	27.0	1.0	0.5
Original SBF	142.0	5.0	1.5	2.5	148.8	4.2	1.0	0
Corrected SBF (c-SBF)	142.0	5.0	1.5	2.5	147.8	4.2	1.0	0.5
Revised SBF (r-SBF)	142.0	5.0	1.5	2.5	103.0	27.0	1.0	0.5
Newly improved SBF (n-SBF)	142.0	5.0	1.5	2.5	103.0	4.2	1.0	0.5

Since then, the corrected SBF composition has been used as "SBF" by many researchers. It should be also noted here that SBF is a solution highly supersaturated with respect to apatite [52]. It is not easy to prepare clear SBF with no precipitation. Therefore, a detailed recipe for preparation of SBF was reported in 1995 by Cho *et al.* [53]. However, it can be seen from Table 1.4.2.1 that the corrected SBF is still richer in

Cl^- ion and poorer in HCO_3^- ion than human blood plasma (HBP). In 2003, Oyane *et al.* [54] tried to correct this difference by preparing a revised SBF (r-SBF) in which the concentrations of Cl^- and HCO_3^- ions were decreased and increased, respectively, to the levels of human blood plasma. However, calcium carbonate has a strong tendency to precipitate from this SBF, as it is supersaturated with respect to not only apatite, but also to calcite [55]. In 2004, Takadama *et al.* [56] proposed a newly improved SBF (n-SBF) in which they decreased only the Cl^- ion concentration to the level of human blood plasma, leaving the HCO_3^- ion concentration equal to that of the corrected SBF (c-SBF). This improved SBF was compared with the corrected, *i.e.*, conventional, c-SBF in its stability and the reproducibility of apatite formation on synthetic materials. Both SBFs were subjected to round robin testing in ten research institutes. As a result, it was confirmed that the c-SBF does not differ from n-SBF in stability and reproducibility [56]. Through this round robin testing, the method for preparing c-SBF was carefully checked and refined so that the SBF could be easily prepared. This refined recipe for preparing SBF is given in Appendix A of this paper, accompanied with procedure of apatite-forming ability test. In 2003, conventional SBF with the refined recipe was proposed to the Technical Committee ISO/TC150 of International Organization for Standardization as a solution for *in vitro* measurement of apatite-forming ability of implant materials

1.4.2.2. Mechanism of HCA layer deposition

Even though the compositions of bioactive glasses synthesized are quite different, it seems that the mechanism of HCA formation involves some specific steps that are analogous for all of them. For example, the presence of silica in these glasses was proved

to be necessary in order to obtain HCA nucleation within 30 days. When both $CaO-P_2O_5$ and $CaO-SiO_2$ based glasses were immersed in body fluid, the ion activity product of apatite was increased by a similar amount. However, a layer of HCA was deposited only on $CaO-SiO_2$ based glasses [57-58].

It was hypothesized that a hydrated silica layer forms on the surface of these glasses prior to the deposition of HCA, and silanol groups could be specific sites of nucleation of apatite. Clark and Hench [59] first proposed the following well-detailed sequence of reactions occurring at the surface of silica-based bioactive glasses:

(i) Rapid exchange of Na^+ or K^+ with H^+ or H_3O^+ from solution;

$Si\text{-}O\text{-}Na^+ + H^+ + OH^- \rightarrow Si\text{-}OH^+ + Na^+(solution) + OH^-$

(ii) Loss of soluble silica in the form of $Si(OH)_4$ to the solution, resulting from breaking of Si-O-Si bonds and subsequent formation of surface silanol groups (Si-OH) in the process; $Si\text{-}O\text{-}Si + H_2O \rightarrow Si\text{-}OH + OH\text{-}Si$

(iii) Condensation and re-polymerization of surface silanols to form an SiO_2 rich surface layer;

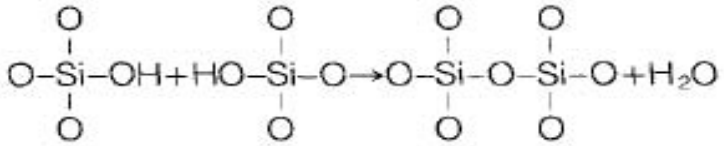

(iv) Migration of Ca^{2+} and PO_4^{3-} to the surface through the silica-rich layer and formation of a Ca-P rich layer on the surface of the glass;

(v) Incorporation of OH^-, CO_3^{2-} from the solution and subsequent crystallization of the Ca-P layer to form HCA.

After these physical chemical reactions occur, biological moieties begin to interact with the glass surface.

1.5. Survey of literature on bioglass and bioactive glass-ceramics

Recently, a lot of work has been reported in the area of bioactive glass and glass-ceramics by various groups using a variety of constituent materials. Ebisawa *et al.* [60] have studied the compositional dependence of bioactivity of P_2O_5-free and Na_2O-free $CaO.SiO_2$ glasses through *in vitro* studies. The surface structural changes have been investigated by soaking the glasses in SBF. They have also observed the effects of adding third components, such as MgO, B_2O_3, Fe_2O_3 and CaF_2 on the bioactivity of these glasses. The observed results indicate that P_2O_5-free $CaO.SiO_2$ glass bonds to the living bone. In addition, an increase in bioactivity with addition of Na_2O and P_2O_5 content, and a decrease in the same with the addition of MgO, B_2O_3, CaF_2 and Fe_2O_3 have been revealed. It has also been demonstrated that $CaO\text{-}SiO_2$ based glasses without phosphate formed an apatite layer on their surface when exposed for 2 to 30 days in SBF [44]. Work carried out by Locker *et al*. [61] determined the effect of substituting sodium oxide for calcium oxide on some glass properties. Ohtsuki *et al*. [62] studied the mechanism of apatite formation on CaO-SiO2-P_2O_5 glasses by *in vitro* studies. They found that $CaO\text{-}SiO_2$-based glasses formed the surface apatite layer in SBF, whereas, $CaO\text{-}P_2O_5$-based glasses did not form it. Studies on bioactivity of $1.25CaO.SiO_2$ glass by Branda *et al*. [63] revealed that the mechanism involves the rapid reactions of hydrolysis and successive condensation and re-polymerization of silicate substrate. Martinez *et al*. [64] studied $CaO\text{-}SiO_2$ binary system with different silica content (50-90 mole %) *in vitro*. The FTIR, XRD, SEM and EDS analysis of the surface of these glasses after *in vitro* assays reveal the formation of a HCA layer. The growth rate of this layer was found to mainly depend

on the glass composition. Glasses with lower SiO_2 content and higher CaO content exhibited higher apatite layer growth rates. Ohtsuki *et al*. [65] investigated the effect of Al_2O_3 on the bioactivity of CaO-SiO_2 glasses. CaO-SiO_2-Al_2O_3 glasses containing Al_2O_3 less than 1.5 mole % as well as Al_2O_3-free CaO-SiO_2 glasses formed the surface apatite, whereas, CaO-SiO_2-Al_2O_3 glasses containing more than 1.7 % mole Al_2O_3 as well as SiO_2-free CaO-Al_2O_3 glass did not form it. This indicates that only a small amount of addition of Al_2O_3 to glass compositions suppresses the bioactivity of glasses and glass-ceramics by suppressing apatite formation on their surfaces in the body.

Attempts have been made to study the bioactivity of binary calcium silicate glass CaO-SiO_2 by adding a third component such as Na_2O, B_2O_3, Al_2O_3, Fe_2O_3, P_2O_5 and F^- after soaking the bioactive glasses *in vitro* for 8 - 25 weeks. All glasses, except the Fe_2O_3 containing glass, formed a Ca/P-rich layer in combination with a Si-rich layer on their surfaces within 8 weeks. A detachment test performed 8 weeks after implantation showed that only glasses containing B_2O_3, P_2O_5 and F^- have good compatibility and hence, bonded tightly with bone, while the Fe_2O_3 containing glass did not form these layers, nor did it attach to bone even after 25 weeks [66].

Fujii *et al.* [67] probed the structural roles of fluorine on the bioactivity of NaF-CaO-SiO_2 glasses. Three calcium silicate glasses containing 10 mole % fluoride ions had different apatite-forming abilities. In the case of 10NaF.45CaO.45SiO_2 and 50CaO.50SiO_2 glasses containing the same CaO/SiO_2 ratio, apatite-forming ability was lower for the former. This indicated that the addition of fluoride ions suppressed the apatite-forming ability, irrespective of the structural similarity of the silicate network based on the ratio of CaO/SiO_2 between the glasses. Franks *et al*. [68] prepared phosphate

based glasses in the system $CaO–Na_2O–P_2O_5$ and studied their thermal parameters. The glasses had a fixed P_2O_5 content of 45 mole % and the CaO/Na_2O ratio was varied. In high Na_2O containing glasses, $NaPO_3$ and a second unidentified phase that is probably calcium rich formed. In the middle compositional region, multiple phases precipitated out, which were identified as $NaPO_3$ and $Na_4Ca(PO_3)_6$. For the high CaO content glasses, $Na_4Ca(PO_3)_6$ was the only phase formed. Further, $NaPO_3$ forms via a bulk nucleation mechanism whereas, $Na_4Ca(PO_3)_6$ forms via surface nucleation. Cacaina *et al*. [69] looked at the behavior of yttrium containing bioactive glasses SiO_2-Na_2O-P_2O_5-CaO-K_2O-MgO in SBF environments. The addition of yttrium to a bioactive glass increases its structural stability which therefore, induced a different behaviour of the glasses in SBF environment. Lee *et al*. [70] observed the effect of iron state on crystallization and dissolution in Fe_2O_3-CaO-SiO_2 glasses. It was found that higher CaO content interrupts the crystallization of magnetite crystallites as well as the oxidation of iron, that is, the transformation from Fe^{3+} to Fe^{2+}. In order to use as thermoseed in hyperthermia treatment, compositions with low CaO content would be most useful. Roman *et al*. [71] have studied the bioactivity of $CaO–MgO–SiO_2–P_2O_5–CaF_2$ (G13) glass. A non-bioactive glass-ceramic (GC13) that contains hydroxyapatite [$Ca_5(PO_4)_3OH$], diopside [$CaMg(SiO_3)_2$] and althausite (Mg_2PO_4OH) as crystalline phases has been obtained by thermal treatment of a parent bioactive glass G13. However, in order to induce bioactivity, GC13 was chemically treated with 1 M HCl for different periods of time. A new bioactive glass-ceramics containing CaO-MgO-SiO_2-P_2O_5-CaF_2 has been developed by Liu [72] exhibits flexural strength of 233 MPa and fracture toughness of 2.95 $MPam^{1/2}$. It contains stable, randomly distributed crystalline phases (*i.e.* akermanite,

wollastonite and apatite phases) at temperatures of 930-1150 ºC. The prospects of utilization of glass-ceramics in medical applications, especially those requiring load-bearing capacity are promising. Kokubo *et al*. [30] carefully studied the formation of glass-ceramics by observing the microstructure of the crystallized products. Crystallization of the parent glass in a bulk form led to the occurrence of large cracks in the crystallized product. Crystallization of the same glass in a powder compact led to the formation of a crack-free dense crystallized product due to uniform precipitation of both apatite and wollastonite fine crystals throughout the glass matrix. Kokubo [49] have also reported bioactivity in MgO-CaO-SiO_2-P_2O_5 glass-ceramics. These glass-ceramics showed bioactivity and a fairly high mechanical strength which decreased only slowly, even under load-bearing conditions in body. The bioactivity of this glass-ceramics was attributed to apatite formation on its surface body. Dissolution of calcium and silicate ions from the glass-ceramics was considered to play an important role in forming the surface apatite layer. Oliveira *et al*. [73] have prepared the glass and glass-ceramics of MgO-CaO-P_2O_5-SiO_2 glass in different compositions. A Ca/P-rich layer identified as hydroxyapatite developed on both samples after immersion in SBF for various days. The precipitated film on the glassy sample was weakly bonded, whereas the one formed on the glass-ceramics surface was strongly adherent. Although, the glass-ceramics has higher chemical and mechanical stability, the glasses are expected to be capable of bone bonding with bone which results in good bioactivity. Salinas *et al*. [74] reported *in vitro* bioactivity in glass and glass-ceramics of the CaO-SiO_2-P_2O_5-MgO-CaF_2 system. The glass sample showed *in vitro* bioactivity evidenced by the formation of a calcium phosphate-rich layer on its surface when soaked in SBF. However, the glass-ceramics

containing diopside, althausite and akermanite did not form any mineralized layer even after 6 weeks in SBF. The same glass-ceramics attacked with 1M HCl selectively deposits an apatite layer after 4 days in SBF. Serra *et al*. [75] studied the bonding configuration of bioactive silica based glasses and identified the silicon-oxygen groups by spectroscopic techniques.

Kamitakahara *et al*. [76] investigated the effect of the addition of ZnO in a modified A/W glass-ceramics. The chemical durability of the glass-ceramics increased with increasing ZnO content and their apatite-forming ability decreased concomitantly. The addition of ZnO may provide CaO-SiO_2-P_2O_5-CaF_2 glass-ceramics with appropriate biodegradation, as well as the enhancement of bone formation. Balamurugan *et al*. [77] studied the development and *in vitro* characterization of CaO-P_2O_5-SiO_2-ZnO bioglass by sol-gel technique. Incorporation of Zn into a bioglass system does not diminish the bioactivity of such a material. Addition of Zn is beneficial for cell attachment and for maintaining the pH of SBF within the physiological limit by forming zinc hydroxide in the SBF solution. Jaroch *et al*. [78] studied the bioactivity of SiO_2-CaO-ZnO system. Zn is an essential trace element which may be effective in promoting hard tissue healing. Using a constant silica content (70 mole %), the ratio of Ca to Zn was varied (1.5, 3.5, or 6.5), as was the stabilization temperature (650, 750, or 850 °C), to examine such effects on the bioactive response and Zn release in SBF. Structural studies revealed the development of $CaSiO_3$ and $Ca_2ZnSi_2O_7$ crystalline phases during stabilization at 850 °C only. N_2 adsorption analysis determined that the specific surface area (BET) varied between 14 and 179 m^2/g, and was dependent of composition and stabilization temperature, as was the average initial pore size (51-125 Å). The formation of

hydroxycarbonate (HCA) and amorphous calcium phosphate (ACP) was observed at 14 days for samples stabilized at 650 or 750 °C. Only ACP layers were observed on such samples prior to 14 day. Relative to the Ca levels at 14 day (60-485 µg/ml), Zn levels in solution were relatively low (0.06-1.18 µg/ml). Compositional analysis suggested that released Zn was incorporated into the forming calcium phosphate reaction layer, thereby preventing concentrations of the essential trace element from reaching potentially toxic levels. Ivanova *et al*. [79] examined bioactive ceramics in CaO-Al_2O_3-P_2O_5-ZnO system. It was found that the main crystalline phases in the glass ceramics were $Ca(PO_3)_2$ and $Ca_2P_2O_7$. This glass ceramic is claimed to be more bioactive than hydroxylapatite in the initial stage after implantation. Du *et al*. [80] have prepared Zn-containing glass by the substitution of CaO in 58S bioactive glass with 0.5 and 4 wt. % ZnO. Glass-ceramics was obtained by heat-treating the glass at 1200 °C. The results indicate that Zn promotes the crystallization of SiO_2 and wollastonite in glass-ceramics, and proper crystallization can enhance the bending strength of the glass-ceramic. This study suggests that the glass and glass-ceramics with different ZnO content might be used as bioactive bone implant materials.

1.6. Preparative methods and their characteristics

1.6.1. Melt derived bioglass and glass-ceramics

As previously mentioned, the study of bioactive materials began with the discovery that silicate glasses of a specific composition were able to bond to bone. The first bioactive glass *viz*., Bioglass® 45S5, introduced by Hench in 1971 [14], still remains the most used in clinical applications. Bioglass® 45S5 is produced by fusion, and its specific

composition is 45% SiO_2, 24.5% CaO, 24.5% Na_2O, 6% P_2O_5 (expressed as wt.%). The name '45S5' refers to both the SiO_2 content (45 % wt.) and the Ca/P molar ratio (5).

Table 1.6.1: Composition, structure and index of bioactivity of different glasses [32]

Composition	*Bioglass® 45S5*	*S53P4*	*Glass-ceramic Ceravital®*	*Glass-ceramic Cerabone® A-W*	*Glass-ceramic Ilmaplant® L1*	*Glass-ceramic Bioverit®*	*Sintered hydroxypatite $Ca_{10}(PO_4)_6(OH)_2$ > 99.2%*	*Sintered β-3CaO · P_2O_5 > 99.7%*
Na_2O	24.5 wt%	22.6 wt%	5–10 wt%	0 wt%	4.6 wt%	3–8 wt%		
K_2O	0		0.5–3.0	0	0.2	3–8 wt%		
MgO	0		2.5–5.0	4.6	2.8	2–21		
CaO	24.5	21.8	30–35	44.7	31.9	10–34		
Al_2O_3	0		0	0	0	8–15		
SiO_2	45.0	53.9	40–50	34.0	44.3	19–54		
P_2O_5	6.0	1.7	10–50	16.2	11.2	2–10		
CaF_2	0			0.5	5.0	F 3–23		
B_2O_3	0							
Phase	Glass	Glass	Apatite	Apatite ($Ca_{10}(PO_4)_6(O,F_2)$)	Apatite	Apatite	Apatite ($Ca_{10}(PO_4)_6(OH)_2$)	Whitlockite (β-3CaO · P_2O_5)
			Glass	β-Wollastonite ($CaO \cdot SiO_2$)	β-Wollastonite	Phlogopite ($(Na,K)Mg_3(AlSiO_{10})F_2$)		
				Glass	Glass	Glass		
Density (g/cm^3)	2.6572			3.07		2.8	3.16	3.07
Hardness (Vickers) (HV)	458 ± 9.4			680		500	600	
Compressive strength (MPa)			500	1080		500	500–1000	460–687
Bending strength (MPa)	42(Tensile)			215	160	100–160	115–200	140–154
Young modulus (GPa)	35		100–150	118		70–88	80–110	33–90
Fracture toughness, K_{Ic}(MPa $m^{1/2}$)				2.0	2.5	0.5–1.0	1.0	
Slow crack growth, n				33			12–27	
Index of bioactivity I_B	12.5	3.8	5.6	7.5 (est)			3.1	

Hench`s group explored many other compositions in the same SiO_2-CaO-Na_2O-P_2O_5 system, and later other groups tried to synthesize more complex bioactive glasses or glass-ceramics. A comparison between composition and index of bioactivity of a few of them is shown in Table 1.6.1 [32]. All these materials are bioactive, in that they form a biologically active layer of HCA on their surface when implanted.

1.6.2. Sol-gel bioglass and glass-ceramics

In the early 1990s, Li *et al.* [81-82] synthesized some bioactive glasses by sol-gel technique. This new class of bioactive glasses showed a higher compositional range of bioactivity. Glasses in the SiO_2-CaO-P_2O_5 system could form a layer of HA with silica content up to 90 %. This is quite different with respect to that observed on melt-derived bioactive glasses, which showed bioactivity only up to 60 % SiO_2 content.

One of the main differences between sol-gel and melt-derived glasses lies in surface area. For sol-gel glasses, surface area ranges from ~ 200 to 650 m^2/g, whereas melt-derived glasses show surface area < 1 m^2/g for rough particles, and ~ 2 m^2/g for micron sized particles. This big difference is due to the temperature and synthesis conditions of two types of materials. Sol-gel glasses are synthesized in an aqueous environment, and then dried and stabilized at temperatures that do not exceed 600 °C. Surface and structural properties (such as surface area and porosity) can be finely modulated depending on composition and synthesis conditions. Melt derived bioactive glasses are melted at temperatures higher than 1000 °C and cooled rapidly. The resulting material does not have any porosity at all, and surface area depends only on particle size obtained by grinding up the powders. HA is claimed to be deposited much faster on sol-gel bioactive glasses than on traditional melt derived glasses, and the materials can be resorbed, in some cases. In fact, the porous structure of gel bioactive glasses allows the formation of a hydrated layer inside the material, where biological moieties can enter maintaining their structural configuration and biological activity [83-85].

Many different systems synthesized by sol-gel technique showed bioactivity when immersed in SBF. Their composition was chosen in the binary system $CaO\text{-}SiO_2$ [86-87], ternary system $SiO2\text{-}CaO\text{-}P_2O_5$ [88-91] and quaternary system $SiO_2\text{-}CaO\text{-}P_2O_5\text{-}MgO$ [92-93]. In general, higher amount of SiO_2 in glass composition induces larger surface area, but lower degree of porosity. Moreover, higher temperatures used in the synthesis process decrease the glass surface area. However, the influence of surface, textural and composition parameters on bioactivity of the sol-gel derived samples is not completely clear yet.

The study of sol-gel bioactive glasses opened the field to the research of even simpler sol-gel synthesized materials. In the early 1990s, Li and colleagues showed that HA is deposited on the surface of a gel of silica when soaked for a few days in SBF [94-96]. Different factors influence HA deposition. A first relevant one is the presence of pores. HA did not precipitate on non-porous silica, such as quartz [94], or gel-silica treated at temperatures $\geq$ 900 °C [97] (sintering occurred at such temperatures, and porosity was eliminated). Pores could be sites of nucleation of HA because the degree of supersaturation of the solution is usually higher there than in the solution bulk. Some distinction depending on the pore size should be made: if the pores were smaller than ~ 6 Å, HA could not precipitate, because phosphate ions were too big to diffuse into the pores. Peltola *et al*. [90] showed that mocroporous silica gels obtained with basic catalysis. Hydroxylation is another relevant factor for HA precipitation: Cho *et al*. [97] proposed that silanol groups formed when porous silica is immersed in SBF could be sites for HA nucleation. Still, experimental evidence for the bonding of HA to silanol

groups has not been given yet, and a clear distinction between the relevance of surface hydroxylation, surface area extension and degree of porosity has not been outlined.

1.6.3. Thin film deposition of bioglass and bioglass ceramics

Bioactive coating materials mimic the excellent bioactivity of the bioactive glasses or ceramics, apart from possessing the advantageous mechanical properties of metals or alumina. The bone-bonding capacity of these coatings may help provide cementless fixation of orthopedic prostheses, especially in short term stabilization of the implants. But in long term implantation, the bioactive coating materials have deficiencies with respect to reliability of the coating / implant interface. Another approach to solving the mechanical limitations of bioactive glasses and ceramics for load-bearing applications is to apply the material as a coating on a mechanically tough substrate. Various techniques are available to deposit calcium phosphate coatings on metal implants, including hot isostatic pressing, plasma or flame spraying, ion-beam sputter deposition, electrophoretic deposition, pulsed laser deposition (PLD) and radio frequency magnetron sputtering [98-101]. Recently, a lot of work has been reported in the area of bioactive glass and glass-ceramics by various groups using a variety of constituent materials.

Gyorgy *et al.* [102] studied the bioactive glass, HA, and ZrO_2-doped HA thin films prepared by pulsed laser deposition on Ti substrates. The depositions were performed in oxygen and water vapour atmospheres, at pressure values in the range of 5-40 Pa. Biocompatibility tests showed that cell growth was better on HA than on bioactive glass thin films. Cannillo *et al.* [103] studied apatite and wollastonite (A/W) crystals in the MgO-CaO-SiO_2-P_2O_5 glassy matrix, thermally sprayed by atmosphere plasma

spraying on Ti-6Al-4V substrates. Since in the as-sprayed conditions the coating microstructure was defective because of pores and cracks, thermal treatments on A/W plasma-sprayed coatings were conducted to enhance the coating microstructure. Zhao *et al.* [104] studied the role of the pressure in pulsed laser deposition (PLD) of SiO_2-Na_2O-CaO-P_2O_5 bioactive glass films. Takamasa *et al.* [105] studied apatite forming and hydroxyapatite bonding ability of Ti-based bulk metallic glasses (BMGs). Powder mixture of $CaHPO_4.2H_2O$ and $Ca(OH)_2$ and the BMGs disks were treated with autoclave for hydrothermal hot-pressing (HHP) simultaneously. Borrajo *et al.* [106] studied *in vitro* behavior of bioactive glass coatings grown by PLD on silicon and titanium substrates. The temporal evolution of the bioactivity process was followed for thick bioactive glass coatings deposited on biomorphic silicon carbide ceramics. Verne *et al.* [107] studied double-layer glass-ceramic coatings on Ti6Al4V substrates by dipping coating and firing. The optimized coating method was then used to coat Ti6Al4V screws for dental applications. Mardare *et al.* [108] studied of thin films of MgO-CaO-P_2O_5-SiO_2 system bioactive glass-ceramics deposited on titanium and silicon substrates by RF magnetron sputtering. The adhesion strength for as-deposited films was approximate 40 MPa, but after crystalline the strength dropped to about half this value due to the presence of cracks. Samples kept in SBF showed an apatite-like layer, suggesting that the films are bioactive. Ishizawa *et al.* [109] studied an anodic titanium oxide film containing Ca and P (AOFCP) by hydrothermal treatment. HA crystals were precipitated by hydrothermally heating the AOFCP at 300 ℃. *In vitro* tests for 300 days suggested that the stability of the film was high.

1.7. Biomaterials and magnetism

Magnetism, which is an intrinsic property of every atom, has a profound influence on living organisms. The hemoglobin in our blood is an iron complex and is magnetic in nature. Magnetism and magnetic materials have a strong role to play in health care and biological applications [100-114]. Some of the early medical applications of magnetic materials were, for example, the removal of metallic objects from the body of animals and humans [115]. The use of materials in biological environment for implantation or for replacement of a part or a function of the body in a reliable and physiologically acceptable manner was a challenge for the last several decades. Of late the combination of fine particles and magnetism in the field of biology and biomaterials has been found useful in sophisticated bio-medical applications such as cell separation [116-118], drug delivery, and magnetic intracellular hyperthermia treatment of cancer [119-121].

1.7.1. Role of magnetism in biomaterials

Magnetism has a strong role play in some specific bio applications. For example, in sorting of cells, interactions between biological cells and magnetic nanoparticle occurs which lead to separation under the action of magnetic field gradient. The characteristics of hard and soft magnetic materials as well as the particle size dependent properties have been exploited for different bio applications. In magnetic hyperthermia, the ferromagnetic, ferrimagnetic, as well as superparamagnetic properties of particles are useful. The losses due to magnetization and reorientation of these particles depend upon the type of demagnetization process, which is determined by intrinsic properties such as magnetocrystalline anisotropy and extrinsic properties such as particles size and

microstructure. A great deal of information can be learned about the magnetic properties of a material by studying its hysteresis loop. A hysteresis loop shows the relationship between the induced magnetization (M) and the applied magnetic field (H). It is often referred to as the M-H loop. An example hysteresis loop is shown in Fig. 1.7.1.

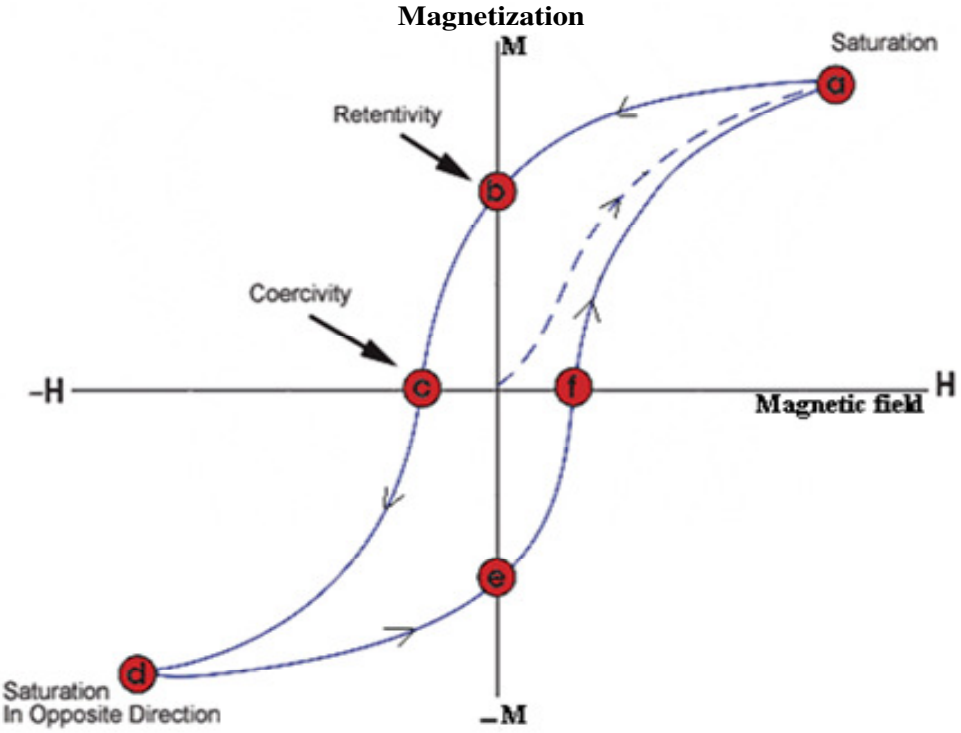

Fig. 1.7.1: Response of a ferro or ferrimagnetic material to applied magnetic field.

The loop is generated by measuring the magnetization of a ferrimagnetic material while the magnetic field is changed. The dashed line shows the initial magnetization curve of a demagnetized material. The magnetization increases with increasing applied magnetic field and saturates at higher magnetic fields. At point 'a', almost all of the magnetic domains are aligned and an additional increase in the magnetic field will

produce very little increase in magnetisation. The material has reached the point of magnetic saturation (M_s). When the magnetic field is decreased to zero, the curve will move from point 'a' to point 'b'. The induced magnetization does not decrease to zero, but the alignment of most of domains during magnetization results in a remanent magnetization or remanence (M_r). When the magnetic field is reversed, the curve moves to point 'c', the induced magnetization decreases and finally becomes zero at a value of the magnetic field strength called the coercive force or coercivity (H_c). As the magnetic field is increased in the negative direction, the material will again become magnetically saturated (M_s) but in the opposite direction (point 'd'). Reducing H to zero brings the curve to point 'e'. Increasing H back in the positive direction will return M to zero. Magnetic saturation in the reverse direction and produces a saturation (M_s), coercivity (H_c) and remanence (M_r) values of the same magnitudes as in the first quadrant. As an applied field is cycled from one direction to the other direction, the hysteresis is followed. The curve will take a different path from point 'f' back to the saturation point where it with complete the loop. Since the area of the hysteresis loop represents the energy or work to bring about changes in the magnetic domain structure, the maximum value of $(MH)_{max}$, called the energy product, represents a net loss in the system, usually in form of heat. The area inside the second quadrant of the loop determines the energy consumed in one cycle. The hysteretic power loss of an AC device can be dissipated in the form of heat for hyperthermia applications. Superparamagnetic particles would not exhibit hysteresis losses. But Neel relaxation in them is equally useful in generating and dissipating heat.

1.7.2. Hyperthermia treatment for cancer

Cancer is a general term for more than 100 diseases that are characterized by uncontrolled, abnormal growth of cells. Cancer is a group of many related diseases that begin in cells, the body's basic unit of life. Normally, cells grow and divide to produce more cells only when the body needs them. This orderly process helps keep the body healthy. Sometimes, however, cells keep divided when new cells are not needed. These extra cells form a mass of tissues, called a growth or tumor. Heat above 41 °C also pushes cancer cells toward acidosis (decreased cellular pH) which decreases the cell viability and transplant ability [122].

Hyperthermia is basically a heat treatment process. The temperature of the tissue is elevated artificially with the aim of receiving therapeutic benefits [122]. In the last decades of the nineteenth century, it was observed that a few patients with high fever demonstrated reduction of tumors. Also, a few others demonstrated that moderately elevated temperatures (< 45 °C) cause a significant regression and even complete destruction of tumors. As a result, the heat treatment of cancer gained a lot of attention not only as a modality by itself, but it was also demonstrated that it gives significant results when used in combination with other modalities such as radiotherapy and chemotherapy. It is often very difficulty to target the cancerous cells specifically. Any attempt to destroy cancer cells may also result in the damage to surrounding normal cells. Heat treatment has the advantage that it can specifically target the cancer cells. Heat treatments of organs, such that the temperature is increased to 42-46 °C and the viability of cancerous cells reduces, is know as hyperthermia. It is based on the fact that tumors cells are more sensitive to temperature than normal cells [123]. In hyperthermia it is

essential to establish a heat delivery system, such that the tumor cells are heated up or inactivated while the surrounding normal tissues are unaffected. Using magnetic drug carriers is one method of drug targeting. In this technique, a powerful external magnet is placed over the tumor. After being injected into the blood stream, the magnetic drug carriers would be pulled by the magnetic field into the tumor region (Fig. 1.7.2).

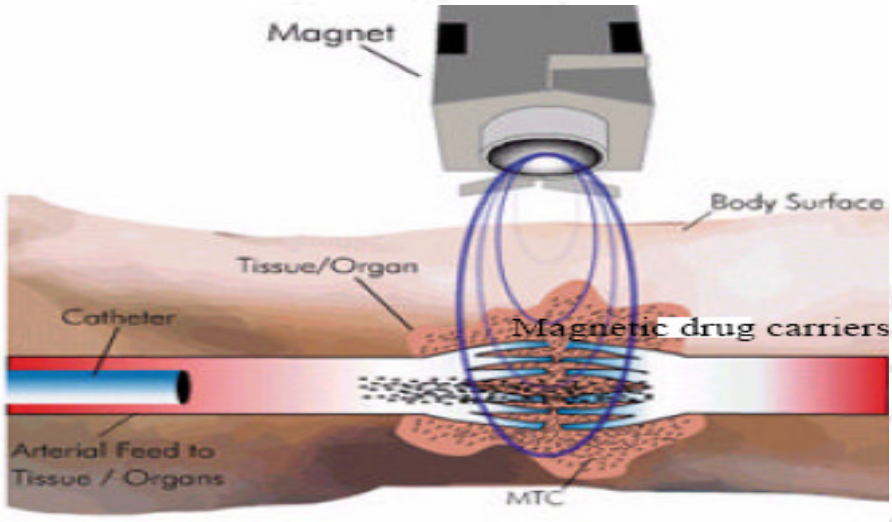

Fig. 1.7.2: Magnetic drug targeting into the tumor region [124].

Hyperthermia treatment can be classified in various ways. One way to classify hyperthermia is as external and internal hyperthermia. In external hyperthermia, the heat is applied from outside the body using various means such as microwaves, radiofrequencies, ultrasound etc. whereas in internal hyperthermia, certain foreign substances are inserted inside the body to act as sources of heat. Hyperthermia is also classified as local (heat is applied to a small area, such as a tumor), regional (heat is applied to large areas of tissue, such as a body cavity, organ or limb) and whole body hyperthermia (heat is applied to the entire body using thermal chambers or hot water blankets) [125]. The therapeutic benefits of heat have been known for many centuries.

But its use in the treatment of cancer has been developed recently. It has been demonstrated that hyperthermia when combined with radiotherapy produced better results over radiation alone. As a result hyperthermia has gained a lot of attention and significant research is going on in this new modality for treatment of cancer.

1.7.3. Bioactive magnetic glass-ceramics for hyperthermia application

Magnetic hyperthermia is the method of heating body tissue using magnetic materials. In this process, magnetic (ferrimagnetic or ferromagnetic) materials in the form of rods or pellets (thermoseeds) are introduced near the tumor. When these thermoseeds are subjected to oscillating magnetic fields, the materials are heated due to induction heating. The rate and the extent of heat generated can be controlled by changing the strength and the frequency of the applied alternating magnetic field. Recently, a lot of work has been done in the area of magnetic hyperthermia by various groups using a variety of materials.

Bretcanu *et al*. [126] studied the effect of melting temperature (between 1440-1500 °C) on magnetic properties in SiO_2-Na_2O-CaO-P_2O_5-FeO-Fe_2O_3 ferrimagnetic glass-ceramics samples. These glass-ceramics contain magnetite and hematite crystals in a glassy matrix. The magnetic hysteresis parameters are strongly influenced by glass-ceramics microstructure, which depends on melting temperature. The highest specific power loss is obtained for samples melted at 1550 °C (29 W/g), which presents the highest hysteresis area. Kawashita *et al*. [127] reported the preparation of pure Fe_3O_4 microspheres, 20-30 µm in diameter. These microspheres, however, showed heat generation as low as 10 W/g, at 300 Oe and 100 kHz, as they were composed of Fe_3O_4 crystals of 1 µm size. The heat-treated microspheres showed heat generation as high as

41 W/g, under the same magnetic field. Bretcanu *et al*. [128] studied two different ferrimagnetic glass-ceramics with the composition of the system Na_2O-CaO-SiO_2-P_2O_5-FeO-Fe_2O_3. The magnetite crystallite size increased with iron oxides concentration from 34 nm to 54 nm in glass-ceramics samples. The glass-ceramics samples showed heat generation 65 W/g and 25 W/g, at 500 Oe and 440 kHz. Singh *et al*. [129] reported on the effect of iron oxides on the bioactivity and magnetic properties in SiO_2-Na_2O-Fe_2O_3-CaO-P_2O_5-B_2O_3. The glass-ceramics samples exhibited Na_3CaSiO_3 and $Na_{3-x}Fe_xPO_4$ phases. High coercive force and small magnetic moments were observed in all the samples. However, magnetic moment of the samples decreased with increased iron concentration. Bretcanu *et al*. [130] have also studied the bioactivity and magnetic properties of SiO_2-Na_2O-CaO-P_2O_5-FeO-Fe_2O_3 glass-ceramics. The magnetite crystals in their samples were about 50 nm in dimension. The as prepared glass-ceramics has a saturation magnetization of 34 $A.m^2/kg$ and a coercive force of 6.7 kA/m. The estimated magnetic loss / cycle under the magnetic field up to796 kA/m is around 1.45 mJ/g. This material showed a bioactivity after 2 weeks of soaking in SBF with the formation of a hydroxylapatite layer on their surfaces. Leventouri *et al*. [131] studied the effect of processing parameters on the magnetic properties in SiO_2–CaO–Fe_2O_3–P_2O_5-Na_2O glass-ceramics. Two major phases develop in the bulk material: calcium phosphate crystallizing in monoclinic and rhombohedral structures and magnetite in an orthorhombic structure. A trend of increased magnetic hysteresis loss was observed when the concentration of iron oxide was increased. Ebisawa *et al*. [132] studied the bioactivity of ferrimagnetic glass-ceramics in CaO-SiO_2-FeO-Fe_2O_3 system and reported that glass-ceramics with Na_2O or B_2O_3 added in combination with P_2O_5 in the matrix helps these

samples to exhibit bioactivity. Kawashita *et al*. [133] studied glass-ceramics containing zinc ferrite ($Zn_xFe_{3-x}O_4$) in a $CaO\text{-}SiO_2$ based glass matrix and reported heat treatment of $ZnO\text{-}Fe_2O_3\text{-}CaO\text{-}SiO_2$ glasses between 700 °C to 1150 °C for different time periods in a 95 CO_2 + 5 H_2 atmosphere. The content and crystallite size of the $Zn_xFe_{3-x}O_4$ increased with increasing heat treatment temperature from 2.2 mass % and 6 nm at 700 °C to 37.0 mass % and 130 nm at 1150 °C. The coercive force of the heat treated powders increased from 10.7 Oe at 700 °C to 167.6 Oe at 1000 °C, and then decreased to 63.0 Oe at 1150 °C. The saturation magnetization of the heat treated powders increased with increasing heat treatment temperature from 6.7 emu/g at 700 °C to 38.4 emu/g at 1150 °C. The powder heat treated at 1150 °C for 5 h in a 95 CO_2 + 5 H_2 atmosphere showed the maximum amount of heat generation of 12.4 W/g. Eniu *et al*. [134] examined the vicinity and magnetic interactions of iron ions of $CaO\text{-}P_2O_5\text{-}SiO_2\text{-}Fe_2O_3$ glass and glass-ceramics. Maintaining Ca/P ratio similar to that in hydroxyapatite, up to 30 mole % of iron oxide was added. After heat treatment, the iron preponderantly crystalliises as magnetite, but hematite and maghemite are also developed. Iron ions seem to form low-sized magnetic domains even in glass samples. A ferromagnetic behavior with the Curie temperature around 547 °C was observed in the glass-ceramics samples. Lee *et al*. [135] studied ferrimagnetic glass-ceramics formed in the $Fe_2O_3\text{-}CaO\text{-}SiO_2$ system and reported that the lyses of carcinoma cells were examined after exposure to an alternative magnetic field both *in vitro* and *in vivo*. Kawashita *et al*. [136] have synthesised crack-free ferrimagnetic $\gamma\text{-}Fe_2O_3$ microspherers of 20-30 μm diameter. Their saturation magnetasation and coercive force were 68 emu/g and 198 Oe, respectively. Their heat generation in an alternating magnetic field of 300 Oe at 100 kHz was estimated to be 42 W/g. The

microspheres showed *in vitro* heat generation when they were dispersed in an agar phantom and placed under an alternating magnetic field. Ebisawa *et al*. [4] reported that the bone bonding ability and bone heating ability in CaO-SiO_2-Fe_2O_3-B_2O_3-P_2O_5 glass-ceramics system. The resulting glass-ceramics containing magnetite and wollastonite crystals showed high saturation magnetization. The bone-heating ability of this glass-ceramics was investigated by applying a maximum 300 Oe, 100 kHz magnetic field. The granules of glass-ceramics filled in the rabbit tibiae heated the whole surrounding bone to more than 42 °C and maintained this temperature for 30 min.

Various techniques such as treatment with hot water, infrared rays, ultrasound and microwaves have been attempted for heating the tumours. Of these, the non-invasive ultrasound and electromagnetic techniques are claimed [A.Y. Cheung and A. Neyzari, Cancer Research (Suppl.) **44** (1984) 4736] to be potentially useful for deep local hyperthermia treatment of deep-seated tumours. Hyperthermia treatment based on magnetic bioglass-ceramics has turned out to be an alternative and promising technique in such applications. One cannot go forward without quoting two excellent patents on this topic, viz., U.S. Patent 4323056 entitled "Radio frequency induced hyperthermia for tumor therapy" filed by N.F. Borrelli, A.A.. Luderer, G.R.Mansfield, J.N. Panzarino in 1982 and U. S. Patent 6167313 entitled "Targeted Hysteresis hyperthermia as a method for treating diseased tissue filed by B. N. Gray and S. K. Jones in 2000.

1.8. Motivation and preview of the thesis work

Magnetic bioglass-ceramics (MBC) are mulitiphase, biocompatible and bioactive materials that were introduced as thermoseeds for hyperthermia treatment of cancer. Such glass-ceramics, were first prepared by Kokubo [49] for hyperthermia treatment of bone

cancer, and they have been tested to be effective in curing animal bone cancer [4]. MBC are synthesized by melting procedures of the original bioglass with addition of Fe_2O_3 in the oxides (P_2O_5, CaO, SiO_2). Fe_2O_3 forms magnetite (Fe_3O_4) upon heat treatment of the glass. It can heat the surrounding bone locally by magnetic hysteresis loss to temperatures that are effective for cancer treatment, when subjected to an external alternating magnetic field. Application of MBC is based on the fact that cancer cells survive less on heat treatment than ordinary tissue cells in the temperature range 42-45 °C. When granular particles of MBC are implanted around a bone tumor, they bond to the bone as well as with each other forming a surface apatite layer. Then, when the bone tumor is placed under an alternating magnetic field, it will be locally heated up to temperatures that are effective for bone cancer treatment. Generally, tumors are heated easier than the surrounding tissues, since blood vessels and nervous systems are poorly developed in the tumor. So, cancer cells are easily killed by heat treatment, since oxygen supply via the blood vessels is not sufficient in the tumor [123]. A survey of the literature showed that there is ample scope of work in these exciting and application orientation materials.

After a careful survey of the literature, it was decided to study MBCs derived from the following three glass compositions:

(i) $41CaO(52\text{-}x)SiO_2 4P_2O_5 x Fe_2O_3 3Na_2O$, ($x$ = 0, 2, 4, 6, 8 and 10 mole %) . This is basically the original bioglass [14] with the addition of Fe_2O_3.

(ii) $4.5MgO(45\text{-}x)CaO 34SiO_2 16P_2O_5 0.5CaF_2 x\ Fe_2O_3$ (x = 0, 5, 10, 15 and 20 wt. %). MgO based glasses (without Fe_2O_3) have high mechanical strength [30, 49]. Since the glass-ceramics are expected to have higher mechanical strength than the base glasses, this system could offer high strength MBCs suitable for load-bearing applications.

(iii) (65-x)SiO_2-20(CaO, P_2O_5)-15Na_2O-x(ZnO,Fe_2O_3) (x = 6, 9, 12, 15, 18 and 21 mole %) with [molar ratio Ca/P =1.67 and Fe/Zn = 6.5]. In this series of glasses, Ca/P molar ratio is maintained at 1.67, which is close to the molar ratio of the mineral phase in human bone. When crystallized, solid solutions of $Zn_xFe_{1-x}[Fe_{1-x}Fe_{1+x}]O_4$ (=$Zn_xFe_{3-x}O_4$), and $Zn_{0.4}Fe_{2.6}O_4$ (x = 0.4) form. These phases show higher saturation magnetization than Fe_3O_4 [137-138]. Therefore, glass-ceramics containing $Zn_{0.4}Fe_{2.6}O_4$ (Fe/Zn = 6.5) is expected to give higher heat generation for the same applied magnetic field as compared to the other two systems.

This thesis work is focused on (i) optimization of preparative conditions of the above MBCs, (ii) evaluation of the physical properties of MBCs relevant to applications, and (iii) evaluation of bioactivity of the MBCs *in vitro* by treating them in SBF. Since preparation of bioactive glasses is the first stage in the preparation of the bioactive glass-ceramics, optimization of glass compositions and evaluation of the properties of the base glasses need to be addressed first before attempting to optimize the properties the MBCs derived from them. Hence both the base glasses and the glass-ceramics derived from them are studied in this thesis work. It is worthy to point out that no systematic study has been reported on the influence of Fe_2O_3 content (in the starting composition) on the physical properties or biocompatibility of these MBCs. Moreover, a detailed account of the preparative conditions required to obtain optimized bone mineral phases in these MBCs is not available in the literature to the best of our knowledge. The potential application, general lack of systematic work and the rich scope for unraveling the physics of these materials have motivated the work presented in this thesis work.

Chapter 2

Experimental Techniques

In this chapter, the experimental techniques used in the current investigations are discussed together with the relevant theory associated with these techniques. Specific instruments used and the measurement methodology employed are also discussed. The experimental results presented in chapters 3, 4 and 5 are based on the experimental procedures outlined in this chapter.

2.1. X-ray diffraction

A commercial X-ray powder diffraction system (Seifert XRD 3003 T/T) was used for the verification of the amorphous nature of the as-quenched glass samples and to study the phase purity and crystal structure of the glass-ceramics samples. Cu-K_α radiation (1.541 Å) with a nickel filter was used in all measurements. The X-ray generator was operated with an acceleration voltage of 40 kV and tube current of 30 mA. The theta-theta goniometer was used in the reflection (Bragg-Brentano) geometry [Fig. 2.1] [139]. The data were collected in the usual θ-θ scan with an angular speed 1-2°/min. and a step size

of 0.02-0.05°. A thick layer of coarsely powdered glass/glass-ceramics sample was evenly spread over a polymetamethyacrylate (PMMA) place with a square depression and mounted on the goniometer for recording the X-ray diffraction (XRD) patterns. The XRD data provides the variation of intensity / counts per second (cps), recorded by the scintillation detector as a function of 2θ, where θ is the glancing angle. A standard polycrystalline silicon (Si) sample, provided with the instrument was used for the calibration of the instrument. The diffracted beam is detected by using a moveable detector, which is connected to a computer which controls all the functions of the X-ray diffractometer and records XRD patterns.

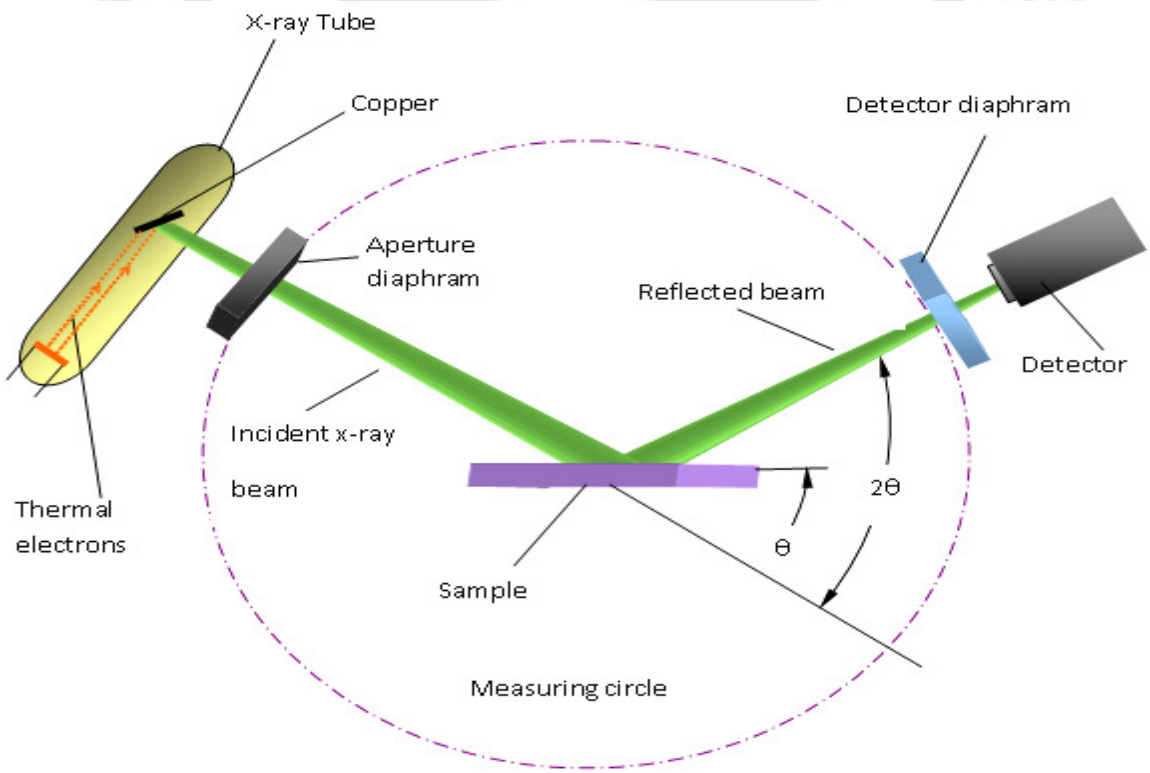

Fig. 2.1: Schematic diagram of the X-ray diffractometer. θ is the glancing angle and 2θ is the diffraction angle.

The XRD technique allows identification of various crystalline phases present in the material and provides other structural information such as the size of the crystallites, strains present inside the crystallites, *etc*. The average crystallite size (d) of the fine crystallites present in the sample was estimated from the peak broadening by using the Scherrer's formula [139]

$$d = \frac{\kappa\lambda}{\beta \cos \theta} \tag{2.1}$$

where, β is the full width at half maximum (FWHM) of the Bragg peak, λ is the wavelength of the Cu-K_α radiation, θ is the diffraction angle at the peak maximum and κ is a constant which depends upon the shape of the crystallite. Here, it is taken as 0.89 by assuming the shape of the crystallites to be spherical. The instruments broadening effect has been taken into account in the estimation procedure.

2.2. Differential Scanning Calorimetry

Differential scanning calorimeter (DSC) is a thermal analysis technique with which the thermal behavior of a sample can be studied over a wide temperature range, under isothermal as well as non-isothermal conditions. This thermal technique was commercially developed by Watson *et al*. [140]. In this technique, the sample and a reference material are maintained at the same temperature with respect to each other by proper application of electrical energy. The heat flow, *dH/dt* to the sample and a reference at the same temperature is recorded as a function of temperature. The reference is an inert material such as alumina or just an empty aluminum sample pan. In non-isothermal measurements, the temperature of the sample and reference are increased at a

constant heating rate. Thermal changes in a sample may be of exothermic or endothermic nature. Some of the endothermic transitions are the glass transition, reduction, dehydration and some decomposition reactions. Crystal-crystal structure transformation, glass-crystal transition, oxidation and some decomposition reactions are the most frequently studied exothermic transitions.

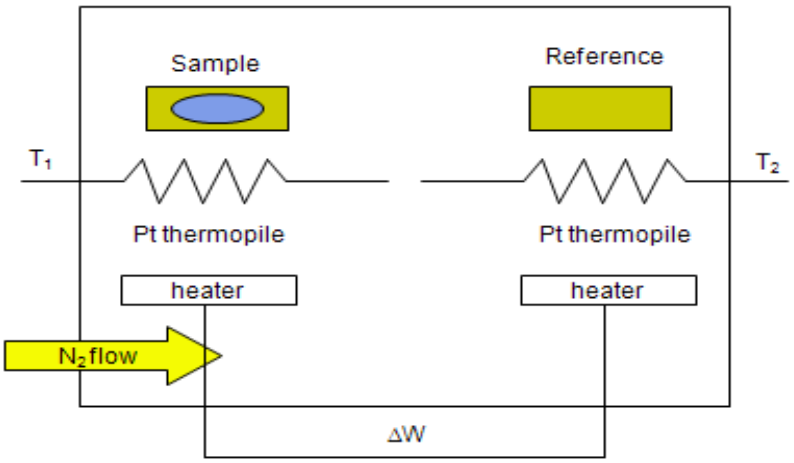

Fig. 2.2.1: Schematic diagram of a DSC.

A commercial instrument (Perkin-Elmer, DSC 7) was used in the present investigations. A temperature sensor (platinum thermopile) and a heater (made of platinum wire) are embedded in each of the two micro-furnaces (Fig. 2.2.1). The measuring range could be extended from 25 ºC to 725 ºC. In the present studies, the instrument was calibrated for optimal operation from room temperature to 700 ºC. High purity zinc (m.p. = 418.6 ºC) and indium (m.p. = 156 ºC) were used to calibrate the instrument's temperature and enthalpy scales. Measurements were done with weighed quantities (~ 20 mg) of glass samples taken in crimped aluminium sample pans. High purity nitrogen gas was continuously purged during the entire duration of the experiment.

DSC curves were recorded at constant heating rates of 20 ºC min^{-1}. A typical DSC curve of a glass is shown in Fig. 2.2.2. As a glass is heated at a constant heating rate in a DSC, the heat flow exhibits an endothermic base line shift at the glass transition temperature (T_g), followed by an exothermic crystallization peak at T_c. Further heating results in melting of the sample at T_m, which is an endothermic transformation. Generally, it has been observed that glasses, which are unstable, show one or more exothermic peaks corresponding to devitrification of various crystalline phases. Such glasses may sometimes show multiple melting endothermic as well. The T_g values reported in the present studies correspond to the on-set of the glass transition (Fig. 2.2.2). The crystallization temperature reported corresponds to the value at the maximum of the exothermic peak.

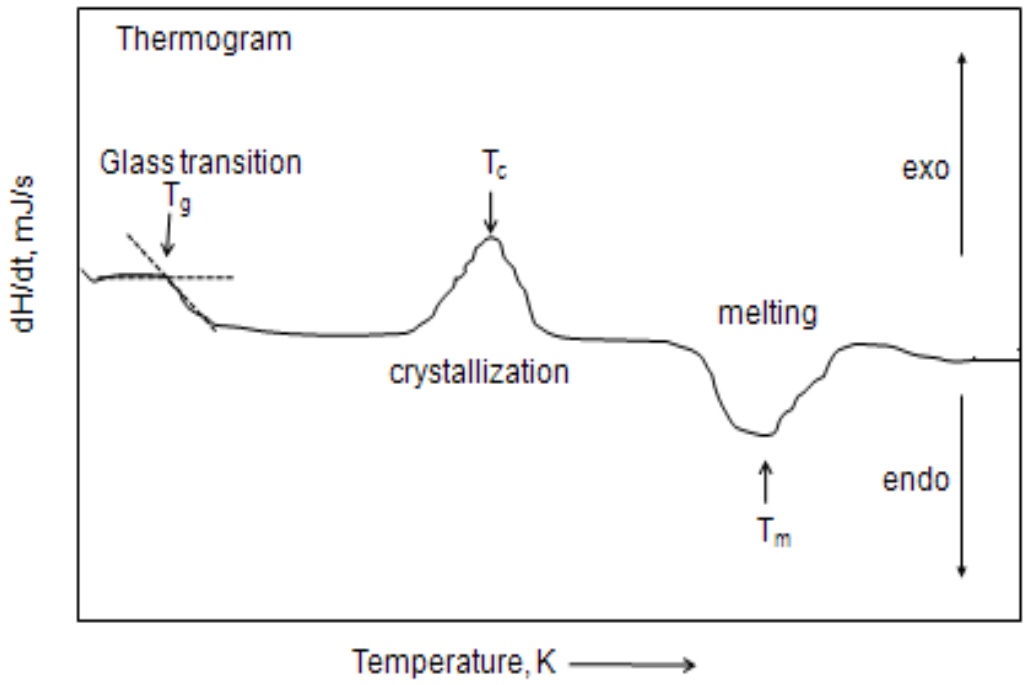

Fig. 2.2.2: A typical DSC curve of a glass.

2.3. Density

Density is measured by weighing a suitably selected piece of glass in air and delivering this weight by the buoyancy, when the sample is suspended in water. According to Archimedes' principle, the buoyancy equals the weight of the displaced fluid, which, for water, equals the volume. If W_a is the weight of the specimen in air and W_b in water, then the buoyancy is (W_a-W_b) and density (assuming density of water to be 1 gm/cm^3),

$$\rho = \frac{W_a}{W_a - W_b} \tag{2.2}$$

Glass samples may react with water, in which case, a suitable inert liquid such as xylene is selected as the immersion fluid. If W_1 is the weight of the density bottle filled with xylene and W_2 is the weight of the density bottle with xylene and sample outside the density bottle, then the weight of the sample is (W_2-W_1). If W_3 is the weight of the density bottle with the sample immersed in xylene, then the sample weight loss in the immersion medium is (W_2-W_3). Then the specimen volume is,

$$V = \frac{W_2 - W_3}{\rho_m} \tag{2.3}$$

where ρ_m is the density of xylene and the density of the specimen [141] is,

$$\rho = \frac{W_2 - W_1}{W_2 - W_3} \times \rho_m \tag{2.4}$$

The molar volume of the samples can be calculated from the following expression [142-143],

$$\text{Molar volume} = \frac{M}{\rho} \tag{2.5}$$

where ρ is the density of the glass and M is the molecular weight. For a typical

multicomponent oxide glass, say $CaO\text{-}SiO_2\text{-}P_2O_5\text{-}Na_2O\text{-}Fe_2O_3$, M can be expressed as

$$M = xM(CaO) + yM(SiO_2) + zM(P_2O_5) + rM(Na_2O) + (1\text{-}x\text{-}y\text{-}z\text{-}r)M(Fe_2O_3) \quad (2.6)$$

where x, y, z, r and $(1\text{-}x\text{-}y\text{-}z\text{-}r)$ are the mole fractions of the constituents and M(CaO), $M(SiO_2)$, $M(P_2O_5)$, $M(Na_2O)$ and $M(Fe_2O_3)$ are the molecular weights of the constituents. In the present measurements, high purity xylene was used as the immersion fluid and each density value reported is the average of at least three independently measured values. Measurements were performed in a room maintained at 24 ± 1 ˚C.

2.4. Microhardness

The microhardness (or simply the hardness measured over a micron distance scale) is a characteristic property of solids. The hardness is a measure of the resistance of a material to being penetrated and eroded by another material's sharp projections. The measurement method involves the use of a diamond micro indenter in the shape of a square pyramid (Vickers indenter). Fig. 2.4.1 explains the process of a small diamond pyramidal indenter being pushed into the material under a known load. The indentation size is generally of the order of a few microns under 5 to 1,000 g loads and hence the term 'microhardness'.

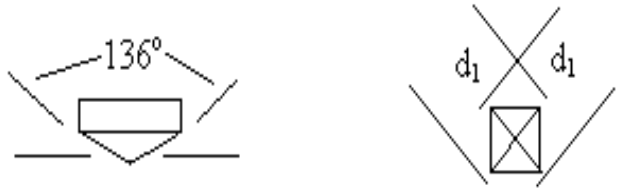

Fig. 2.4.1: Geometry of a micro indenter of the Vickers' type.

For the Vickers indenter,

$$\text{VHN} = \frac{\text{force}}{\text{area}} = \frac{2\,\text{F}\,\sin\left(\frac{\theta}{2}\right)}{\text{d}^2} \tag{2.7}$$

where F is the force in kg, θ is the inclined angle of Vickers pyramid and d is the average diagonal of the impression in mm. Since $\theta = 136^0$ for the Vickers pyramid, the Vickers hardness number (VHN) which is usually expressed in units of kg/mm^2 may be written as

$$\text{VHN} = \frac{1.8544\ \text{F}}{\text{d}^2} \tag{2.8}$$

Generally, a total indentation time of 15-25 seconds is used for the measurement, which is sufficient for the load to gradually descend onto the surface and reach an equilibrium penetration depth. Although the physics of hardness is still not understood completely, one can discuss hardness in relation to elastic moduli and bond strength parameters according to the model of Yamane and Mackenzie [144] using elastic moduli to constrain the effective bond strength. High bond strengths cause high elastic moduli preventing breakage, while small bond strengths result in a higher percentage of bonds breaking concomitant irreversible, plastic flow. This concept led Yamane and Mackenzie [144] to estimate VHN from the square root of the bond strength, bulk modulus B and shear modulus G using the relation,

$$\text{VHN} = \text{C}\sqrt{\alpha\ \text{BG}} \tag{2.9}$$

where C is a proportionality constant and α is the bond strength factor. From equation (2.9) it is evident that the VHN decreases as the elastic moduli of the glass decreases. This behaviour has been observed in many glasses [145-146]. When the number of non-bridging oxygen's in a glass increases, the elastic moduli of the glass decreases [145].

From equation (2.9) it is also obvious that a decrease in the elastic moduli decreases the micro-hardness in a glass.

Careful preparation of the sample surface is necessary prior to indentation. For this, the samples are mounted on resin and polished to a mirror finish. The polished samples are then indented using the Vickers indenter mounted in a microhardness tester (Buehler 2100) and the lengths of the diagonals of the indent are measured using the graduated microscope in the tester. A typical indent made on a polished glass sample is shown in Fig. 2.4.2. The indent corresponds to an applied load of 100 gm and loading time of 15 s. The microhardness values reported in this thesis are the average values of at least 10 independent indents made on each sample composition under identical loading conditions. All measurements were made at room temperature (24 ± 1 ˚C).

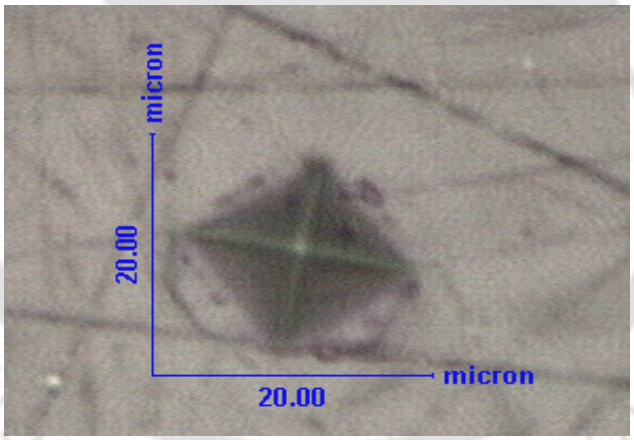

Fig. 2.4.2: Typical indent made on typical glass sample using a Vickers pyramidal indenter.

2.5. Magnetometry

The Vibrating Sample Magnetometer (VSM) has become a widely used instrument for determining magnetic properties of a large variety of magnetic materials. This

experimental technique was invented in 1956 by Simon Foner [147]. It has a flexible design and combines high sensitivity with easy of sample mounting and exchange. Measurements of magnetic moments as small as $5x10^{-5}$ emu are possible in magnetic fields from zero to 3 Tesla. Maximum applied fields of 3 Tesla are reached using conventional laboratory electromagnets and superconducting solenoids, respectively. Using a VSM, one can measure the DC magnetic moment as a function of temperature, magnetic field, angle and time. So, it allows performing susceptibility and magnetization studies. Some of the most common measurements done are magnetic hysteresis loops, susceptibility or saturation magnetization as a function of temperature (thermomagnetic analysis) [147].

A block diagram of the VSM is shown in Fig. 2.5. The VSM operates on the principle of Faraday's law of induction, which tells us that a changing magnetic field will produce an electric field [148]. This electric field can be measured, which in turn can provide us information about the magnetic moment of the sample as magnetic field and temperature are varied. The VSM normally consists of a water cooled electromagnet and power supply, a vibration exciter and sample holder (with angular position indicator), sensing coils, a Hall probe, an amplifier, the control chassis, a lock-in amplifier, a Gauss meter, and a computer interface. In a VSM, the sample is mounted on the end of a rigid rod attached to a mechanical resonator which oscillates the sample (usually in a vertical direction) at a fixed frequency. Surrounding the sample is a set of sensing coils. As the sample moves, its magnetization (M) alters the magnetic flux through the coils. This produces an AC voltage directly proportional to M, which can be amplified and detected using a lock-in amplifier. The external magnetizing field is usually provided by a

horizontal electromagnet. The measurement sequence is then programmed using the software provided with the instrument.

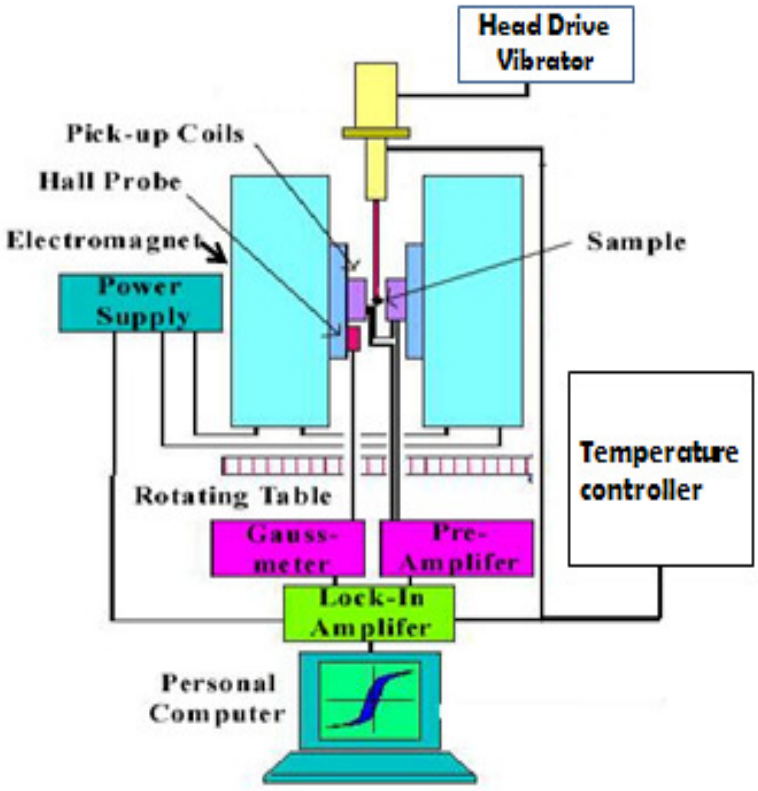

Fig. 2.5: Block diagram of the vibrating sample magnetometer.

The vibration exciter is then started and the signal received from the probe and the pick-up coils is converted into the magnetic moment value of the sample. Magnetic field up to 30 kOe can be applied to the sample with a 10 inch diameter electromagnet. Normally, magnetic field is automatically increased in steps at a constant temperature (*M-H* measurement) by setting the program. The VSM was calibrated using a standard reference (high purity nickel sphere), supplied with the instrument. The quantity of magnetic phase presented in the glass-ceramic samples was determined from the

saturation magnetization ratio between the sample and pure magnetite (M_s = 92 emu/g [148]). From this measurement, the value of magnetization at different applied magnetic fields is obtained in emu/g. These data provide M_{sat} value of the sample. Magnetization as a function of temperature at a constant applied field (*M-T* measurement) is recorded to obtain information of transition or Curie / Neel temperature. Magnetic susceptibility measurements of glass-ceramics containing iron oxide reveal the nature of interaction between the iron ions apart from providing information on the valence states of iron ions.

Magnetic susceptibility data of the glass ceramics was obtained from temperature dependent magnetization measurements carried out over a temperature range of 300 K to 1050 K at a constant applied field of 79.6 kA/m (1 kOe) using a Vibrating sample magnetometer (Lakeshore model 7410) equipped with a high temperature oven. The magnetic hysteresis loop of the glass-ceramics samples was obtained using two different external magnetic fields of ± 20 kOe and ± 500 Oe. Low field (± 500 Oe) measurements were used to evaluate the power loss (or heat generation capability) of the sample at fields amenable to clinical conditions. Magnetic susceptibility measurements of glasses containing iron oxide reveal the nature of interaction between the iron ions apart from providing information on the valence states of iron ions. Magnetic susceptibility data of the glasses was obtained from temperature dependent magnetization measurements carried out over a temperature range of 300 K to 600 K at a constant applied field of 1 kOe. Temperature dependence of the reciprocal of magnetic susceptibility of paramagnetic materials (glass samples) shows a Curie-Weiss type behavior which can be expressed as [148],

$$\chi^{-1} = \frac{T - \theta_p}{C_M} \qquad (2.10)$$

where χ is the magnetic susceptibility, C_M is the Curie constant, and θ_p is the paramagnetic Curie temperature.

2.6. Electron Paramagnetic Resonance

Electron paramagnetic resonance (EPR) or electron spin resonance (ESR) spectroscopy is a technique for studying chemical species that have one or more unpaired electrons, such as organic and inorganic free radicals or inorganic complexes possessing a transition metal ion. EPR studies of glass/glass-ceramics containing transition metals ions probe the site symmetry around the transition metal ions present and provide information on the glassy network. EPR absorption measurements at room temperature of glasses / glass-ceramics containing iron oxide reveal the nature of interactions between the iron ions apart from providing information on the valance state of iron ions. Every electron has a magnetic moment and spin quantum number $s = 1/2$, with magnetic components $m_s = \pm 1/2$. In the presence of an external magnetic field with strength B_0, the electron's magnetic moment aligns itself either parallel ($m_s = -1/2$) or antiparallel ($m_s = +1/2$) to the field, each alignment having a specific energy (see the Zeeman effect). The parallel alignment corresponds to the lower energy state, and the separation between it and the upper state is $\Delta E = g_e \mu_B B_0$, where g_e is the electron's so-called g-factor (see also the Landé g-factor) and μ_B is the Bohr magneton. This equation implies that the splitting of the energy levels is directly proportional to the magnetic field's strength, as shown in the diagram Fig. 2.6.1. An unpaired electron can move between the two energy levels by either absorbing or emitting electromagnetic radiation of energy $\varepsilon = h\nu$ such that the resonance condition, $\varepsilon = \Delta E$, is obeyed. Substituting in $\varepsilon = h\nu$ and $\Delta E = g_e \mu_B B_0$ leads to

the fundamental equation of EPR spectroscopy, *viz*., $h\nu = g_e \mu_B B_0$. Experimentally, this equation permits a large combination of frequency and magnetic field values, but the great majority of EPR measurements are made with microwaves in the 9 – 10 GHz region, with fields corresponding to about 8000 G (0.8 T).

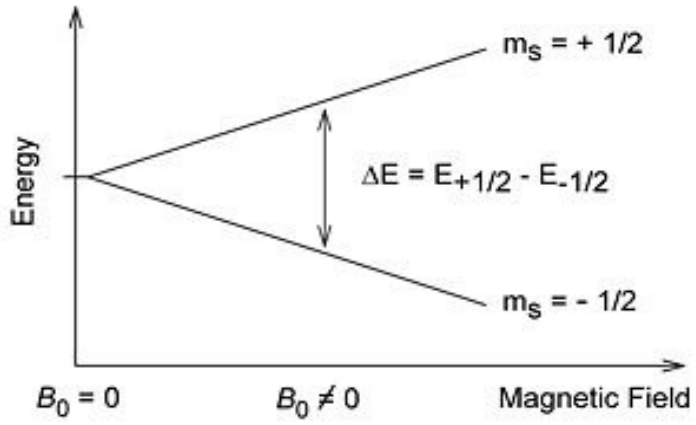

Fig. 2.6.1: Energy level splitting of electron of spin s=1/2 in a static magnetic field B_o.

A block diagram of the EPR is shown in Fig. 2.6.2. EPR absorption spectra of glasses and glass-ceramics in powder form were obtained using a JEOL Spectrometer (model JES-FA200) operating at X-band frequency (ν = 9.4 GHz) with 100 kHz field modulation at room temperature. The magnetic field was scanned from 0 to 800 mT and microwave power was set at 1 mW. Powdered glass or glass-ceramics specimen weighing ~50 mg was taken in a quartz tube for the EPR measurements. The EPR spectrometer was calibrated with the in-built software which uses EPR spectrum of Mn^{2+} ions in MgO as reference. In principle, EPR spectra can be generated by either varying the photon frequency incident on a sample while holding the magnetic field constant, or doing the reverse. In practice, it is usually the frequency which is kept fixed. A collection

of paramagnetic centers, such as free radicals, is exposed to microwaves at a fixed frequency. By increasing an external magnetic field, the gap between the $m_s = +1/2$ and $m_s = -1/2$ energy states is widened until it matches the energy of the microwaves, as represented by the double-arrow in the diagram (Fig. 2.6.1). At this point, the unpaired electrons can move between their two spin states. Since there are more electrons in the lower state due to the Maxwell-Boltzmann distribution, there is a net absorption of energy, and it is this absorption which is monitored and converted into a spectrum. Most EPR spectra are recorded and published only as first derivatives.

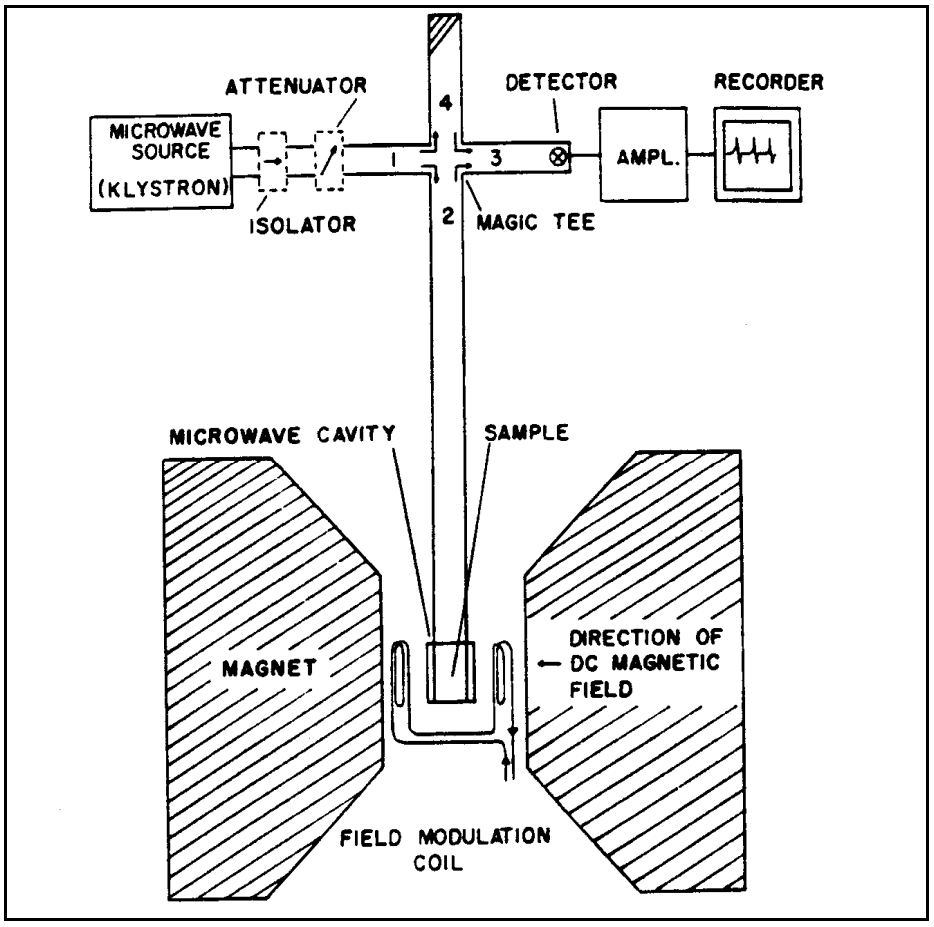

Fig. 2.6.2: A block diagram of the electron paramagnetic resonance spectrometer.

2.7. Bioactivity test

2.7.1. Preparation of SBF and in vitro test

Kukubo and his colleagues developed [44-45] an acellular simulated body fluid (SBF) that has inorganic ion concentrations similar to those of human blood plasma (HBP), in order to reproduce formation of apatite on bioactive materials *in vitro*. This fluid can be used for not only evaluation of bioactivity of artificial materials *in vitro*, but also for coating apatite on various materials under biomimetric conditions. The ion concentrations of SBF are given on Table 2.7.1. The following reagent grade chemicals stored in vacuum desiccators and ion-exchanged distilled water were used for the preparation of SBF:

(1) sodium chloride (NaCl), (2) sodium hydrogen carbonate ($NaHCO_3$), (3) potassium chloride (KCl), (4) di-potassium hydrogen phosphate trihydrate ($K_2HPO_4.3H_2O$), (5) magnesium chloride hexahydrate ($MgCl_2.6H_2O$), (6) calcium chloride ($CaCl_2$), (7) sodium sulfate (Na_2SO_4), (8) Tris-hydroxymethyl aminomethane $(CHOCH_2)_3CNH_2$) (Tris), (9) 1m (mol/l) Hydrochloric Acid, 1m-HCl, (10) pH standard solutions (pH 4, 7 and 9).

Table 2.7.1: Nominal ion concentrations of SBF in comparison with those in HBP.

Ion (mM)	Na^+	K^+	Mg^{2+}	Ca^{2+}	Cl^-	HCO_3^-	HPO_4^{2-}	SO_4^{2-}
SBF	142	5	1.5	2.5	147.8	4.2	1	0.5
HBP	142	5	1.5	2.5	103	27	1	0.5

Table 2.7.2: Order, amounts, weighing containers, purities and formula weights of reagents for preparing 1000 ml of SBF

Order	Reagent	Amount	Container	Purity (%)	Formula weight
1	NaCl	8.035 g	Weighing paper	99.5	58.4430
2	$NaHCO_3$	0.355 g	Weighing paper	99.5	84.0068
3	KCl	0.225 g	Weighing bottle	99.5	74.5515
4	$K_2HPO_4 \cdot 3H_2O$	0.231 g	Weighing bottle	99.0	228.2220
5	$MgCl_2 \cdot 6H_2O$	0.311 g	Weighing bottle	98.0	203.3034
6	1.0m-HCl	39 ml	Graduated cylinder	—	—
7	$CaCl_2$	0.292 g	Weighing bottle	95.0	110.9848
8	Na_2SO_4	0.072 g	Weighing bottle	99.0	142.0428
9	Tris buffer	6.118 g	Weighing paper	99.0	121.1356
10	1.0M HCl	0–5 ml	Syringe	—	—

Since SBF is supersaturated with respect to apatite, an inappropriate preparation method can lead to the precipitation of apatite in the solution. The preparing solution has to be kept colorless and transparent with no deposits on the surface of the bottle. In order to prepare 1000 ml of SBF, 700 ml of ion-exchanged and distilled water is taken in a 1000 ml plastic beaker. Water in the beaker is heated to 36.5 ± 1.5 °C under constant stirring. The reagent number 1 to 8 are dissolved in the solution at 36.5 ± 1.5 °C one by

one in the order given in Table 2.7.2. The 9th (Tris) and 10th reagents are then added for pH adjustment in a careful and methodical manner to a pH value of 7.40. Additional water is then added to make up the solution to 1000 ml. The prepared SBF is then preserved in dark coloured plastic bottles with a tightly placed lid and kept at 5−10 °C in a refrigerator. The SBF stock was preserved and used for a maximum of 30 days only.

The glass/glass-ceramics pieces to be tested *in vitro* were polished with 2000 grit silicon carbide paper to dimensions of 10 × 10 × 2 mm^3. The polished specimens were washed with acetone in an ultrasonic cleaner. *In vitro* bioactivity test was carried out by soaking the glass / glass-ceramics pieces in 30 ml of SBF. The temperature of the solution was maintained at 36.5 ^{o}C. Specimens immersed in SBF were taken out after 1, 3, 7, 10, 20 and 30 days, lightly washed with acetone and dried in a sterile environment.

2.7.2. Analysis of samples treated in SBF

Surface structural changes in the dried glass and glass-ceramics samples treated in SBF were analyzed by grazing incidence X-ray diffraction (GI-XRD), Fourier transform infra-red reflection spectroscopy (FT-IRS) and scanning electron microscopy (SEM) techniques. The surface chemical analysis was carried out by energy dispersive X-ray spectroscopy (EDS) analysis. The specific techniques and procedures adopted are described below:

2.7.2.1. Glancing incidence X-ray Diffraction

Grazing incidence X-ray diffraction (GI-XRD) is a commonly used method for structural evaluation of surface layers or thin films. GI-XRD measurements were carried out at

room temperature using a commercial X-ray diffractometer (Bruker D8 Advance). The GI-XRD measurements were performed in the 2θ range of 20–50° using CuK_α (λ = 1.5418 Å) radiation at a scan rate of 1°/min and with 2° glancing angle against the incident beam on the specimen surface. All the XRD data were collected with the X-ray generator setting of 40 kV / 30 mA.

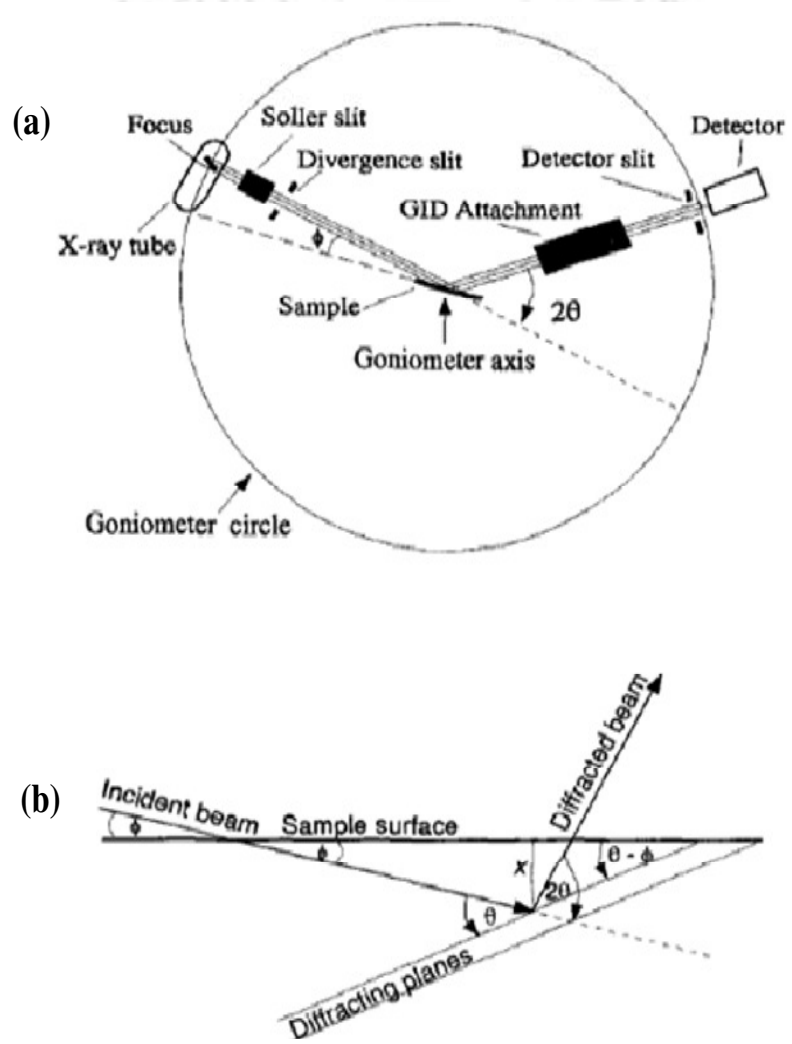

Fig. 2.7.2.1: (a) X-ray diffraction geometry for glancing incidence asymmetric diffraction and (b) path of a diffracted X-ray beam in GID.

X-ray diffraction geometry for glancing incidence asymmetry diffraction and path diffraction of the X-ray beam in the glancing incidence diffraction (GID) are pictorially depicted in Fig. 2.7.2.1(a) and Fig. 2.7.2.1(b), respectively. In glancing incidence asymmetric Bragg diffraction, the sample surface and X-ray source are set a low-incidence angle and they remain stationary throughout the detector scan {Fig. 2.7.2.1(a)}. In a typical measurement, the glancing-incidence angle is fixed and the sample is scanned by moving the detector only. Unlike the Bragg-Brentano geometry, a focusing circle is not maintained in GID geometry {Fig. 2.7.2.1(a)}. GID is a non-focusing geometric arrangement which makes use of parallel, rather than divergent X-rays diffracted from suitably oriented crystallographic planes. A GID attachment placed between the diffracting planes and detector slit absorbs converging and diverging diffracted X-rays and allows only parallel X-rays to pass {Fig. 2.7.2.1(a)}.

2.7.2.2. Scanning Electron Microscopy

Analysis of microstructure and composition has been carried out by using LEO 1430VP Scanning Electron Microscope (SEM) equipped with Oxford energy dispersive spectrometer (EDS Model 7353). The SEM-EDS was operated with an acceleration potential of 10 kV to 20 kV and each spectrum was collected for about 100 s duration. Elemental analysis of the samples was done by recording energy dispersive spectrum. Basic principles of SEM & EDS analysis are briefly presented below.

In a typical SEM (schematically shown as in Fig. 2.7.2.2), electrons are thermionically emitted from a tungsten filament cathode are accelerated towards an anode. The types of signals produced by an SEM include secondary electrons, back

scattered electrons (BSE), characteristic X-rays, light (cathodoluminescence), specimen current and transmitted electrons. Each of these signals requires specialized detectors for their detection which are all not usually present in a single machine. The signals result from interactions of the electron beam with atoms at or near the surface of the sample. In the most common or standard detection mode, secondary electron imaging (SEI), the SEM can produce very high-resolution images of a sample surface, revealing details about 1 to 5 nm in size. Due to the way these images are created, SEM micrographs have a very large depth of field yielding a characteristic three-dimensional appearance useful for understanding the surface structure of a sample. A wide range of magnifications is possible, ranging from about 25× to about 250,000×.

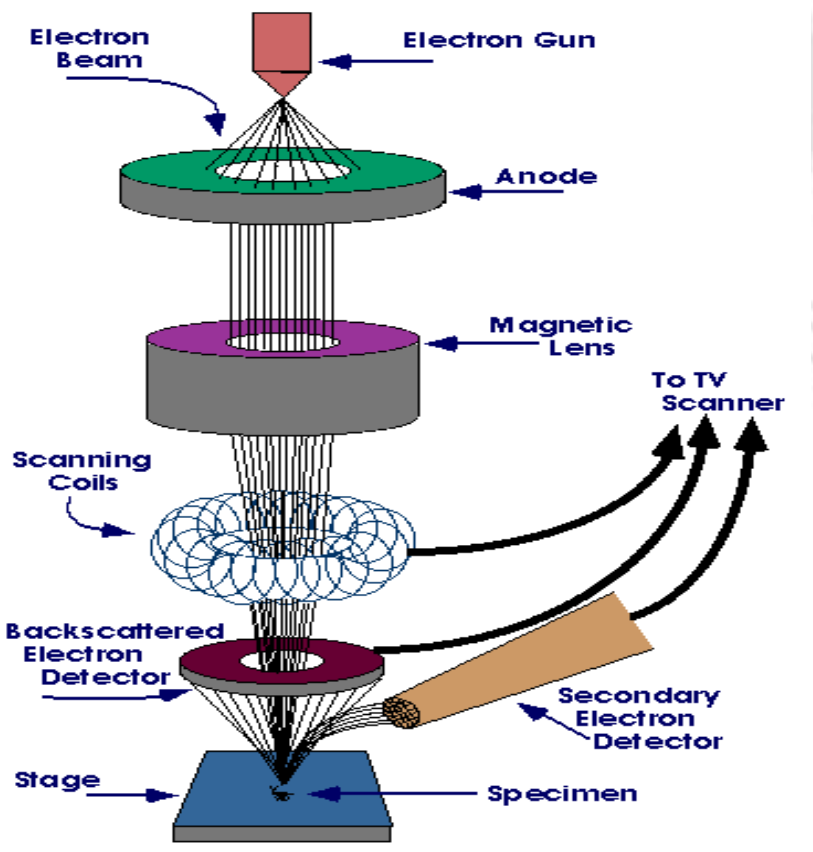

Fig. 2.7.2.2: A schematic diagram of a SEM.

The electron beam, which typically has an energy ranging from a few hundred eV to 40 keV, is focused by one or two condenser lenses to a spot of about 0.4 nm to 5 nm in diameter. The beam passes through pairs of scanning coils or pairs of deflector plates in the electron column, typically in the final lens, which deflect the beam in the *x* and *y* axes so that it scans in a raster fashion over a rectangular area of the sample surface. When the primary electron beam interacts with the sample, the electrons lose energy by repeated random scattering and absorption within a teardrop-shaped volume of the specimen known as the interaction volume, which extends from less than 100 nm to around 5 µm into the surface. The size of the interaction volume depends on the electron's landing energy, the atomic number of the specimen and the specimen's density. The energy exchange between the electron beam and the sample results in the reflection of high-energy electrons by elastic scattering, emission of secondary electrons by inelastic scattering and the emission of electromagnetic radiation, each of which can be detected by specialized detectors. The beam current absorbed by the specimen can also be detected and used to create images of the distribution of specimen current. Electronic amplifiers of various types are used amplify the signals which are displayed as variations in brightness on a cathode ray tube. The raster scanning of the CRT display is synchronised with that of the beam on the specimen in the microscope, and the resulting image is therefore a distribution map of the intensity of the signal being emitted from the scanned area of the specimen. The image can be digitally captured and displayed on a computer monitor and saved to a computer's hard disk.

EDS Analysis stands for Energy Dispersive X-ray Spectroscopy. It is a technique used for identifying the elemental composition of the specimen. The EDS analysis

system works as an integrated feature of a SEM, and cannot operate on its own without the latter. During EDS Analysis, the specimen is bombarded with an electron beam inside the SEM. The bombarding electrons collide with the specimen atoms' own electrons, knocking some of them off in the process. A position vacated by an ejected inner shell electron is eventually occupied by a higher-energy electron from an outer shell. To be able to do so, however, the transferring outer electron must give up some of its energy by emitting an X-ray. The amount of energy released by the transferring electron depends on which shell it is transferring from, as well as which shell it is transferring to. Furthermore, the atom of every element releases X-rays with unique amounts of energy during the transferring process. Thus, by measuring the amounts of energy present in the X-rays being released by a specimen during electron beam bombardment, the identity of the atom from which the X-ray was emitted can be established. The EDS spectrum is just a plot of how frequently an X-ray is received for each energy level. An EDS spectrum normally displays peaks corresponding to the energy levels for which the most X-rays had been received. Each of these peaks are unique to an atom, and therefore corresponds to a single element. The higher a peak in a spectrum, the more concentrated the element is in the specimen.

2.7.2.3. Fourier transforms infrared spectroscopy

Infrared spectroscopy is an important technique which provides an easy way to identify the presence of certain functional groups in a molecule. One can also use the unique collection of absorption bands to confirm the identity of a pure compound or to detect the

presence of specific impurities. The basic configuration of an FT-IR spectrometer is schematically shown in Fig. 2.7.2.3.

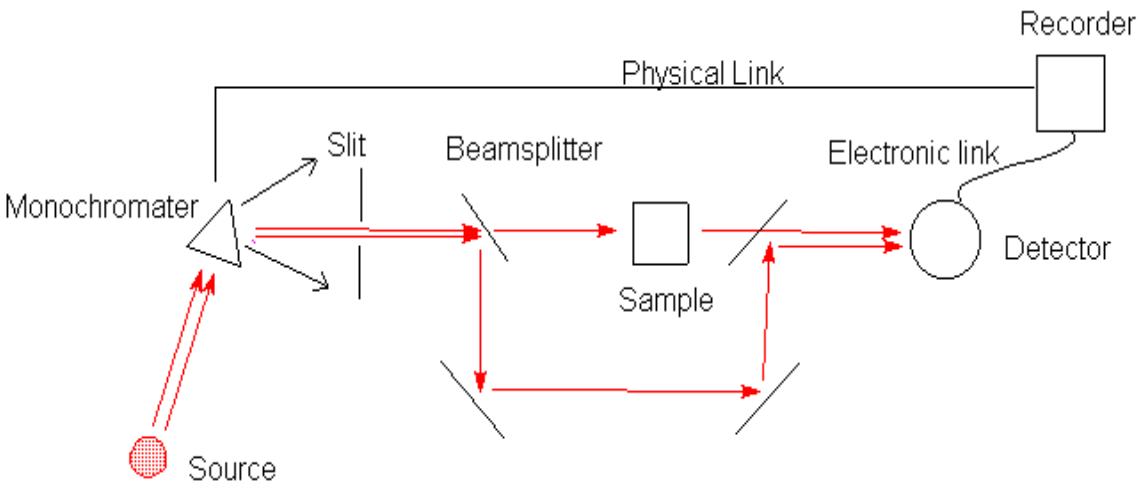

Fig. 2.7.2.3: A schematic diagram of an FT-IR spectrometer.

The essential component of this spectrometer is a Michelson interferometer that consists of a fixed mirror, a moving mirror, and a beam splitter. When the IR beam coming from a source reaches the beam splitter, it is divided into two halves. Half of the beam is reflected in the beam splitter to the fixed mirror, while the remaining half passes through the beam splitter toward the moving mirror. These two beams are reflected in the fixed and moving mirrors, respectively, and come back to the beam splitter, where they recombine into a new beam that passes through the sample. The sample absorbs all the different wavelengths characteristic of its spectrum, and this subtracts specific wavelengths from the interferogram. The detector now reports variation in energy versus time for all wavelengths simultaneously. A laser beam is superimposed to provide a reference for the instrument operation.

The infrared reflection spectra were measured using FT-IR spectrometer (PerkinElmer Spetrum- BX). The samples were scanned in the wave number range of 2000-400 cm^{-1} at a resolution 2 cm^{-1} and scanning speed 2 mms^{-1}. The purpose of infrared studies is to obtain information about the chemical bonding and structure of the surface layer formed on the specimens treated in SBF through a detailed examination of infrared absorption bands.

Chapter 3

Investigations on $CaO-SiO_2-P_2O_5-Na_2O-Fe_2O_3$ glasses and glass-ceramics

A systematic study of $CaO-SiO_2-P_2O_5-Na_2O$ glasses with varying iron oxide content and the glass-ceramics derived from them is presented in this chapter. EPR absorption spectroscopy, microhardness, density, differential scanning calorimetry, magnetic susceptibility and *in vitro* bioactivity studies have been performed on the parent glass compositions. Glass-ceramics have been derived from these glasses by appropriate heat treatment. The evolution of structural and magnetic properties in the glass-ceramics along with EPR absorption, microhardness and *in vitro* bioactivity studies carried out on the glass-ceramic samples are also presented in this chapter.

3.1. Preparation of glasses and glass-ceramics

Glass samples with composition of $41CaO(52-x)SiO_2 4P_2O_5\ xFe_2O_3 3Na_2O$ (x = 0, 2, 4, 6, 8 and 10 mole %) were prepared by melt quenching technique. Appropriately weighed quantities of high purity SiO_2 (99.9 % purity), $Na_2CO_3H_2O$ (99.9 % purity), Fe_2O_3 (99.9

% purity), $CaCO_3$ (99.9 % purity) and $NH_4(H_2PO_4)$ (99.9 % purity) were thoroughly mixed in an agate pestle and mortar. The well mixed charge taken in a platinum crucible was calcined at 800 °C for 24 hours and then held at 1550 °C for 2 hours to completely melt the charge. The melt was then poured on to a copper plate at room temperature and pressed with a copper plate to form glass samples of a few millimeter thickness. The as-quenched glasses were annealed at 500 °C (well below their glass transition temperature) for 10 hours in air atmosphere to remove residual stresses. These heat-treated samples were used for all measurements. Identical preparation conditions such as furnace temperature and quenching procedure were followed while preparing the entire series of glasses. The glass plates obtained by the method described above were placed on alumina boats and heat-treated at 1050 °C for 3h and slowly cooled to room temperature to form glass-ceramic samples. The heat-treatment temperature was chosen to ensure the complete crystallization of the two phases observed in thermograms of the glass samples (to be discussed in the section 3.2.2 of this chapter).

3.2. Characterization of the glasses

Systematic characterization of the glass samples was first carried out, the details of the characterizations performed on the glasses are given below:

3.2.1. XRD studies

As a first step in the investigations, all the CaO-SiO_2-P_2O_5-Na_2O-Fe_2O_3 glasses prepared were checked for amorphous nature by recording their X-ray powder diffraction (XRD) patterns. In the present investigations, a Seifert XRD 3003 T/T X-ray powder diffraction

system was used as explained in chapter 2. A typical XRD pattern from a CaO-SiO_2-P_2O_5-Na_2O-Fe_2O_3 glass is shown in Fig. 3.2.1. The diffractograms of all the as quenched glass samples showed no sharp peaks, thereby signifying the total lack of crystallinity in the samples.

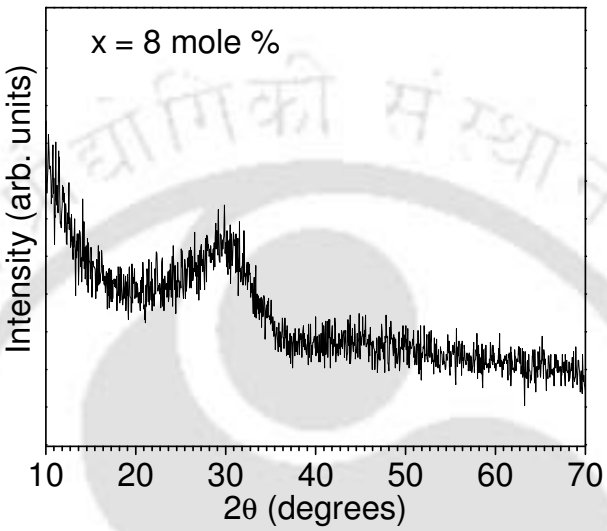

Fig. 3.2.1: X-ray diffraction pattern of a typical CaO-SiO_2-P_2O_5-Na_2O-Fe_2O_3 glass.

3.2.2. DSC studies

DSC studies on $41CaO(52\text{-}x)SiO_2 4P_2O_5\ xFe_2O_3 3Na_2O$ glasses with x = 2, 4, 6, 8 and 10 mole % have been performed following the procedure explained in chapter 2. The experiments were performed with ~ 20 mg samples. Fig. 3.2.2 is the typical DSC curve obtained for $41CaO(52\text{-}x)SiO_2 4P_2O_5\ xFe_2O_3 3Na_2O$ glasses with x = 8 mole % iron oxide under a constant heating rate of 20 °C/min. Single glass transition temperature (T_g) and two crystallization temperatures (T_{c1} and T_{c2}) were observed in the DSC curves of all the glass samples. The glass transition temperature was marked by a distinct endothermic

baseline shift within the temperature range 600 to 650 °C and crystallization temperature range was between 850 °C and 1056 °C when heated under a constant rate of 20 °C/min.

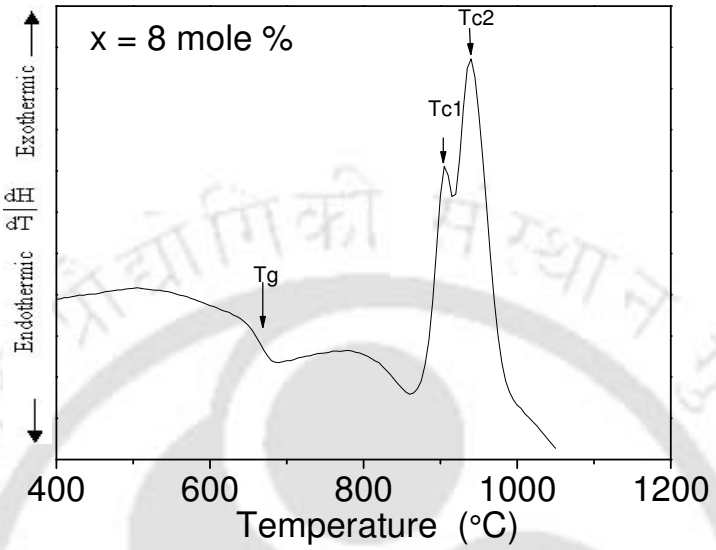

Fig. 3.2.2: Typical DSC curve obtained for $41CaO(52\text{-}x)SiO_2 4P_2O_5 x Fe_2O_3 3Na_2O$ glasses (x = 8 mole %) with constant heating rate (φ) of 20 °C/min.

Table 3.2.2: DSC data of $41CaO(52\text{-}x)\ SiO_2\ 4P_2O_5\ xFe_2O_3 3Na_2O$ glasses.

***x* (mole %)**	**T_g (°C)**	**T_{c1} (°C)**	**T_{c2} (°C)**
2	656	1020	1056
4	639	970	1004
6	629	941	991
8	621	906	939
10	605	871	897

It can be seen from the DSC curve that hydroxyapatite crystals precipitated between 870 and 1020 °C, and wollastonite crystals between 897 and 1056 °C as a function of increasing *x* (iron oxide content). T_g and T_c's decreased with increasing *x* (*cf.* Table 3.2.2). T_g values listed in the table correspond to a constant heating rate of 20 ^oC/min. T_g is closely related to the change in the coordination number of the network forming oxides and the number of non-bridging oxygens present in the glass. A decrease in the number of non-bridging oxygens in these glasses with the addition of Fe_2O_3 results in the depolarization of the glass skeleton. Hence the decrease in T_g as a function of Fe_2O_3 concentration in the glasses is a result of the decrease in the depolymerization of the glass skeleton. Such conclusions have been drawn in earlier studies [149] in support of this argument.

3.2.3. Density

The mass density (ρ) measurements on CaO-SiO_2-P_2O_5-Fe_2O_3-Na_2O glasses were carried out using a density bottle with xylene as the immersion liquid. From the density data, the molar volumes of the glasses were calculated (Table 3.2.3) using equations (2.4) and (2.5). Fig. 3.2.3 shows the composition dependence of density and molar volume of $41CaO(52\text{-}x)SiO_2 4P_2O_5\ xFe_2O_3 3Na_2O$ glasses. The density of the glass increases and molar volume decreases as iron oxide mole % content is increased. When iron oxide mole % is increased, Fe_2O_3 progressively replaces SiO_2. Since the molecular weight of Fe_2O_3 (159.697) is higher than the molecular weight of SiO_2 (60.088), one would expect the overall density of the glass to increase. Increase in density from 2.56 to 2.99 g/cm^3 (Table 3.2.3) with increasing iron oxide content is a result of strengthening of cross-

linking within the glassy network as the volumetric portion of the four-coordinated Fe ion increases at the cost of the six-coordinated Fe [150].

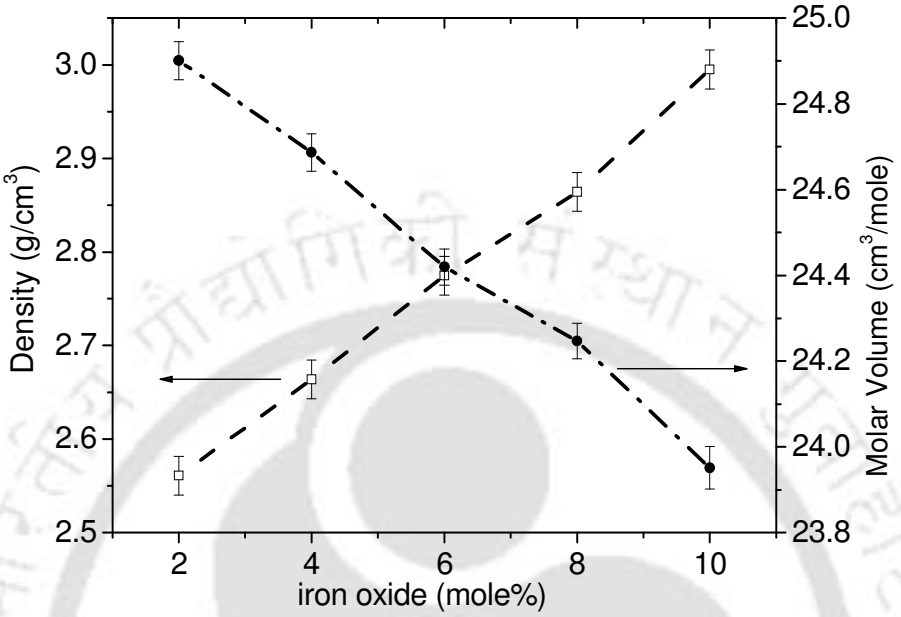

Fig. 3.2.3: Composition dependence of density and molar volume of CaO glasses.

Table 3.2.3: Density, molar volume and microhardness of $41CaO(52\text{-}x)SiO_2 4P_2O_5$ $xFe_2O_3 3Na_2O$ glasses.

***x* mole %**	**Density (gm/cm^3)**	**Mol.vol.(cm^3/mol)**	**VHN (kg mm^{-2})**
2	2.56	24.90	576
4	2.66	24.69	689
6	2.77	24.42	725
8	2.86	24.25	744
10	2.99	23.95	771

The decrease in the molar volume with increasing Fe_2O_3 mole % content indicates that the glassy network shrinks in size with the addition of Fe_2O_3. The decrease in the molar volume of the samples can be attributed to the increase in the probability of formation of FeO_4 group in glass, as result of the decrease in the number of non-bridging oxygens [150]. This may cause a decrease in the volume of the glass network structure. The decrease in molar volume in glasses can also be attributed to the formation of a closed packed structure due to the change of the coordination of iron ions to the four-fold coordination.

3.2.4. Microhardness

The microhardness of glasses has been measured following the procedure outlined in second chapter. All the glass samples were uniformly subjected a load of 100 gm for a duration of 15 s. The measured microhardness values are tabulated in Table 3.2.3.

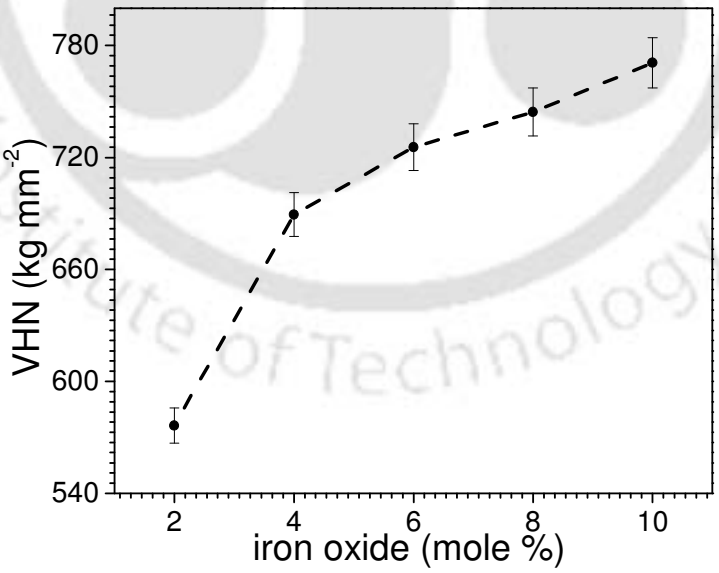

Fig. 3.2.4: Variation of VHN of $41CaO(52\text{-}x)SiO_2 4P_2O_5 x Fe_2O_3 3Na_2O$ glasses.

Fig. 3.2.4 shows the variation of VHN with iron oxide content in 41CaO(52-*x*) $SiO_2$4P_2O_5 *x*$Fe_2O_3$3Na_2O glasses. It shows that the VHN increases as the iron oxide mole % content is increased. As the number of non-bridging oxygen in glass decreases, the bulk (*B*) and shear (*G*) elastic moduli of the glass increase. When the number of non-bridging oxygens in a glass decreases, the elastic moduli of the glass increase [145]. From equation (2.9), it is evident that an increase in the elastic moduli increases the microhardness, which is the behaviour exhibited by the glasses depicted in Fig. 3.2.4.

3.2.5. EPR studies

EPR absorption spectra of Fe^{3+} ions in oxide glasses are generally characterized by the appearance of resonance absorptions at g ≈ 2.1, 4.3 and 6.0, with their relative intensities being strongly dependent on composition [151-155]. The g ≈ 2.1 resonance is assigned to those ions which interact by a superexchange coupling and can be considered as distributed in clusters [151-153]. The g ≈ 4.3 resonance line is characteristic of isolated Fe^{3+} ions predominantly situated in rhombically distorted octahedral or tetrahedral oxygen environments [151-155]. The g ≈ 6.0 resonance line arises from axially distorted sites. EPR spectra of phosphate [156], borate [157-160], bismuthate [161-162], tellurite [163-164], silicate [165-167] glasses have been reported, as functions of Fe_2O_3 content. Iron ions exist in different valence states with different local symmetries in the glass matrices, for example, as Fe^{3+} with both tetrahedral and octahedral coordination, and/or as Fe^{2+} with octahedral coordination. Fe^{3+} and Fe^{2+} are paramagnetic ions. However, only Fe^{3+} ($3d^5$,$^6S_{5/2}$) shows ESR absorptions at room temperature.

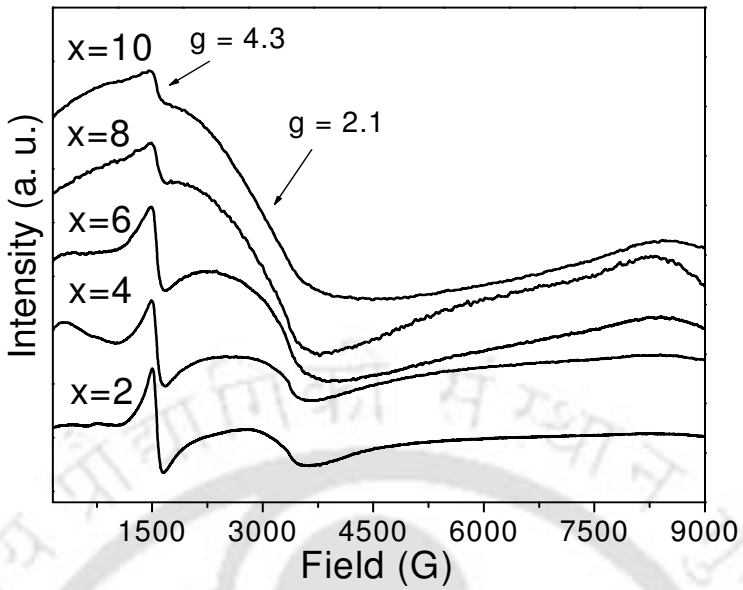

Fig. 3.2.5.1: EPR absorption spectra of $41CaO(52\text{-}x)SiO_2 4P_2O_5\, xFe_2O_3\, 3Na_2O$ glasses.

EPR absorption spectra of $41CaO(52\text{-}x)SiO_2 4P_2O_5 xFe_2O_3 3Na_2O$ ($2 \leq x \leq 10$ mole %) samples recorded at room temperature are shown in Fig. 3.2.5.1. The resonance absorptions observed at $g \approx 2.1$ and $g \approx 4.3$ are due to Fe^{3+} ions ($3d^5 {}^6S_{5/2}$). The EPR parameters of the first derivative resonance curve that were determined are the linewidth (ΔH) and the intensity of absorption line J. While J was estimated from peak to peak height (I) and the linewidth was calculated using the relation $J = I(\Delta H)^2$. Analysis of the $g \approx 2.1$ resonance line was performed by integrating the relevant part of the first derivative EPR curve. The relative intensity and linewidths of the two absorptions lines vary with glass composition.

The analysis of the EPR spectra usually begins with a discussion on the spin Hamiltonian which can be expressed as [168]

$$\mathbf{H} = \beta g \cdot H \cdot S + D[S^2_z - \frac{1}{3} S(S+1)] + E(S^2_x - S^2_y) \qquad (3.1)$$

where S_x, S_y, S_z, are components of spin along three mutually perpendicular crystalline axes x, y, and z, D and E are the usual second–order crystal field terms with axial and rhombic symmetry, and H is the applied field, respectively. If D and E are zero, the g value is expected to lie very near the free electron value of 2.0. If D or E is large as compared with $g\beta H$, then, in the two limiting cases of $D \neq 0$, $E = 0$, and $D = 0$, $E \neq 0$, the energy levels in zero magnetic field turn out to be three Kramer's doublets. In the first case ($D \neq 0$, $E = 0$), the lowest doublet has effective g values of $g \approx 2.0$ and $g \approx 6.0$. In the second case ($E \neq 0$, $D = 0$), the middle doublet has an isotropic g value of 4.3. Castner *et al*. [169] were the first to apply the spin Hamiltonian given in eqn. (3.1) to the $g \approx 4.3$ absorption line of Fe^{3+} ions in glass and Wickman *et al*. [170] identified the origin of the $g \approx 4.3$ resonance as Fe^{3+} ions in sites which have undergone rhombic distortion from cubic symmetry. The generalized spin Hamiltonian has been diagonalised within the $S = 5/2$ manifold, with $0 < \lambda (= E/D) < 1/3$, exhausting the physically acceptable possibilities. In particular, the resonance at $g \approx 2.0$ and 6.0 are the parallel and perpendicular g values of Kramer's doublets when $\lambda = E/D = 0$. The isotropic resonance at $g \approx 4.3$ corresponds to $\lambda = E/D = 1/3$. This assignment identifies the feature at $g \approx 2.0$ with weak crystal field terms and the feature at $g \approx 4.3$ with the rhombic distortions of the crystal field about a site of tetrahedral or octahedral symmetry.

Fig. 3.2.5.2 shows the composition dependence of the EPR parameters corresponding to the $g \approx 4.3$ resonance line. It can be seen from Fig. 3.2.5.1 that the peak to peak height (I) decreases with an increase in iron oxide concentration and the linewidth (ΔH) increases with increase in iron oxide concentration. The overall intensity of the absorption line J increases steadily in glasses with $x = 2$ to 6 mole % iron oxide and then

decreases as depicted in Fig. 3.2.5.2. Intensity of the g ≈ 2.1 resonance shows an increasing trend as the iron oxide content is increased as depicted in Fig. 3.2.5.3.

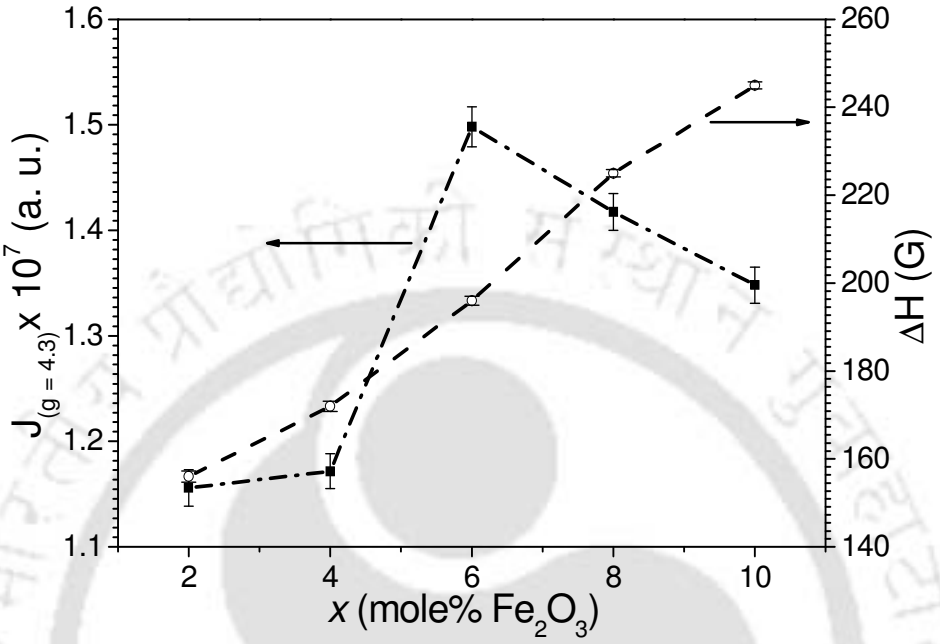

Fig. 3.2.5.2: Composition dependence of the line intensity and linewidth of g ≈ 4.3 resonance absorption line of $41CaO(52\text{-}x)SiO_2 4P_2O_5 x Fe_2O_3 3Na_2O$ glasses.

The origin of the g values in the EPR spectra of glasses shown in Fig. 3.2.5.1 is closely related to the coordination numbers of Fe ions. The g ≈ 4.3 absorption line can be produced by low symmetry (rhombic) sites of either tetrahedral or octahedral coordination. The behaviour depicted in Fig. 3.2.5.2 shows that the concentration of Fe^{3+} ions in octahedral (tetrahedral) environments increases in the composition range of $2 < x < 6$. The slow increase in g ≈ 4.3 line intensities at low Fe_2O_3 concentrations indicates that fewer Fe^{3+} ions reside in low symmetry sites at these compositions. The decrease in g ≈ 4.3 line intensity beyond $x = 6$ mole % reflects a reduction in the number of Fe^{3+} ions in octahedral (tetrahedral) environment in the vitreous matrix. One can observe that the

decrease in the intensity of the signal at g ≈ 4.3 is accompanied by the appearance of a broad signal centered at g ≈ 2.1. The latter could be attributed to the formation of clusters of paramagnetic ions containing two or more ions coupled together. It can also be seen from Fig. 3.2.5.2 that the linewidth of the g ≈ 4.3 resonance line increases monotonically with Fe_2O_3 content. These observations lead to the conclusion that at lower concentrations, iron sites are populated randomly in the glass, while at higher iron concentrations (*i.e.*, for $x > 6$ mole %) the site population deviates from randomness and results in the formation of clusters. When the site population deviates from randomness at higher iron (*i.e.*, for $x > 6$ mole %) concentrations, superexchange type interaction begins to dominate. Their strength is far too weak to favour macroscopic magnetic ordering and so the sample remains essentially paramagnetic. The superexchange interaction between the nearest neighbours (which increases with iron oxide content due to their increased proximity), acts as narrowing mechanism of the absorption line. This narrowing process is balanced by other broadening processes such as increase in network disordering and interaction between multivalent iron ions (*i.e.*, Fe^{2+} and Fe^{3+}).

The nonlinear behaviour depicted in Fig. 3.2.5.3 can be attributed to the process by which iron enters in the vitreous matrix *i.e.*, either as Fe^{3+} or Fe^{2+}. Fe^{2+} ions are not involved in the EPR absorption, but their interaction with Fe^{3+} ions influences the characteristics of the absorption lines. The resonance line at g ≈ 2.1 shows a shift towards lower values of the magnetic field when the iron oxide content increases. The g value (magnetic field) shifts from 2.10994 ± 0.00001 (3206 G) for the $x = 2$ sample to 2.22448 ± 0.00001 (3030 G) for the $x = 10$ sample. The g ≈ 2.1 resonance arises due to the formation of iron clusters which give rise to superexchange type interaction between iron

ions. Superexchange mechanisms tend to narrow the absorption line. On the other hand, interactions between Fe^{3+} and Fe^{2+} ions tend to broaden the linewidth. The final linewidth depends on the relative strengths of the two mechanisms influencing the linewidth. The increase in the linewidth of the $g \approx 2.1$ resonance with Fe_2O_3 concentrations shows the dominance of the broadening mechanisms which in turns indicates a larger increase in Fe^{2+} ion concentration as Fe_2O_3 concentration is increased in the glass.

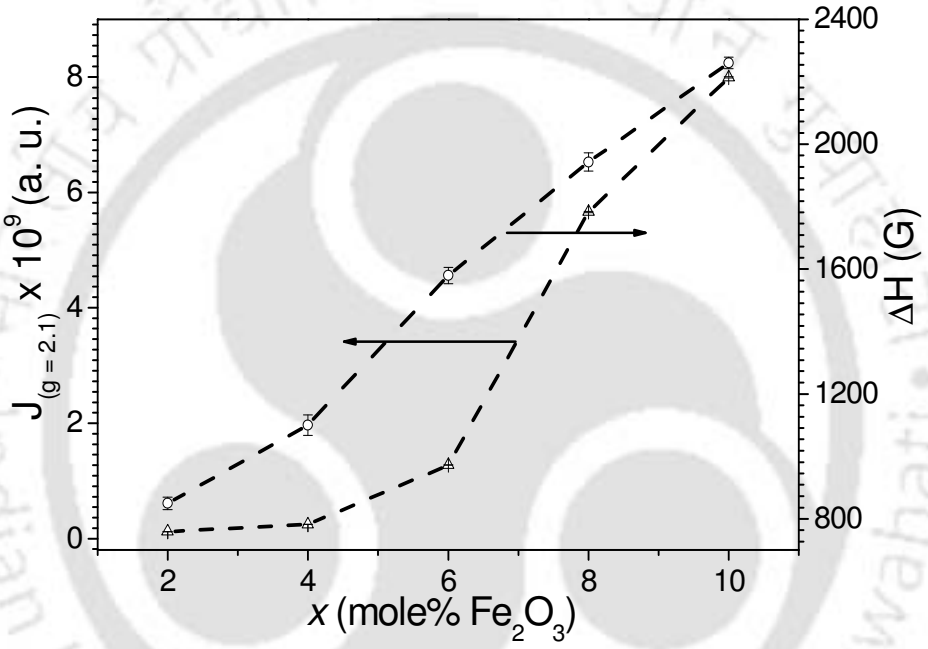

Fig. 3.2.5.3: The composition dependence of the line intensity and linewidth of $g \approx 2.1$ resonance absorption line of $41CaO(52\text{-}x)SiO_2 4P_2O_5 x Fe_2O_3 3Na_2O$ glasses.

3.2.6. Magnetic susceptibility

Magnetic susceptibility measurements of glasses containing iron oxide reveal the nature of interactions between the iron ions apart from providing information on the valence states of iron ions. Magnetic properties of glasses containing iron oxide depend on the concentration of the 3*d* element and the ratio of valence states [153-154, 156-157, 160-

162, 171-173] as well as on the structure of the vitreous matrix and implicitly on the conditions of sample preparation [157, 173]. Inverse of susceptibility (χ^{-1}) versus temperature plots for various glass compositions are shown in Fig. 3.2.6.1. Temperature dependence of the reciprocal of magnetic susceptibility of paramagnetic materials shows a Curie-Weiss type behavior expressed by equation (2.10). The straight lines in Fig. 3.2.6.1 represent the least squares fit to equation (2.10). The negative paramagnetic Curie temperature calculated for the glasses (*cf.* Fig. 3.2.6.2 and Table 3.2.6) indicates superexchange magnetic interactions between the iron ions in the glass which are predominantly anti-ferromagnetically coupled. The superexchange interaction of the iron ions in the oxide glasses has been mostly attributed to an antiferromagnetic coupling within the pairs Fe^{3+}-Fe^{2+}, Fe^{3+}-Fe^{3+} and Fe^{2+}-Fe^{2+} [163]. An antiferromagnetic coupling between iron ions was reported in borate [157, 174], phosphate [166-164], silicate [171, 175], tellurite [164] and bismuthate [161-162] oxide glasses. The vitreous oxide structure imposes the short-range character of magnetic interaction and enhances the structural image of the clusters. So, the magnetic behavior of the glasses can be described by the micromagnetic type behavior [176]. Analysis of the present data shows that the iron ions in the CaO-SiO_2-P_2O_5-Na_2O glass matrix behave magnetically similar to iron ions in Bi_2O_3-PbO [161], TeO_2-B_2O_3-PbO [163], B_3O_4-CaO [177] and CaO-P_2O_5 [178] glasses. Composition dependence of paramagnetic Curie temperature is illustrated in Fig. 3.2.6.2. The absolute magnitude of paramagnetic Curie temperature and the value of the exchange integral increase with increase in iron oxide content in the glasses. Composition dependence of the Curie constant is shown in Fig. 3.2.6.2. The presence of iron in the form of Fe^{2+} and Fe^{3+} ions has been reported in many oxide glasses [165, 171, 179].

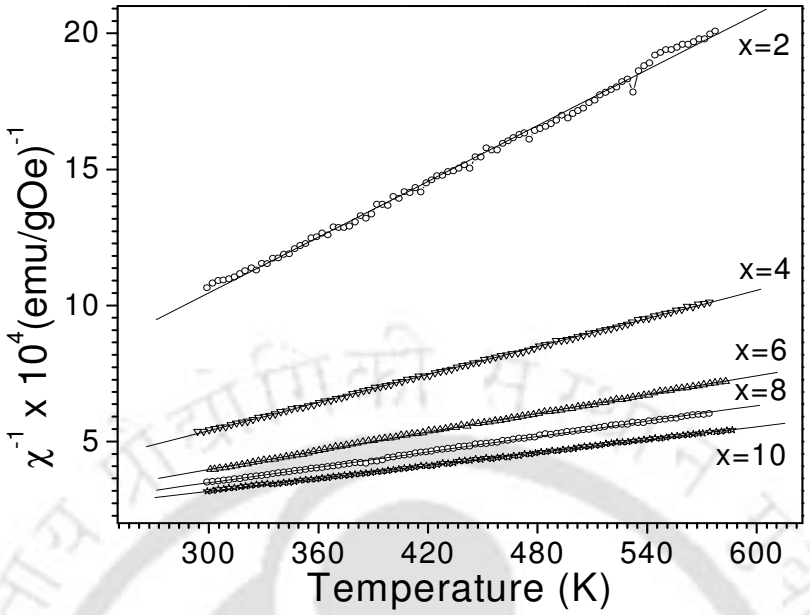

Fig. 3.2.6.1: χ^{-1} versus T plots of 41CaO.(52-*x*)SiO_2.4P_2O_5.*x*Fe_2O_3.3Na_2O glasses .

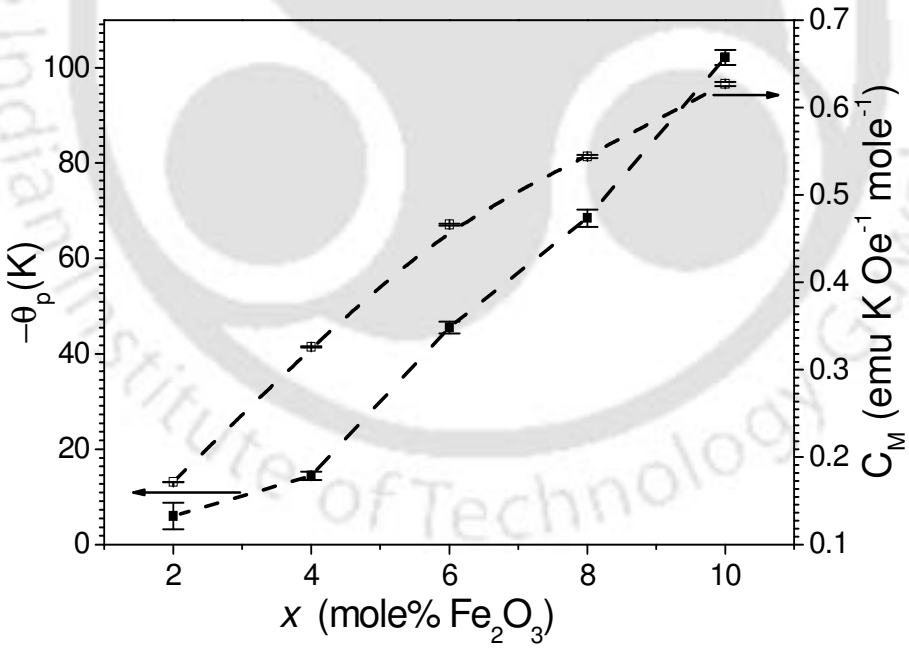

Fig. 3.2.6.2: Variation of paramagnetic Curie temperature and the Curie constant of 41CaO(52-*x*)$SiO_2$4P_2O_5*x*$Fe_2O_3$3Na_2O glasses with composition.

Table 3.2.6: Molar Curie constant, exp. magnetic moment μ_{exp}, molar fraction of Fe^{3+} (x_1) and Fe^{2+} (x_2) ions and Fe^{2+} ion ratio in $41CaO(52\text{-}x)SiO_2 4P_2O_5 xFe_2O_3 3Na_2O$ glasses.

x (mole %)	$C_M \pm 1\times10^{-4}$ (emuKOe^{-1}mole^{-1})	$\mu_{exp} \pm 1\times10^{-2}$ (μ_B)	$x_1 \pm 1\times 10^{-2}$ (mole% $Fe_2^{3+}O$)	$x_2 \pm 1\times 10^{-2}$ (mole% $Fe_2^{2+}O_3$)	$x_2/(x_1+x_2) \pm 1\times 10^{-2}$
2	0.1715	5.85	1.85	0.15	0.08
4	0.3262	5.71	3.11	0.89	0.22
6	0.4660	5.57	3.81	2.19	0.37
8	0.5440	5.22	2.35	5.65	0.71
10	0.6270	5.01	0.99	9.01	0.90

The Fe^{2+} valence state of iron in $41CaO.(52\text{-}x)\ SiO_2.\ 4P_2O_5.\ xFe_2O_3.3Na_2O$ glasses might have been favoured by the presence of the Ca^{2+} and Si^{4+} ions in the vitreous matrix. Using the atomic magnetic moments of free ions, *viz.*, $\mu_{Fe}^{2+} = 4.90\mu_B$ and $\mu_{Fe}^{3+} = 5.92\mu_B$, one can estimate [180] the molar fraction of Fe^{2+} and Fe^{3+}ions in the glasses using the relations,

$$x.\mu^2_{exp} = x_1.\mu^2_{Fe^{3+}} + x_2.\mu^2_{Fe^{2+}} \qquad (3.2)$$

and

$$x = x_1 + x_2 \qquad (3.3)$$

where $\mu_{exp} = 2.827(C_M/2x)^{1/2}$ is the experimental magnetic moment, and x_1 and x_2 are mole fractions of iron ions in Fe^{3+} and Fe^{2+} valence states, respectively. μ_{exp} obtained from relations (3.2) and (3.3) using experimentally determined values of C_M, were found to be lower than μ_{Fe}^{3+} (*cf.* Table 3.2.6). Comparison of x_1 (mole % $Fe_2^{3+}O_3$) and x_2 (mole %

$Fe_2^{2+}O_3$) for various glasses listed in Table 3.2.6 shows that iron ions exist in both $Fe^{3+}$and Fe^{2+} valence states in all the glass compositions. While the x_1 and x_2 values show an increasing trend up to 6 mole % Fe_2O_3, x_1 decreases in glasses with x > 6 mole % Fe_2O_3. The ratio of the number of ions in Fe^{2+} state (x_2) to the total number of ions (x_1+x_2) in various glass compositions is listed in Table 3.2.6. This shows that the relative domination of Fe^{3+} ions in glasses with lower concentrations of Fe_2O_3 is reduced as x is increased giving way to more and more Fe^{2+} ions at higher x values. The glass composition near $x \approx 7$ mole% Fe_2O_3 is expected to contain an equal distribution of these two species of Fe ions. The molar fraction of Fe^{+2} ions obtained from the intensity of the g ≈ 2.1 absorption line increases with an increase in x (Fig. 3.2.5.3). The molar fraction of Fe^{3+} ions as indicated by the intensity of the g ≈ 4.3 line (Fig. 3.2.5.2) shows a maximum for the glass composition with x = 6 mole%. μ_{exp} decreases from 5.85 (which is close to μ_{Fe}^{3+} value) for the glass with composition x = 2 mole % to 5.01 (which is close to μ_{Fe}^{2+} value) for the glass with x = 10 mole %. The magnetic data of the glasses can be understood on the basis of the relative concentration of the iron ions if one presumes the existence of Fe^{2+}-Fe^{2+}, Fe^{3+}-Fe^{3+} and Fe^{2+}-Fe^{3+} magnetic exchange pairs. Based on these two results, one can conclude that as x is increased in this series of glasses, the dominating magnetic exchange pairs change from Fe^{3+}-Fe^{3+} to Fe^{2+}-Fe^{3+} and ultimately to Fe^{2+}-Fe^{2+}.

3.2.7. *In vitro* bioactivity test of glass samples

In vitro bioactivity test was carried out by soaking the glass pieces in 30 ml of SBF, following the procedure detailed in chapter 2. Bioactive samples treated with SBF show the growth of a calcium phosphate layer on their surface. Glass pieces with nominal

compositions of $41CaO(52\text{-}x)SiO_2 4P_2O_5 xFe_2O_3 3Na_2O$ immersed in SBF were taken out after 1, 3, 7, 10, 20 and 30 days, lightly washed with acetone. Surface structural changes of the glass samples treated in SBF were analyzed by glancing incidence X-ray powder diffraction (GI-XRD), Fourier transform infra-red reflection spectroscopy (FT-IRS) and scanning electron microscopy (SEM). The surface chemical analysis was carried out by energy dispersive X-ray spectroscopy (EDS) analysis.

3.2.7.1. GI-XRD studies of the glass samples soaked in SBF

Fig. 3.2.7.1(a) shows the typical GI-XRD patterns obtained from the surfaces of glasses before and after soaking in SBF for various time periods (*i.e.* 0, 1, 3, 7, 10, 20 and 30 days). The GI-XRD patterns of the glass sample with $x = 8$ mole % Fe_2O_3 is shown in the figure. GI-XRD patterns of all untreated samples [designated as 0 d in Fig. 3.2.7.1(a)] were devoid of crystalline peaks, indicating the amorphous nature of the glassy samples. On immersion in SBF for a day or more, crystalline peaks appear in the GI-XRD patterns, indicating the formation of a crystalline layer on the surface of the glass. Initially, two well defined peaks at 2θ values of ~26° and ~32° develop after 3 days of soaking in SBF. After 7 days of soaking in SBF, these two peaks intensify and two new peaks develop at 2θ values of ~40° and ~46°. The four peaks could be assigned to (002), (211), (130) and (222) reflections of hydroxyapatite (HA) crystallites (JCPDS file no: 74-0565). Apatite formation on the surface of the glasses in the SBF is governed by chemical reaction of the surface of the matrix with the fluid. The wide diffraction peak at 2θ ranging from 30˚ to 34˚ corresponds to the overlap of (112), (300) and (202) reflection of the well-crystallized HA.

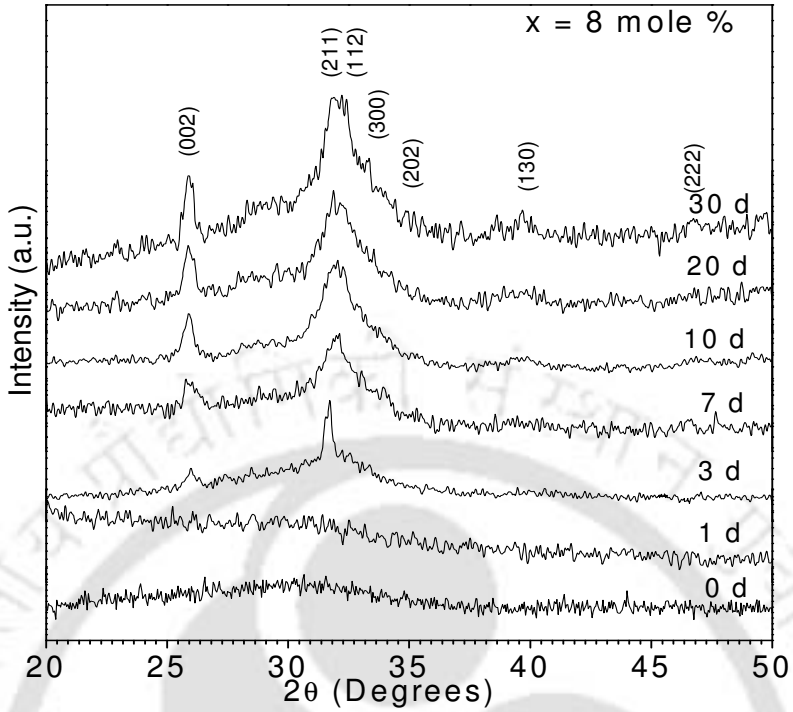

Fig. 3.2.7.1 (a): Thin-film X-ray diffraction patterns of glass sample x = 8 mole % soaked in SBF for various periods.

The GI-XRD patterns depicted in Fig. 3.2.7.1(a) show the preferential growth mechanism of the surface apatite layer. Formation of the hydroxyapatite layer over the glass surface shows that the glass samples are bioactive. The bonding of bioactive glass and glass-ceramics to bone tissue was associated with a series of chemical interactions at the interface with the surrounding fluids and tissue. Hench [3] has described the bonding mechanism as a sequence of reactions between the glass/glass-ceramics and the surrounding fluid. A silica-rich layer is formed initially, followed by the formation of a calcium-phosphate-rich layer. It has been shown that most of the bioactive glasses [58, 181-182] and glass-ceramics [4, 42, 183] form a layer of a carbonate containing hydroxyapatite similar to the apatite in the bone on their surface in the body, and bond to

the living bone through this apatite layer. Formation of this apatite-like layer on the surface of materials immersed in SBF is now accepted as a confirmation of the bioactivity of the material [44-45, 58, 60, 66]. The gradual growth in the intensity of the individual reflection, appearance of other low intensity apatite reflections and the narrowing of the peak width clearly show the evolution of the crystalline HA surface layer as a function of immersion time in SBF. The intensity of two major reflections, *viz*., (002) and (211), increase [cf. Fig. 3.2.7.1 (b)] with an increase in the concentration of Ca^{2+} and PO_4^{3-} ions on the surface of the glass immersed in SBF for various days. It is obvious that the intensity of the reflections attain saturated values within 10 days of immersion in SBF.

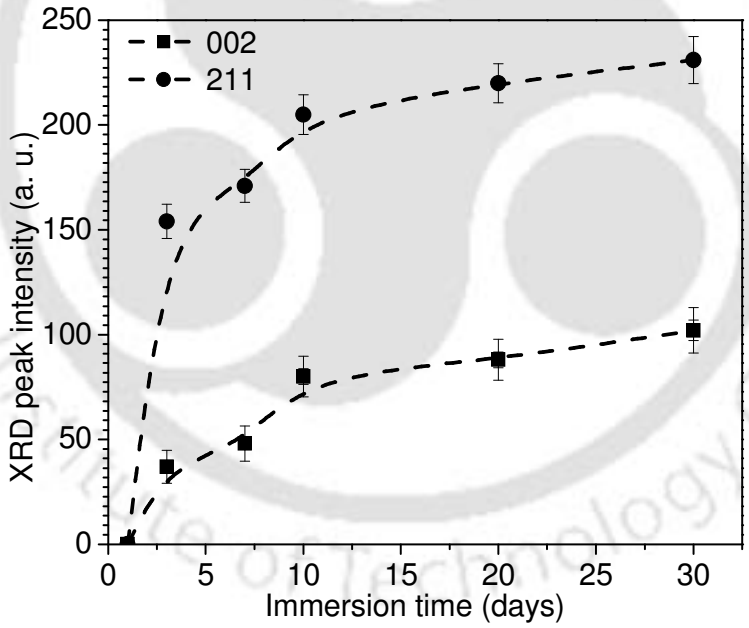

Fig. 3.2.7.1 (b): Variation of GI-XRD intensity of (002) and (211) reflections of glass sample x = 8 mole % as a function of soaking time in SBF.

The average crystallite size (d) in a direction perpendicular to the crystallographic plane can be estimated using the Scherrer`s formula equation (2.1) [139]. The average size of crystallised HA was calculated from the peak profile of (002) reflection using equation (2.1). Fig. 3.2.7.1 (c) reveals an increase in the average particle size of the crystalline surface layer on the glass immersed in SBF for various days, which is consistent with results of reported earlier [184]. The crystallite size increases from about 14.1 (± 0.36) nm to 17.8 (± 0.45) nm in samples immersed for 3 days to 30 days. The size of HA crystalline depends on the rate of crystalline growth on the surface of the glass immersed in SBF. The variation of the crystallite size with immersion time shows a sharp increase in crystallite size in samples treated in SBF for 10 days, followed by a slower increase in crystallite size in samples treated in SBF for longer periods.

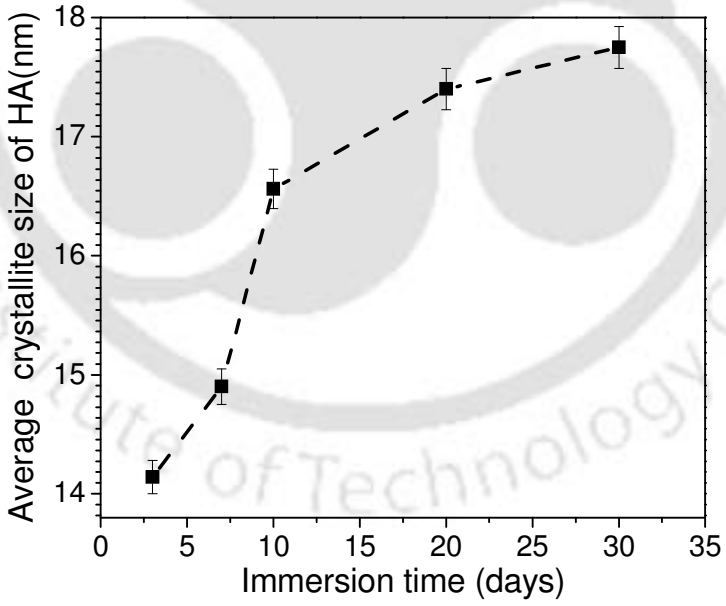

Fig. 3.2.7.1 (c): The averages size of HA crystalline (nm) corresponds to the (002) reflection peak for sample x = 8 mole % soaked in SBF for 3, 7, 10, 20 and30 days.

Fig. 3.2.7.1(d) shows the GI-XRD patterns obtained from the surfaces of glasses with x = 2, 4, 6, 8 and 10 mole % Fe_2O_3 after treatment in SBF for 30 days. The hydroxyapatite (HA) peaks appearing between 2θ values of 30° to 34° sharpen in samples with higher x. Since the broad peaks signify the presence of small sized crystallites, one can infer that on immersion in SBF, the HA formation gradually improves from small sized crystalline aggregates to a well-crystallized HA phase as the amount of iron oxide is increased in the system. Formation of the HA layer over the glass surface shows that the glass samples are bioactive. The relative intensity and peak width of the characteristic apatite reflections show considerable composition dependence. It is interesting to observe the growth in the intensity and reduction in the width of the apatite reflections as a function of increasing iron oxide content in this series of glasses.

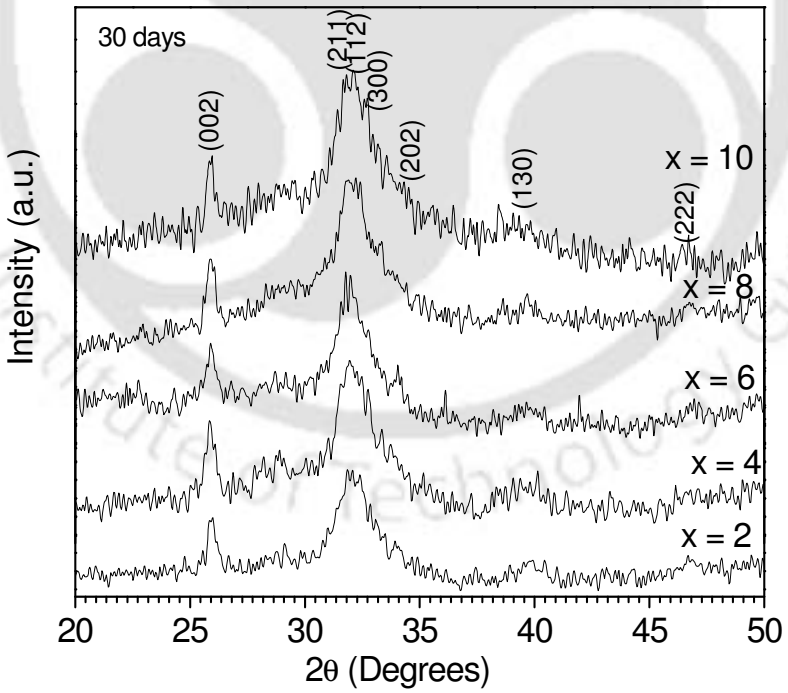

Fig. 3.2.7.1 (d): GI-XRD patterns of various samples x = 2, 4, 6, 8 and10 mole % soaked in SBF for 30 days.

Addition of Fe_2O_3 in $CaO.SiO_2$ glass [66, 185] or an increase in Fe^{3+} ion concentration in $Na_2O.CaO.P_2O_5.SiO_2$ glass [186] have been reported to reduce their apatite forming ability. Addition of Fe_2O_3 in CaO-SiO_2 based glass has been reported [60] to reduce its apatite forming ability when immersed in SBF decreased. On the other hand, addition of Na_2O or P_2O_5 facilitates apatite formation in CaO-SiO_2 based glasses. Heat treatment of CaO-SiO_2 based glasses containing Fe_2O_3 results in the precipitation of the ferrimagnetic magnetite (Fe_3O_4) crystallites [4, 131-132, 134]. Such ferrimagnetic bioactive glass-ceramics [4, 130-132, 134, 187] find potential application as thermoseeds for hyperthermia treatment of cancer. We observe better apatite formation in this series of glasses when the iron oxide content is increased. This might be due to the fact that in this series of glasses, Fe_2O_3 replaces SiO_2, leaving the amount of CaO and P_2O_5 undisturbed. Such compositional variation seems to aid the apatite forming ability on the surface of these glasses.

3.2.7.2. FT-IR spectroscopy of the glass samples soaked in SBF

Fig. 3.2.7.2 (a) shows the infrared reflection spectra of the glass sample with x = 8 mole % Fe_2O_3 before and after the immersion in SBF for 0, 1, 3, 7, 10, 20 and 30 days. The spectrum before the immersion reveals bands at 1238, 937, 773, 640 543 and 490 cm^{-1}. The peaks at 1238, 937, 773, 640, 543 and 490 cm^{-1} correspond [188-190] to v_3 P-O stretching, Si-O stretching [with one non bridging oxygen (NBO)], Si-O-Si stretching, O-H stretching, v_4 P-O bending and v_4 Si-O-Si bending frequencies, respectively. After 1 day of immersion in SBF, new peaks appear at 479, 860, 901, 1339 and 1566 cm^{-1}. The peaks at 479 cm^{-1} and 901 cm^{-1} correspond to v_2 P-O bending and v_1 P-O-P stretching

frequency, respectively. The band located at 860 cm^{-1} and the large bands at 1339 and 1566 cm^{-1} can be assigned to C-O vibration mode of CO_3^{2-}. These bands signify the incorporation of carbonate anions from the SBF in the apatite crystal lattice. After 7 days of immersion in SBF, the appearance of the band at 970 cm^{-1}, which is related to calcium phosphate (hydroxyapatite) surface layer is observed. The peak at 970 cm^{-1} corresponds to the v_1 P-O symmetric stretching frequency. It indicates the obviation of phosphate ions from the ideal tetrahedral structure. This is a Raman active only mode when v_1 P-O symmetric stretching is in the free ion state. This Raman active mode can be seen in the infrared spectra because of lowering of the symmetry in the crystalline state [191]. After 20 days of immersion in SBF, the appearance of the peak at 1024 cm^{-1} reflects the v_3 P-O antisymmetric stretching vibration.

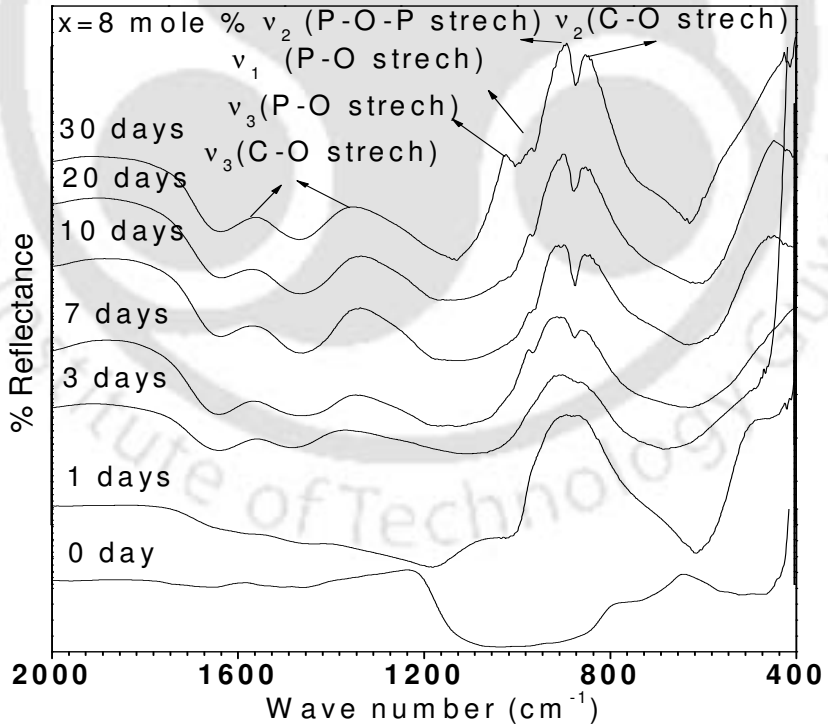

Fig. 3.2.7.2(a): FT-IR reflection spectra of surfaces of glass x = 8 mole % soaked in SBF for various days.

With further increase in immersion time, the intensity of the bands related to the CO_3^{2-} group increases. Carbonate ions occupy two different sites in carbonated apatite as indicated by peaks in the region of 1650 to 1300 cm^{-1} which are due to v_3 vibration mode, whereas the peak at 860 cm^{-1} is due to the v_2 vibration mode of carbonate ion [190]. The v_3 band splits into two peaks centered at 1339 and 1566 cm^{-1}, respectively, with the distribution of the carbonate v_3 sites depending on the maturation and formation of apatite crystals. Occupancy of the v_2 sites is considered to occur competitively between the OH^{-1} and carbonate groups at the interface of growing crystal, whereas, occupancy of the v_3 sites depends on competition between the phosphate and carbonate ions [190]. Presence of v_2 and v_3 vibration modes of carbonate is the signature of the development of HCA layer on the surface of the sample.

Fig. 3.2.7.2 (b) shows the infrared reflection spectra of glass samples with x = 2, 4, 6, 8 and 10 mole % Fe_2O_3 after the immersion in SBF for 30 days. Spectral bands of HA assigned to PO_4^{3-} groups (ν_3–1024 cm^{-1}, ν_1–970 cm^{-1}, ν_1–901 cm^{-1} and ν_2–473 cm^{-1}), CO_3^{2-} functional groups (v_2–860 cm^{-1}, ν_3–1339 $cm^{-1}$and ν_3–1566 cm^{-1}) and OH^- groups (631 cm^{-1}) appear in the spectra. The band at 932 cm^{-1} Si-O stretch (with 1 NBO) disappears in the samples with x = 8 and 10 mole %. A new band at 1024 cm^{-1} develops in samples with x = 8 and 10 mole %, which is related to calcium phosphate (hydroxyapatite) surface layer. The peak at 901 cm^{-1} reflects the v_1 P-O-P stretching mode. These bands (860 and 901 cm^{-1}) sharpen and their relative intensities increase with increase in iron oxide content signifying the formation of a well crystallized HCA layer in these samples. The FTIR studies thus clearly show an increased bioactivity in these glasses as the iron oxide content is increased in the composition range studied.

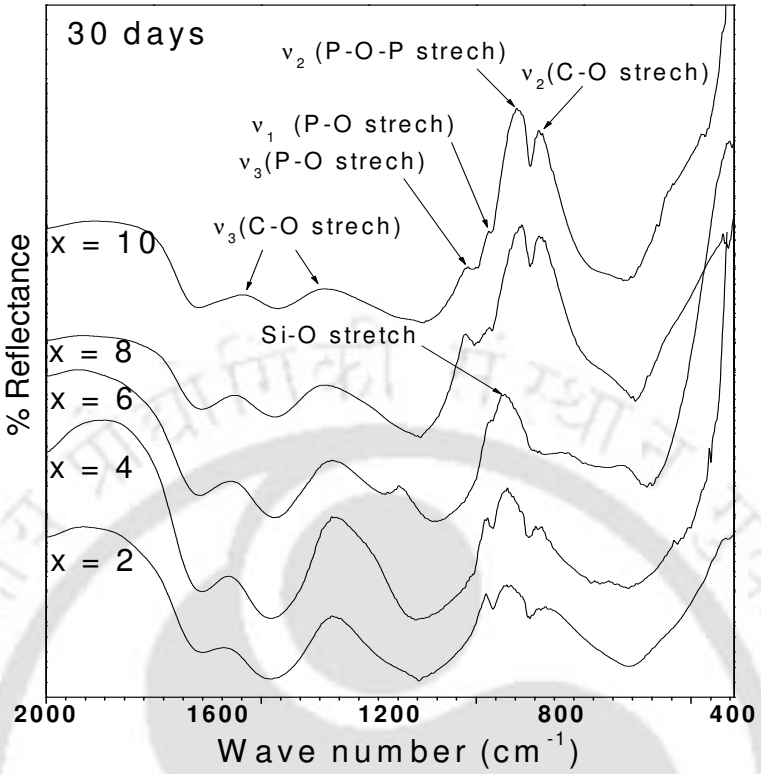

Fig. 3.2.7.2(b): FT-IR reflection spectra of surfaces of various glasses soaked in SBF for 30 days.

3.2.7.3. SEM-EDS studies of the glass samples soaked in SBF

Fig. 3.2.7.3 (a) shows the SEM micrographs of the glass sample with x = 8 mole % Fe_2O_3 after immersion in SBF for 1, 3, 7, 10, 20 and 30 days, respectively. The micrograph shows images magnified 1000 times. The micrographs provide visual evidence of the formation of a surface layer on the glasses, which can now be presumed to be an apatite layer. After 30 days of immersion, the whole surface of the specimen is covered with spherical Ca-P particulate apatite layer. Results from EDS analysis reveal the gradual development of an HCA layer on the surface of glass samples after immersion for various time periods in SBF. The spherical particles in the sample treated in SBF for 30 days are

made up of calcium and phosphorus and the Ca/P molar ratio (calculated from EDS analysis) was of ~1.67, corresponding to the value of hydroxyapatite.

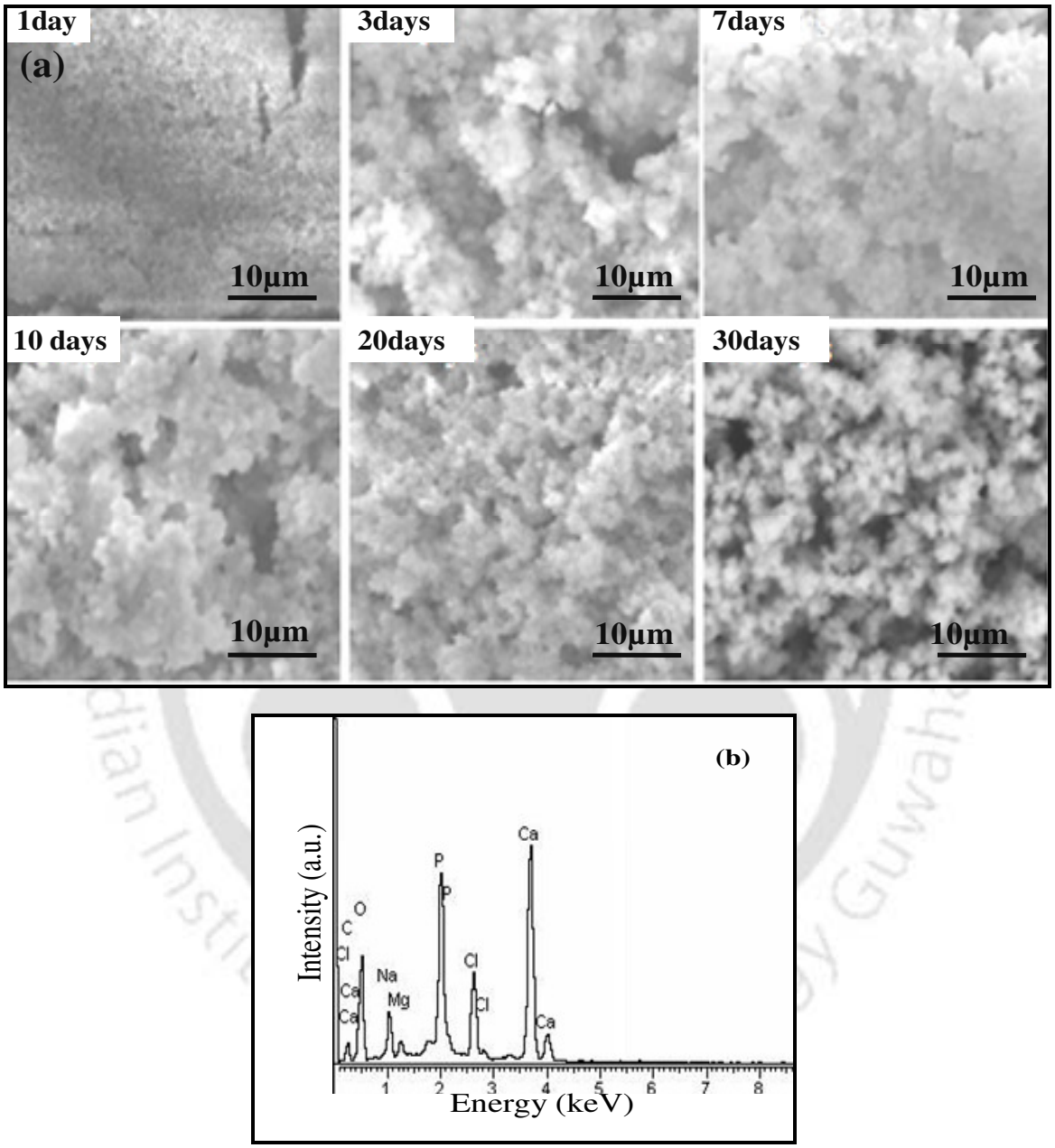

Fig. 3.2.7.3: (a) SEM micrographs of glass with x = 8 mole % (magnified 1000×) soaked in SBF for various days, and (b) EDS spectra of sample soaked in SBF for 30 days.

Microanalysis of the precipitates reveals the presence of small quantities of Na, Mg and Cl as shown in EDS spectra [Fig. 3.2.7.3(b)]. This finding is in agreement with reports which claim that the growth of hydroxyapatite in SBF results in the incorporation of sodium, magnesium and chlorine [192] as well. It may thus be concluded that the surface layer on the glasses treated in SBF contains carbonate, sodium, magnesium and chlorine substituted hydroxyapatite [193].

3.3. Characterization of glass-ceramics samples

Powder X-ray diffraction analysis was used to identify the crystalline phases in the glass-ceramics derived from the parent glasses. The magnetic hysteresis loop was obtained using at room temperature at two different external magnetic fields of ± 20 kOe (kA/m) and ± 500 Oe. Magnetic susceptibility measurements of glasses containing iron oxide reveal the nature of interactions between the iron ions apart from providing information on the valence states of iron ions. EPR absorption spectra were analaysed to understand the local environments and valence state of Fe ions in glass-ceramics at room temperature. Room temperature microhardness provides information on the mechanical strength of the glass-ceramics samples. *In vitro* bioactivity test was performed on the samples by immersion of samples in SBF and the changes in the surface structure of the glass-ceramics were examined by grazing incidence XRD, reflectance FT-IR spectroscopy and Scanning Electron Microscopy (SEM) . The surface chemical analysis was carried out by energy dispersive X-ray spectroscopy (EDS) analysis.

3.3.1. XRD studies of glass-ceramics samples

XRD patterns of $41CaO.(52\text{-}x)SiO_2.4P_2O_5.xFe_2O_3.3Na_2O$ (x = 2, 4, 6, 8 and 10 mole %) glass-ceramic samples are shown in Fig. 3.3.1.1. Three major phases, *viz.*, calcium hydroxide phosphate [hydroxyapatite $Ca_{10}(PO_4)_6(OH)_2$] [PDF # 74-0566], magnetite (Fe_3O_4) [PDF # 88-0315] and wollastonite ($CaSiO_3$) [PDF # 84-0655] were identified in all glass-ceramics samples. Hydroxyapatite and wollastonite are bone minerals and their presence is indicative of the biocompatibility of all the glass-ceramic samples. The percentage of hydroxyapatite was found to increase in samples with increasing iron oxide concentration.

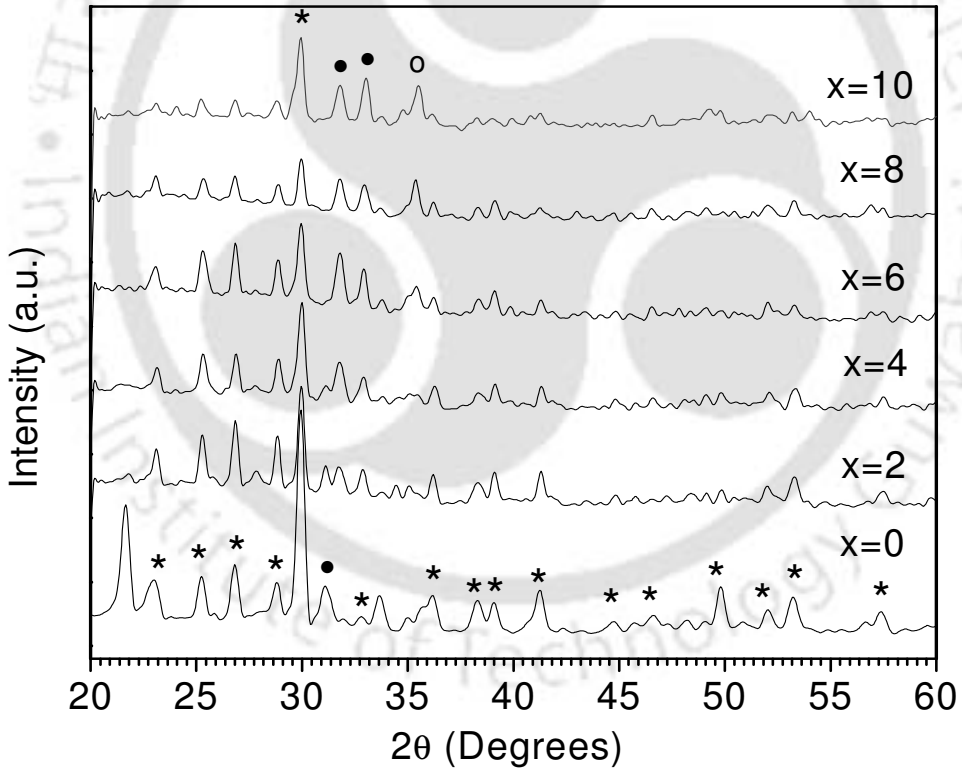

Fig. 3.3.1.1: XRD patterns of glass-ceramic samples derived from glasses with composition $41CaO.(52\text{-}x)SiO_2.4P_2O_5.xFe_2O_3.3Na_2O$. The three major crystalline phases present are magnetite (open circle) hydroxyapatite (filled circle) and wollastonite (stars).

The average crystallite size was calculated from the broadening of the primary magnetite peak [(311)] using Scherrer's equation (2.1) [139]. The average crystallite size of the magnetite phase increased in the samples as the iron oxide content was increased from 2 to 10 mole % as depicted in Fig. 3.3.1.2. The average crystallite size of the magnetite phase *d* ranged between 31 nm to 56 nm in various samples (*cf*. Table 3.3.4.1).

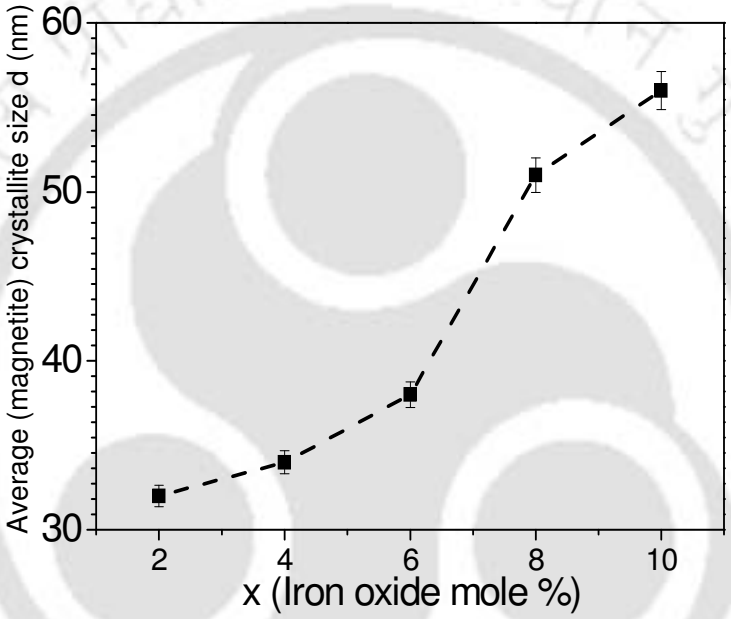

Fig. 3.3.1.2: Variation of average magnetite crystallite size with iron oxide content.

3.3.2. Microhardness studies of glass-ceramics samples

Microhardness of the above glass-ceramics was measured following the procedure outlined in the second chapter. All specimens were uniformly subjected a load of 100 g for a duration of 15 s. The measured VHN values are tabulated in Table 3.3.4.1. Fig. 3.3.2 shows the variation of VHN with the iron oxide mole % in $41CaO(52\text{-}x)SiO_2 4P_2O_5$ $xFe_2O_3 3Na_2O$ glass-ceramics. The glass-ceramics samples show a higher VHN as

compared to the corresponding parent glasses. VHN of the glass-ceramics samples increases as a function of iron oxide content as shown in Fig. 3.3.2 and Table 3.3.4.1. The presence of crystalline phases increases the VHN of the glass-ceramics. An increase in the VHN can then be interpreted as due to the increase in the percentage of the crystalline phases in the glass-ceramics as a function of iron oxide content. Thus, addition of iron oxide increases the hardness of this series of samples.

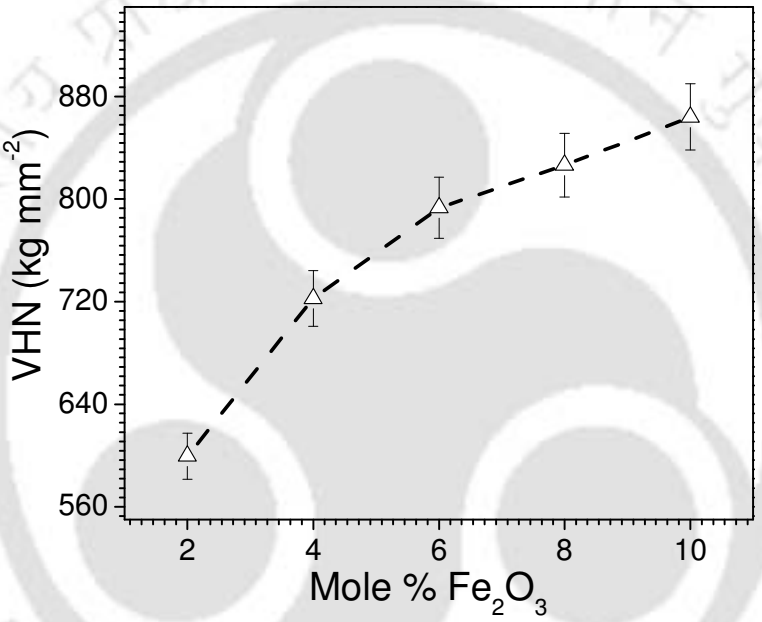

Fig. 3.3.2: Variation of VHN of 41CaO(52-*x*) SiO_2 $4P_2O_5$*x*$Fe_2O_3$3Na_2O glass-ceramics.

3.3.3. EPR studies of glass-ceramics samples

The EPR spectra of 41CaO(52-*x*)SiO_2 $4P_2O_5$ *x*Fe_2O_3 3Na_2O ($2 \leq x \leq 10$ mole %) glass-ceramic samples are shown in Fig. 3.3.3.1. EPR spectra of Fe^{3+} ions in oxide glasses and glass-ceramics are generally characterized by the appearance of resonance absorptions at g ≈ 4.3 and 2.1 with their relative intensity being strongly dependent on composition [134, 157, 167, 194-196]. The g ≈ 4.3 resonance line is characteristic of isolated Fe^{3+} ions

predominantly situated in rhombically distorted octahedral or tetrahedral oxygen environments. The g ≈ 2.1 resonance is assigned to those ions which interact by a superexchange coupling and can be considered as distributed in clusters [134,151, 165, 194-195]. The spectra mainly consist of absorption lines centered at g ≈ 4.3 and g ≈ 2.0 which are due to Fe^{3+} ions ($3d5^6S_{5/2}$). The relative intensity and linewidth of these absorption lines show a strong dependence on Fe_2O_3 concentration.

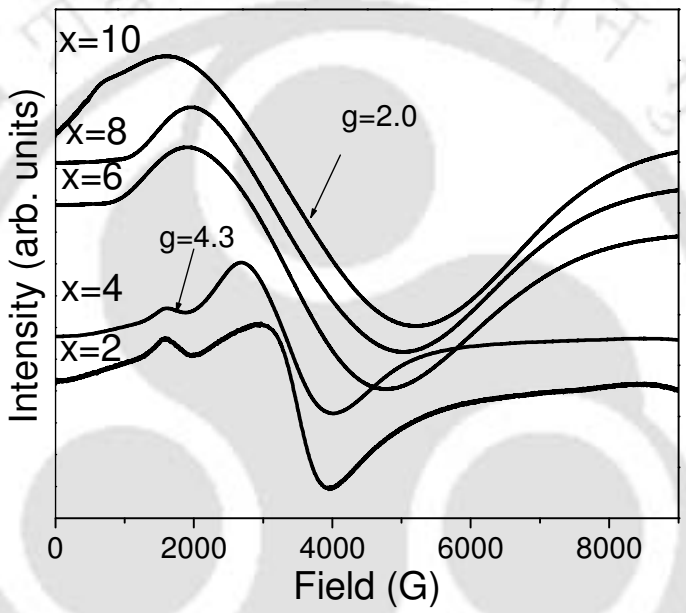

Fig. 3.3.3.1: Room temperature EPR spectra of $41CaO(52\text{-}x)SiO_2 4P_2O_5 x Fe_2O_3 3Na_2O$ glass-ceramics.

The composition dependence of the EPR parameters of the glass-ceramics is plotted in Fig. 3.3.3.2 for the absorption centered at g ≈ 2.0. The figure illustrates the variations in the EPR parameters, *viz.*, the relative peak to peak height *I*, the linewidth of the derivative plots ΔH, and the intensity of the absorption line *J*, approximated as $J = I(\Delta H)^2$ of the absorption at g ≈ 2.0. It is apparent from the figure that the intensity ($J_{(g=2.0)}$)

and linewidth ($\Delta H_{(g=2.0)}$) of the g ≈ 2.0 absorption line increase as function of *x*. The g ≈ 2.0 resonance arises due to the formation of iron clusters which give rise to superexchange type interaction between iron ions. The increase in $J_{(g=2.0)}$ as a function of iron oxide content indicates an increase in the ferrimagnetically coupled superexchange type interactions in the glass-ceramic samples.

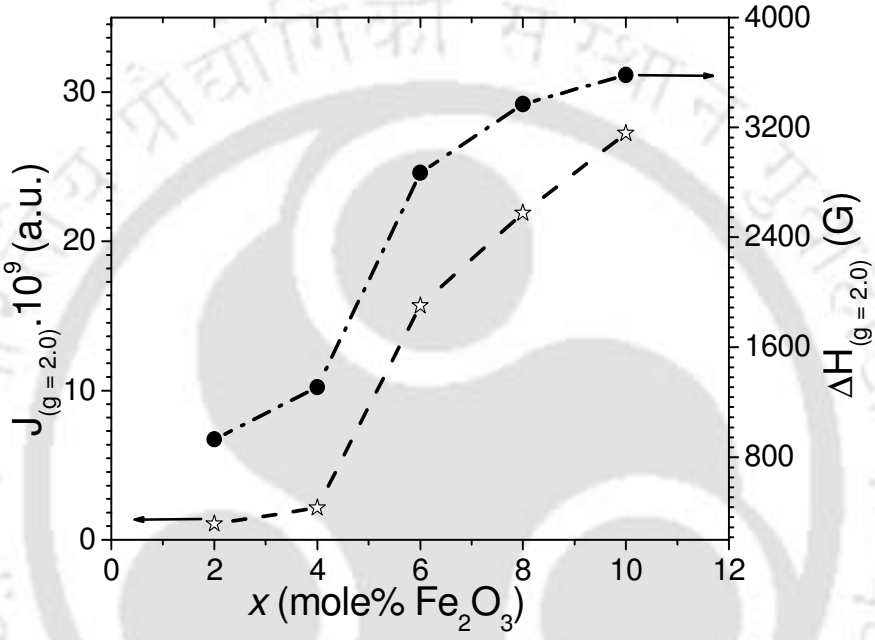

Fig. 3.3.3.2: Composition dependence of intensity and linewidth for g ≈ 2.0 absorption line of $41CaO(52\text{-}x)SiO_2 4P_2O_5 x Fe_2O_3 3Na_2O$ glass-ceramic samples.

However, the nonlinear increase of $J_{(g=2.0)}$ and $\Delta H_{(g=2.0)}$ with Fe_2O_3 concentration depicted in Fig. 3.3.3.2 shows that iron ions are present as Fe^{3+} as well as Fe^{2+} in the samples. Fe^{2+} ions are not involved in the EPR absorption but their interaction with Fe^{3+} influences the characteristics of the absorption lines. Superexchange mechanisms tend to narrow the absorption line. On the other hand, interactions between Fe^{3+} and Fe^{2+} ions tend to broaden the linewidth. The final linewidth depends on the relative strengths of the

two mechanisms influencing the linewidth. The increase in the linewidth of the g ≈ 2.0 resonance with Fe_2O_3 concentration signifies the dominance of the broadening mechanisms as the Fe_2O_3 content is increased, which in turns indicates an increase in Fe^{2+} ion concentration as a function of Fe_2O_3 concentration in the glass-ceramic samples. It can be observed in Fig. 3.3.3.1 that the g ≈ 2.0 line shifts from 0.342 T (or g = 1.971) for the *x* = 2 mole % sample to 0.326 T (or g = 2.069) for the *x* = 10 mole % sample. This shift can be attributed to an increase in the number of ferrimagnetic multi-domain crystallites in the samples. It is worthy to point out that the average magnetite crystallite size increases in the samples as a function of *x*. Fig. 3.3.3.1 shows that the EPR absorption at g ≈ 4.3 is observed only in samples with *x* = 2 and 4 mole % Fe_2O_3. The concentration dependence of the EPR parameters of the absorption line centered at g ≈ 4.3 is plotted as a function of composition in Fig. 3.3.3.3.

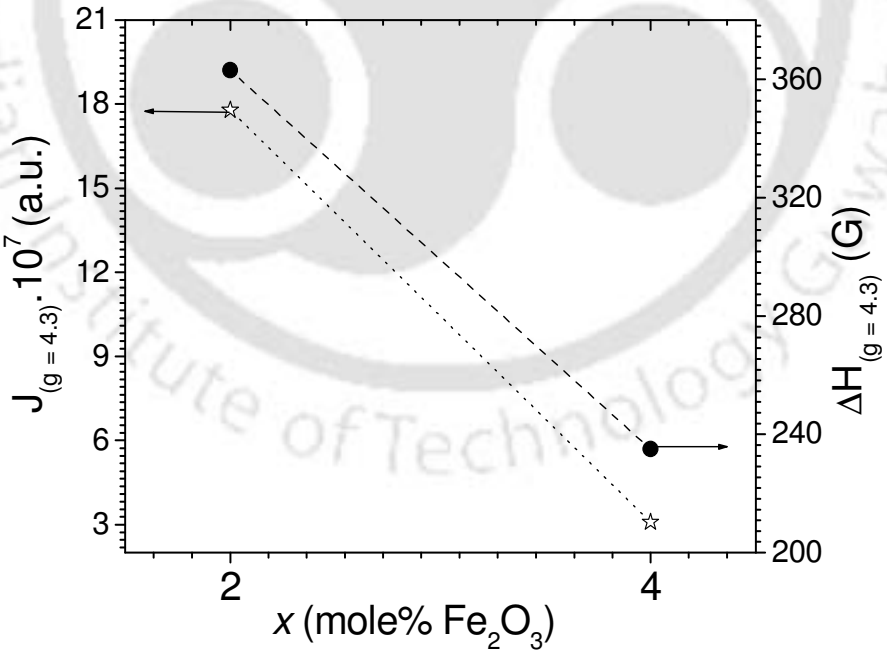

Fig. 3.3.3.3: Composition dependence of intensity and linewidth for g ≈ 4.3 absorption line of $41CaO(52\text{-}x)SiO_2 4P_2O_5 x Fe_2O_3 3Na_2O$ glass-ceramic samples.

The intensity ($J_{(g=4.3)}$) and linewidth ($\Delta H_{(g=4.3)}$) of the $g \approx 4.3$ absorption line decreases as x is increased. Since the $g \approx 4.3$ line arises from Fe^{3+} ions in low symmetry sites, the disappearance of the $g \approx 4.3$ line signifies a decrease of low symmetry sites at Fe^{3+} ions and a corresponding increase in Fe^{3+} sites of higher symmetry in the crystallization process. In other words, the EPR spectra indicate that low symmetry sites whose crystal fields are equal and very near to the special crystal fields with $D = 0$, $E \neq 0$ and $\lambda = E/D = 1/3$ have been removed during the crystallization process. As already pointed out, XRD studies have confirmed that magnetite ($Fd\bar{3}m$) crystallizes when the glasses are heat-treated at 1050 °C.

3.3.4. Magnetic properties of glass-ceramics samples

Fig. 3.3.4.1 depicts the room temperature magnetic hysteresis (M-H) loops of different glass-ceramic samples derived from respective glasses with composition $41CaO(52\text{-}x)SiO_2 4P_2O_5 x Fe_2O_3 3Na_2O$. All the samples attained magnetic saturation within a magnetic field of 20 kOe. The coercive field and the remanent magnetization are individuated in the inset in Fig. 3.3.4.1, where an enlarged view of the central part of the hysteresis cycles is shown. It can be seen that the magnetic field necessary to saturate the samples increased with increasing mole % iron oxide. The sample with $x = 2$ mole % iron oxide showed a weak magnetic response. The coercive field decreased from 171 Oe to 91 Oe, whereas the saturation magnetization increased from 0.496 emu/g to 7.945 emu/g as the iron oxide percentage was increased from 2 to 10 mole %. With increasing iron oxide concentration, the magnetic response of the samples increases. The magnetic

behaviour observed is similar to soft magnetic materials with narrow hysteresis loop and low coercivity. The quantity of magnetic phase present in the glass-ceramic samples was determined from the magnetization ratio between the sample and pure magnetite (M_s = 92 emu/g [148]). The saturation magnetization increases with the amount of magnetic phases crystallised in the sample (*cf.* Table 3.3.4.1). The highest amount of magnetite phase is obtained for the sample x = 10 mole % which contains the highest value of saturation magnetization (M_s). The results are summarized in Table 3.3.4.1.

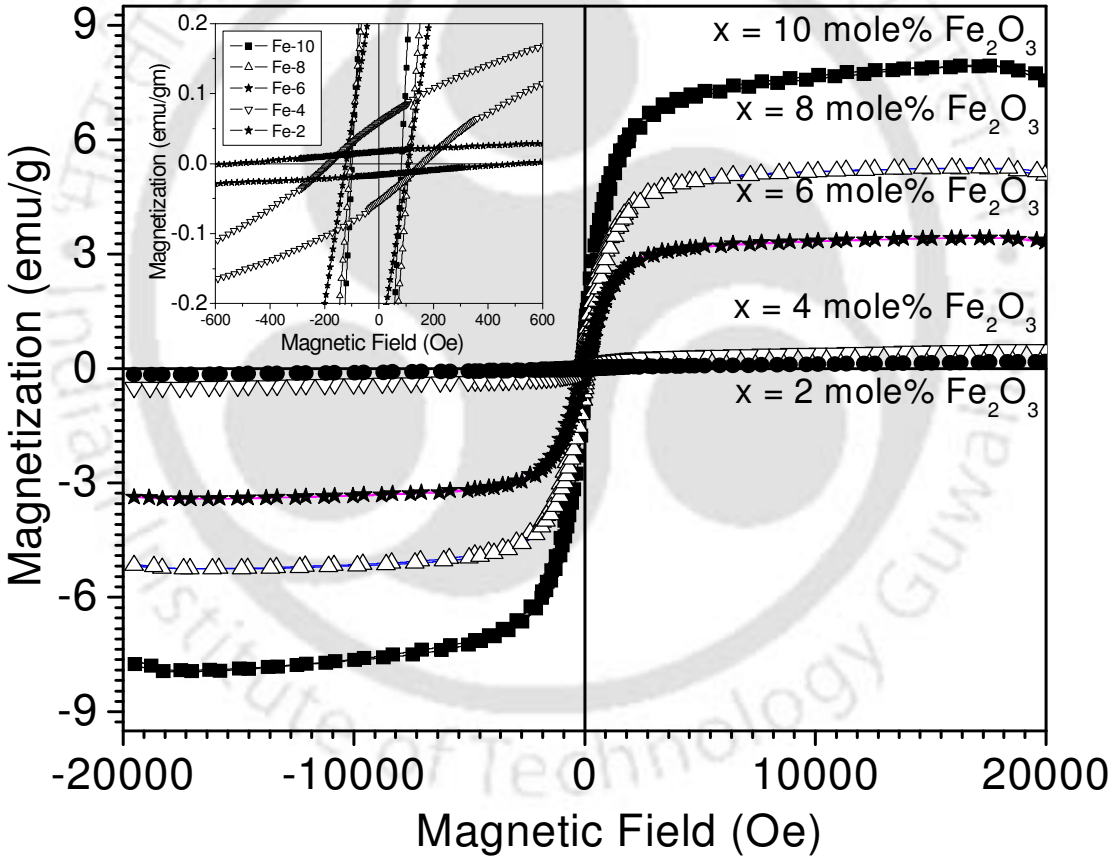

Fig. 3.3.4.1: Room temperature M-H curves of $41CaO(52\text{-}x)SiO_2 4P_2O_5 xFe_2O_3 3Na_2O$ glass-ceramics under ± 20 kOe field. Data close to the origin is expanded in the inset.

Table 3.3.4.1: Physical parameters of the glass-ceramics samples.

Magnetic and structural parameters	**Sample (*x*) (mole % of iron oxide)**				
	$x = 2$	$x = 4$	$x = 6$	$x = 8$	$x = 10$
Average (magnetite) crystallite size *d* (nm)	32	34	38	51	56
Percentage of magnetic phase	0.18	0.53	3.71	5.7	8.64
Saturation magnetization M_s (emu/g)	0.17	0.49	3.42	5.25	7.95
Coercive force, H_C (Oe)	523	171	114	108	91
Remanent magnetization M_r (emu/g)	0.02	0.06	0.29	0.51	0.71
Hysteresis area ± 20 kOe (erg/g)	293	625	2992	4285	6842
Hysteresis area ± 500 Oe (erg/g)	4	32	246	408	642
Vickers hardness number (VHN) (kg mm^{-2})	599	722	793	826	864

Fig. 3.3.4.2 displays the relevant magnetic parameters obtained from M-H loops for samples with different iron oxide content. The saturation magnetization (M_S) (Fig. 3.3.4.2a) increased with increasing iron oxide concentration from x = 2 to 8 mole % and showed a tendency to saturate for $x = 10$ with the maximum value of about 7.945 emu/g. The increase of M_s with an increase in iron oxide concentration could be attributed to the development of magnetite phase in the samples, which can be inferred from Fig. 3.3.1.1 and Table 3.3.4.1. Coercivity of the samples (*cf.* Fig. 3.3.4.2b) decreases with increasing iron oxide concentration from 2 to 10 mole %, revealing soft magnet-like behaviour in the samples with higher iron oxide concentration.

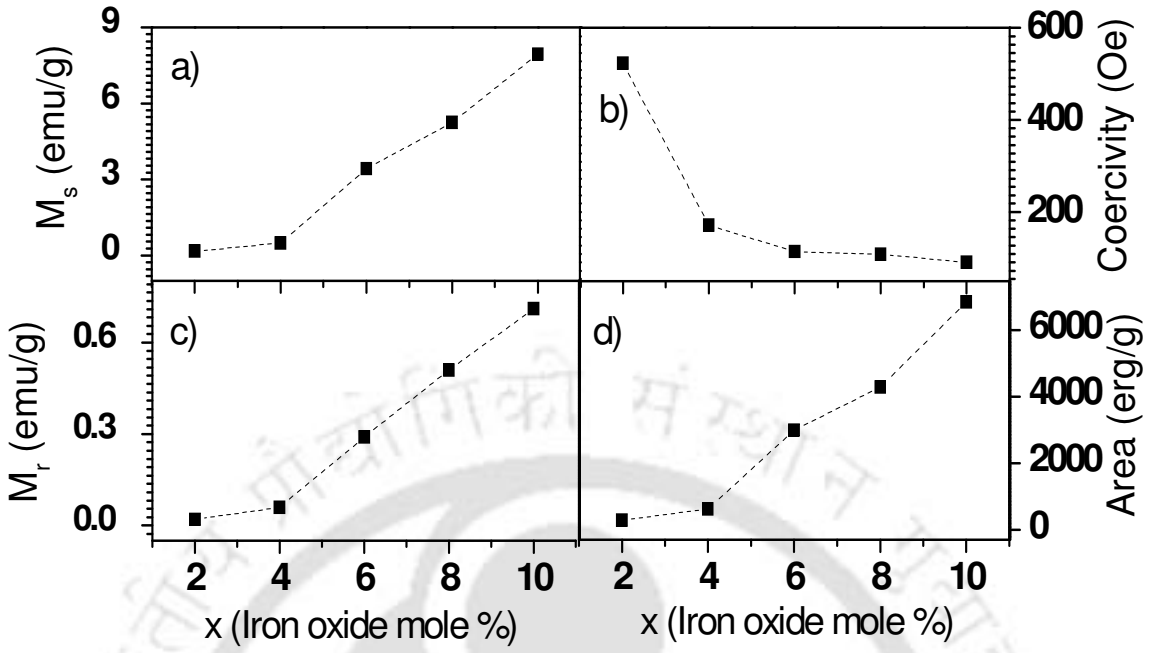

Fig. 3.3.4.2: Variation of (a) saturation magnetization, (b) coercivity, (c) remanent magnetization, and (d) area under the hystersis loop under ± 20 kOe of $41CaO(52\text{-}x)\ SiO_2\ 4P_2O_5 x Fe_2O_3 3Na_2O$ glass-ceramics as a function of iron oxide content.

The remanent magnetization values are much lower than M_s values due to structural characteristics of the glass-ceramic samples. Fig. 3.3.4.2 d illustrates the variation of the area of hysteresis loop as a function of iron oxide content. The areas were obtained by integrating the extrapolated loop area under ± 20 kOe field sweep. The area of hysteresis cycle calculated for each glass-ceramics sample is presented in Table 3.3.4.1. The highest value is obtained for the x = 10 % mole sample, which also exhibits the highest M_s and lowest coercivity. The area under the hysteresis loop increased with increasing iron oxide content. Since the area under the loop is proportional to the energy loss and hence the heat generated by a sample under an alternating field, samples with higher iron oxide concentration are capable of generating more heat in hyperthermia

applications. The large variation in the area under the loops for samples with x = 2 to x = 10 mole % iron oxide provides a means for controlled heat generation by appropriate choice of sample composition. Since such a high magnetic field is difficult to realize in a clinical laboratory, hysteresis loops were measured using a magnetic field 40 times smaller (± 500 Oe). The corresponding M-H loops are shown in Fig. 3.3.4.3. When magnetic saturation is not reached, decreasing the maximum magnetic field value results in a rapid reduction of the loop area. Therefore, the magnetic loss per cycle for x = 10 mole% iron oxide sample is the highest. The variation of the loop area with composition is shown as in-set in Fig. 3.3.4.3. A comparison of this plot with Fig. 3.3.4.2d shows that the area of the plots scales linearly with magnetic field.

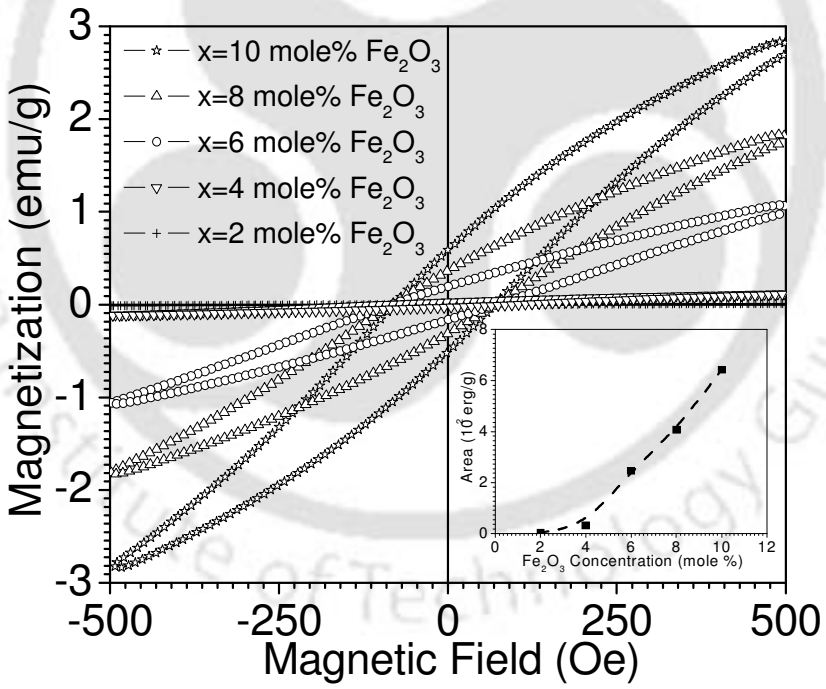

Fig. 3.3.4.3: Room temperature M-H loops of glass-ceramics under ± 500 Oe field sweep. Inset shows the variation of loop area as a function of iron oxide concentration.

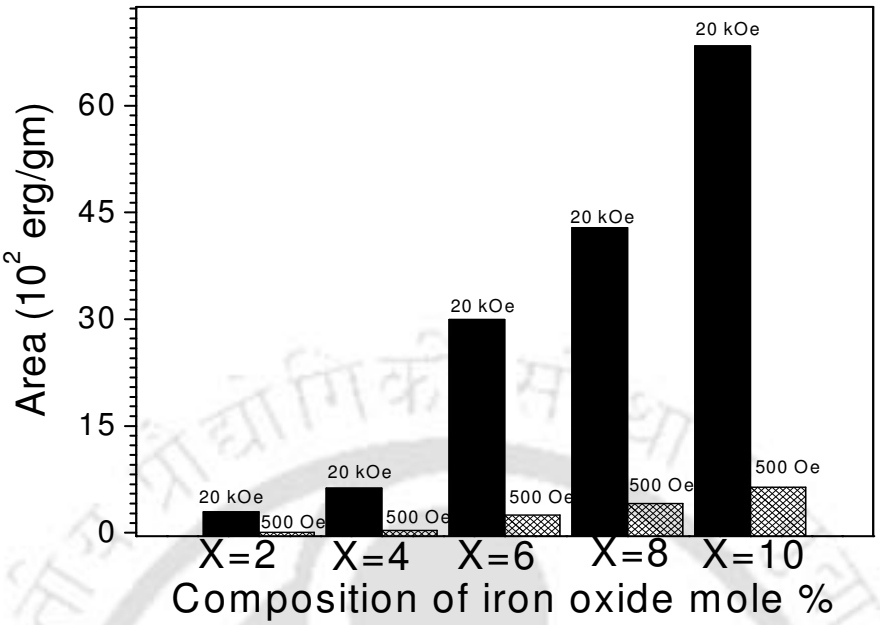

Fig. 3.3.4.4: Variation of hysteresis loop area as a function of iron oxide concentration, for applied fields of 20 kOe and 500 Oe.

The calculated values of hysteresis loop area for an applied field of 20 kOe and 500 Oe, (reported in Table 3.3.4) are plotted in Fig. 3.3.4.4. For an applied magnetic field of 500 Oe, magnetic saturation is not reached; the magnetic loss/cycle for sample with 10 mole % iron oxide is the highest. For an applied of 20 kOe, the saturation magnetization is reached for all samples and the loop area increase with iron oxide concentration. In this case, the saturation magnetization has the predominant effect.

Fig. 3.3.4.5 shows the initial magnetization curves for all samples measured at room temperature. The magnetization curves of the x = 2 and 4 samples are not saturated up to an applied magnetic field of 20 kOe as seen from the in-set of Fig. 3.3.4.5. It can be inferred from the nature of the curves that the samples with x = 2 and 4 mole % Fe_2O_3 exhibit a combination of paramagnetic and ferrimagnetic behaviour. Such behaviour has

also been reported in annealed CaO-P_2O_5-Fe_2O_3 glasses [171]. A comparison with the EPR spectra of these samples (Fig. 3.3.3.1) would clarify that both these techniques yield results that support and complement each other. The magnetization curves of samples with x = 6, 8, and 10 are saturated at a magnetic field ± 20 kOe. These compositions exhibit only ferrimagnetic behaviour. EPR spectra of these compositions show only one absorption at g ≈ 2.0, which indicates enhanced magnetic superexchange interaction between iron ions.

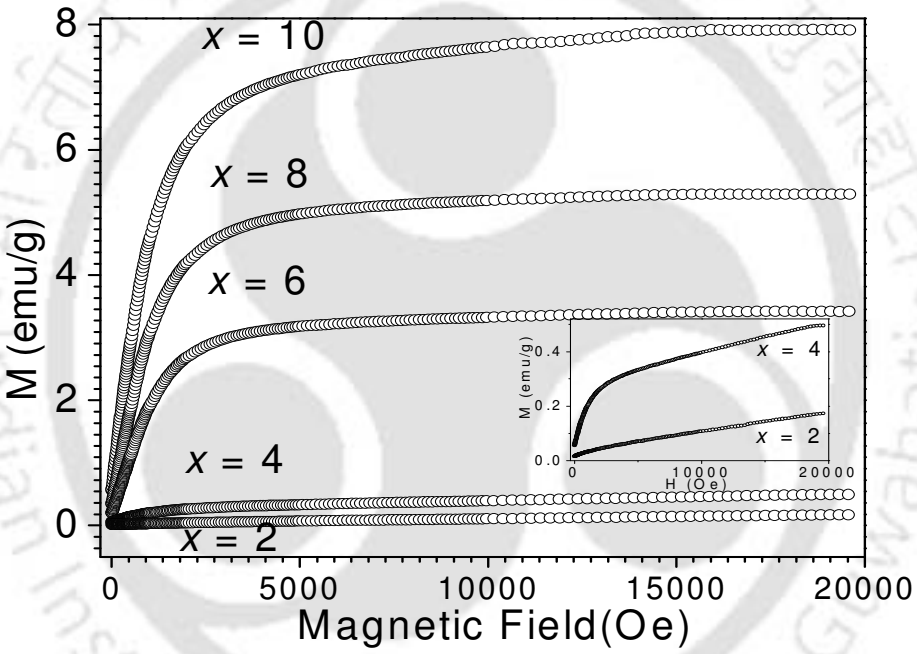

Fig. 3.3.4.5: Room temperature initial magnetization curves of the glass-ceramic samples. In-set shows M-H plots for the samples with x = 2 and 4 mole % Fe_2O_3.

Fig. 3.3.4.6 shows magnetization as a function of temperature (M-T) curves of all the glass-ceramics samples under a constant applied magnetic field of 1 kOe. During heating, a steady decrease in magnetization is observed. The ferrimagnetic behavior of the investigated samples is obvious from the nature of the M-T curves.

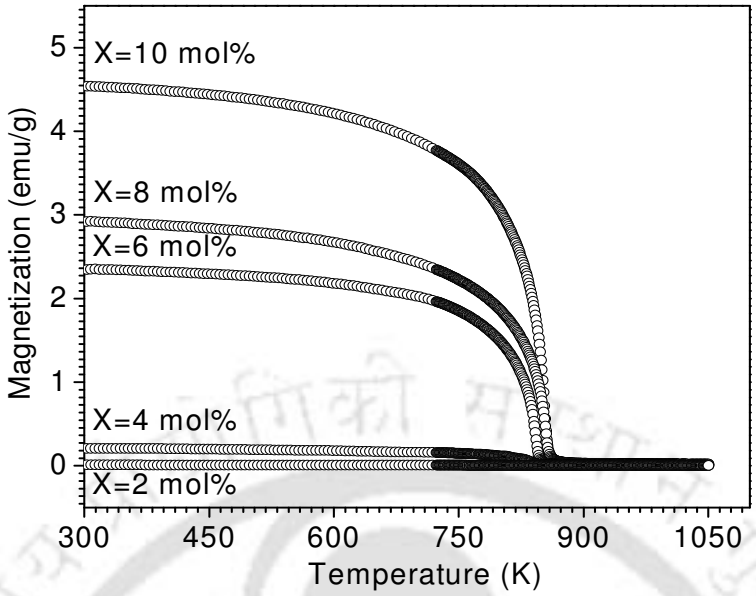

Fig. 3.3.4.6: Variation of magnetization as a function of temperature of 41CaO(52-*x*) $SiO_2$4P_2O_5*x*$Fe_2O_3$3Na_2O glass-ceramics samples.

Magnetic susceptibility (χ) of CaO-Na_2O-Fe_2O_3-B_2O_3 [196], CaO-P_2O_5-Fe_2O_3 [171], CaO-P_2O_5-SiO_2-Fe_2O_3 [134] and basalt [165, 197] glass-ceramics has been used to understand the magnetic interactions in these glass-ceramics. The variation of inverse magnetic susceptibility (χ^{-1}) with temperature over the range of 600 to 1050 K is shown in Fig. 3.3.4.7. The χ^{-1} - T plots which are nearly linear above 950 K show a downward drop at low temperatures. The deviation from linearity and the systematic downward drop of χ^{-1} - T curves indicate the onset of short-range order just above the ferrimagnetic Neel temperature (T_N). The heat treatment given to the glass samples modifies the internal network structure of the specimen and induces increased crystallization of magnetite in samples with higher *x* due to an increase in Fe^{3+} ions. Comparison with the literature [198] reveals that the main contribution to magnetization in these glass-ceramics comes from iron ions in magnetite (Fe_3O_4).

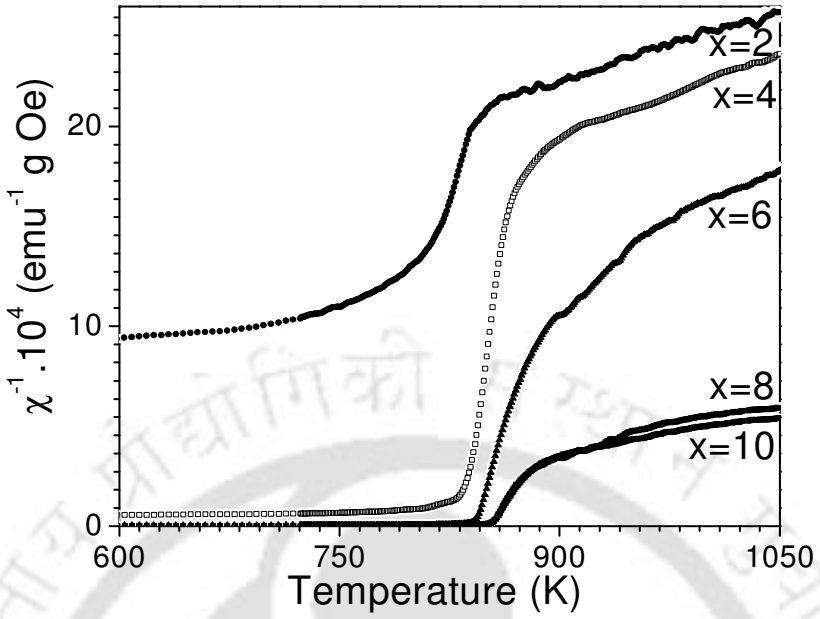

Fig. 3.3.4.7: Plots of temperature dependent inverse magnetic susceptibility of $41CaO(52\text{-}x)SiO_2 4P_2O_5 x Fe_2O_3 3Na_2O$ (x = 2, 4, 6, 8 and 10 mole % iron oxide) glass-ceramic samples.

The Neel temperature (T_N) of the glass-ceramic samples increases from 830 to 853 K as x is varied from 2 to 10 mole %. The Neel temperature increase with increase in Fe_2O_3 concentration may be correlated with the corresponding increase in the intensity of the g ≈ 2.0 resonance line [Fig. 3.3.3.2]. A closer look at Fig. 3.4.4.7 would show a departure in the manner in which inverse susceptibility decreases as temperature is lowered in the case of the x = 2 and x = 4 samples *vis-a-vis* the x ≥ 6 samples. χ^{-1} should tend to zero at $T = T_N$ if the sample is entirely ferrimagnetic. Any departure from this behaviour as observed in the case of samples with x = 2 and 4 shows the coexistence of a paramagnetic phase along with the ferrimagnetic phase in these samples.

3.3.5. *In vitro* bioactivity test of glass-ceramics samples

Glass-ceramics samples $41CaO(52\text{-}x)SiO_2 4P_2O_5 xFe_2O_3 3Na_2O$ immersed in SBF were taken out after 1, 3, 7, 10, 20 and 30 days, lightly washed with acetone. Surface structural changes of the glass-ceramics samples treated in SBF were analyzed by glancing incidence X-ray powder diffraction (GI-XRD), Fourier transform infra-red reflection spectroscopy (FT-IR) and scanning electron microscopy (SEM). The surface chemical analysis was carried out by energy dispersive X-ray spectroscopy (EDS) analysis.

3.3.5.1. GI-XRD studies of the glass-ceramics samples soaked in SBF

Fig. 3.3.5.1(a) shows the GI-XRD patterns obtained from the surfaces of the glass-ceramics (x = 2, 4, 6, 8 and 10 mole % Fe_2O_3) after soaking in SBF for 30 days.

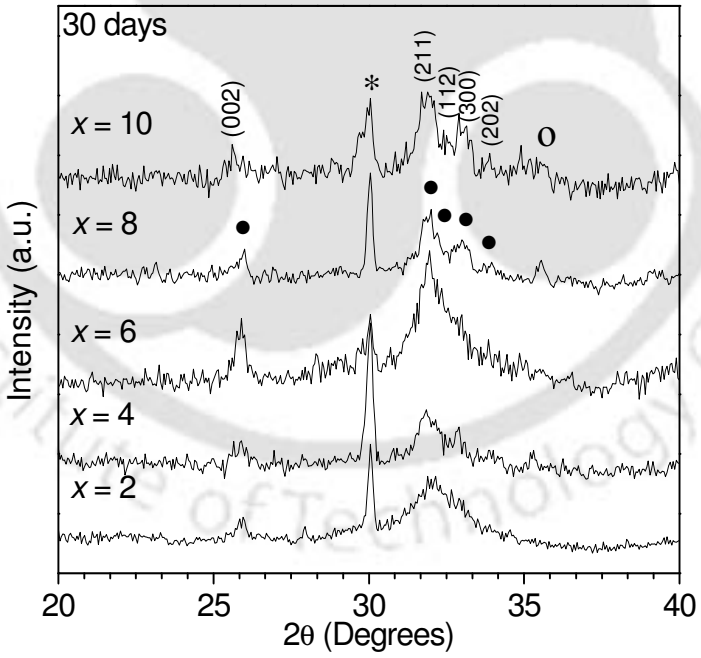

Fig.3.3.5.1(a): GI-XRD patterns of glass-ceramics with x = 2, 4, 6, 8 and 10 mole % soaked in SBF for 30 days.

The HA peaks appearing between 2θ values of 30° to 34° sharpen in samples with higher x. Since the broad peaks signify the presence of small sized crystallites, one can infer that on immersion in SBF for 30 days, the HA formation gradually improves from small sized crystalline aggregates to a well-crystallized HA phase as the amount of iron oxide is increased in the system. Formation of the hydroxyapatite layer over the glass-ceramics surface shows that the glass-ceramics samples are bioactive.

Fig. 3.3.5.1(b) shows the GI-XRD patterns from the surfaces of the sample with x = 8 mole % iron oxide before and after soaking in SBF for various time periods (*i.e.*, 0, 1, 3, 7, 10, 20 and 30 days). The characteristic apatite peaks are indicated by closed circles in the figure. It is obvious from the figure that broad crystalline peaks develop in samples treated with SBF for 3 days and more.

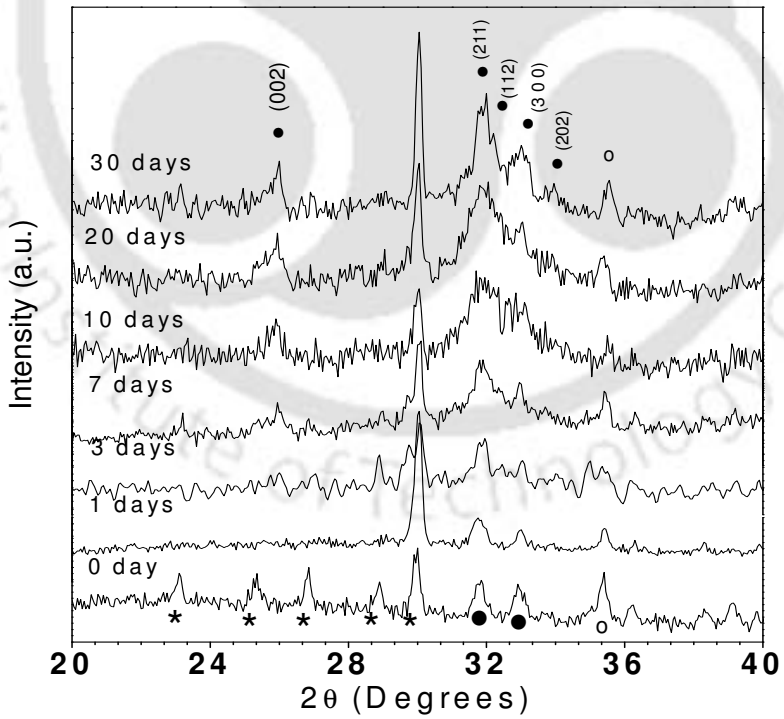

Fig.3.3.5.1(b): GI-XRD patterns of sample with x = 8 mole % soaked in SBF.

Initially, two peaks at 2θ values of ~26° and ~32° develop after 3 days of soaking in SBF. The two peaks could be assigned to (002) and (211) reflections of hydroxyapatite (HA) crystallites (JCPDS file no: 74-0565). Intensities of the (002) and (211) reflections rise monotonically with an increase in the accumulation of Ca^{2+} and PO_4^{3-} ions on the surface of the glass-ceramics immersed in SBF. The wide diffraction peak spread over a 2θ range of 30° to 34°, could be assigned to three closely placed reflections from (112), (300) and (202) planes for the well-crystallized HA. The increase in the intensities and decrease in the width of the apatite peaks of the samples immersed for longer periods in SBF clearly shows the evolution of the apatite layer on the surface of the glass-ceramic samples in physiological conditions. Hench [3] has described the bonding mechanism as a sequence of reactions between the glass / glass-ceramics and the surrounding fluid. A silica-rich layer is formed initially, followed by the formation of a calcium-phosphate-rich layer. It has been shown that most of the bioactive glasses [58, 181-182] and glass-ceramics [4, 42, 183] form a layer of a HCA layer similar to the apatite in the bone on their surface in the body, and bond to the living bone through this apatite layer. Formation of this apatite-like layer on the surface of materials immersed in SBF is now accepted as a confirmation of the bioactivity of the material [44-45, 58, 60, 66].

3.3.5.2. FT-IR studies of the glass-ceramics samples soaked in SBF

Fig. 3.3.5.2(a) shows the FT-IR reflection spectra of the bioglass-ceramics samples (x = 2, 4, 6, 8 and 10 mole %) after the immersion in SBF for 30 days. Spectral bands of HA assigned to PO_4^{3-} groups (ν_3–1024 cm^{-1}, ν_1–970 cm^{-1} and ν_2–473 cm^{-1}), CO_3^{2-} functional groups (ν_2–863 cm^{-1}, ν_3–1399 $cm^{-1}$and ν_3–1560 cm^{-1}) and OH^- groups (631 cm^{-1}) appear

in the spectra. These bands sharpen and their relative intensities increase with increase in iron oxide concentration.

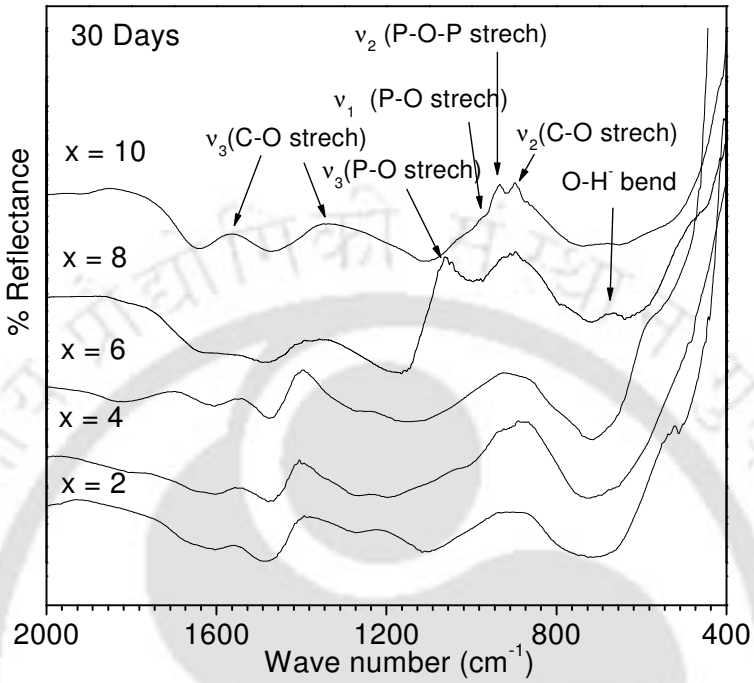

Fig. 3.3.5.2 (a): FT-IR reflection spectra of surfaces of various glass-ceramics (x = 2, 4, 6, 8 and 10 mole %) soaked in SBF for 30 days.

Fig. 3.3.5.2(b) shows the FT-IR spectra of the sample with x = 8 mole % before and after the immersion in SBF for 0, 1, 3, 7, 10, 20 and 30 days. The spectrum before the immersion reveals bands at 1075, 1038, 957, 895, 603 and 563 cm^{-1}. The peaks at 1075, 1038, 957, 895, 603 and 563 cm^{-1}correspond to v_3 Si-O-Si stretch, v_3 P-O stretch, v_1 P-O strech, Si-O stretch, v_4 P-O bend and v_4 Si-O-Si bend, respectively [188-190]. After one day of immersion, new bands start developing at 479, 863, 901, 1399 and 1560 cm^{-1}. The peaks at 479 cm^{-1} and 901 cm^{-1} correspond to v_2 P-O bend and v_1 P-O-P stretching frequency, respectively. The band located at 863 cm^{-1} and the large bands at 1399 and

1560 cm^{-1} can be assigned to C-O vibration mode in CO_3^{2-}. These bands signify the incorporation of carbonate anions from the SBF in the apatite crystal lattice. After 7 days of immersion, the appearance of bands at 970 and 1024 cm^{-1} can be seen, which are related to calcium phosphate (hydroxyapatite) surface layer. The peak at 970 cm^{-1} reflects the v_1 P-O symmetric stretching mode. This band indicates the obviation of phosphate ions from the ideal tetrahedral structure. This is a Raman active only mode when v_1 P-O symmetric stretch is in the free ion state. This Raman active mode can be seen in the infrared spectra because of the lowering of the symmetry in the crystalline state [191]. The peak at 1024 cm^{-1} is associated with the v_3 P-O antisymmetric stretching mode. With further increase in immersion time, the intensity of the bands due to CO_3^{2-} increases. Carbonate ions occupy two different sites in carbonated apatite: peaks in the region of 1650 to 1300 cm^{-1} are due to v_3 vibrational mode whereas the peak at 863 cm^{-1} is due to the v_2 vibrational mode [190] of carbonate ion.

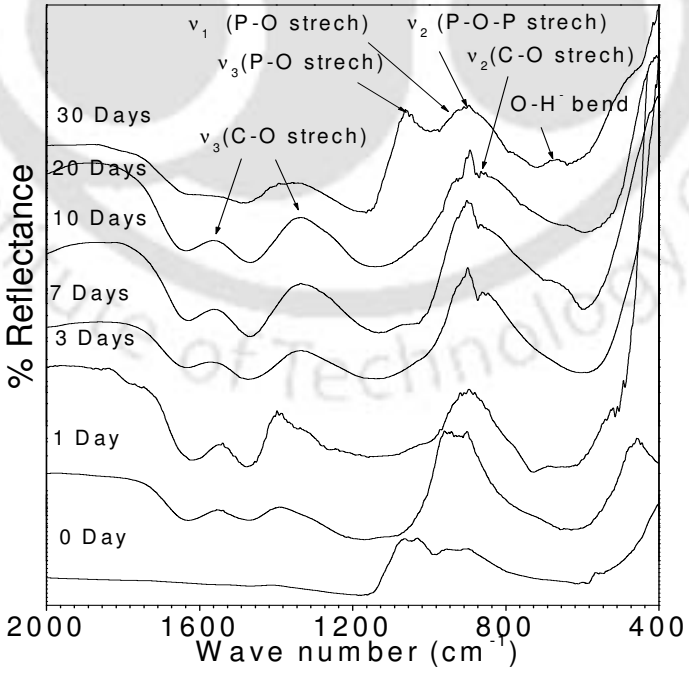

Fig. 3.3.5.2 (b): FT-IR spectra of glass-ceramic sample with x = 8 mole% soaked in SBF.

The v_3 band splits into two peaks centered at 1399 and 1560 cm^{-1}, respectively, with the distribution of the carbonate v_3 sites depending on the maturation and formation of apatite crystals. Occupancy of the v_2 sites is considered to occur competitively between the OH^{-1} and carbonate groups at the interface of growing crystal, whereas occupancy of the v_3 sites depends on competition between the phosphate and carbonate ions [190]. Presence of v_2 and v_3 vibrational modes of carbonate is the signature of the development of HCA layer on the surface of the sample.

3.3.5.3. SEM-EDS studies of the glass-ceramics samples soaked in SBF

Fig. 3.3.5.3(a) shows the SEM micrographs of the bioglass-ceramics sample x = 8 mole% after the immersion in SBF for 1, 3, 7, 10, 20 and 30 days. The micrographs (magnified 1000×) show the formation of surface layer on the surface of the bioglass-ceramics which is assumed to be due to formation of apatite. After 30 days, the whole surface of the specimen was covered with spherical Ca-P particles apatite layer. Results from EDS analysis revealed the gradual development of HCA on the surfaces of glass-ceramics samples after immersion for various times in SBF. The spherical particles were constituted of Ca and P and the Ca/P molar ratio (calculated by EDS peak) was ~ 1.67, corresponding to the value of hydroxyapatite. Microanalysis of the precipitates revealed the presence of small quantities of Na and Cl [*cf.* Fig. 3.3.5.3(b)]. This finding is in agreement with reports that the growth of hydroxyapatite in SBF solutions results in the incorporation of sodium, magnesium and chlorine [192]. It may thus be concluded that the solid precipitated on hydroxyapatite seed crystals in SBF solutions consists of carbonate and sodium, magnesium, chlorine substituted hydroxyapatite [193].

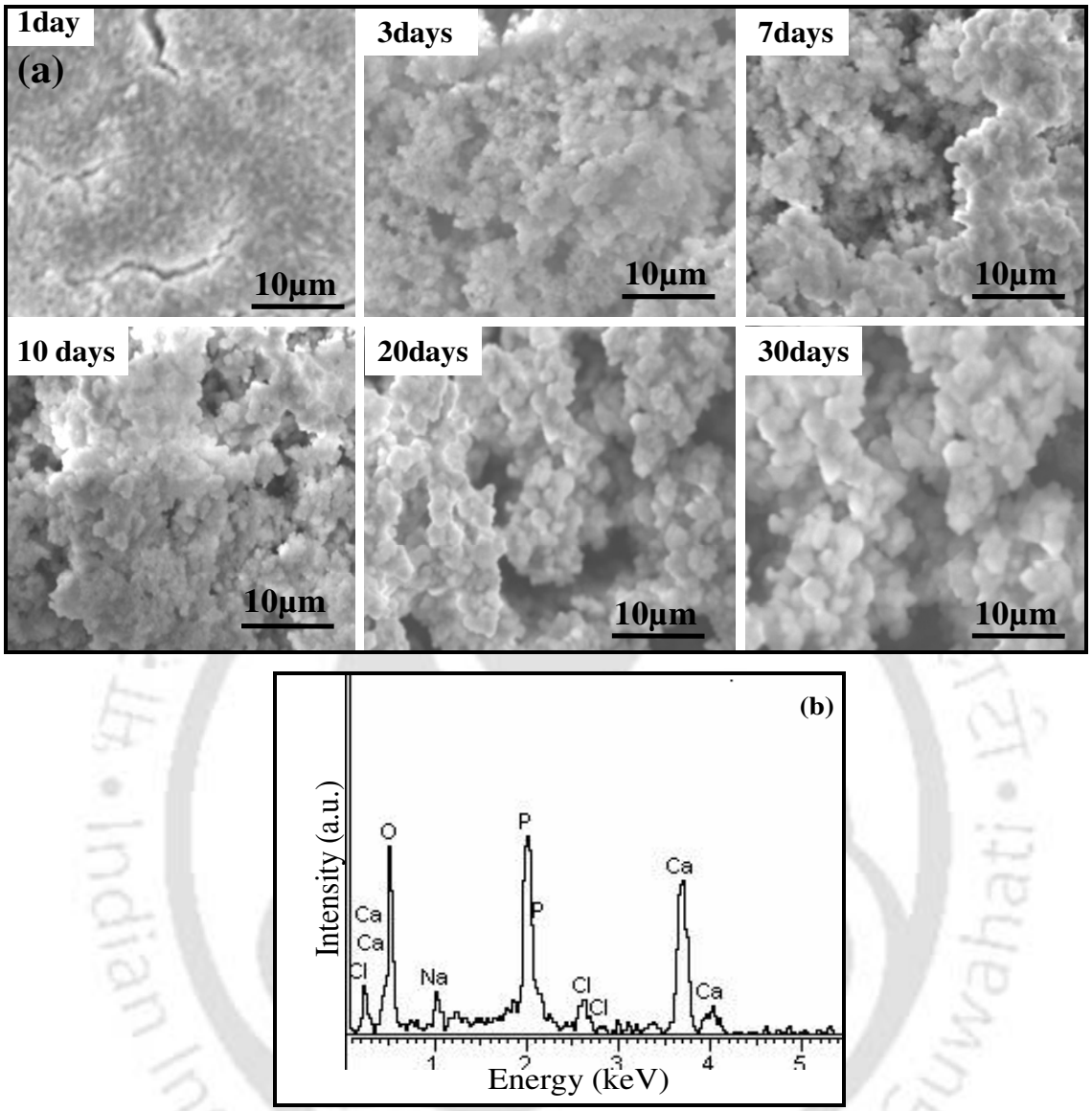

Fig. 3.3.5.3 : (a) SEM images of the surfaces of x = 8 mole % soaked in SBF for various days, and (b) EDS spectra of x = 8 mole % soaked in SBF for 30 days.

3.4. Summary

The salient features of the studies on $41CaO.(52\text{-}x)SiO_2.4P_2O_5.xFe_2O_3.3Na_2O$ glasses are

1. Good quality glasses could be obtained in $41CaO.(52\text{-}x)SiO_2.4P_2O_5.xFe_2O_3.3Na_2O$ system with x up to 10 mole %.

2. Hydroxyapatite, wollastanite and magnetite crystallized in all glass compositions when heated to 1050 °C.

3. Composition dependence of T_g showed a decrease in the depolarization of the glass skeleton with increasing iron oxide content.

4. Addition of iron oxide increased the density and VHN of the glasses.

5. In compositions with low x, the iron sites are populated randomly in the glass, whereas in glasses $x > 6$ mole%, the site population deviates from randomness and results in the formation of clusters. These result in superexchange type magnetic interactions between the iron ions in these glasses which are predominantly anti-ferromagnetically coupled.

6. While x_1 (mole % $Fe_2^{3+}O_3$) and x_2 (mole % $Fe_2^{2+}O_3$) values showed an increasing trend up to 6 mole % Fe_2O_3, x_1 decreases in glasses with x > 6 mole % Fe_2O_3. All glasses were paramagnetic at room temperature.

7. Bioactivity of this series of glasses increased as the iron oxide content is increased.

8. GI-XRD and FT-IR studies on SBF surfaces revealed the evolution of the HCA layer on the surface of the glass treated with SBF. EDS analysis showed that the Ca/P ratio of samples immersed in SBF for 30 days reach the value of 1.67 (value in HA).

The salient features of the studies on glass-ceramics derived from the parent glass compositons $41CaO.(52\text{-}x)SiO_2.4P_2O_5.xFe_2O_3.3Na_2O$ are

1. Hydroxyapatite and wollastonite are the major biocompatible crystalline phases developed in all the glass-ceramic samples. The percentage of hydroxyapatite increased in samples with higher iron oxide concentration. Nanocrystalline magnetite was present as the third crystalline phase in all the glass-ceramic samples containing iron oxide.

2. VHN increased with increase in iron oxide content.

3. An increase in ferrimagnetically coupled superexchange type interactions with increase in iron oxide content has been inferred from EPR studies on the glass-ceramic samples. Samples with x = 2 and 4 mole % Fe_2O_3 exhibit a combination of paramagnetic and ferrimagnetic behaviour.

4. Samples exhibited narrow hysteresis loop and low coercivity. The area under the hysteresis loop increased with increasing iron oxide content. This showed that these bio-glass ceramics could be useful in the localized hyperthermia treatment of cancer.

5. Bioactivity of the glass-ceramics samples increased with increase in iron oxide content. Thus, compositions with higher iron oxide content contain higher amounts of bone mineral phases as well as the magnetic phase in this series of glass-ceramics.

6. GI-XRD and FT-IR studies on SBF treated surfaces reveal the evolution of the HCA layer on the surface of the glass-ceramic samples treated with SBF. EDS analysis showed that the Ca/P ratio of samples immersed in SBF for 30 days reach the value of 1.67 (value in HA).

7. These studies showed that these ferrimagnetic bioglass-ceramics can be used in hyperthermia applications.

Chapter 4

Investigations on MgO-CaO-SiO_2-P_2O_5-CaF_2-Fe_2O_3 glass and glass-ceramics

A systematic study of MgO-CaO-SiO_2-P_2O_5-CaF_2 glasses with varying iron oxide content and the glass-ceramics derived from them is presented in this chapter. EPR absorption spectroscopy, microhardness, density, differential scanning calorimetry, magnetic susceptibility and *in vitro* bioactivity studies have been performed on the parent glass compositions. Glass-ceramics have been derived from these glasses by appropriate heat treatment. The evolution of structural and magnetic properties in the glass-ceramics along with EPR absorption, microhardness and *in vitro* bioactivity studies carried out on the glass-ceramic samples are also presented in this chapter.

4.1. Preparation of bioactive glasses and glass-ceramics

Various glass samples of $4.5MgO(45\text{-}x)CaO34SiO_2 16P_2O_5 0.5CaF_2 xFe_2O_3$ ($5 \leq x \leq 20$ wt. %) were prepared by melt quenching technique. The MgO based glasses (without Fe_2O_3) have high mechanical strength [30, 49]. Since the glass-ceramics are expected to

have better mechanical strength than the base glasses, this system could yield high strength magnetic bioglass-ceramics suitable for applications involving implants with better load bearing capability. Appropriately weighed quantities of high purity SiO_2 (99.9 % purity), MgO (99.9 % purity), CaF_2 (99.9 % purity), Fe_2O_3 (99.9 % purity), $CaCO_3$ (99.9 % purity) and $NH_4(H_2PO_4)$ (99.9 % purity) were thoroughly mixed in a pestle and mortar. The well-mixed oxide mixture was then transferred to a platinum crucible and melt at about 1550 °C in an electric furnace. The melts were then poured on to a cupper plate and pressed into a plate of 2-3 mm thickness at room temperature to form glass samples. The as-quenched glasses were annealed at 400 °C (well below their glass transition temperature) for 10 hours in air to remove residual stresses. These heat-treated samples were used for all measurements. Identical preparation conditions such as furnace temperature and quenching procedure were followed while preparing the entire series of glasses. The glass plates obtained by the method described above were placed on alumina plates and heat-treated at 1050°C for 3h and slowly cooled to room temperature to obtain glass-ceramic samples.

4.2. Characterization of bioactive glasses

Systematic characterization of the glass samples were first carried out, the details of which are given below:

4.2.1. XRD studies

All the glass samples prepared were checked for amorphous nature by obtaining X-ray powder diffraction (XRD) patterns. A typical XRD pattern for a MgO-CaO-SiO_2-P_2O_5-

CaF_2-Fe_2O_3 glass is shown in Fig. 4.2.1. The XRD pattern of the as quenched glass samples showed no sharp peaks declaring the amorphous nature of the samples. As explained in the previous chapter, the glassy nature of the samples was confirmed from the observation of the glass transition temperature (T_g).

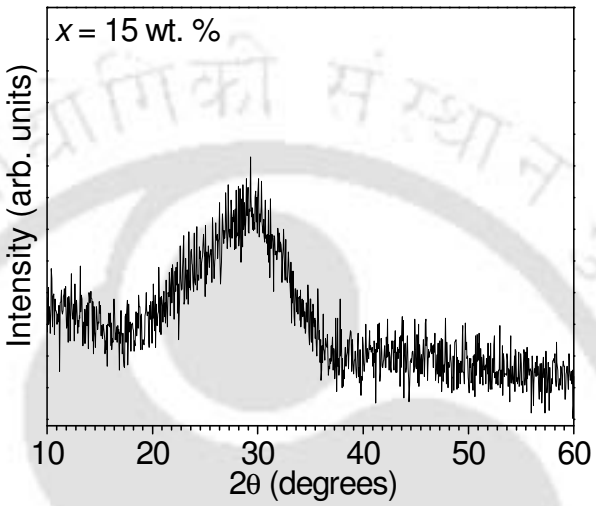

Fig. 4.2.1: X-ray diffraction pattern of a typical MgO-CaO-SiO_2-P_2O_5-CaF_2-Fe_2O_3 glass.

4.2.2. DSC studies

The experimental observation of the glass transition temperature (T_g) is necessary to classify the sample as a glass. So, DSC curves were recorded for 4.5MgO(45-*x*)CaO $34SiO_2 16P_2O_5 0.5CaF_2 xFe_2O_3$ glasses, following the procedure explained in the chapter 2. A high temperature DSC (NETZSCH STA 409 PC/PG) was used for these samples since the T_g of the samples were beyond the range of PerkinElmer DSC 7. The DSC curves showed an endothermic base line shift corresponding to the glass transition temperature. It confirmed that the prepared samples are glasses. Fig. 4.2.2 is the typical DSC curve obtained for 4.5MgO(45-*x*)CaO$34SiO_2 16P_2O_5 0.5CaF_2 xFe_2O_3$ glasses with *x* = 10 wt. % iron oxide under a constant heating rate of 20 °C/min. Single glass transition

temperature (T_g) and two crystallization temperatures (T_c) were observed. The glass transition temperature was marked by a distinct endothermic baseline shift within the temperature at 670 °C and crystallization temperature range was between 780 °C and 1035 °C when heated under a constant rate of 20 °C/min. It can be seen from the DSC curve that hydroxyapatite crystals precipitated at 780 °C, and wollastonite crystals at 1035 °C.

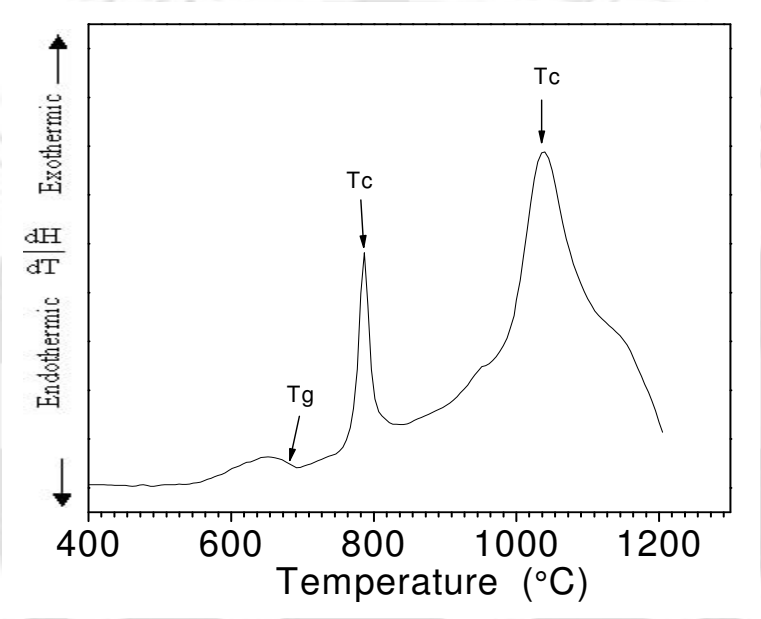

Fig. 4.2.2: Typical DSC curve obtained for 4.5MgO(45-*x*)CaO34$SiO_2$16$P_2O_5$0.5CaF_2 *x*Fe_2O_3 glasses (*x* = 10 wt. %) with constant heating rate of 20 °C/min.

4.2.3. Density and molar volume

Density (ρ) measurements on MgO-CaO-SiO_2-P_2O_5-CaF_2-Fe_2O_3 glasses were performed as per the procedure outlined in chapter 2. From the density data, the molar volume of the glasses was calculated (Table 4.2.3) using equations (2.4) and (2.5).

Table 4.2.3: Density, molar volume and microhardness of 4.5MgO(45-*x*) CaO34SiO_2 16$P_2O_5$0.5CaF_2*x*Fe_2O_3 glasses.

***x* wt. %**	**Density (gm/cm^3)**	**Mol.vol. (cm^3/mol)**	**VHN (kg mm^{-2})**
5	2.76	25.68	655
10	2.79	25.41	709
15	2.82	25.19	772
20	2.85	25.05	843

Fig. 4.2.3 shows the composition dependence of density and molar volume of 4.5MgO(45-*x*)CaO34$SiO_2$16$P_2O_5$0.5CaF_2*x*Fe_2O_3 glasses. The density of the glass increases and molar volume decreases as iron oxide wt. % content is increased. When iron oxide wt. % is increased, Fe_2O_3 progressively replaces CaO. Since the molecular weight of Fe_2O_3 (159.697) is higher than the molecular weight of CaO (56.079), one would expect the overall density of the glass to increase. As the molar volume decreases with increasing Fe_2O_3 wt. % content, the glassy network shrinks in size. On the other hand, density of the glasses increases from 2.76 to 2.85 g/cm^3 (Table 4.2.3) with increasing iron oxide content as a result of a strengthening of cross-linking within glass network as the volumetric portion of the four-coordinated Fe ion increases at the cost of the six-coordinated Fe [150]. Composition dependence of the molar volume of the glasses is also shown in Fig. 4.2.3. A decrease in the molar volume can be observed with an increase in iron oxide concentration. The decrease in the molar volume of the samples can be attributed to the increase in the probability of formation of FeO_4 group in glass, as

result of the decrease in the number of non-bridging oxygens [150]. This may cause a decrease in the volume of the glass network structure. The decrease in molar volume in glasses may be attributed to the formation of a closed packed structure due to the change of the coordination of iron ions to four-fold coordination.

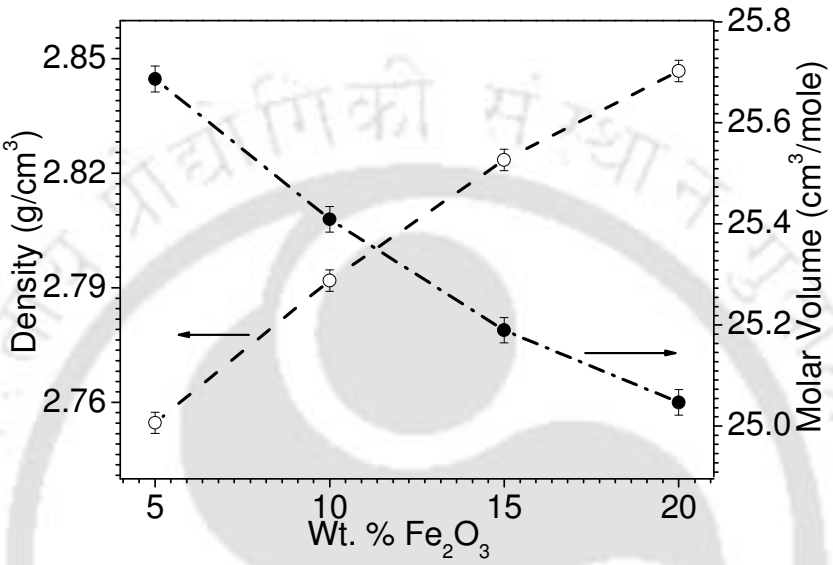

Fig. 4.2.3: Composition dependence of density and molar volume of MgO glasses.

4.2.4. Microhardness

Microhardness of glasses has been measured following the procedure already explained in the second chapter. All glass samples were uniformly subjected a load of 100 gm for the duration of 15 seconds. The measured microhardness values are tabulated in Table 4.2.3. Fig. 4.2.4 shows the variation of VHN with iron oxide wt. % in 4.5MgO(45-*x*) CaO $34SiO_2 16P_2O_5 0.5CaF_2 xFe_2O_3$ glasses. It shows that the VHN increases as the iron oxide content is increased. As the number of non-bridging oxygen in glass decreases, the bulk (B) and shear (G) elastic moduli of the glass increase. When the number of non-bridging oxygen in a glass decreases, the elastic moduli of the glass increases [145]. From

equation (2.9) it is obvious that an increase in the elastic moduli increases the microhardness, which explains the behaviour exhibited by the 4.5MgO(45-*x*)CaO34SiO_2 16$P_2O_5$0.5CaF_2*x*Fe_2O_3 glasses depicted in Fig. 4.2.4.

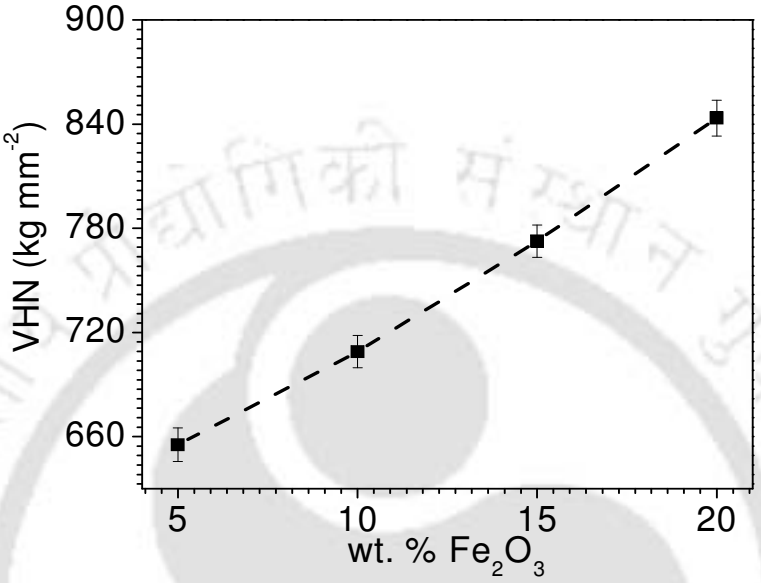

Fig. 4.2.4: Variation of VHN of 4.5MgO(45-*x*)CaO34$SiO_2$16$P_2O_5$0.5CaF_2*x*Fe_2O_3 glasses.

4.2.5. EPR studies

EPR absorption spectra of 4.5MgO(45-*x*)CaO 34SiO_2 16P_2O_5 0.5CaF_2 *x*Fe_2O_3 ($5 \leq x \leq 20$ wt. %) glass samples recorded at room temperature are shown in Fig. 4.2.5.1. The resonance absorptions observed at $g \approx 2.1$ and $g \approx 4.3$ are due to Fe^{3+} ions ($3d^5 {}^6S_{5/2}$) and there is a strong dependence of the structure of the absorption spectra on the Fe_2O_3 content in the sample. The EPR parameters of the first derivative resonance curve that were determined are the linewidth (ΔH) and the intensity of absorption line *J*. While *J* was estimated from peak to peak height (*I*) and the linewidth was calculated using the relation $J = I(\Delta H)^2$. Analysis of the $g \approx 2.1$ resonance line was performed by integrating the

relevant part of the first derivative EPR curve. The relative intensity and linewidths of the two absorptions lines vary with glass composition.

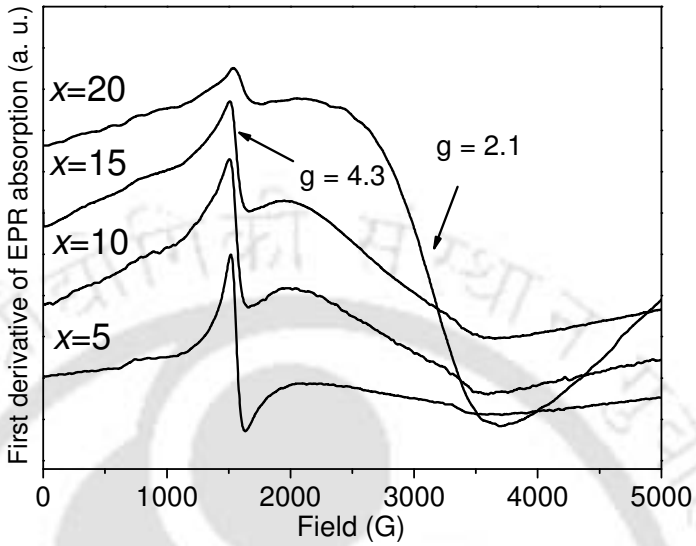

Fig. 4.2.5.1: EPR absorption spectra of 4.5MgO(45-*x*)CaO 34SiO_2 16P_2O_5 0.5CaF_2 *x*Fe_2O_3 glasses.

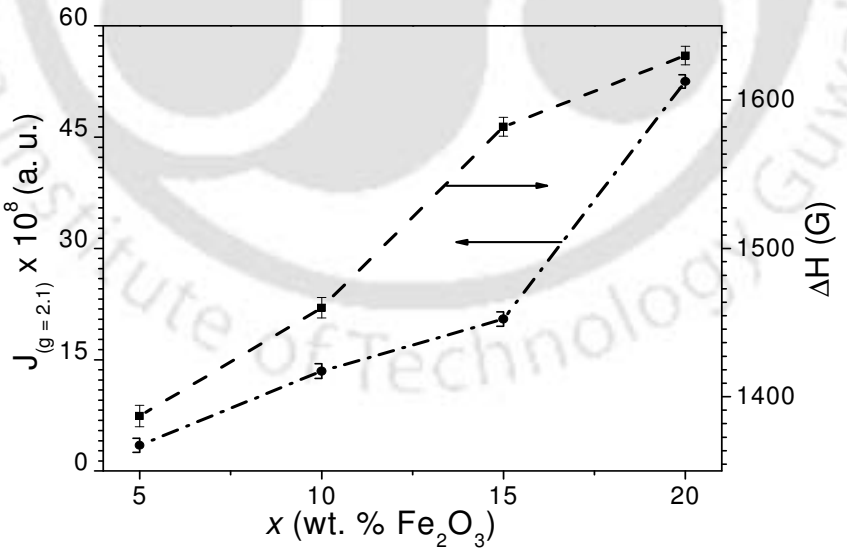

Fig. 4.2.5.2: The composition dependence of the line intensity and linewidth of g ≈ 2.1 resonance absorption line of 4.5MgO(45-*x*)CaO 34SiO_2 16P_2O_5 0.5CaF_2 *x*Fe_2O_3glasses.

The variations of the EPR parameters for the resonance lines centred at g ≈ 2.1and g ≈ 4.3 are plotted in Fig. 4.2.5.2 and Fig. 4.2.5.3, respectively. It can be seen from Fig. 4.2.5.1 that the peak to peak height (I) decreases with an increase in iron oxide concentration and the line width (ΔH) increases with increase in iron oxide concentration. The overall intensity of the absorption line $J_{g \approx 4.3}$ increases in glasses with x = 5 to 10 wt. % iron oxide and then decreases as depicted in Fig. 4.2.5.3. The overall intensity of the absorption line $J_{g \approx 2.1}$ shows an increasing trend as the iron oxide content is increased as depicted in Fig. 4.2.5.2.

The nonlinear behaviour depicted in Fig. 4.2.5.2 can be attributed to the process by which iron enters in the vitreous matrix *i.e.*, either as Fe^{3+} or Fe^{2+}. Fe^{2+} ions are not involved in the EPR absorption, but their interaction with Fe^{3+} ions influences the characteristics of the absorption lines. The absorption line centred at g ≈ 2.1 is due to the isolated Fe^{3+} in a slightly distorted structural unit in samples with a low Fe_2O_3 content and to the clustered formations of the iron ions for higher concentrations. Fe^{2+} ions are not involved in the EPR absorption but their interactions with Fe^{3+} influence the characteristics of the absorption lines. Thus, Fe^{2+} ionic species were also present in the glasses along with Fe^{3+} ions. The line width of the g ≈ 2.1 resonance absorption depends also on Fe_2O_3 concentration. The superexchange interaction between the nearest neighbours (which increases with iron oxide content due to their increased proximity), acts as narrowing mechanism of the absorption line. This narrowing process is countered by other broadening processes such as increase in network disordering and interaction between multivalent iron ions (*i.e.*, Fe^{2+} and Fe^{3+}). The final line width depends on the relative strengths of the two mechanisms influencing the line width. The increase in the

line width of the g ≈ 2.1 line with Fe_2O_3 concentrations shows the dominance of the broadening mechanisms which in turns indicates a larger increase in Fe^{2+} ion concentration as Fe_2O_3 concentration is increased in the glass.

The origin of the resonance line at g ≈ 4.3 can be attributed to isolated Fe^{3+} ions situated in distorted octahedral symmetry (rhombic or tetragonal) sites and subjected to strong crystal field effects. The decrease in line intensity of the g ≈ 4.3 absorption line with increasing Fe_2O_3 content signifies the destruction of the neighborhood configuration of the iron ions, which results in their magnetic isolation. From Fig. 4.2.5.1, we can observe that as Fe_2O_3 content is increased beyond 10 wt. %, the signal at g ≈ 4.3 begins to disappear and a broad signal centered at g ≈ 2.1 starts developing. The decrease in intensity of the signal centred at g ≈ 4.3 for glasses with x > 10 wt. % may be due to the formation of clusters of paramagnetic ions. The increase in intensity of the g ≈ 2.1 resonance line as a function of Fe_2O_3 concentration lends support to this conclusion.

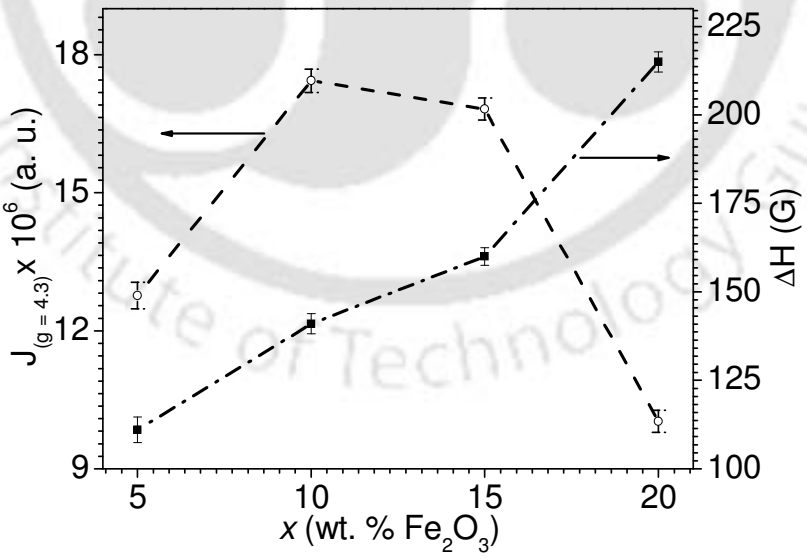

Fig. 4.2.5.3: Composition dependence of the line intensity and linewidth of g ≈ 4.3 resonance absorption line of 4.5MgO(45-x)CaO34$SiO_2$16$P_2O_5$0.5$CaF_2$$x$$Fe_2O_3$ glasses.

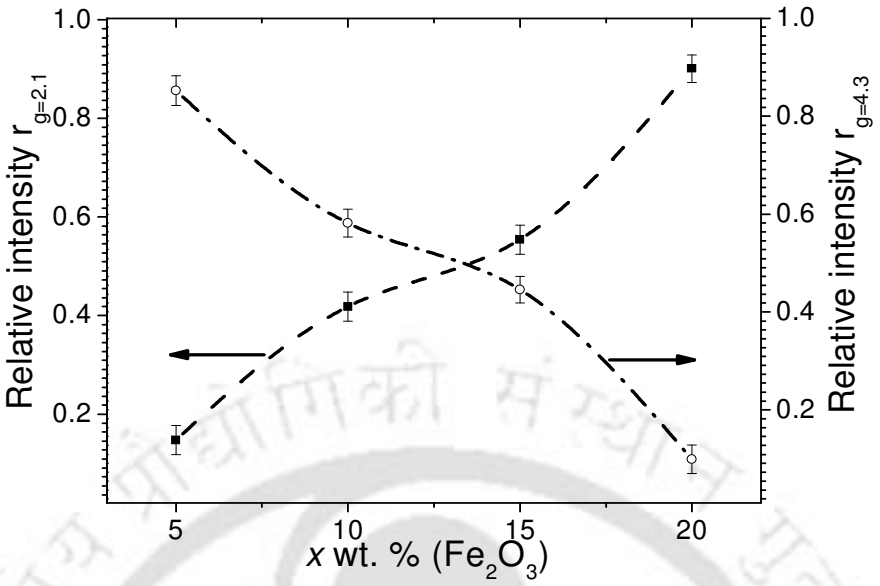

Fig. 4.2.5.4: Variation of relative intensities $r_{g \approx 4.3}$ and $r_{g \approx 2.1}$ as a function of Fe_2O_3 content in various glass compositions

Variation of relative intensities $r_{g\approx4.3}$ and $r_{g\approx2.1}$ as a function of Fe_2O_3 concentration in MgO glasses are plotted in Fig. 4.2.5.4. Variations in the relative intensities of the two lines, *viz.*, $r_{g \approx 4.3} = I_{g \approx 4.3}/(I_{g \approx 4.3} + I_{g \approx 2.1})$] and $r_{g \approx 2.1}$ [$= I_{g \approx 2.1}/(I_{g \approx 4.3} + I_{g \approx 2.1})$] as a function of Fe_2O_3 content for the glasses are plotted in Fig. 4.2.5.4, where $I_{g \approx 4.3}$ and $I_{g \approx 2.1}$ denote intensities at g ≈ 4.3 and g ≈ 2.1, respectively. The relative intensity $r_{g \approx 2.1}$ increases with increase in Fe_2O_3 content, while the relative intensity $r_{g \approx 4.3}$ decreases rapidly with increase in Fe_2O_3 content. It can also be seen from Fig. 4.2.5.3 that the linewidth of g ≈ 4.3 resonance line increases with Fe^{3+} ions concentration. Hence, it can be concluded that at lower concentrations, iron sites are populated randomly in the glass, while at higher iron concentrations (*i.e.*, in glasses with $x > 10$ wt %) the site population deviates from randomness and results in the formation of clusters. When the

site population deviates from randomness at higher iron (*i.e.*, for x > 10 wt %) concentrations, superexchange type interactions begin to dominate.

4.2.6. Magnetic susceptibility

Inverse of susceptibility (χ^{-1}) versus temperature plots for various 4.5MgO(45-x)CaO 34$SiO_2$16$P_2O_5$0.5$CaF_2$$x$$Fe_2O_3$ glass compositions are shown in Fig. 4.2.6.1. Temperature dependence of χ^{-1} of paramagnetic materials shows a Curie-Weiss type behavior expressed by equation (2.10). The straight lines in Fig. 4.2.6.1 represent the least squares fit to equation (2.10). The negative paramagnetic Curie temperature calculated for the glasses (*cf.* Fig. 4.2.6.2 and Table 4.2.6) indicates superexchange magnetic interactions between the iron ions in the glass which are predominantly anti-ferromagnetically coupled. In these glasses, iron is expected to be present in the form of Fe^{2+} and of Fe^{3+} ions.

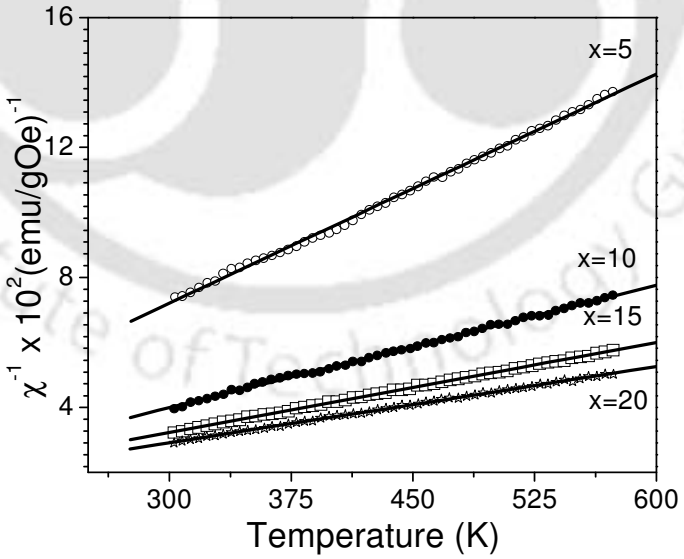

Fig. 4.2.6.1: Temperature dependence of the inverse magnetic susceptibility of MgO-CaO-SiO_2-P_2O_5-CaF_2-Fe_2O_3 glasses.

The superexchange interaction of the iron ions in oxide glasses has been mostly attributed to an antiferromagnetic coupling within Fe^{3+}-Fe^{2+}, Fe^{3+}-Fe^{3+} and Fe^{2+}-Fe^{2+} pairs [163, 199]. Earlier reports on the temperature dependence of the magnetic susceptibility of borate [157, 174], phosphate [164-166], silicate [171, 175, 199], tellurite [164] and bismuthate [161-162] oxide glasses have indicated an antiferromagnetic interaction. Due to the disordered structure, the magnetic order is confined to short range scales, which results in micromagnetic type behavior in the glasses [176]. Analysis of the present data shows that the iron ions in the MgO-CaO-SiO_2-P_2O_5-CaF_2 glass matrix behave magnetically similar to iron ions in Bi_2O_3-PbO [161], TeO_2-B_2O_3-PbO [163], B_3O_4-CaO [177] CaO-P_2O_5 [178] and CaO-P_2O_5-SiO_2-Na_2O [199] glasses. The absolute magnitude of θ_p values increases with increase in Fe_2O_3 content in the glasses (Fig. 4.2.6.2). The value of the exchange integral increases as the iron ions concentrations is increased in the glass, and as a result of this, the magnitude of θ_p increases.

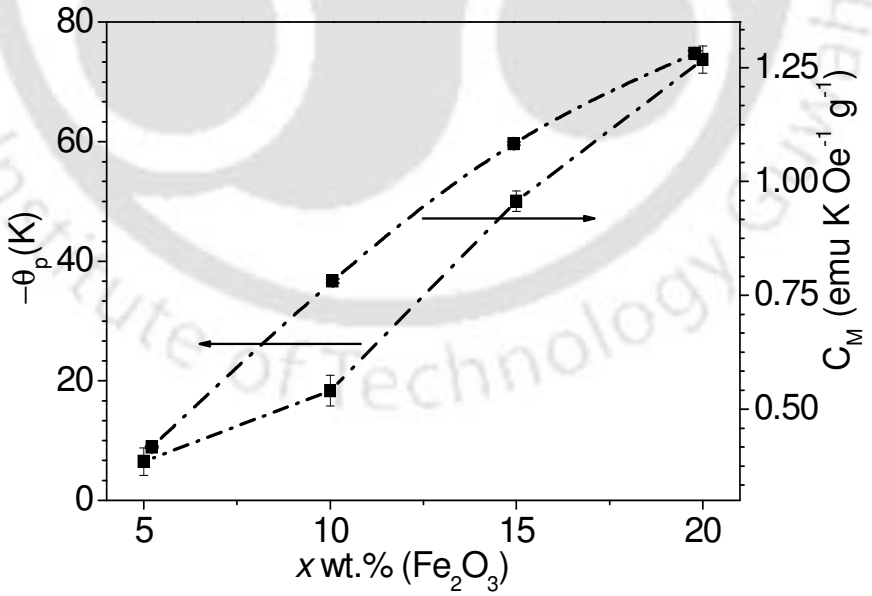

Fig. 4.2.6.2: Variation of paramagnetic Curie temperature and the Curie constant of $4.5MgO(45\text{-}x)CaO34SiO_2 16P_2O_5 0.5CaF_2 xFe_2O_3$ glasses with composition.

Table 4.2.6: Curie constant (C_M), paramagnetic Curie temperature (θ_p). experimental magnetic moment μ_{exp}, weight fractions of Fe^{3+} (x_1) and Fe^{2+} (x_2) ions, and relative concentration of Fe^{2+} ion in $4.5MgO(45-x)CaO34SiO_2 16P_2O_5 0.5CaF_2 xFe_2O_3$ glasses.

x (wt. %)	$C_M \pm 1\times10^{-4}$ (emuKOe^{-1}g^{-1})	μ_{exp} $\pm1\times10^{-2}$ (μ_B)	$x_1 \pm 1\times 10^{-2}$ (wt. % $Fe_2^{3+}O$)	$x_2 \pm 1\times 10^{-2}$ (wt. % $Fe_2^{2+}O_3$)	$x_2/(x_1+x_2)$ $\pm 1\times 10^{-2}$
5	0.4253	5.83	4.52	0.48	0.09
10	0.7971	5.64	7.06	2.94	0.29
15	1.0831	5.37	6.56	8.44	0.56
20	1.2811	5.06	2.89	17.11	0.86

Composition dependence of the Curie constant (C_M) is presented in the right hand side axis of Fig. 4.2.6.2. C_M values increase with iron oxide concentration. The composition dependence of the Curie constant (C_M) and effective magnetic moment (μ_{exp}) is listed in Table 4.2.6. It is evident from Table 4.2.6 that iron is present as both Fe^{3+} and Fe^{2+} ions in the glasses. The presence of iron in the form of Fe^{2+} and Fe^{3+} ions has been reported in many oxide glasses [165, 171, 179, 199] as discussed in chapter 3. Atomic magnetic moment values of free ions, *viz*., $\mu_{Fe^{2+}} = 4.90\mu_B$ and $\mu_{Fe^{3+}} = 5.92\mu_B$, have been used [180] to estimate the weight fraction of Fe^{2+} and Fe^{3+}ions in the glasses using the relations,

$$x.\mu^2_{exp} = x_1.\mu^2_{Fe^{3+}} + x_2.\mu^2_{Fe^{2+}} \quad (4.1)$$

and

$$x = x_1 + x_2 \quad (4.2)$$

where $\mu_{exp} = 2.827(C_M/2x)^{1/2}$ is the experimental magnetic moment, and x_1 and x_2 are weight fractions of iron ions in Fe^{3+} and Fe^{2+} valence states, respectively. μ_{exp} obtained from relations (4.1) and (4.2) using experimentally determined values of C_M, were found to be lower than μ_{Fe}^{3+} (*cf.* Table 4.2.6). Comparison of x_1 (wt. % $Fe_2^{3+}O_3$) and x_2 (wt. % $Fe_2^{2+}O_3$) for various glass compositions listed in Table 4.2.6 shows that iron ions exist in both $Fe^{3+}$and Fe^{2+} valence states in all the glass compositions. The weight fraction of Fe^{2+} ions x_2 increases with Fe_2O_3 concentration, and its values are higher than those of Fe^{3+} ions in glasses with $x \geq 10$ wt. %. This result is supported by the EPR spectra of the glasses, in which an increase in the intensity of the $g \approx 2.1$ absorption line can be observed with increasing x (Fig. 4.2.5.2). The estimated weight fraction of Fe^{3+} ions x_1 increases in glass compositions with $x \leq 10$ wt. % and then decreases in glasses with higher x. Compositional dependence of the estimate x_1 has a strong similarity to the compositional dependence exhibited by the intensity of the EPR line centred at $g \approx 4.3$ (Fig. 4.2.5.3). Moreover, μ_{exp} decreases from 5.83 (which is close to μ_{Fe}^{3+} value) for the glass with composition $x = 5$ wt. % to 5.06 (which is close to μ_{Fe}^{2+} value) for the glass with $x = 20$ wt. %. The ratio of the number of ions in Fe^{2+} state (x_2) to the total number of ions (x_1+x_2) in various glass compositions is listed in Table 4.2.6. It is evident that the relative domination of Fe^{3+} ions in glasses with lower concentrations of Fe_2O_3 decreases as x is increased, leading to the domination of Fe^{2+} ions at higher x values. The glass composition near $x \approx 12$ wt. % Fe_2O_3 is expected to contain an equal distribution of these two species of Fe ions. The magnetic data of the glasses can be understood on the basis of the relative concentration of the iron ions if one presumes the existence of Fe^{2+}-Fe^{2+}, Fe^{3+}-Fe^{3+} and Fe^{2+}-Fe^{3+} magnetic exchange pairs. Based on these two results, one can conclude that as x

is increased in this series of glasses, the dominating magnetic exchange pairs change from Fe^{3+}-Fe^{3+} to Fe^{2+}-Fe^{3+} and then ultimately to Fe^{2+}-Fe^{2+}.

4.2.7. *In vitro* bioactivity test of glass samples

In vitro bioactivity test was carried out by soaking the glass pieces in SBF, as detailed in chapter 2. Glass pieces immersed in SBF were taken out after 1, 3, 7, 10, 20 and 30 days, and lightly washed with acetone. Surface structural changes of the glass samples treated in SBF were analyzed by GI-XRD), FT-IR spectroscopy and SEM. The surface chemical analysis was carried out by energy dispersive X-ray spectroscopy (EDS) analysis. The details of these studies are presented below.

4.2.7.1. GI-XRD studies of the glass samples soaked in SBF

Fig. 4.2.7.1(a) shows the typical GI-XRD patterns obtained from the surfaces of glasses before and after soaking in SBF for various time periods (i.e. 0, 1, 3, 7, 10, 20 and 30 days). The GI-XRD patterns obtained for the glass sample with x = 15 wt. % Fe_2O_3 is shown in the figure as a typical example. GI-XRD pattern of all untreated sample (designated as 0d in Fig. 4.2.7.1(a)) is devoid of crystalline peaks, indicating the amorphous nature of the glassy samples. Crystalline peaks appear in the GI-XRD patterns of glass samples immersed in SBF for a day or more, indicating the formation of a crystalline layer on the surface of the glass. Initially, two well defined peaks at 2θ values of ~26° and ~32° develop after 3 days of soaking in SBF. The two peaks could be assigned to (002) and (211) reflections of hydroxyapatite (HA) crystallites (JCPDS file no: 74-0565). Apatite formation on the surface of the glasses in the SBF is governed by

chemical reaction of the surface of the matrix with the fluid. The wide diffraction peak at 2θ ranging from 30˚ to 34˚ corresponds to the overlap of (112), (300) and (202) reflection of the well-crystallized hydroxyapatite.

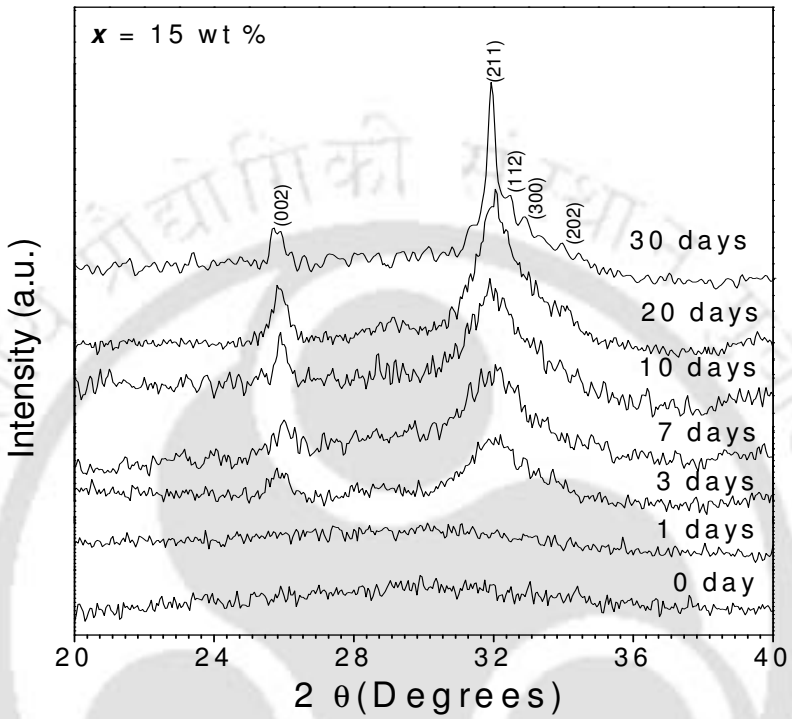

Fig. 4.2.7.1 (a): GI-XRD patterns of glass sample x = 15 wt. % soaked in SBF.

The GI-XRD patterns depicted in Fig. 4.2.7.1(a) show the preferential growth mechanism of the surface apatite layer. Formation of the hydroxyapatite layer over the glass surface shows that the glass samples are bioactive. Formation of this apatite-like layer on the surface of materials immersed in SBF is now accepted as a confirmation of the bioactivity of the material [44-45, 58, 60, 66, 181-182]. The gradual growth in the intensity of the individual reflection, appearance of other low intensity apatite reflections and the narrowing of the peak width clearly show the evolution of the crystalline HA surface layer as a function of immersion time in SBF. The intensity of two major

reflections, *viz*., (002) and (211), increase [cf. Fig.4.2.7.1 (b)] with an increase in the concentration of Ca^{2+} and PO_4^{3-} ions on the surface of the glass immersed in SBF for various days. It is obvious that the intensity of the reflections attain saturated values within 10 days of immersion in SBF. The average crystallite size (*d*) in a direction perpendicular to the crystallographic plane can be estimated using the Scherrer`s formula equation (2.1) [139].

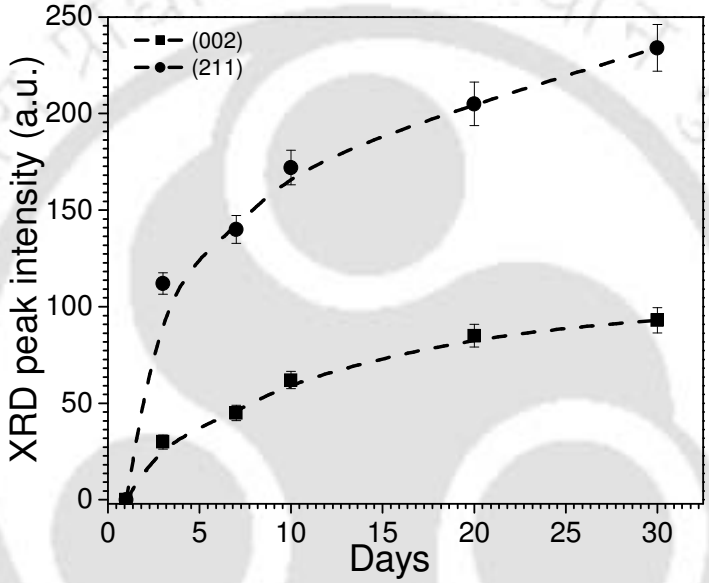

Fig. 4.2.7.1 (b): GI-XRD intensity of glass sample *x* = 15 wt. % corresponds to the (002) and (211) reflection peak for soaked in SBF for 1, 3, 7, 10, 20 and 30 days.

The average size of HA crystallized was calculated from the (002) reflection using equation (2.1). Fig. 4.2.7.1 (c) reveals an increase in the average particle size of the crystalline surface layer on the glass immersed in SBF for various days, which is consistent with earlier reports [184, 200]. The crystallite size increases from about 12.8 (± 0.42) nm to 22.4 (± 0.59) nm in samples immersed for 3 days to 30 days. The size of HA crystalline depends on the rate of crystalline growth on the surface of the glass in the

SBF in various days. The variation of the crystallite size with immersion time shows a sharp increase in crystallite size in samples treated in SBF for 10 days, followed by a slower increase in crystallite size in samples treated in SBF for longer periods.

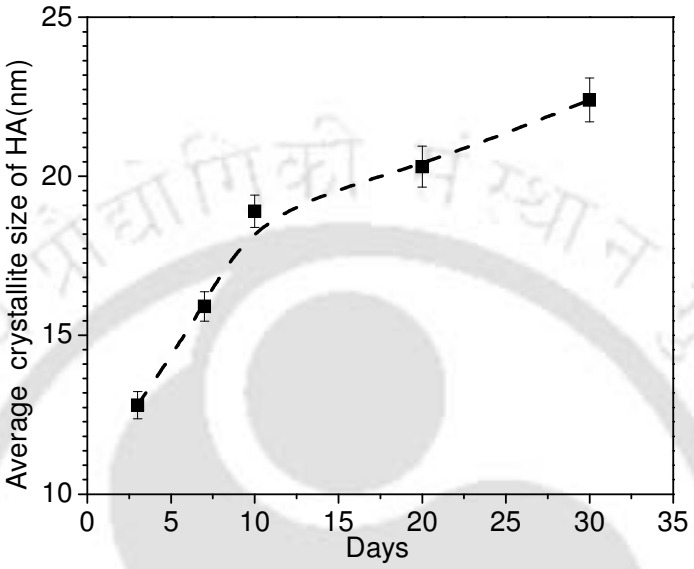

Fig. 4.2.7.1 (c): The averages size of HA crystalline (nm) corresponds to the (0 0 2) reflection peak for sample x = 15 wt. % soaked in SBF for 3, 7, 10, 20, 30 days

Fig. 4.2.7.1 (d) shows the GI-XRD patterns obtained from the surfaces of glasses with x = 5, 10, 15 and 20 wt. % Fe_2O_3 after treatment in SBF for 30 days. The hydroxyapatite (HA) peaks appearing between 2θ values of 30° to 34° sharpen in samples with higher x. Since the broad peaks signify the presence of small sized crystallites, one can infer that on immersion in SBF, the HA formation gradually improves from small sized crystalline aggregates to a well-crystallized HA phase as the amount of iron oxide is increased in the system. Formation of the HA layer over the glass surface shows that the glass samples are bioactive. The relative intensity and peak width of the characteristic apatite reflections show considerable composition dependence. It is interesting to observe

the growth in the intensity and reduction in the width of the apatite reflections as a function of increasing iron oxide content in this series of glasses. We observe better apatite formation in this series of glasses too when the iron oxide content is increased. This might be due to the fact that in this series of glasses, Fe_2O_3 replaces CaO, leaving the amount of SiO_2 and P_2O_5 undisturbed. Such compositional variation seems to aid the apatite forming ability on the surface of these glasses.

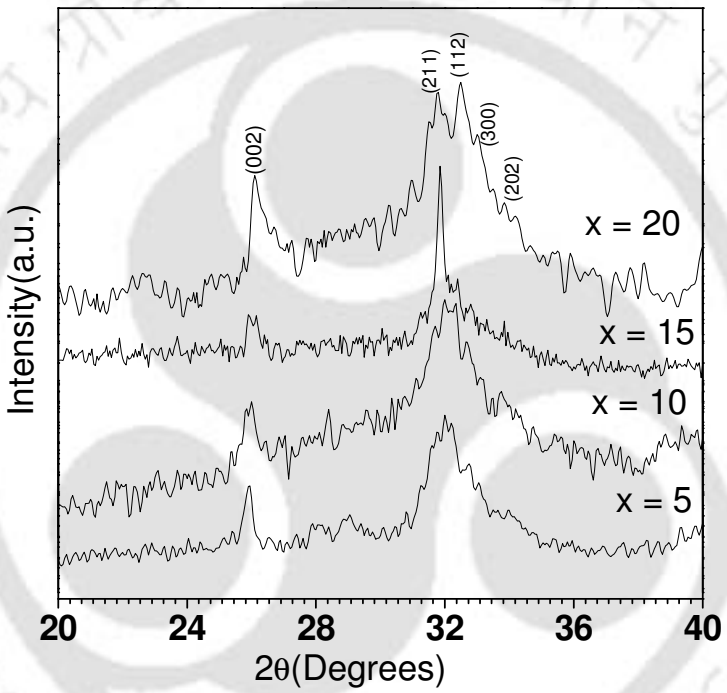

Fig. 4.2.7.1 (d): GI-XRD patterns of various samples *x* = 5, 10, 15 and 20 wt. % soaked in SBF for 30 days.

4.2.7.2. FT-IR spectroscopy of the glass samples soaked in SBF

Fig. 4.2.7.2(a) shows the infrared reflection spectra of the glass sample with *x* = 15 wt. % Fe_2O_3 before and after the immersion in the simulated body fluid for 0, 1, 3, 7, 10, 20 and 30 days. The spectrum before the immersion reveals bands at 1248, 1020, 937, 773, 640

and 420 cm^{-1}. The peaks at 1248, 1020, 773, 640 and 420 cm^{-1} correspond [188-190] to v_3 P-O stretching, Si-O stretching [with one non bridging oxygen (NBO)], Si-O-Si stretching, O-H stretching, and v_4 Si-O-Si bending frequencies, respectively. After 1 day of immersion in SBF, new peaks appear at 470, 840, 901, 1080, 1160, 1339 and 1569 cm^{-1}. The peaks at 470 cm^{-1}, 901 cm^{-1} and 1160 cm^{-1} correspond to v_2 P-O bending, v_1 P-O-P stretching and v_3 P=O stretching frequency, respectively. The peaks at 1040 cm^{-1} correspond to v_3 Si-O stretching frequency. The band located at 840 cm^{-1} and the large bands at 1339 and 1569 cm^{-1} can be assigned to C-O vibration mode of CO_3^{2-}. These bands signify the incorporation of carbonate anions from the SBF in the apatite crystal lattice. After 3 days of immersion in SBF, disappears of the band at 1080 cm^{-1}, this is related to ν_3 Si-O stretching surface layer.

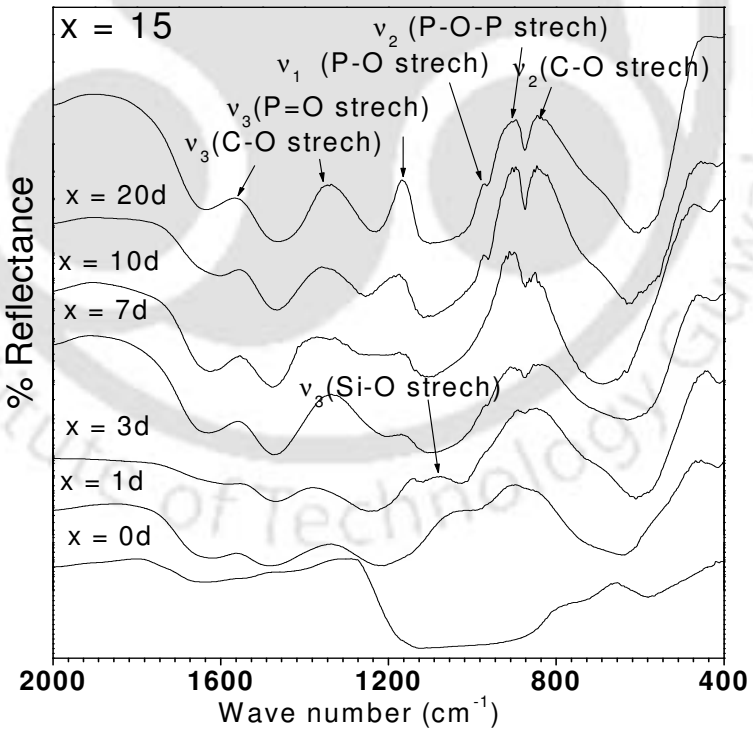

Fig. 4.2.7.2 (a): FT-IR reflection spectra of surfaces of glass-ceramics x = 15 wt. % soaked in SBF for various days.

After 3 days of immersion in SBF, the appearance of the band at 970 cm^{-1}, which is related to calcium phosphate (hydroxyapatite) surface layer is observed. The peak at 970 cm^{-1} corresponds to v_1 P-O symmetric stretching frequency. It indicates the obviation of phosphate ions from the ideal tetrahedral structure. This is a Raman active only mode when v_1 P-O symmetric stretching is in the free ion state. This Raman active mode can be seen in the infrared spectra because of lowering of the symmetry in the crystalline state [191]. These bands (1160 and 901cm^{-1}) sharpen and their relative intensities increase with increase in longer immersion times. These peaks are characteristic of apatite crystals. With further increase in immersion time, the intensity of the bands related to the CO_3^{2-} group increases. Carbonate ions occupy two different sites in carbonated apatite as indicated by peaks in the region of 1650 to 1300 cm^{-1} which are due to v_3 vibration mode, whereas the peak at 860 cm^{-1} is due to the v_2 vibration mode of carbonate ion [190]. The v_3 band splits into two peaks centered at 1339 and 1569 cm^{-1}, respectively, with the distribution of the carbonate v_3 sites depending on the maturation and formation of apatite crystals. Occupancy of the v_2 sites is considered to occur competitively between the OH^{-1} and carbonate groups at the interface of growing crystal, whereas, occupancy of the v_3 sites depends on competition between the phosphate and carbonate ions [190]. Presence of v_2 and v_3 vibration modes of carbonate is the signature of the development of HCA layer on the surface of the sample.

Fig. 4.2.7.2 (b) shows the infrared reflection spectra of all glass samples with x = 5, 10, 15 and 20 wt. % iron oxide after the immersion in SBF for 30 days. Spectral bands of HA assigned to PO_4^{3-} groups (ν_3–1160 cm^{-1}, ν_1–970 cm^{-1}, ν_1–901 cm^{-1} and ν_2–470 cm^{-1}) and CO_3^{2-} functional groups (v_2–840 cm^{-1}, ν_3–1339 $cm^{-1}$and ν_3–1559 cm^{-1}) appear in

the spectra. The band at 1038 cm^{-1} (ν_3 Si-O stretching mode) disappears in the samples with x = 15 and 20 wt. %. The peak at 901 cm^{-1} reflects the ν_1 P-O-P stretching mode. These bands (1160, 840 and 901 cm^{-1}) sharpen and their relative intensities increase with increase in iron oxide content signifying the formation of a well crystallized HCA layer in these samples. The FTIR studies thus clearly show an increased bioactivity in these glasses as the iron oxide content is increased in the composition range studied.

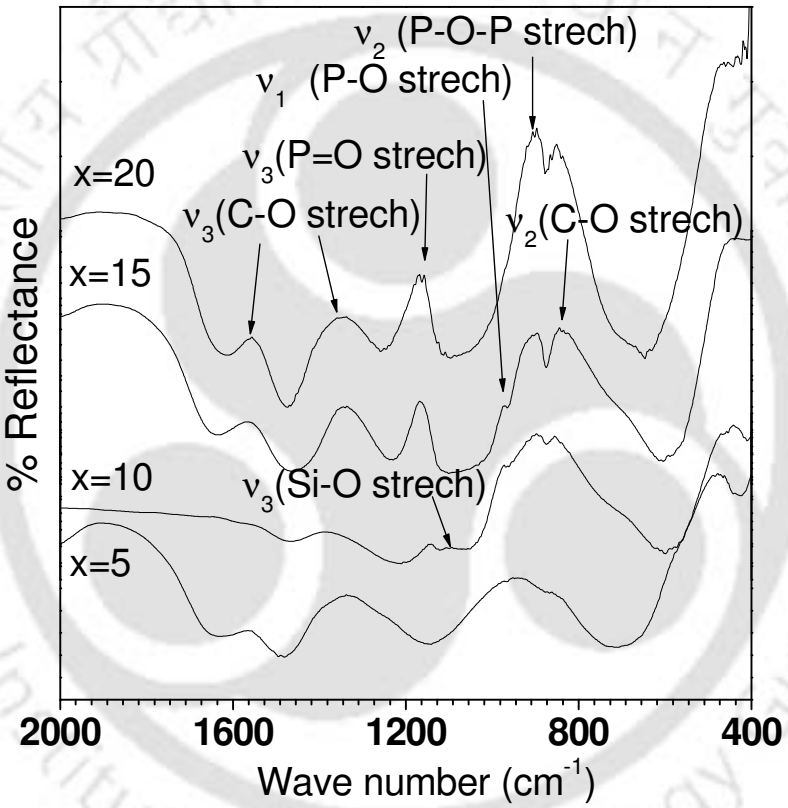

Fig. 4.2.7.2(b): FT-IR reflection spectra of surfaces of various glass-ceramics (x = 5, 10, 15 and 20 wt. %) soaked in SBF for 30 days.

4.2.7.3. SEM-EDS studies of the glass samples soaked in SBF

Fig. 4.2.7.3(a) shows the SEM micrographs (at 1000× magnification) of the sample x = 15, after immersion in SBF for 1, 3, 7, 10, 20 and 30 days.

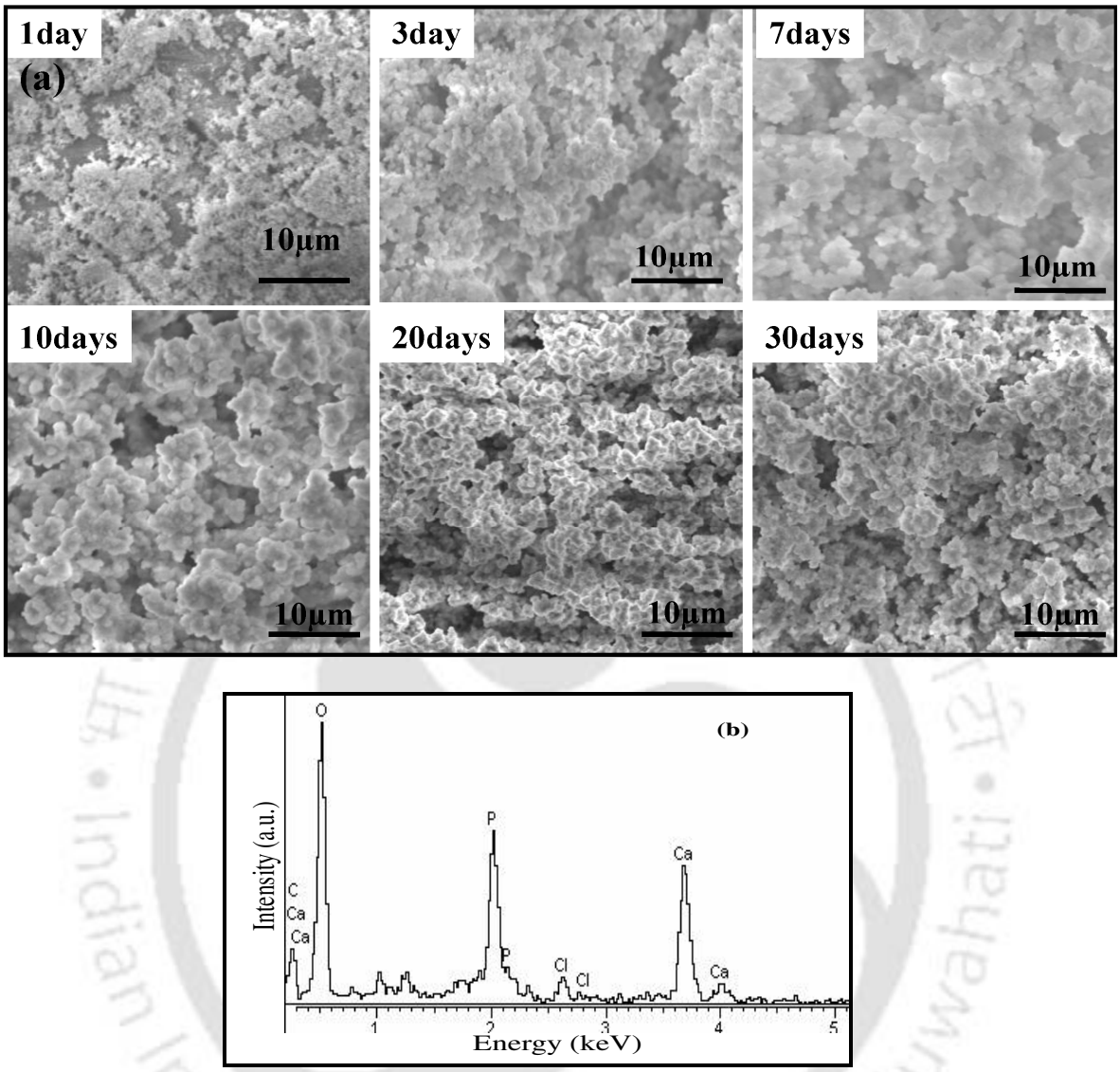

Fig. 4.2.7.3: (a) SEM micrographs of glass with x = 15 wt. % (magnified 1000×) soaked in SBF for various days, and (b) EDS spectra of sample soaked in SBF for 30 days.

The micrographs show the formation of surface layer on the surface of the bioglass which can be now presumed to be due to formation of apatite-like layer. After 30 days, the whole surface of the specimen was covered with spherical Ca-P particles apatite layer. Results from EDS analysis revealed the gradual development of HCA on the surfaces of glass samples after immersion for various times in SBF. The spherical

particles were constituted of calcium and phosphorus and the Ca/P molar ratio (calculated by EDS peak) was of ~ 1.67, corresponding to the value of hydroxyapatite. The microanalysis of the precipitates revealed the presence of small quantities of Na and Cl as may be seen in the spectra presented in Fig. 4.2.7.3(b). This finding is in agreement with reports that the growth of hydroxyapatite in SBF solutions results in the incorporation of sodium, magnesium and chlorine [192]. It may thus be concluded that the solid precipitated on hydroxyapatite seed crystals in SBF solutions consists of carbonate and sodium, magnesium, chlorine substituted hydroxyapatite [193].

4.3. Characterization of glass-ceramics samples

Powder X-ray diffraction analysis was used to identify the crystalline phases in the glass-ceramics derived from the parent glasses. The magnetic hysteresis loop was obtained using at room temperature at two different external magnetic fields of ± 20 kOe (kA/m) and ± 500 Oe. Magnetic susceptibility measurements of glasses containing iron oxide reveal the nature of interactions between the iron ions apart from providing information on the valence states of iron ions. EPR absorption spectra were analysed to understand the local environments and valence state of Fe ions in glass-ceramics at room temperature. Room temperature microhardness was used as a probe of the mechanical strength of the glass-ceramics samples. *In vitro* bioactivity test was performed on the samples by immersion of samples in SBF and the changes in the surface structure of the glass-ceramics were examined by GI XRD, reflectance FT-IR spectroscopy and SEM. The surface chemical analysis was carried out by EDS analysis.

4.3.1. XRD studies of glass-ceramics samples

Pieces of as-quenched glass were heat-treated at 1050 °C for 3 hours in air to form the glass-ceramics. XRD patterns of the glass-ceramic samples with different iron oxide content are shown in Fig. 4.3.1.1. Three major crystalline phases, *viz*., hydroxyapatite [$Ca_{10}(PO_4)_6(OH)_2$, JCPDS file no. 74-0566], magnetite [Fe_3O_4, JCPDS file no. 88-0315] and wollastonite [$CaSiO_3$, JCPDS file no. 84-0655] were identified in all samples. An additional phase which was identified as akermanite [$Ca_2MgSi_2O_7$, JCPDS file no. 35-0592] developed in glass-ceramics with higher Fe_2O_3 content. Hydroxyapatite and wollastonite are bone minerals and their presence indicates the biocompatible nature of the glass-ceramics.

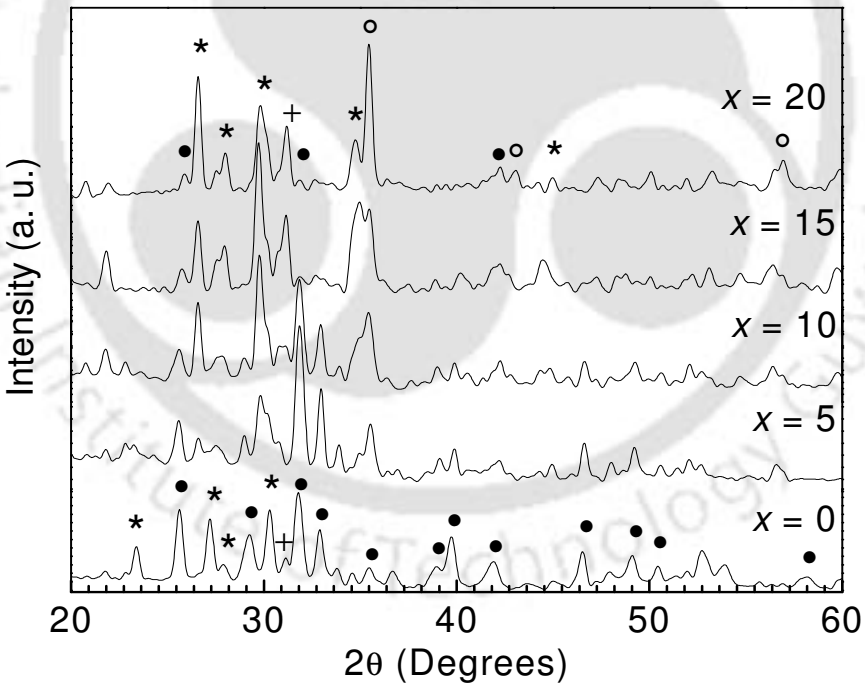

Fig. 4.3.1.1: XRD patterns of freshly prepared glass-ceramic samples. Crystalline phases present are magnetite (○), hydroxyapatite (●), wollastonite (*) and akermanite (+).

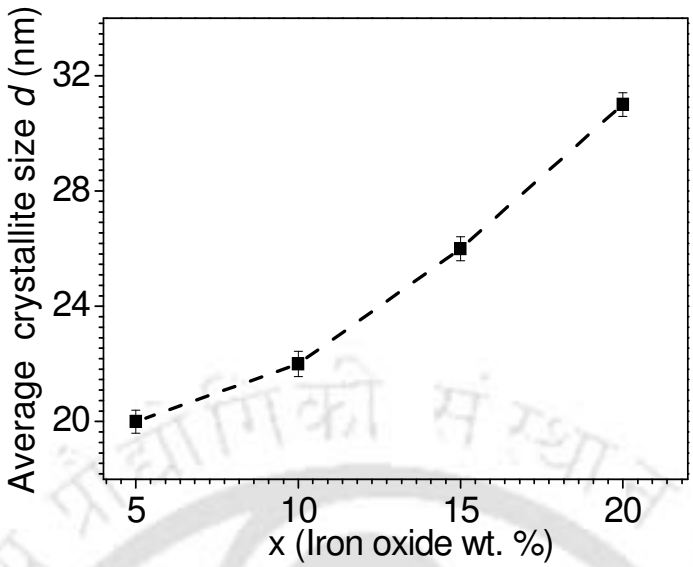

Fig. 4.3.1.2: Variation of average magnetite crystallite size as a function of iron oxide concentration.

Since the magnetite phase is expected to contribute to the magnetic properties of the glass-ceramics its average crystallite size was calculated from the broadening of the primary [(311)] peak in their XRD patterns using Scherrer's formula (equation 2.1). The average crystallite size (*d*) of the magnetite phase increased in the samples as the iron oxide concentration was increased from 5 to 20 wt. % as depicted in Fig. 4.3.1.2. The values of *d* show an increase from 20 to 31(± 0.40) nm as the iron oxide content is increased from 5 to 20 wt. % (Table 4.3.4).

4.3.2. Microhardness studies of glass-ceramics samples

Microhardness of glass-ceramics was measured following the procedure outlined in second chapter. All glass samples were uniformly subjected a load of 100 gm for duration of 15 seconds. The measured microhardness values are tabulated in Table 4.3.4. Figure

Fig. 4.3.2 shows the variation of hardness value with the iron oxide wt. % content in the $4.5MgO(45\text{-}x)CaO34SiO_2 16P_2O_5 0.5CaF_2 xFe_2O_3$ glass-ceramics. The glass-ceramics samples show a higher VHN as compared to the corresponding parent glasses. VHN of the glass-ceramics samples increases as a function of iron oxide content as shown in Fig. 4.3.2 and Table 4.3.4. The presence of crystalline phases increases the VHN of the glass-ceramics. An increase in the VHN can then be interpreted as due to the increase in the percentage of the crystalline phases in the glass-ceramics as a function of iron oxide content. Thus, addition of iron oxide increases the hardness of this series of samples. MgO based glass-ceramic samples exhibited higher microhardness when compared to the CaO based glass-ceramics samples. This feature can be attributed to the presence of akermanite ($Ca_2MgSi_2O_7$) in these glass-ceramics, which increases the strength of these glass ceramics. This MgO system could offer high strength magnetic bioglass and glass-ceramics suitable for load-bearing applications.

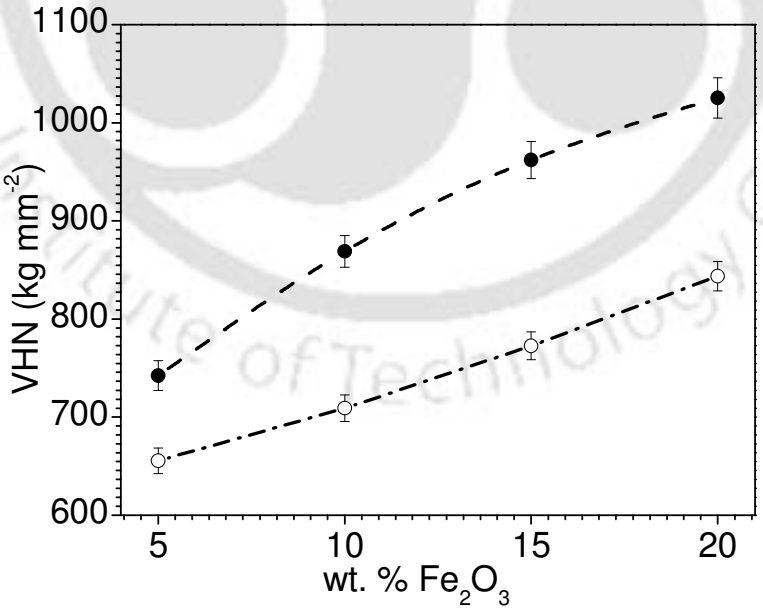

Fig. 4.3.2: Variation of VHN of MgO glass (o) and glass-ceramics (•).

4.3.3. EPR studies of glass-ceramics samples

EPR absorption spectra of $4.5MgO(45\text{-}x)CaO34SiO_2 16P_2O_5 0.5CaF_2 x Fe_2O_3$ ($5 \leq x \leq 20$ wt. %) glass-ceramics samples are shown in Fig. 4.3.3.1. The relative intensity and linewidth of these absorption lines show a strong dependence on Fe_2O_3 concentration. The EPR parameters, *viz.*, the line width (ΔH) and the intensity of absorption line J, corresponding to various glass-ceramics compositions were determined from the curves depicted in Fig. 4.3.3.1. The variations of the parameters are plotted in Fig. 4.3.3.2 for the resonance lines centred at $g \approx 2.1$. It is apparent from Fig. 4.3.3.2 that the intensity [$J_{(g \approx 2.1)}$] and line width [$\Delta H_{(g \approx 2.1)}$] of the $g \approx 2.1$ absorption line increase as a function of iron oxide concentration.

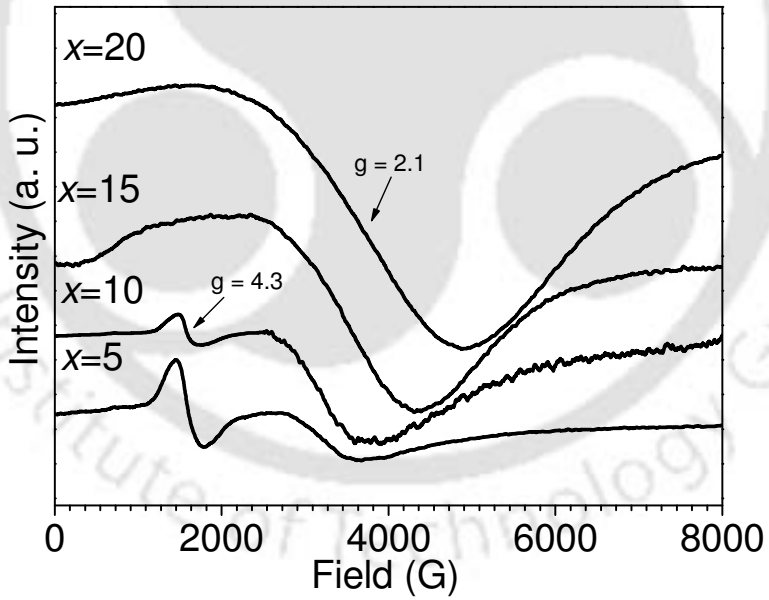

Fig. 4.3.3.1: Room temperature EPR absorption spectra of $4.5MgO(45\text{-}x)CaO34SiO_2 16P_2O_5 0.5CaF_2 x Fe_2O_3$ glass-ceramic samples.

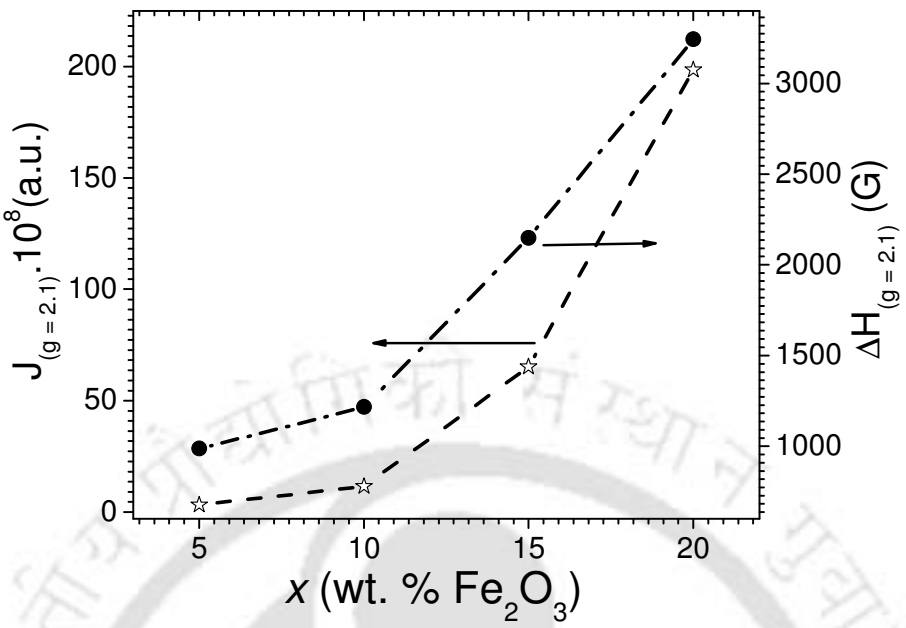

Fig. 4.3.3.2: Composition dependence of intensity and linewidth for g ≈ 4.3 absorption line of 4.5MgO(45-*x*)CaO34$SiO_2$16$P_2O_5$0.5CaF_2*x*Fe_2O_3 glass-ceramic samples.

The absorption line centred at g ≈ 2.1 is due to the isolated Fe^{3+} ions in a slightly distorted structural unit in samples with low iron oxide concentration and to the clustered formation of the iron ions for higher concentrations. The nonlinear increase of $J_{(g=2.1)}$ and $\Delta H_{(g=2.1)}$ with iron oxide concentration depicted in Fig. 4.3.3.2 shows that iron irons are present as Fe^{3+} as well as Fe^{2+} in the samples. From Fig. 4.3.3.1, one can observe that as iron oxide content is increased, the signal at g ≈ 4.3 begins to disappear and the broad signal centered at g ≈ 2.1 starts to develop. The line width of the g ≈ 2.1 resonance absorption depends also on the iron oxide concentration. As mentioned earlier, the absorption at g ≈ 2.1 can be attributed to the formation of iron clusters which give rise to superexchange type interaction between iron ions. In this context, it is worthy to point out that the saturation magnetization increases in the samples as a function of *x* (*cf.* Fig.

4.3.4.4.). The increase in $J_{(g=2.1)}$ as a function of iron oxide content indicates an increase in the ferrimagnetically coupled superexchange type interactions in the glass-ceramic samples. Superexchange mechanisms tend to narrow the absorption line. On the other hand, interactions between Fe^{3+} and Fe^{2+} ions tend to broaden the line width. The final line width depends on the relative strengths of these two mechanisms influencing the line width. The increase in the line width of the absorption at g ≈ 2.1 with iron oxide concentrations shows the dominance of the broadening mechanisms, which in turn indicates a larger increase in Fe^{2+} ion concentration as iron oxide content is increased in the glass-ceramics.

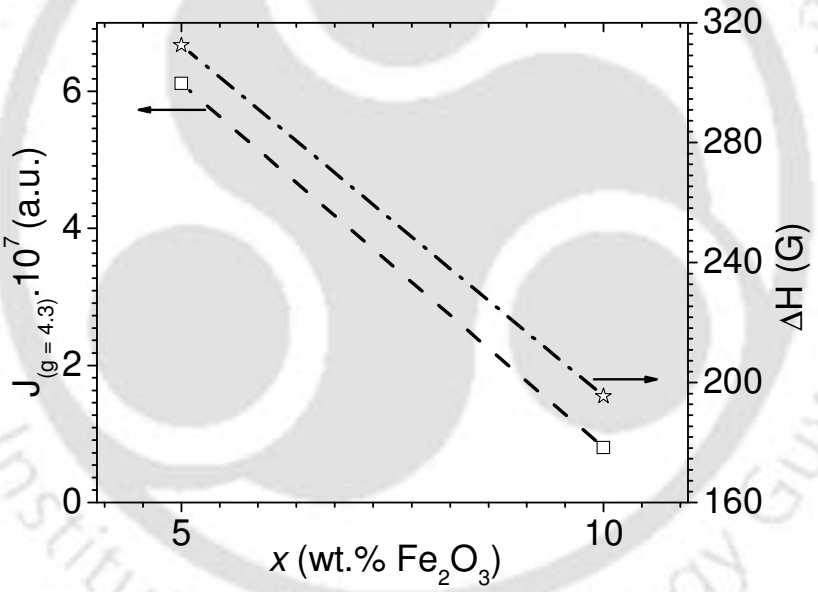

Fig. 4.3.3.3: Composition dependence of intensity and linewidth for g ≈ 4.3 absorption line of $4.5MgO(45\text{-}x)CaO34SiO_2 16P_2O_5 0.5CaF_2 xFe_2O_3$ glass-ceramic samples.

Fig. 4.3.3.1 also shows that the EPR absorption line at g ≈ 4.3 appears only in samples with x = 5 and 10 wt. % iron oxide. The concentration dependence of the EPR parameters of the absorption line centered at g ≈ 4.3 is plotted as a function of

composition in Fig. 4.3.3.3. The intensity [$J_{(g=4.3)}$] and line width [$\Delta H_{(g=4.3)}$] of the $g \approx 4.3$ absorption line decreases as x is increased. The decrease in intensity of the signal centred at $g \approx 4.3$ may be due to the formation of iron clusters which give rise to superexchange type interaction between iron ions. The increase in intensity of the absorption at $g \approx 2.1$ as a function of iron oxide concentration lends support to this conclusion. Since the $g \approx 4.3$ absorption arises from Fe^{3+} ions in low symmetry sites, the disappearance of the $g \approx 4.3$ line signifies a decrease of low symmetry sites at Fe^{3+} ions and a corresponding increase in Fe^{3+} sites of higher symmetry in the crystallization process. In other words, the EPR spectra indicate that low symmetry sites whose crystal fields are equal and very near to the special crystal fields with $D = 0$, $E \neq 0$ and $\lambda = E/D = 1/3$ have been removed during the crystallization process of the parent glass. As already pointed out, XRD studies have confirmed (Fig. 4.3.1.1) that magnetite ($Fd\bar{3}m$) crystallizes when the glasses are heat-treated at 1050 °C.

4.3.4. Magnetic properties of glass-ceramics samples

Fig. 4.3.4.1 depicts the room temperature magnetic hysteresis (M-H) loops of different glass-ceramic samples derived from respective glasses with composition $4.5MgO(45\text{-}x)CaO34SiO_2 16P_2O_5 0.5CaF_2 x Fe_2O_3$. The linear variation of H_C versus $1/d$ plot shows as an inset in Fig. 4.3.4.1(a). The coercive field (H_C) and the remanent magnetization (M_r) are individuated in the inset Fig. 4.3.4.1(b). The magnetic field necessary to saturate the samples increases with increasing iron oxide content. The coercive field varies from 575 to 149 Oe, while the saturation magnetization varies from 0.21 to 8.89 emu/g over the composition range explored. The saturation magnetization

(M_s) increases with the amount of magnetic phase in the sample. The highest amount of magnetite phase is obtained in the sample with x = 20 wt. %, which also has the highest M_s. Amount of magnetic phase presented in the glass-ceramic samples was determined from the saturation magnetization ratio between the sample and pure magnetite (M_s = 92 emu/g [148]). The saturation magnetization increases with the amount of magnetic phases crystallised in the sample (*cf.* Table 4.3.4). The highest amount of magnetite phase is obtained for the sample x = 20 wt. % which contains the highest value of saturation magnetization (M_s). The results are summarised in Table 4.3.4.

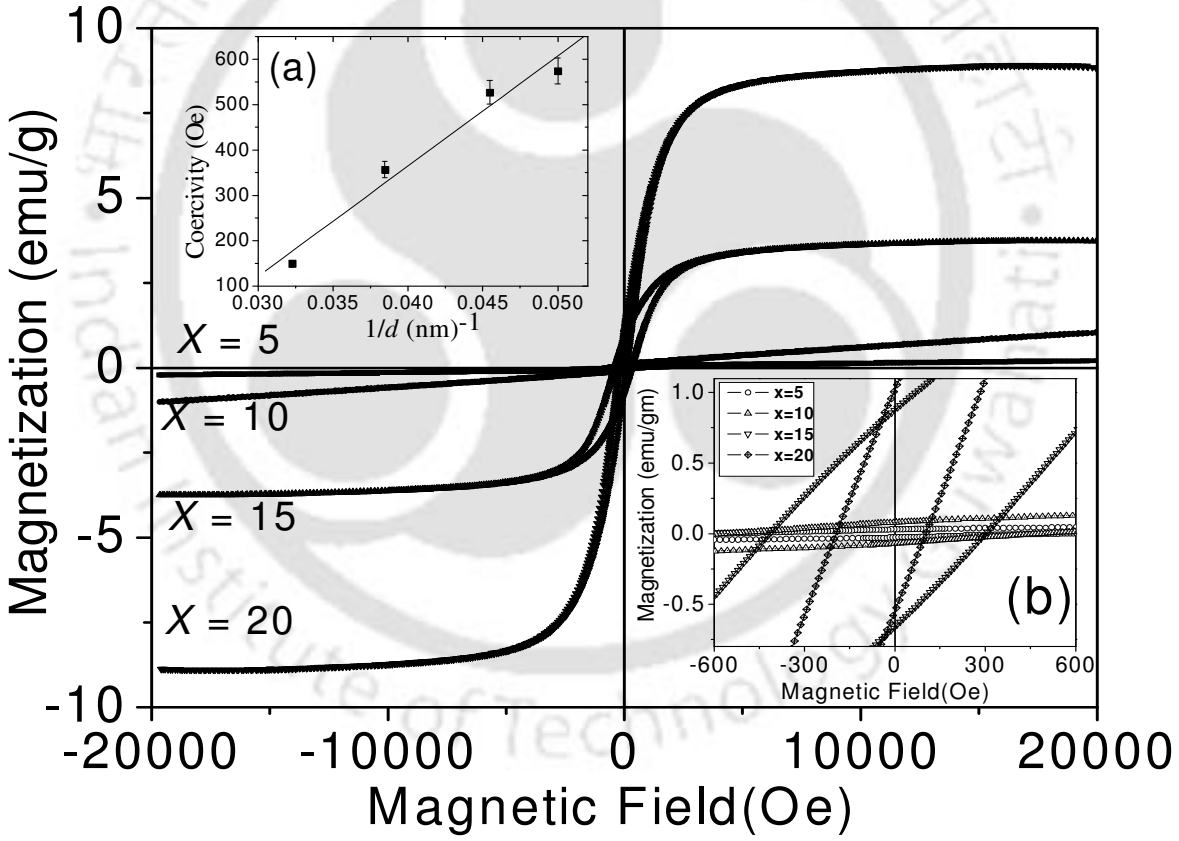

Fig. 4.3.4.1: Room temperature M-H curves of the glass-ceramic samples. Insets show (a) H_C versus 1/*d* plot, and (b) enlarged view of M-H loops near the origin.

Table 4.3.4: Magnetic and structural parameters of glass-ceramics derived from glasses with composition $4.5MgO(45-x)CaO34SiO_2 16P_2O_5 0.5CaF_2 xFe_2O_3$.

Magnetic and structural parameters	Sample (*x*) (wt. % of iron oxide)			
	x = 5	*x* = 10	*x* = 15	*x* = 20
Average (magnetite) crystallite size *d* (nm)	20	22	26	31
Amount of magnetic phase (wt. %)	0.23	1.12	4.07	9.66
Saturation magnetization M_s (emu/g)	0.21	1.03	3.75	8.89
Coercive force, H_C (Oe)	575	527	357	149
Remanent magnetization M_r (emu/g)	0.03	0.08	0.77	0.81
Interpolated hysteresis area ± 20 kOe (erg/g)	348	1308	5171	6618
Interpolated hysteresis area ± 500 Oe (erg/g)	9	42	286	784
Vickers hardness number (kg mm^{-2})	742	868	962	1025

Fig. 4.3.4.2 displays the relevant magnetic parameters obtained from M-H loops for samples with different iron oxide content. The saturation magnetization (M_S) (Fig. 4.3.4.2 a) increased with increasing iron oxide concentration from x = 5 to 15 wt. % and shows a tendency to saturate for *x* = 20 with the maximum value of about 8.89 emu/g. The increase of saturation magnetization with an increase in iron oxide concentration could be attributed to the development of magnetite phase in the samples, which can be inferred from Fig. 4.3.1.1 and Table 4.3.4. On the other hand, H_C of the samples (Fig.

4.3.4.2 b) decreases with increasing iron oxide concentration. H_C is influenced in a significant way by the crystallite dimensions. The linear variation of H_C versus $1/d$ plot shown as an inset in Fig. 4.3.4.1 confirms the influence of crystallite size on the coercive field. Remanence signifies the nature of the magnetic material to be spontaneously magnetized, even in the absence of external magnetic field. Thus, the increase in M_r, M_s and hysteresis area, and the decrease in H_C with an increase in iron oxide content can be attributed to the increase in the amount and size of magnetite crystallites in the glass-ceramic samples. The area under the hysteresis loop increases with an increase in iron oxide content (Fig. 4.3.4.2 d). Area under the loop is proportional to the energy loss and hence the heat generated by a sample subjected to an alternating field.

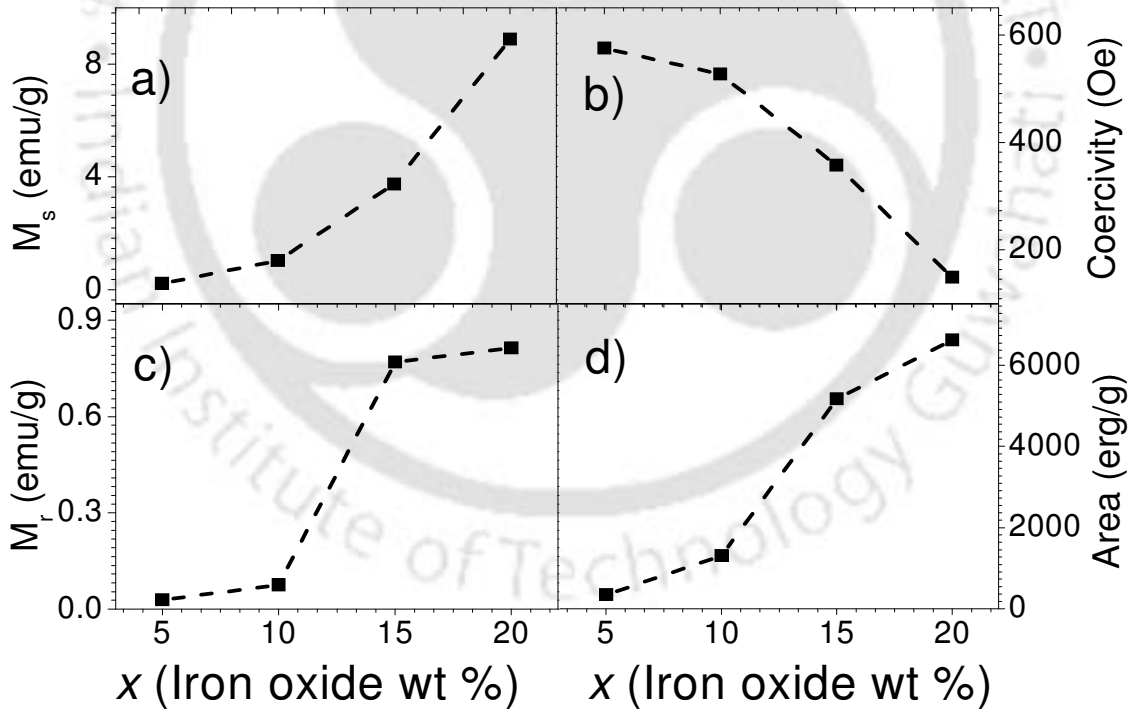

Fig. 4.3.4.2: Variation of room temperature (a) saturation magnetization, (b) coercive field, (c) remanent magnetization, and (d) area under the M-H loop of glass-ceramics as a function of iron oxide content of the glass-ceramic samples.

The results obtained indicate that samples with higher iron oxide concentration are capable of generating more heat for the same magnetic field sweep. The large variation in the area under the loop for samples with x = 5 and x = 20 wt. % shows that controlled heat generation can be achieved at a constant field strength by appropriate choice of glass-ceramic composition. High magnetic fields of the order of ± 20 kOe are difficult to realize in a clinical laboratory due to technical reasons. Therefore, room temperature hysteresis cycles were performed at much lower field amplitudes (i.e., ± 500 Oe) in order to evaluate the materials for hyperthermia applications. The corresponding M-H loops are shown in Fig. 4.3.4.3. It can be seen that the loop area drastically reduces when the magnetic field is reduced. However, all loop parameters scale down proportionally to the applied field amplitude. This shows that the properties of these glass-ceramics are preserved even at clinically amenable low magnetic fields.

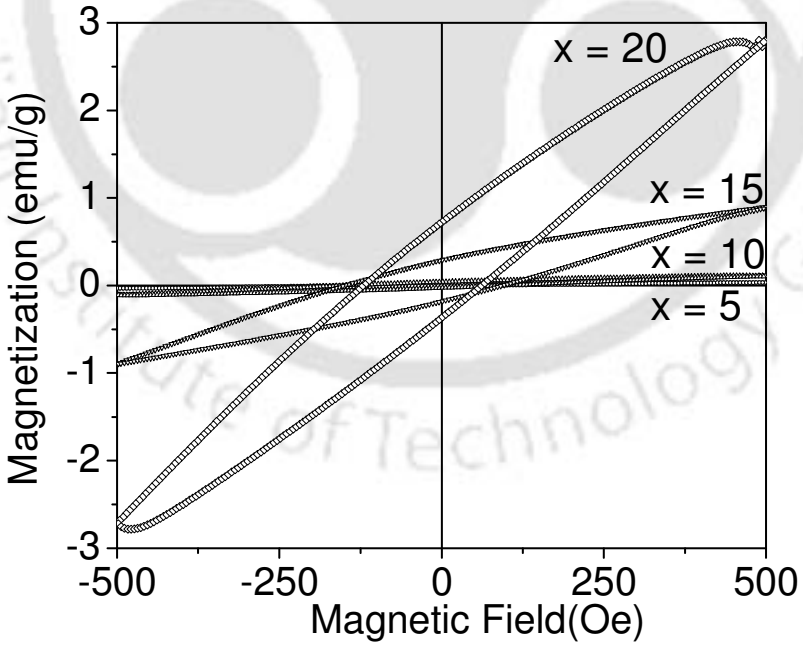

Fig. 4.3.4.3: Room temperature magnetic hysteresis loops of glass-ceramics with different iron oxide concentration under ± 500 Oe field sweep.

Fig. 4.3.4.4 shows the room temperature initial magnetization curves of all the samples. The magnetization curves of the samples with x = 5 and 10 did not saturate up to an applied magnetic field of 1592 kA/m (20 kOe) as revealed by the in-set in the figure.

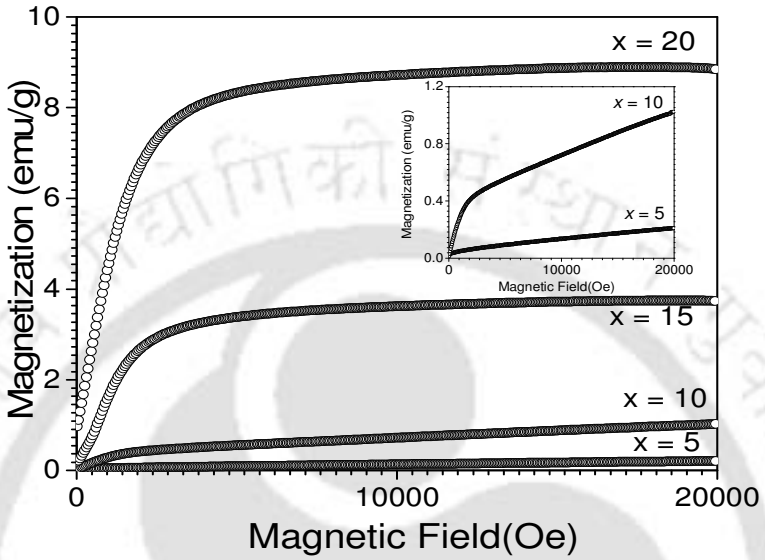

Fig. 4.3.4.4: Room temperature initial magnetization curves of the glass-ceramic samples. In-set shows M-H plots for the samples with x = 5 and 10 wt. % iron oxide.

It can be inferred from the nature of the curves that the samples with x = 5 and 10 wt. % iron oxide exhibit a combination of paramagnetic and ferrimagnetic behaviour. Such behaviour has also been reported in annealed CaO-P_2O_5-Fe_2O_3 glasses [171, 201]. The EPR absorption line at g ≈ 4.3 and g ≈ 2.1 are observed only in samples with x = 5 and 10 wt. % iron oxide content. These samples exhibit a combination of paramagnetic and ferrimagnetic behaviour. A comparison with the EPR spectra of these samples would clarify that both these techniques yield results that support and complement each other. The magnetization curves of samples with x = 15 and 20 saturate at a magnetic field of 20 kOe. These compositions exhibit only ferrimagnetic behavior. EPR spectra of these

compositions show only one absorption line at g ≈ 2.1, which is an indication of enhanced magnetic superexchange interaction between the iron ions.

Fig. 4.3.4.5 shows that plots of magnetization as a function of temperature (M-T curves) recorded under a constant magnetic field of 79.6 kA/m (1 kOe). A steady decrease in magnetization is observed as the temperature is increased. The ferrimagnetic behaviour of the investigated samples is obvious from the nature of the M-T curves. Magnetic susceptibility (χ) measurements reveal the type of interactions between iron ions and the nature of magnetism in the sample.

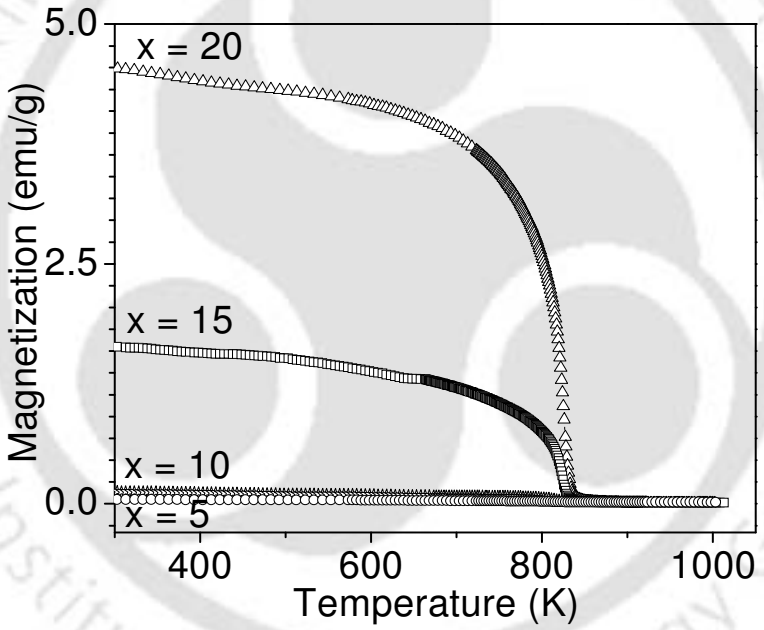

Fig. 4.3.4.5: Variation of magnetization as a function of temperature of 4.5MgO(45-*x*) CaO34$SiO_2$16$P_2O_5$0.5CaF_2*x*Fe_2O_3 glass-ceramics samples.

The variation of inverse magnetic susceptibility (χ^{-1}) with temperature over the range of 750 to 1030 K is shown in Fig. 4.3.4.6. The χ^{-1} - T plots which are nearly linear above 950 K show a downward drop at low temperatures indicating the symmetry

breaking transition. The deviation from linearity and the systematic downward drop of χ^{-1} - T curves indicate the onset of short-range order just above the ferrimagnetic Neel temperature (T_N). Comparison with the literature [198] reveals that the main contribution to magnetization in these glass-ceramics is from iron ions in magnetite (Fe_3O_4). T_N of the glass-ceramic samples increases from 818 to 826 K as *x* is varied from 5 to 20 wt. %. T_N increase with increase in iron oxide concentration may be correlated with the corresponding increase in the intensity of the $g \approx 2.1$ resonance line [Fig. 4.3.3.2].

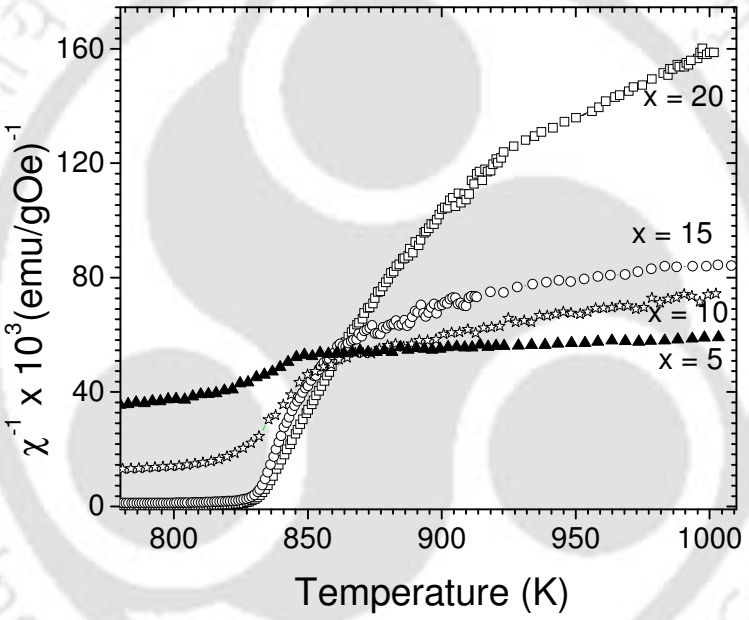

Fig. 4.3.4.6: Plots of temperature dependent inverse magnetic susceptibility of 4.5MgO (45-*x*)CaO34$SiO_2$16$P_2O_5$0.5CaF_2*x*Fe_2O_3 (*x* = 5, 10, 15 and 20 wt. % iron oxide) glass-ceramic samples.

T_N obtained from the present analyses is lower than the T_N value of bulk magnetite (856 K [198]), which is the typical feature of nanomagnetic materials. A closer look at Fig. 4.3.4.6 would show a deviation in the manner in which χ^{-1} decreases as the

temperature is lowered in the case of the x = 5 and x = 10 samples *vis-a-vis* the $x \geq 15$ samples. χ^{-1} is expected to approach zero at $T = T_N$ if the sample is entirely ferrimagnetic. Any departure from this behaviour as observed in the case of samples with x = 5 and 10 shows the coexistence of a paramagnetic phase along with the ferrimagnetic phase in these samples.

4.3.5. *In vitro* bioactivity test of glass-ceramics samples

Glass-ceramics samples $4.5MgO(45\text{-}x)CaO34SiO_2 16P_2O_5$ $0.5CaF_2 xFe_2O_3$ immersed in SBF were taken out after 1, 3, 7, 10, 20 and 30 days, lightly washed with acetone. Surface structural changes of the glass-ceramics samples treated in SBF were analyzed by GI-XRD, FT-IR spectroscopy and SEM. The surface chemical analysis was carried out by EDS analysis. The outcomes of these studies are described below.

4.3.5.1. GI-XRD studies of the glass-ceramics samples soaked in SBF

Fig. 4.3.5.1(a) shows the GI-XRD patterns from the surfaces of the glass-ceramics sample with x = 15 wt. % iron oxide before and after soaking in SBF for various time periods (*i.e.* 0, 1, 3, 7, 10, 20 and 30 days). It is obvious from Fig. 4.3.5.1(a) that broad crystalline peaks develop in glass-ceramics samples treated with SBF for 3 days and more. Initially, two peaks at 2θ values of ~26° and ~32° develop after 1 days of soaking in SBF. The two peaks could be assigned to (002) and (211) reflections of HA crystallites (JCPDS file no. 74-0565). The intensity of the (002) and (211) reflections of the HA phase increases with an increase in the accumulation of Ca^{2+} and PO_4^{3-} ions on the surface of the glass-ceramics soaked in SBF.

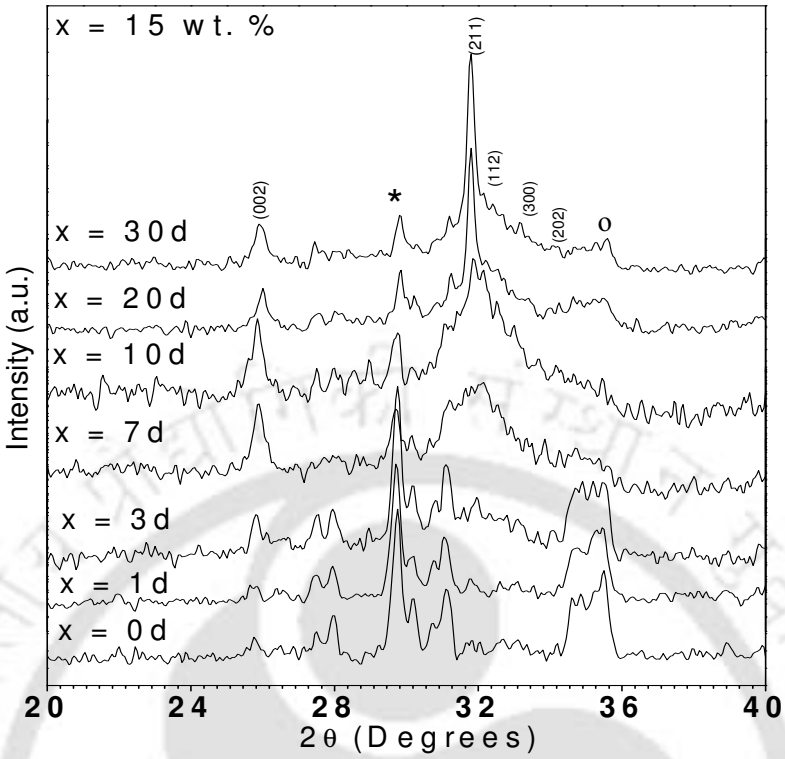

Fig. 4.3.5.1(a): XRD patterns of the sample with x = 15 wt. % soaked in SBF for different days.

The wide diffraction peak spread over 2θ range of 30° to 34° could be assigned to three closely placed reflections from (112), (300) and (202) planes for the well-crystallized HA phase. The increase in the intensities and decrease in the width of the apatite peaks of the samples immersed for longer periods in SBF clearly shows the evolution of the apatite layer on the surface of the glass-ceramic samples in physiological conditions. The gradual growth in the intensity of the individual reflection, appearance of other low intensity apatite reflections and the narrowing of the peak width clearly show the evolution of the crystalline HA surface layer as a function of immersion time in SBF. The intensity of two major reflections, *viz*., (002) and (211), increase [*cf.* Fig. 4.3.5.1(b)]

with an increase in the concentration of Ca^{2+} and PO_4^{3-} ions on the surface of the glass immersed in SBF for various days. It is obvious that the intensity of the reflections attain saturated values within 20 days of immersion in SBF.

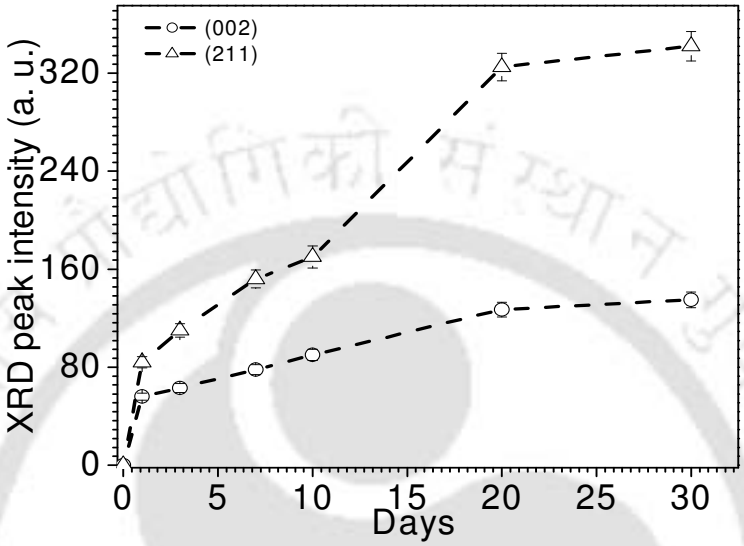

Fig. 4.3.5.1(b): GI-XRD intensity of glass sample x = 15 wt. % corresponds to the (002) and (211) reflection peak for soaked in SBF for 1, 3, 7, 10, 20 and 30 days.

The average crystallite size (d) in a direction perpendicular to the crystallographic plane was estimated using the Scherrer`s formula (equation 2.1). The average size of HA crystallized was calculated from the (002) reflection using equation (2.1). Fig. 4.3.5.1(c) reveals an increase in the average particle size of the crystalline surface layer on the glass immersed in SBF for various days, which is consistent with results of reported earlier [184, 200]. The crystallite size increases from about 12.8 (± 0.38) nm to 26.7 (± 0.69) nm in samples immersed for 3 days to 30 days. The size of HA crystalline depends on the rate of crystalline growth on the surface of the glass in the SBF in various days. The variation of the crystallite size with immersion time shows a sharp increase in crystallite

size in samples treated in SBF for 10 days, followed by a slower increase in crystallite size in samples treated in SBF for longer periods.

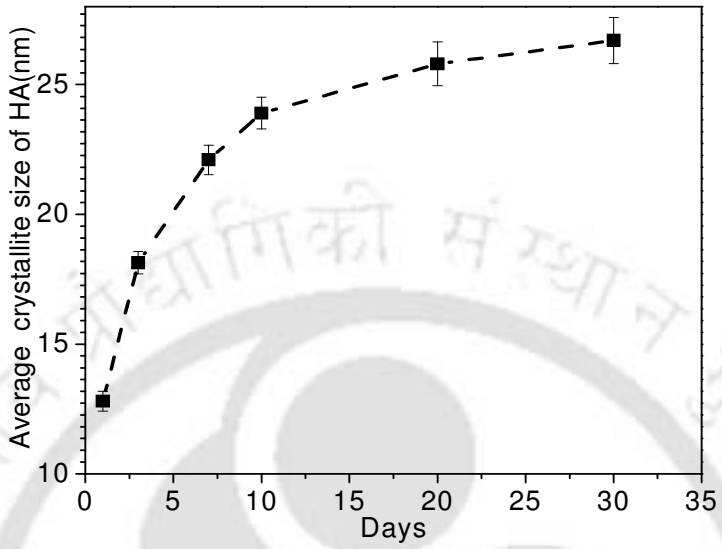

Fig. 4.3.5.1(c): The averages size of HA crystalline (nm) corresponds to the (002) reflection peak for sample x = 15 wt. % soaked in SBF for 1, 3, 7, 10, 20 and 30 days.

Fig. 4.3.5.1(d) shows the GI-XRD patterns obtained from the surfaces of the glass-ceramics after soaking in SBF for 30 days. The hydroxyapatite (HA) peaks appearing between 2θ values of 30° to 34° sharpen in samples with higher x. Since the broad peaks signify the presence of small sized crystallites, one can infer that on immersion in SBF, the HA formation gradually improves from small sized crystalline aggregates to a well-crystallized HA phase as the amount of iron oxide is increased in the system. Formation of the HA layer over the glass-ceramics surface shows that the glass-ceramics samples are bioactive. The relative intensity and peak width of the characteristic apatite reflections show considerable composition dependence. It is interesting to observe the growth in the intensity and reduction in the width of the apatite reflections as a

function of increasing iron oxide content in this series of glass-ceramics. It is interesting to observe the growth in the intensity and reduction in the width of the apatite reflections as a function of increasing iron oxide content in this series of glasses and glass-ceramics. As discussed earlier, this might be due to Fe_2O_3 replacing CaO in this series, without disturbing the amounts of SiO_2 and P_2O_5. Such compositional variation seems to aid the apatite forming ability on the surface of these glass-ceramics.

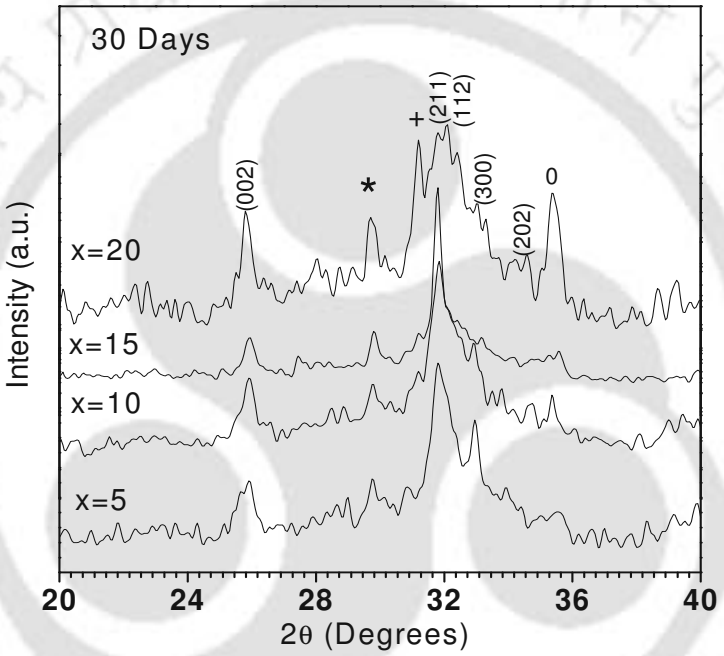

Fig. 4.3.5.1(d): XRD patterns of the glass-ceramic samples soaked in SBF for 30 days.

4.3.5.2. FT-IR studies of the glass-ceramics samples soaked in SBF

Fig. 4.3.5.2(a) shows the FT-IR spectra of the glass-ceramics sample with x = 15 wt. % before and after the immersion in SBF for 0, 1, 3, 7, 10, 20 and 30 days. The spectrum before immersion reveals bands at 1160, 1075, 1025, 890, 815, 636, 570 and 432 cm^{-1}. The peaks at 1160, 1075, 1025, 890, 815, 636, 570 and 432 cm^{-1} correspond [188-190] to v_3 P-O stretching, v_3 Si-O stretching, v_3 P-O stretching, Si-O-Si stretching of non-bridging

oxygen atoms, Si-O-Si symmetric stretching of bridging oxygen atoms between tetrahedral, O-H stretching, v_4 P-O bending and v_4 Si-O-Si bending frequency, respectively. The peak at 1067 cm^{-1}, which is assigned to Si-O stretching vibration in SiO_4 units with bridging oxygens shifts to a lower wavenumber with longer immersion times and disappears after 3 days of immersion in SBF. As the peak at 1067 cm^{-1}shifts and disappears a new vibrational mode is observed at 1030 cm^{-1}, which can be assigned to Si-O bond vibration between two SiO_4 tetrahedra. After 1 day of immersion, new bands start developing at 457, 860, 902, 970, 1145, 1227, 1327 and 1556 cm^{-1}. The peaks at 457 cm^{-1} and 902 cm^{-1} correspond to v_2 P-O bending and v_1 P-O-P stretching frequency, respectively.

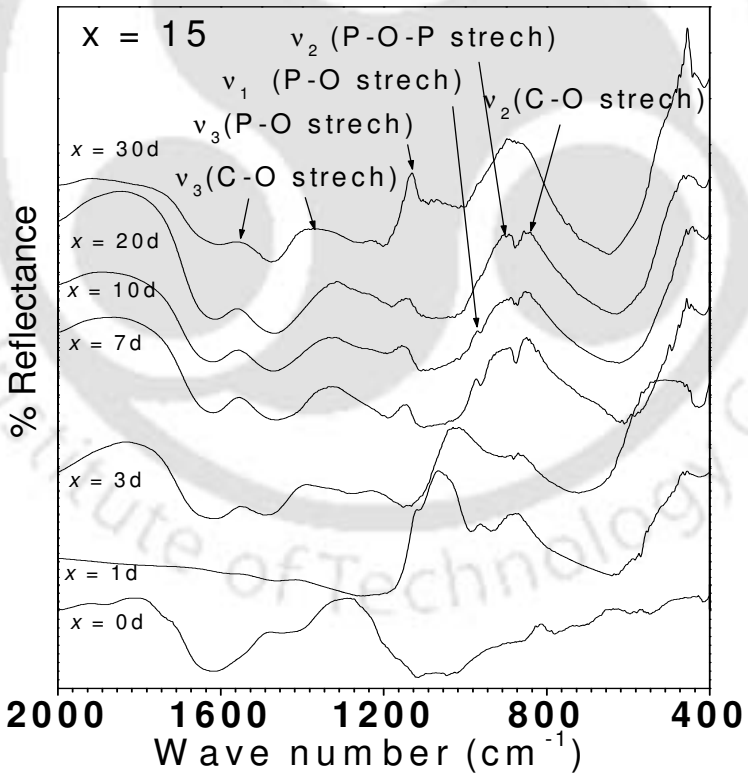

Fig. 4.3.5.2(a): FT-IR spectra of glass-ceramics samples with x = 15 wt. % soaked in SBF.

The band located at 860 cm^{-1} and the broad bands at 1327 and 1556 cm^{-1} can be assigned to C-O vibration mode in CO_3^{2-}. These bands signify the incorporation of carbonate anions from the SBF in the apatite crystal lattice. After 1 day of immersion, the appearance of bands at 970 and 1140 cm^{-1} can be seen, which are related to the calcium phosphate (hydroxyl apatite) surface layer. The peak at 1140 cm^{-1} is associated with the v_3 P-O stretching mode. With further increase in immersion time, the intensity of the bands due to v_3 P-O stretching mode increases. The peak at 970 cm^{-1} reflects the v_1 P-O symmetric stretching mode. This band indicates the obviation of phosphate ions from the ideal tetrahedral structure. This is a Raman active only mode when v_1 P-O symmetric stretch is in the free ion state. This Raman active mode can be seen in the infrared spectra because of the lowering of the symmetry in the crystalline state [191]. With further increase in immersion time, the intensity of the bands due to CO_3^{2-} increases. Carbonate ions occupy two different sites in carbonated apatite: peaks in the region of 1650 to 1300 cm^{-1} are due to v_3 vibrational mode, whereas the peak at 860 cm^{-1} is due to the v_2 vibrational mode [190] of carbonate ion. The v_3 band splits into two peaks centered at 1327 and 1556 cm^{-1}, respectively, with the distribution of the carbonate v_3 sites depending on the maturation and formation of apatite crystals. Occupancy of the v_2 sites is considered to occur competitively between the OH^{-1} and carbonate groups at the interface of growing crystal, whereas occupancy of the v_3 sites depends on competition between the phosphates and carbonate ions [190]. Presence of v_2 and v_3 vibrational modes of carbonate is the imprint of the development of an HCA layer on the surface of the sample.

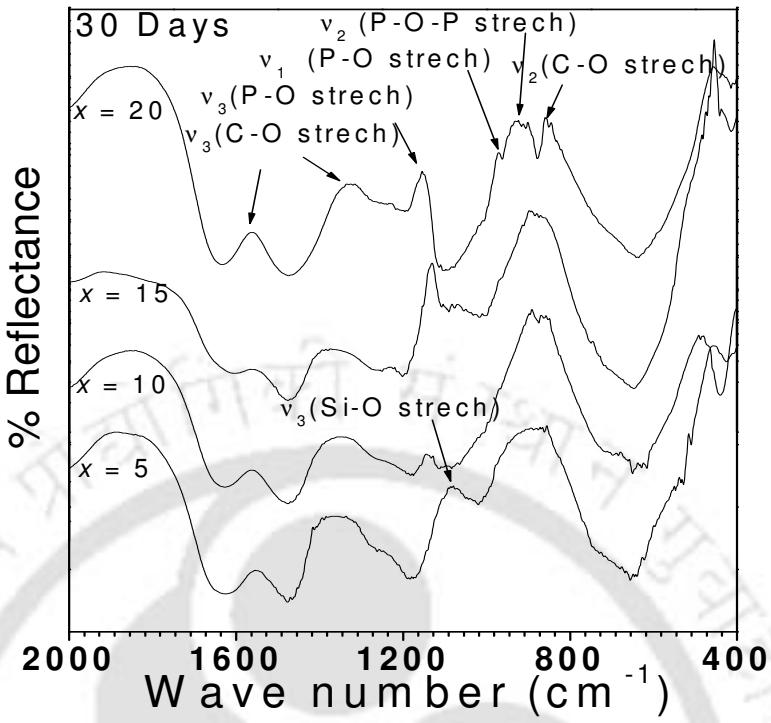

Fig. 4.3.5.2(b): FT-IR spectra of the surfaces of various glass-ceramics soaked in SBF for 30 days.

Fig. 4.3.5.2(b) shows the FT-IR reflection spectra of each glass-ceramic composition after the immersion in SBF for 30 days. Spectral bands of HA assigned to PO_4^{3-} groups (ν_3–1145 cm^{-1}, ν_1–970 cm^{-1} ν_1–902 cm^{-1} and ν_2–457 cm^{-1}) and CO_3^{2-} functional groups (ν_2–860 cm^{-1}, ν_3–1327 $cm^{-1}$and ν_3–1556 cm^{-1}) appear in the spectra. The band at 1040 cm^{-1} ν_3 Si-O stretch disappears in the samples with x = 15 and 20 wt. %. The peak at 905 cm^{-1} reflects the ν_1 P-O-P stretching mode. These bands (1145, 902, 860) sharpen and their relative intensities increase with an increase in iron oxide content signifying the formation of a well crystallized HCA layer in these samples. The FT-IR studies thus clearly show an increased bioactivity in these glass-ceramics as the iron oxide content is increased in the composition range studied.

4.3.5.3. SEM-EDS studies of the glass-ceramics samples soaked in SBF

Fig. 4.3.5.3(a) shows the SEM micrographs of the glass-ceramic sample with x = 15 wt. % after immersion in SBF for 1, 3, 7, 10, 20 and 30 days, respectively. The micrographs have been obtained under 1000× magnification.

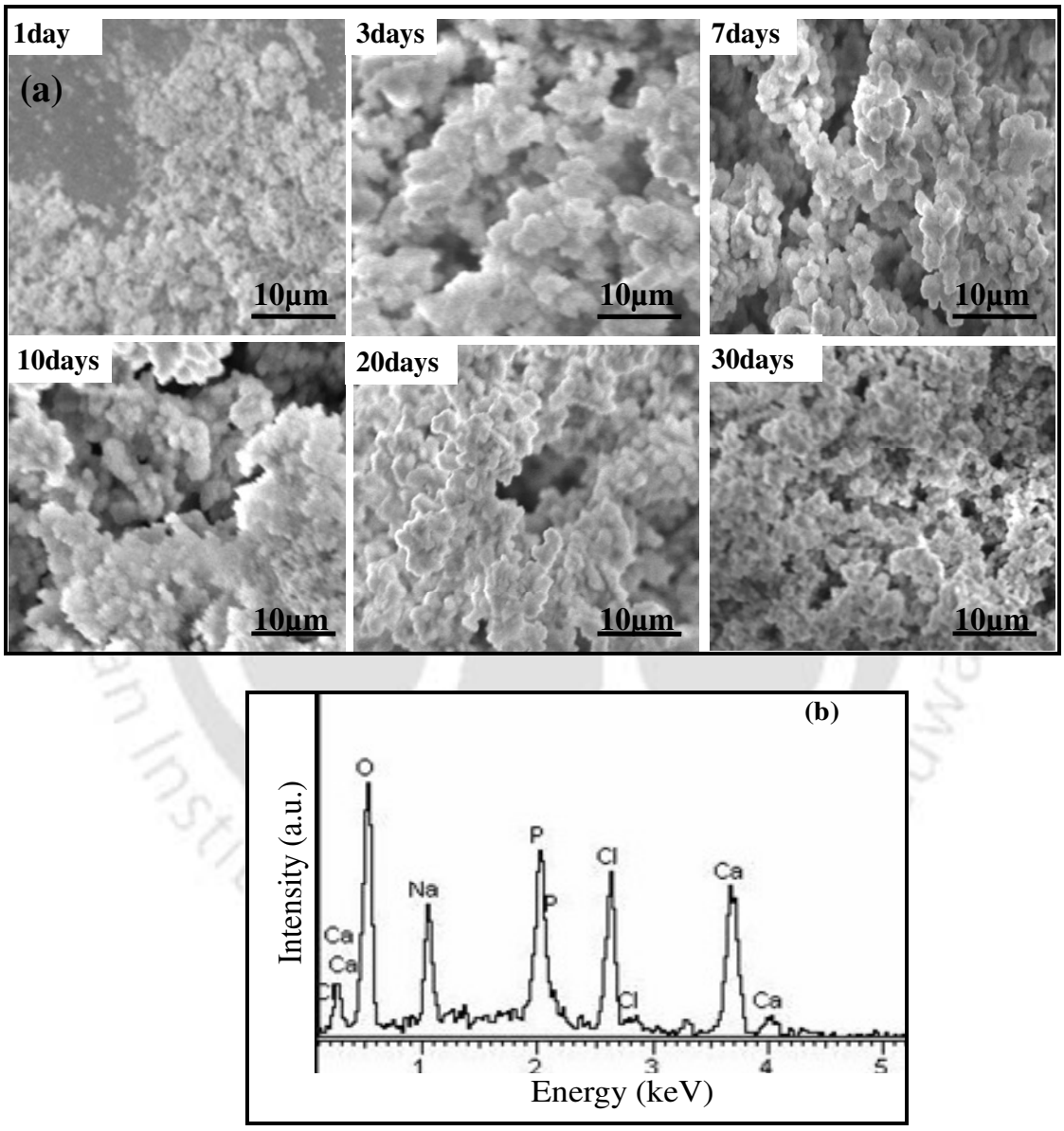

Fig.4.3.5.3: (a) SEM micrographs of glass-ceramic sample with x = 15 soaked in SBF (Magnification: 1000×) and (b) EDS spectra of the specimen soaked in SBF for 30 days.

The micrographs provide visual evidence of the formation of a surface layer on the bioglass-ceramics, which can now be presumed to be an apatite layer. After 30 days of immersion, the whole surface of the specimen is covered with spherical Ca-P particulate apatite layer. Results from EDS analysis reveal the gradual development of hydroxycarbonate apatite on the surface of glass-ceramics samples after immersion for various time periods in SBF. The spherical particles in the sample treated in SBF for 30 days are made up of calcium and phosphorus and the Ca/P molar ratio (calculated from EDS analysis) was of ~1.67, corresponding to the value in HA. Microanalysis of the precipitates reveals the presence of small quantities of Na and Cl as shown in the EDS spectra in Fig. 4.3.5.3 (b). This finding is in agreement with reports which claim that the growth of HA in SBF is accompanied by the incorporation of sodium, magnesium and chlorine ions [192] as well. It may thus be concluded that the surface layer contains carbonate, sodium, magnesium and chlorine substituted hydroxyapatite [193].

4.4. Summary

The salient features of the studies on $4.5MgO(45\text{-}x)CaO34SiO_2 16P_2O_5\ 0.5CaF_2 xFe_2O_3$ glasses are as follows:

1. Good quality glasses could be obtained in $4.5MgO(45\text{-}x)CaO34SiO_2 16P_2O_5\ 0.5CaF_2\ xFe_2O_3$ system with x up to 20 wt. %.

2. Hydroxyapatite, wollastanite, akermanite and magnetite crystallized in all glass compositions when heated to 1050 °C. Akermanite was developed in glass-ceramics with higher Fe_2O_3 content.

3. Addition of iron oxide increased the density and VHN of the glasses.

4. In compositions with low x, the iron sites are populated randomly in the glass, whereas in glasses $x > 10$ wt. %, the site population deviates from randomness and results in the formation of clusters. These result in superexchange type magnetic interactions between the iron ions in these glasses which are predominantly anti-ferromagnetically coupled.

5. While x_1 (wt. % $Fe_2^{3+}O_3$) and x_2 (wt. % $Fe_2^{2+}O_3$) values showed an increasing trend up to 10 wt. % Fe_2O_3, x_1 decreases in glasses with $x > 10$ wt. % Fe_2O_3. All glasses were paramagnetic at room temperature.

6. Bioactivity of this series of glasses increased as the iron oxide content is increased.

7. GI-XRD and FT-IR studies on SBF surfaces revealed the evolution of the HCA layer on the surface of the glass treated with SBF. EDS analysis showed that the Ca/P ratio of samples immersed in SBF for 30 days reach the value of 1.67 (value in HA).

The salient features of the studies on glass-ceramics derived from the parent glass compositons $4.5MgO(45\text{-}x)CaO34SiO_2 16P_2O_5\ 0.5CaF_2 x Fe_2O_3$ are listed below.

1. Hydroxyapatite and wollastonite are the major biocompatible crystalline phases developed in all the glass-ceramic samples. An additional phase which was identified as akermanite developed in glass-ceramics with higher Fe_2O_3 content. Nanocrystalline magnetite phase was present in all the glass-ceramic samples containing iron oxide.

2. VHN increased with increase in iron oxide content. MgO based glass-ceramic samples exhibited higher microhardness when compared to the CaO based glass-

ceramics samples. This feature can be attributed to the presence of akermanite ($Ca_2MgSi_2O_7$) in these glass-ceramics, which increases the strength of these glass ceramics. This MgO system could offer high strength magnetic bioglass and glass-ceramics suitable for load-bearing applications.

3. An increase in ferrimagnetically coupled superexchange type interactions with increase in iron oxide content has been inferred from EPR studies on the glass-ceramic samples. Samples with x = 5 and 10 wt. % Fe_2O_3 exhibit a combination of paramagnetic and ferrimagnetic behaviour.

4. The evolution of magnetic properties in the glass-ceramic samples as a function of iron oxide concentration is correlated with the amount of magnetite phase present in them. The area under the hysteresis loop increased with increasing iron oxide content. This showed that these bio-glass ceramics could be useful in the localized hyperthermia treatment of cancer.

5. Bioactivity of the glass-ceramics samples increases with increase in iron oxide content. Thus, compositions with higher iron oxide content contain higher amounts of bone mineral phases as well as the magnetic phase in this series of glass-ceramics.

6. HCA layer evolves on the surface of the glass-ceramic samples treated with SBF. Ca/P ratio of samples immersed in SBF for 30 days reached the value in HA.

7. These studies showed that these ferrimagnetic bioglass-ceramics can be used in hyperthermia applications.

Chapter 5

Investigations on ZnO-Fe_2O_3-SiO_2-CaO-P_2O_5-Na_2O glass and glass-ceramics

A systematic study of ZnO-Fe_2O_3-SiO_2-CaO-P_2O_5-Na_2O glasses by varying the zinc-iron oxide content and the glass-ceramics derived from them is presented in this chapter. Physical properties and *in vitro* bioactivity test have been performed on these glasses and glass-ceramic samples.

5.1. Preparation of glasses and glass-ceramics

$x(ZnO, Fe_2O_3)(65\text{-}x)SiO_2 20(CaO, P_2O_5)15Na_2O$ (x = 6, 9, 12, 15, 18 and 21 mole %) glasses were prepared by melt quenching technique. The Ca/P and Fe/Zn molar ratios were maintained at 1.67 and 6.5, respectively, in all the glass compositions. The reason for the choice of Ca/P molar ratio is obvious since it is the ratio in the mineral phase of human bone. When crystallized, solid solutions of $Zn_xFe_{1-x}(Fe_{1-x}Fe_{1+x})O_4$ (which is basically $Zn_xFe_{3-x}O_4$) and $Zn_{0.4}Fe_{2.6}O_4$ (x = 0.4) are expected to form. These two magnetic phases show higher saturation magnetization than Fe_3O_4 [137-138]. Therefore, glass-

ceramics containing $Zn_{0.4}Fe_{2.6}O_4$ (obtained by maintaining Fe/Zn molar ratio of 6.5) is expected to give higher heat generation for the same applied magnetic field as compared to the other two systems. We expect this to be an improvement over the other two glass-ceramics systems studied in this thesis. For preparing the base glasses, appropriately weighed quantities of high purity ZnO (99.9 % pure), SiO_2 (99.9 % pure), $Na_2CO_3H_2O$ (99.9 % pure), Fe_2O_3 (99.9 % pure), $CaCO_3$ (99.9 % pure) and $NH_4(H_2PO_4)$ (99.9 % pure) were thoroughly mixed in an agate pestle and mortar. The charge taken in a platinum crucible was calcined at 800 °C for 24 hours and then held at 1350 °C for 2 hours to completely melt the charge. The melts were poured between thick copper blocks held at room temperature and pressed into a plate of 2-3 mm thickness to form glass samples. The as-quenched glasses were annealed at 350 °C (well below their glass transition temperature) for 10 hours in air atmosphere to remove residual stresses. These heat-treated samples were used for all measurements. The glass plates obtained by the method described above were placed on alumina plates and heat-treated at 800°C for 1h and slowly cooled to room temperature to form glass-ceramic samples.

5.2. Characterization of the glasses

Systematic characterization of the glass samples carried out are discussed below:

5.2.1. XRD studies

A typical XRD pattern of a ZnO-Fe_2O_3-SiO_2-CaO-P_2O_5-Na_2O glass composition is shown in Fig. 5.2.1. The XRD patterns of all the glass samples were devoid of any sharp peak, signifying the amorphous character of the samples.

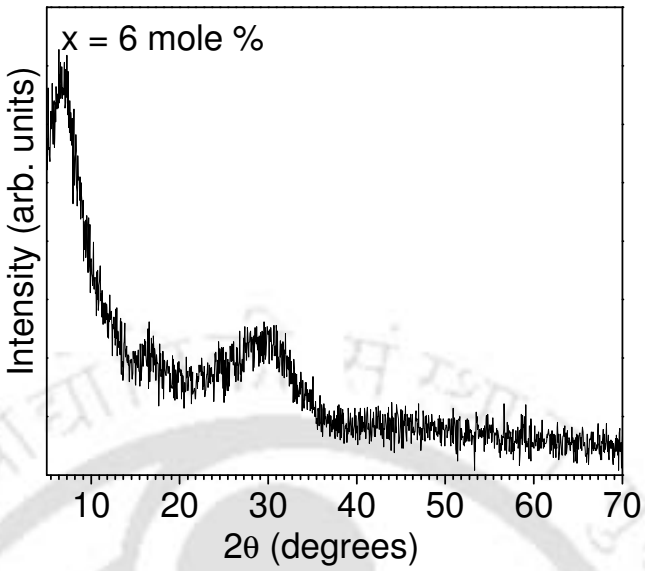

Fig. 5.2.1: XRD pattern of a typical ZnO-Fe_2O_3-SiO_2-CaO-P_2O_5-Na_2O glass.

5.2.2. DSC studies

DSC studies on x(ZnO, Fe_2O_3)(65-x)$SiO_2$20(CaO, P_2O_5)15Na_2O glasses with x = 6, 9, 12, 15, 18, 21 mole % have been performed. Fig. 5.2.2 shows the DSC curves obtained for x(ZnO, Fe_2O_3)(65-x) SiO_2 20(CaO, P_2O_5)15Na_2O glasses with x = 6 mole % zinc-iron oxide under a constant heating rate of 20 °C/min. The DSC curves exhibited a glass transition temperature marked by a distinct endothermic baseline shift within the temperature range 560 to 500 °C and crystallization temperature range 625 to 580°C under a constant heating rate of 20 °C/min with varied composition. It can be seen from the DSC curve that in the glass power compact calcium sodium phosphate crystals are precipitated at 625 to 580 °C as a function of increasing x (zinc-iron oxide content). T_g and T_c's decrease as a function of increasing x (zinc-iron oxide content). The T_g of these glasses decreased as the zinc-iron oxide content was increased (Table 5.2.2). The T_g

values shown in Table 5.2.2 correspond to a constant heating rate of 20 ^oC/min. The glass transition temperature (T_g) of these glasses decreases with an increase in zinc-iron oxide content. T_g continuously shifts to lower temperature as the zinc-iron content is increased. T_g value is closely related to the change in the coordination number of the network former oxides and the number of non-bridging oxygen present in the glasses. A decrease in the number of non-bridging oxygen in these glasses with the addition of ZnO-Fe_2O_3 results in the depolarization of the glass skeleton. It is well known that an increase in the degree of bridging increases T_g [149]. Hence the decrease in T_g as a function of ZnO-Fe_2O_3 concentration in the glasses is a result of the decrease in the depolymerization of the glass skeleton.

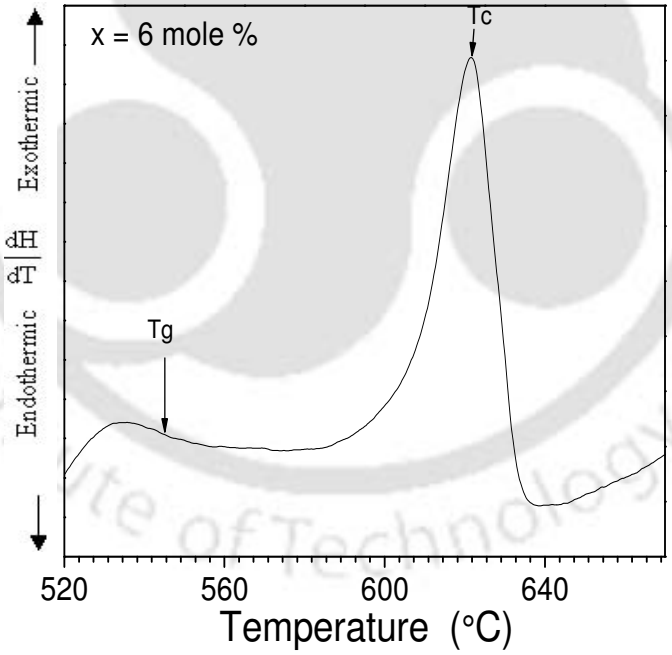

Fig. 5.3.2.1: Typical DSC curve obtained for x(ZnO, Fe_2O_3)(65-x)$SiO_2$20(CaO, P_2O_5) 15Na_2O glasses (x = 6 mole %) with constant heating rate 20 °C/min.

Table 5.2.2: DSC data of x(ZnO, Fe_2O_3)(65-x)$SiO_2$20(CaO, P_2O_5)15Na_2O glasses.

***x* mole %**	**T_g (°C)**	**T_c (°C)**
6	556	622
9	543	611
12	528	597
15	520	594
18	514	588
21	505	582

5.2.3. Density

Composition dependence of density and molar volume of x(ZnO, Fe_2O_3)(65-x)SiO_2 20(CaO, P_2O_5) 15Na_2O glasses are depicted in Fig. 5.2.3.

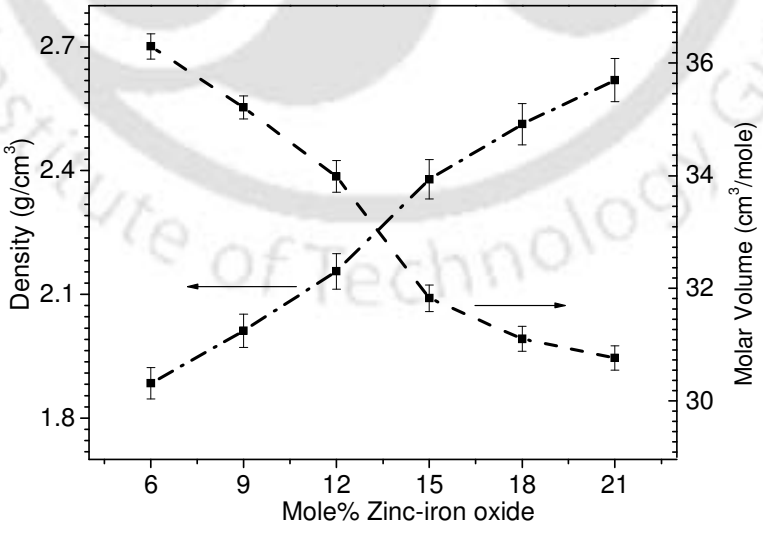

Fig. 5.2.3: Composition dependence of density and molar volume of ZnO glasses.

Density of the glass increases and molar volume decreases as zinc-iron oxide mole % content is increased. As the zinc-iron oxide content is increased, ZnO and Fe_2O_3 progressively replace SiO_2. Since the molecular weight of ZnO-Fe_2O_3 (81.38 + 159.697) is higher than the molecular weight of SiO_2 (60.088), one would expect the overall density of the glass to increase. The increase in the density of the glasses from 1.884 to 2.619 g/cm^3 (Table 5.2.3) with increasing zinc-iron oxide content is due to the strengthening of cross-linking within glass network as the volumetric portion of the four-coordinated Fe ion increases at the cost of the six-coordinated Fe [150].

Table 5.2.3: Density, molar volume and microhardness of $x(ZnO, Fe_2O_3)(65\text{-}x)SiO_2$ $20(CaO, P_2O_5)$ $15Na_2O$ glasses.

***x* mole %**	**Density (gm/cm^3)**	**Mol.vol. (cm^3/mol)**	**VHN (kg mm^{-2})**
6	1.884	36.294	447
9	2.012	35.211	466
12	2.156	33.987	511
15	2.379	31.826	545
18	2.512	31.103	584
21	2.619	30.765	630

Molar volume decreases with increasing ZnO-Fe_2O_3 content, which shows that the glassy network shrinks in size. A decrease in the molar volume can be observed with

an increase in zinc-iron oxide concentration. The decrease in the molar volume of the samples can be attributed to the increase in the probability of formation of FeO_4 group in glass, resulting from a decrease in the number of non-bridging oxygens [150]. The decrease in molar volume in glasses may thus be attributed to the formation of a closed packed structure due to the change of the coordination of iron ions to the four-fold coordination.

5.2.4. Microhardness

Microhardness of x(ZnO, Fe_2O_3)(65-x)$SiO_2$20(CaO, P_2O_5)15Na_2O glasses has been measured following the procedure outlined in second chapter. All samples were uniformly subjected a load of 100 gm for a duration of 15 s. The measured microhardness values are tabulated in Table 5.2.3.

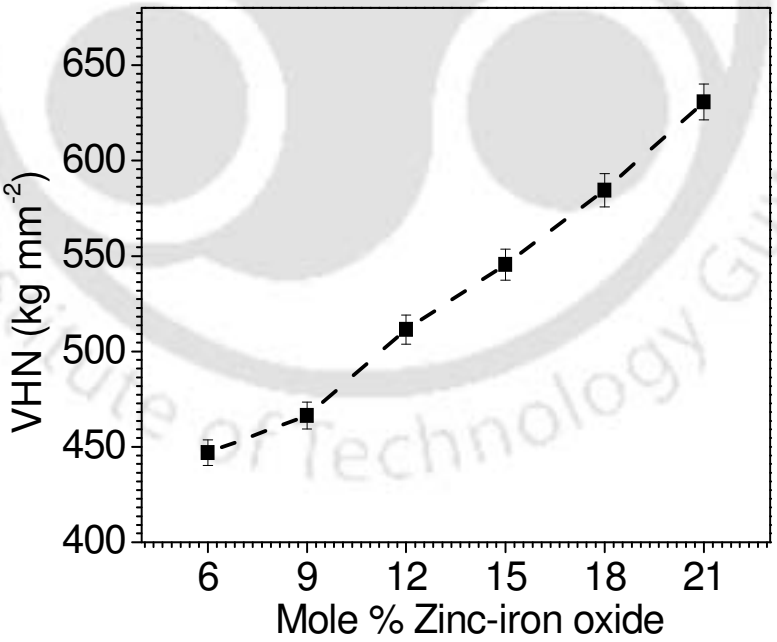

Fig. 5.2.4: Composition dependence of VHN of x(ZnO, Fe_2O_3) (65-x)SiO_2 20(CaO, P_2O_5) 15Na_2O glasses.

Fig. 5.2.4 shows the variation of VHN with zinc-iron oxide content in the glasses. It shows that the VHN increases as the zinc-iron oxide content is increased. As discussed in the case of other glasses, one can try to understand the composition dependence of VHN based on the number of non-bridging oxygen (NBO) in the glass. With an increase in more zinc-iron oxide content, the number of NBO decreases. As the number of NBO decreases, the bulk (*B*) and shear (*G*) elastic moduli of the glass increase [145]. From equation (2.9) it is obvious that an increase in the elastic moduli increases the microhardness, which the behaviour exhibited by the *x*(ZnO, Fe_2O_3) (65-*x*)SiO_2 20(CaO, P_2O_5) 15Na_2O depicted in Fig. 5.2.4.

5.2.5. EPR studies

EPR absorption spectra were obtained to understand the local environments and valence state of Fe ions in glasses at room temperature. EPR spectra of Fe^{3+} ions in oxide glasses have already been discussed in chapter 3. EPR absorption spectra of *x*(ZnO, Fe_2O_3) (65-*x*)SiO_2 20(CaO, P_2O_5) 15Na_2O ($6 \leq x \leq 21$ mole %) samples recorded at room temperature are shown in Fig. 5.2.5.1. The resonance absorptions observed at g ≈ 2.1 and g ≈ 4.3 are due to Fe^{3+} ions ($3d^5 {}^6S_{5/2}$). Since the Fe / Zn molar ratio is maintained at 6.5 in all samples, Fe_2O_3 (as well as ZnO content) increases as *x* is increased. Since the EPR spectra a due to Fe^{3+} ions, one need to focus on the Fe_2O_3 concentration and afford to ignore the ZnO concentration in this analysis. The variations of EPR intensity and linewidths are plotted in Fig. 5.2.5.2 and Fig. 5.2.5.3 for the resonance lines centred at g ≈ 2.1 and g ≈ 4.3, respectively. It can be seen from Fig. 5.2.5.1 that the peak to peak height (*I*) decreases with an increase in zinc-iron oxide concentration and the linewidth of the g ≈ 4.3

resonance line increases within in a short concentration range $6 < x < 9$ mole % zinc-iron oxide, decreases sharply for samples with $x > 9$ mole % zinc-iron oxide content. The overall intensity of the absorption line $J_{g \approx 4.3}$ increases in glasses with $6 < x < 9$ mole% zinc-iron oxide and then decreases as depicted in Fig. 5.2.5.3

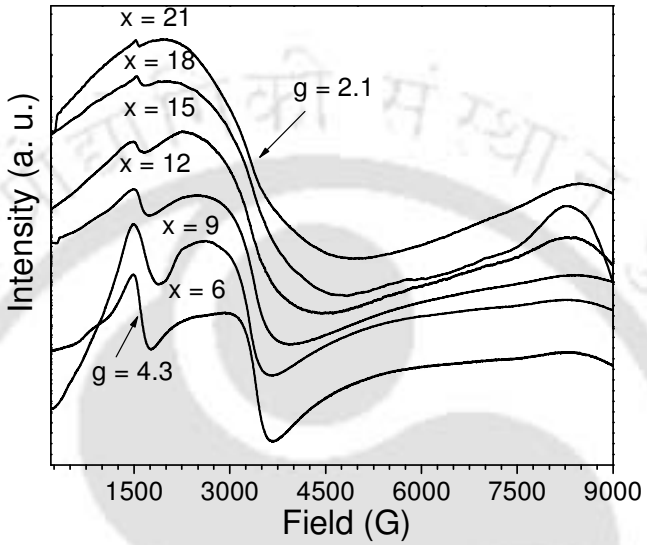

Fig. 5.2.5.1: EPR absorption spectra of $x(ZnO, Fe_2O_3)$ $(65\text{-}x)SiO_2$ $20(CaO, P_2O_5)$ $15Na_2O$ glasses.

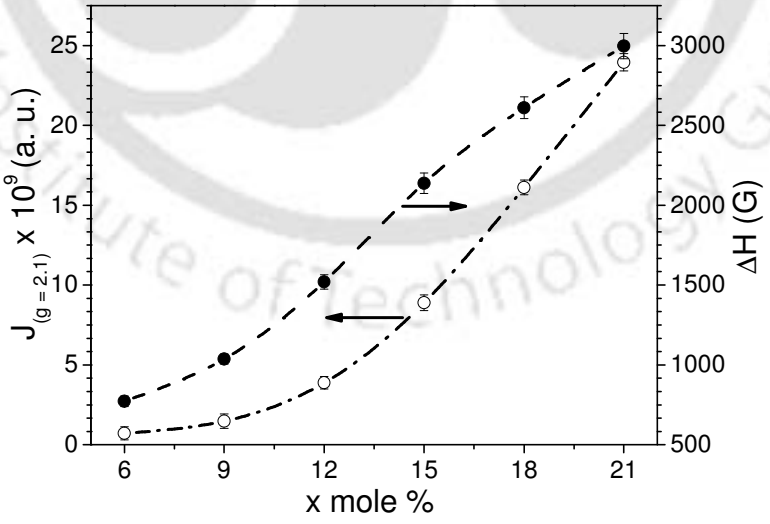

Fig. 5.2.5.2: Composition dependence of the line intensity and linewidth of g ≈ 2.1 resonance absorption line of $x(ZnO, Fe_2O_3)$ $(65\text{-}x)SiO_2$ $20(CaO, P_2O_5)$ $15Na_2O$ glasses.

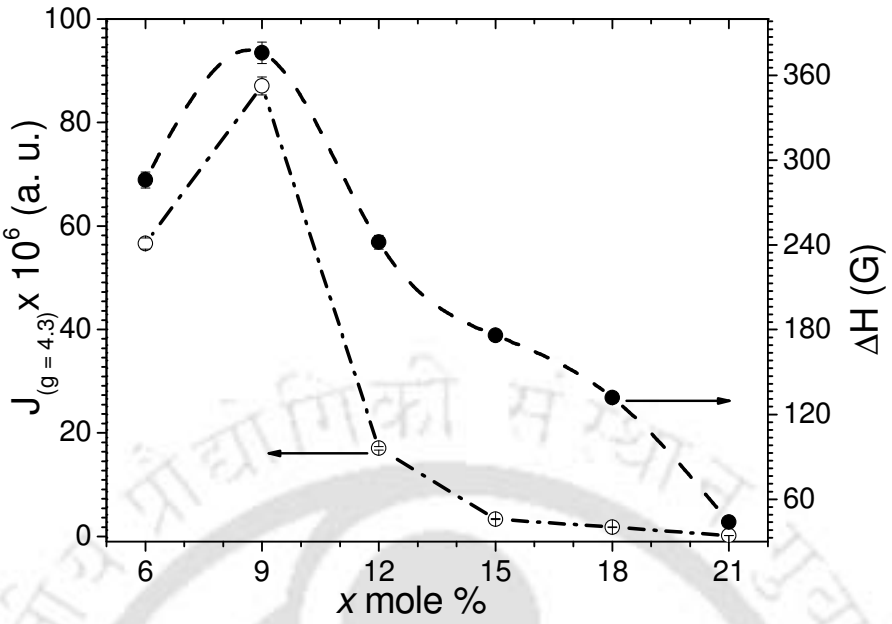

Fig. 5.2.5.3: Composition dependence of the line intensity and linewidth of g ≈ 4.3 resonance absorption line of $x(ZnO, Fe_2O_3)$ $(65\text{-}x)SiO_2$ $20(CaO, P_2O_5)$ $15Na_2O$ glasses.

The overall intensity of the absorption line $J_{g \approx 2.1}$ shows an increasing trend as the zinc-iron oxide content is increased as depicted in Fig. 5.2.5.2. The absorption line centered at g ≈ 2.1 is due to the isolated Fe^{3+} ions in a slightly distorted structural unit in samples with low zinc-iron oxide content and a consequence of clustered formations of the iron ions at higher zinc-iron oxide concentrations. The linewidth of the g ≈ 2.1 resonance absorption depends also on zinc-iron oxide concentration. The g ≈ 2.1 resonance arises due to the formation of iron clusters which give rise to superexchange type interaction between iron ions. The superexchange interaction between the nearest neighbours (which increases with zinc-iron oxide content due to their increased proximity), acts as narrowing mechanism of the absorption line. This narrowing process is countered by other broadening processes such as increase in network disordering and interaction between multivalent iron ions (*i.e.*, Fe^{2+} and Fe^{3+}). The final linewidth depends

on the relative strengths of the two mechanisms influencing the linewidth. The increase in the linewidth of the g ≈ 2.1 line with zinc-iron oxide concentrations shows the dominance of the broadening mechanisms which in turns indicates a larger increase in Fe^{2+} ion concentration as zinc-iron oxide concentration is increased in the glass.

The g ≈ 4.3 absorption lines can be produced by low symmetry (rhombic) sites of either tetrahedral or octahedral coordination. The behaviour depicted in Fig. 5.2.5.3 shows that the concentration of Fe^{3+} ions in octahedral (tetrahedral) environments increases in the composition range of $6 < x < 9$. The slow increase in the g ≈ 4.3 line intensities at low zinc-iron oxide concentrations indicates that fewer Fe^{3+} ions reside in low symmetry sites at these compositions. The decrease in g ≈ 4.3 line intensity beyond x = 9 mole % content is due to the destruction of the configuration from the iron ions neighbourhood, which assures their magnetic isolation. The structural units of defined symmetry involving Fe^{3+} ions although randomly distorted, have at the origin the structure of glass matrix former Ca^{2+} and Si^{4+}. One can observe that the decrease in the intensity of the signal at g ≈ 4.3 is accompanied by the appearance of a broad signal centered at g ≈ 2.1. The latter could be attributed to the formation of clusters of paramagnetic ions containing two or more ions coupled together.

It can also be seen from Fig. 5.2.5.3 that the linewidth of the g ≈ 4.3 resonance line increases within in a short concentration range $6 < x < 9$ mole % zinc-iron oxide concentrations, decreases suddenly for samples with $x > 9$ mole % zinc-iron oxide content. The decreasing of line width is due to the progressive decrease of the concentration of Fe^{3+} ions in structural vicinities giving rise to the g ≈ 4.3 absorption. The failure of absorption at g ≈ 4.3 reflects changes of the matrix structure when the

concentration of zinc-iron ions rises. We can observe from Fig. 5.2.5.1that as zinc-iron oxide content is increased beyond 9 mole %, the signal at g ≈ 4.3 begins to disappear and a broad signal centered at g ≈ 2.1 starts developing. The decrease in intensity of the signal centred at g ≈ 4.3 for glasses with $x > 9$ mole % may be due to the formation of clusters of paramagnetic ions. The increase in intensity of the g ≈ 2.1 resonance line as a function of zinc-iron oxide concentration lends support to this conclusion.

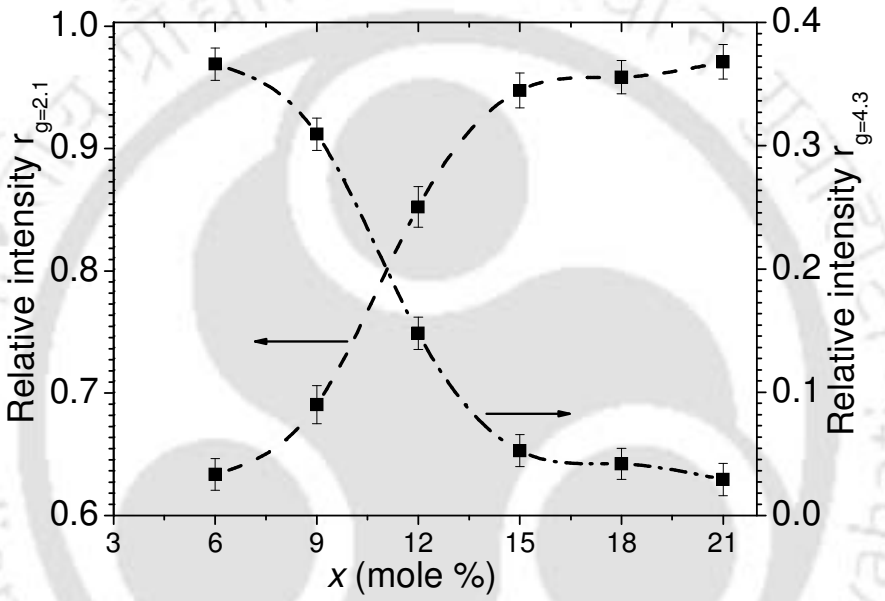

Fig. 5.2.5.4: Variation of relative intensities $r_{g \approx 4.3}$ and $r_{g \approx 2.1}$ as a function of x concentration in various glass compositions.

Variations in the relative intensities of the two lines, $r_{g \approx 4.3} = I_{g \approx 4.3} / (I_{g \approx 4.3} + I_{g \approx 2.1})$ and $r_{g \approx 2.1} = I_{g \approx 2.1} / (I_{g \approx 4.3} + I_{g \approx 2.1})$ as a function of zinc-iron oxide content for the glasses are plotted in Fig. 5.2.5.4, where $I_{g \approx 4.3}$ and $I_{g \approx 2.1}$ denote intensities at g ≈ 4.3 and g ≈ 2.1, respectively. The relative intensity $r_{g \approx 2.1}$ increases with increase in zinc-iron oxide content, while the relative intensity $r_{g \approx 4.3}$ decreases rapidly with increase in zinc-iron oxide content. It can also be seen from Fig. 5.2.5.2 that the intensity of g ≈ 2.1 resonance

line increases with Fe^{3+} ions concentration. Hence, it can be concluded that at lower concentrations, iron sites are populated randomly in the glass, while at higher zinc-iron concentrations (*i.e.*, in glasses with $x > 9$ mole %) the site population deviates from randomness and results in the formation of clusters. When the site population deviates from randomness at higher iron (*i.e.*, for $x > 9$ mole %) concentrations, superexchange type interactions begin to dominate.

5.2.6. Magnetic susceptibility

Inverse of magnetic susceptibility (χ^{-1}) versus temperature plots for various glass compositions are shown in Fig. 5.2.6.1. Temperature dependence of the reciprocal of magnetic susceptibility of paramagnetic materials shows a Curie-Weiss type behavior expressed by equation (2.10). The straight lines in Fig. 5.2.6.1 represent the least squares fit to equation (2.10). The negative paramagnetic Curie temperature calculated for the glasses (*cf.* Fig. 5.2.6.2 and Table 5.2.6) indicates superexchange magnetic interactions between the iron ions in the glass which are predominantly anti-ferromagnetically coupled. In these glasses, the presence of both Fe^{2+} and of Fe^{3+} ions was evidenced. The superexchange interaction of the iron ions in oxide glasses has been mostly attributed to an antiferromagnetic coupling within Fe^{3+}-Fe^{2+}, Fe^{3+}-Fe^{3+} and Fe^{2+}-Fe^{2+} pairs [163, 199]. An antiferromagnetic coupling between iron ions was reported in Phosphate [164-166], silicate [171, 175, 199], tellurite [164] and bismuthate [161-162] oxide glasses.

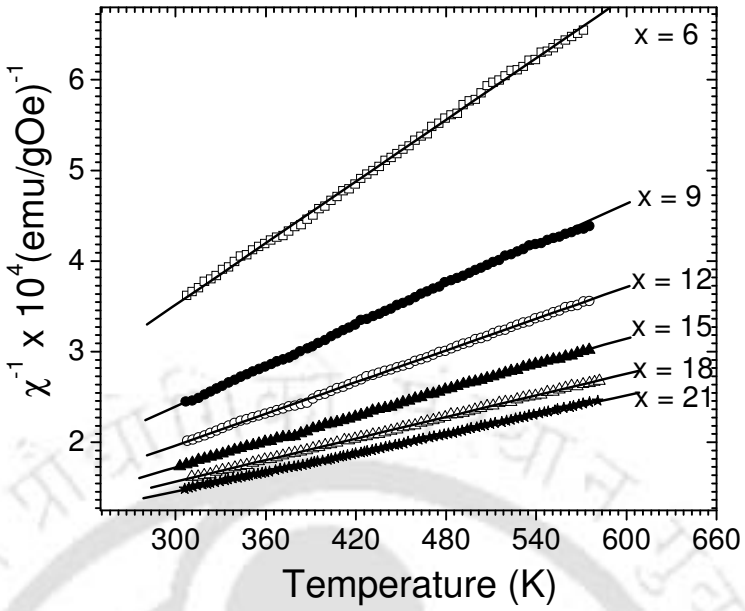

Fig. 5.2.6.1: Temperature dependence of the inverse magnetic susceptibility of *x*(ZnO, Fe_2O_3)(65-*x*)SiO_2 20(CaO, P_2O_5) 15Na_2O glasses.

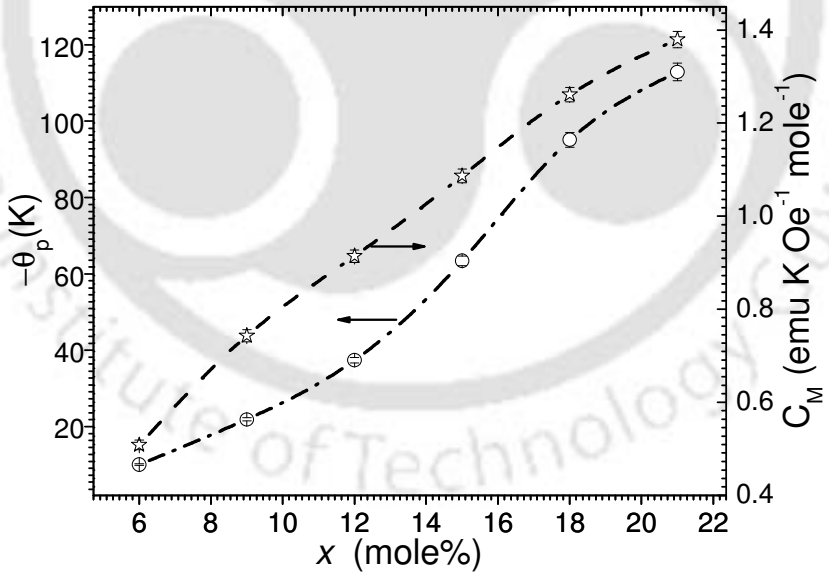

Fig. 5.2.6.2: The composition dependence of the paramagnetic Curie temperature and the Curie constant of *x*(ZnO, Fe_2O_3) (65-*x*)SiO_2 20(CaO, P_2O_5) 15Na_2O glasses.

The magnetic behavior of the glasses can be described by the micromagnetic type behavior [176] as done with the Cao and MgO based glasses. The absolute magnitude of θ_p values increases with increase in zinc-iron oxide content in the glasses (Fig. 5.2.6.2). The value of the exchange integral increases as iron ions concentration is increased in the glass and as a result the magnitude of θ_p increases. Composition dependence of the of the Curie constant (C_M) are presented in the right hand side axis of Fig. 5.2.6.2. C_M values increase with zinc-iron oxide concentration. The composition dependence of the C_M and effective magnetic moment (μ_{exp}) is present in Table 5.2.6.

Table 5.2.6: Curie constant (C_M), paramagnetic Curie temperature (θ_p). experimental magnetic moment μ_{exp}, weight fractions of Fe^{3+} (x_1) and Fe^{2+} (x_2) ions, and relative concentration of Fe^{2+} ion in $x(ZnO, Fe_2O_3)$ $(65\text{-}x)SiO_2$ $20(CaO, P_2O_5)15Na_2O$ glasses.

x (mol %)	$C_M \pm 1\times10^{-4}$ (emuKOe^{-1}mol^{-1})	μ_{exp} $\pm1\times10^{-2}(\mu_B)$	$x_1 \pm 1\times 10^{-2}$ (mol % $Fe_2^{3+}O$)	$x_2 \pm 1\times 10^{-2}$ (mol % $Fe_2^{2+}O_3$)	$x_2/(x_1+x_2)$ $\pm 1\times 10^{-2}$
6	0.5084	5.82	5.36	0.64	0.11
9	0.7428	5.74	7.29	1.71	0.19
12	0.9141	5.52	7.02	4.98	0.42
15	1.0866	5.38	6.71	8.29	0.55
18	1.2612	5.29	6.48	11.52	0.64
21	1.3797	5.12	4.19	16.81	0.80

It is evident from Table 5.2.6 that iron is present as both Fe^{3+} and Fe^{2+} ions in the glasses. The mole fraction of Fe^{2+} and Fe^{3+}ions in the glasses were estimated using relations (3.2 and 3.3), following the procedure mentioned there, and the corresponding data are presented in Table 5.2.6. Comparison of x_1 (mole % Fe^{3+}) and x_2 (mole % Fe^{2+}) for various glass compositions shows that iron ions exist in both $Fe^{3+}$and Fe^{2+} valence states in all the glass compositions. While the x_1 and x_2 values show an increasing trend up to 9 mole % zinc-iron oxide, x_1 decreases in glasses with x > 9 mole % of zinc-iron oxide. The ratio of the number of ions in Fe^{2+} state (x_2) to the total number of ions (x_1+x_2) in various glass compositions is listed in Table 5.2.6. This shows that the relative domination of Fe^{3+} ions in glasses with lower concentrations of zinc-iron oxide is reduced as x is increased giving way to more and more Fe^{2+} ions at higher x values. The molar fraction of Fe^{2+} ions obtained from the intensity of the g ≈ 2.1 absorption line increases with an increase in x (Fig. 5.2.5.2). The molar fraction of Fe^{3+} ions as indicated by the intensity of the g ≈ 4.3 line (Fig. 5.2.5.3) shows a maximum for the glass composition with x = 9 mole %. μ_{exp} decreases from 5.82 (which is close to μ_{Fe}^{3+} value) for the glass with composition x = 6 mole % to 5.12 (which is close to μ_{Fe}^{2+} value) for the glass with x = 21 mole %. The magnetic data of the glasses can be understood on the basis of the relative concentration of the iron ions if one presumes the existence of Fe^{2+}-Fe^{2+}, Fe^{3+}-Fe^{3+} and Fe^{2+}-Fe^{3+} magnetic exchange pairs. Based on these two results, one can conclude that as x is increased in this series of glasses, the dominating magnetic exchange pairs change from Fe^{3+}-Fe^{3+} to Fe^{2+}-Fe^{3+} and ultimately to Fe^{2+}-Fe^{2+}.

5.2.7. *In vitro* bioactivity test of glass samples

In vitro bioactivity test was carried out by soaking the glass pieces in SBF, The procedure followed is explained in detail in chapter 2. Glass pieces with nominal compositions of $x(ZnO, Fe_2O_3)$ $(65\text{-}x)SiO_2$ $20(CaO, P_2O_5)$ $15Na_2O$ immersed in SBF were taken out after 1, 3, 7, 10, 20 and 30 days, and lightly washed with acetone. Surface structural changes of the glass samples treated in SBF were analyzed by GI-XRD, FT-IR spectroscopy and SEM techniques. The surface chemical analysis was carried out by EDS analysis.

5.2.7.1. GI-XRD studies of the glass samples soaked in SBF

Fig. 5.2.7.1(a) shows the typical GI-XRD patterns obtained from the surfaces of glasses before and after soaking in SBF for various time periods (i.e. 0, 1, 3, 7, 10, 20 and 30 days).

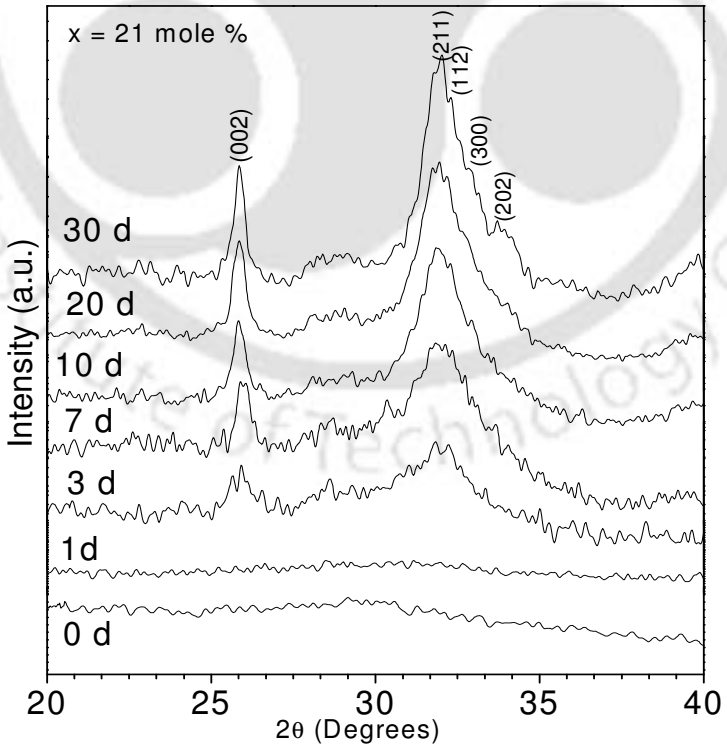

Fig. 5.2.7.1(a): GI-XRD patterns of glass sample x = 21 mole % soaked in SBF.

GI-XRD patterns of all untreated sample (designated as 0 d in Fig. 5.2.7.1(a)) is devoid of crystalline peaks, indicating the fresh amorphous surface of the samples. On immersion in SBF for a day or more, crystalline peaks appear in the GI-XRD patterns, indicating the formation of a crystalline layer on the surface of the glass. Just as in the case of CaO and MgO glasses, two well defined HA peaks at 2θ values of ~26° (002) and ~32° (211) develop in these glasses too after 3 days of soaking in SBF. The wide diffraction peak at 2θ ranging from 30˚ to 34˚ corresponds to the overlap of (112), (300) and (202) reflection of the well-crystallized HA. The GI-XRD patterns depicted in Fig. 5.2.7.1(a) show the preferential growth mechanism of the surface apatite layer. Formation of the hydroxyapatite layer over the glass surface shows that the glass samples are bioactive. The gradual growth in the intensity of the individual reflection, appearance of other low intensity apatite reflections and the narrowing of the peak width clearly show the evolution of the crystalline HA surface layer as a function of immersion time in SBF.

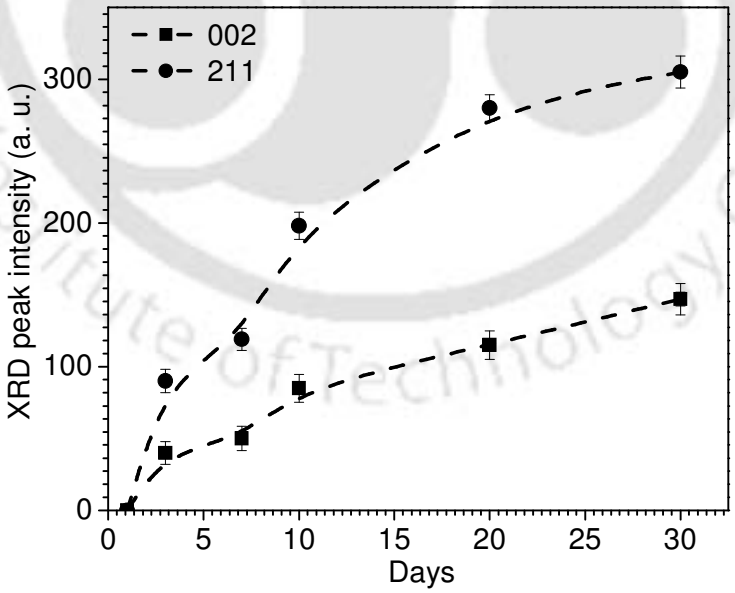

Fig. 5.2.7.1(b): GI-XRD intensity of (0 0 2) and (2 1 1) reflections from x = 21 mole % glass sample soaked in SBF for 3, 7, 10, 20 and 30 days.

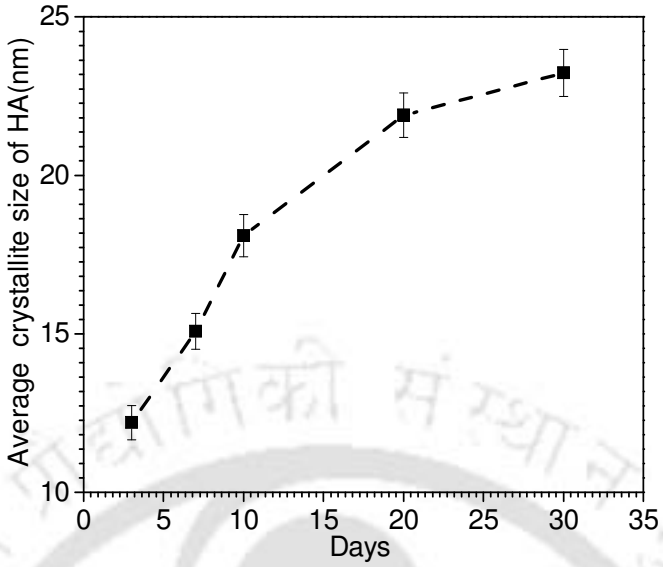

Fig. 5.2.7.1(c): Variation of averages size of HA crystalline (nm) with SBF soaking time. Data corresponds to the x = 21 mole % glass sample.

The intensity of two major reflections, *viz*., (002) and (211), increase {*cf*. Fig. 5.2.7.1(b)} with an increase in the concentration of Ca^{2+} and PO_4^{3-} ions on the surface of the glass immersed in SBF for various days. It is obvious that the intensity of the reflections attain saturated values within 20 days of immersion in SBF. The average crystallite size (d) in a direction perpendicular to the crystallographic plane can be estimated using the Scherrer`s formula equation (2.1) [139]. The average size of HA crystallised was calculated from the (002) reflection using equation (2.1). Fig. 5.2.7.1(c) reveals an increase in the average particle size of the crystalline surface layer on the glass immersed in SBF for various days, which is consistent with results of reported earlier. The crystallite size increases from about 12.2 ± 0.38 nm to 23.23 ± 0.65 nm in samples immersed for 3 days to 30 days. The size of HA crystalline depends on the rate of crystalline growth on the surface of the glass in the SBF in various days. The variation of

the crystallite size with immersion time shows a sharp increase in crystallite size in samples treated in SBF for 10 days, followed by a slower increase in crystallite size in samples treated in SBF for longer periods.

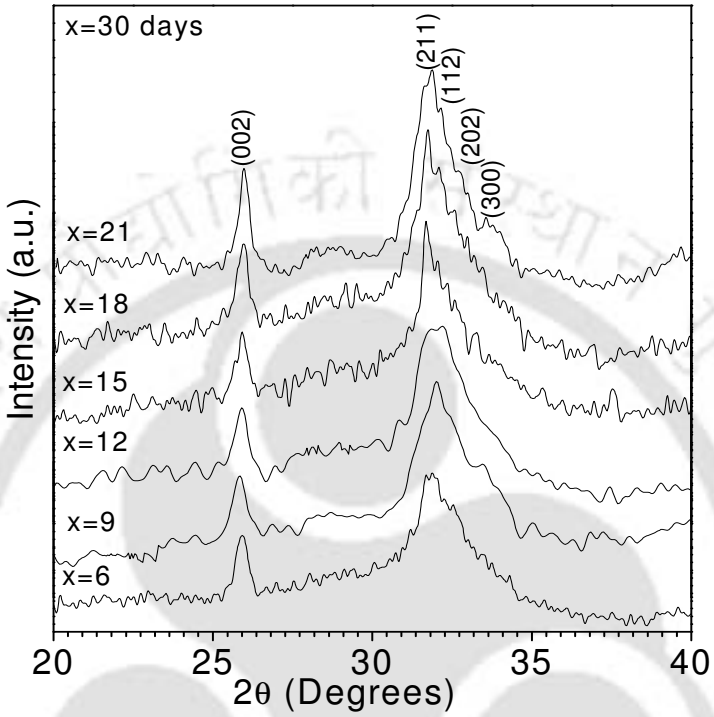

Fig. 5.2.7.1(d): GI-XRD patterns of various samples x = 6, 9, 12, 15, 18 and 21 mole % soaked in SBF for 30 days.

Fig. 5.2.7.1(d) shows the GI-XRD patterns obtained from the surfaces of glasses with x = 6, 9, 12, 15, 18 and 21 mole % zinc-iron oxide after treatment in SBF for 30 days. The HA peaks appearing between 2θ values of 30° to 34° sharpen in samples with higher x. Since the broad peaks signify the presence of small sized crystallites, one can infer that on immersion in SBF, the HA formation gradually improves from small sized crystalline aggregates to a well-crystallized HA phase as the amount of zinc-iron oxide is increased in the system. Formation of the HA layer over the glass surface shows

that the glass samples are bioactive. The relative intensity and peak width of the characteristic apatite reflections show considerable composition dependence. Balamurugan *et al*. [77] studied the bioactivity SiO_2–CaO–P_2O_5-ZnO system *in vitro* and *in vivo* and reported that incorporation of Zn into a bioglass does not diminish the bioactivity of such materials. Better apatite formation is observed in this series of glasses when the zinc-iron oxide content is increased, just as observed in the other two systems. This shows that replacing SiO_2 with ZnO + Fe_2O_3 over this selected composition range aids apatite growth on these glass surfaces.

5.2.7.2. FT-IR spectroscopy of the glass samples soaked in SBF

Fig. 5.2.7.2 (a) shows the infrared reflection spectra of the glass sample with x = 21 mole % zinc-iron oxide before and after the immersion in the simulated body fluid for 0, 1, 3, 7, 10, 20 and 30 days. The spectrum before the immersion reveals bands at 1038, 935, 773, 590 and 450 cm^{-1}. The peaks at 1038, 935, 773, 590 and 450 cm^{-1} correspond [188-190] to v_3 Si-O stretching [with one non bridging oxygen (NBO)], Si-O stretching [with 2 NBO], Si-O-Si stretching, v_4 P-O bending and v_4 Si-O-Si bending frequencies, respectively. After 1 day of immersion in SBF, new peaks appear at 860, 905, 1329 and 1556 cm^{-1}. The peak at 905 cm^{-1} corresponds to v_1 P-O-P stretching frequency, respectively. The band located at 860 cm^{-1} and the large bands at 1329 and 1556 cm^{-1} can be assigned to C-O vibration mode of CO_3^{2-}. These bands signify the incorporation of carbonate anions from the SBF in the apatite crystal lattice. After 3 days of immersion in SBF, the appearance of the band at 955 cm^{-1}, which is related to calcium phosphate (hydroxyapatite) surface layer is observed. The peak at 955 cm^{-1} corresponds to the v_1 P-

O symmetric stretching frequency. It indicates the obviation of phosphate ions from the ideal tetrahedral structure. After 3 days of immersion in SBF, the disappearance of the band at 1038 cm^{-1} is related to ν_3 Si-O stretching surface layer formation.

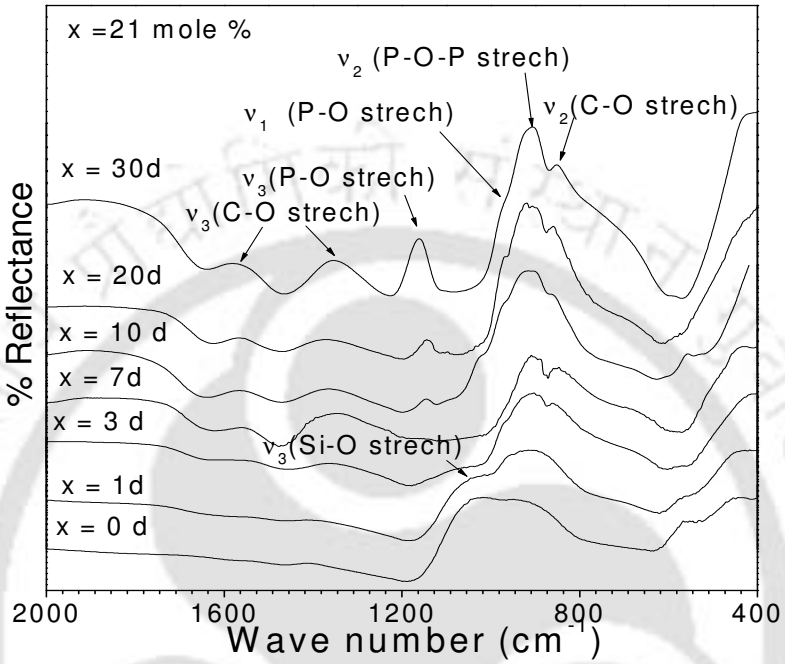

Fig. 5.2.7.2(a): FT-IR reflection spectra of surfaces of glass x = 21 mole % soaked in SBF for various days.

After 7 days of immersion in SBF, the appearance of the peak at 1155 cm^{-1} reflects the v_3 P-O stretching vibration of PO_4 unit. These bands (1155 and 905 cm^{-1}) sharpen and their relative intensities increase with increase in longer immersion times. These peaks are characteristic of apatite crystals. With further increase in immersion time, the intensity of the bands related to the CO_3^{2-} group increases. Carbonate ions occupy two different sites in carbonated apatite as indicated by peaks in the region of 1650 to 1300 cm^{-1} which are due to v_3 vibration mode, whereas the peak at 860 cm^{-1} is due to the v_2 vibration mode of carbonate ion [190]. The v_3 band splits into two peaks

centered at 1329 and 1556 cm^{-1}, respectively, with the distribution of the carbonate v_3 sites depending on the maturation and formation of apatite crystals. Occupancy of the v_2 sites is considered to occur competitively between the OH^{-1} and carbonate groups at the interface of growing crystal, whereas, occupancy of the v_3 sites depends on competition between the phosphate and carbonate ions [190]. Presence of v_2 and v_3 vibration modes of carbonate is the signature of the development of HCA layer on the surface of the sample.

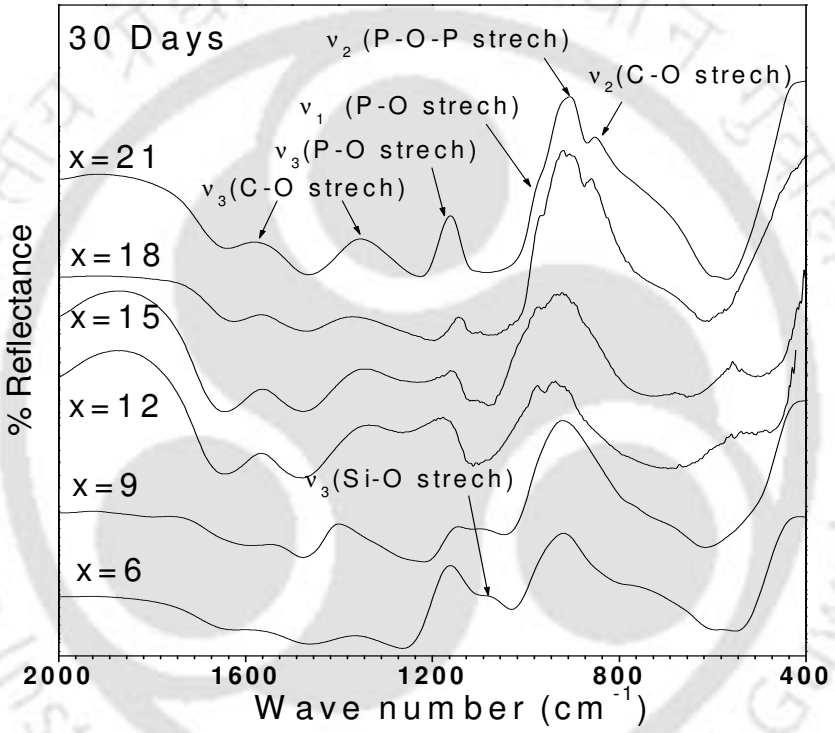

Fig. 5.2.7.2(b): FT-IR spectra from the surfaces of glasses soaked in SBF for 30 days.

Fig. 5.2.7.2(b) shows the infrared reflection spectra of glass-ceramics samples with x = 6, 9, 12, 15, 18 and 21 mole % zinc-iron oxide after the immersion in SBF for 30 days. Spectral bands of HA assigned to PO_4^{3-} groups (v_3–1155 cm^{-1}, v_1–955 cm^{-1}, v_1–905 cm^{-1} and v_2–590 cm^{-1}) and CO_3^{2-} functional groups (v_2–860 cm^{-1}, v_3–1329 $cm^{-1}$and v_3–1556 cm^{-1}) appear in the spectra. The band at 1038 cm^{-1} v_3 Si-O stretch disappears in the

samples with x = 15, 18 and 21 mole %. The peak at 905 cm^{-1} reflects the v_1 P-O-P stretching mode. These bands (1155, 860 and 905 cm^{-1}) sharpen and their relative intensities increase with increase in zinc-iron oxide content signifying the formation of a well crystallized HCA layer in these samples.

5.2.7.3. SEM-EDS studies of the glass samples soaked in SBF

Fig. 5.2.7.3(a) shows the SEM micrographs of the glass sample with x = 21 mole % zinc-iron oxide after immersion in SBF for 1, 3, 7, 10, 20 and 30 days, respectively. Microanalysis of the precipitates reveals the presence of small quantities of Na and Cl as shown in the EDS spectra in Fig. 5.2.7.3(b). This finding is in agreement with reports which claim that the growth of hydroxyapatite in SBF results in the incorporation of sodium, magnesium and chlorine [192-193] as well.

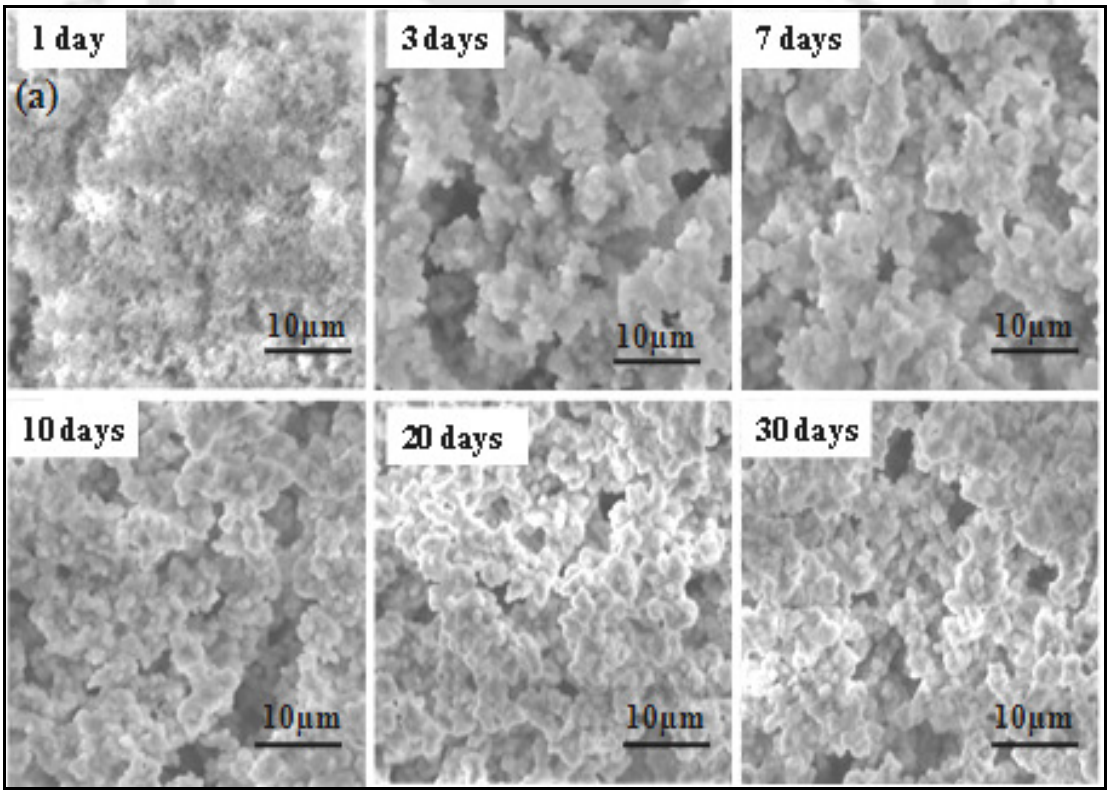

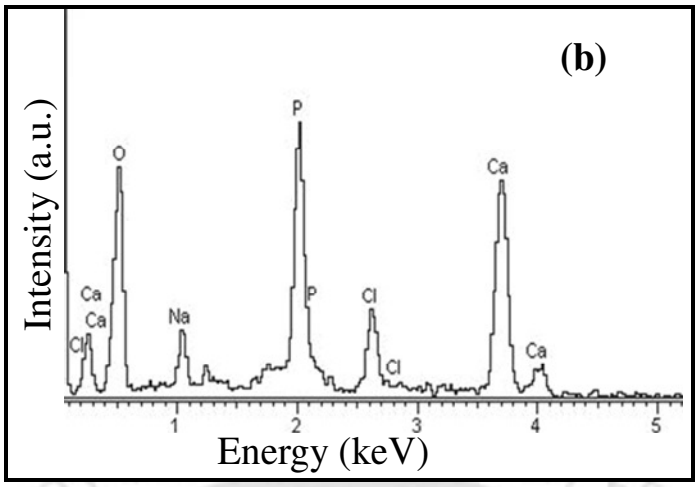

Fig. 5.2.7.3:(a) SEM micrographs (Magnification: 1000×) of x = 21 mole % glass soaked in SBF for various days, and (b) EDS spectra of the sample soaked in SBF for 30 days.

5.3. Characterization of glass-ceramics samples

5.3.1. XRD studies of glass-ceramics samples

Pieces of as-quenched glass were heat-treated at 800 °C for 1 hour in air to form the glass-ceramics. XRD patterns of the glass-ceramic samples are presented in Fig. 5.3.1.1. Indexing the XRD patterns revealed that $6 \leq x \leq 21$ mole % glasses revealed that calcium sodium phosphate ($NaCaPO_4$) [PDF # 76-1456] and zinc ferrite $ZnFe_2O_4$ [PDF # 82-1042] crystallized in all the heat-treated glass samples. Calcium sodium phosphate is a bone mineral and its presence indicates the biocompatible nature of the glass-ceramics.

The percentage of Calcium sodium phosphate was found to decrease in samples with increasing zinc-iron oxide concentration. The average crystallite size was calculated from the broadening of the primary zinc-ferrite peak [(311)] using Scherrer's equation (2.1). The average crystallite size d of $ZnFe_2O_4$, estimated ranged between 8 and 23 nm (± 0.56) (*cf.* table 5.3.4). The average crystallite size of the zinc ferrite phase increased in

the samples as the zinc-iron oxide concentration was increased from 6 to 21 mole % as depicted in Fig. 5.3.1.2.

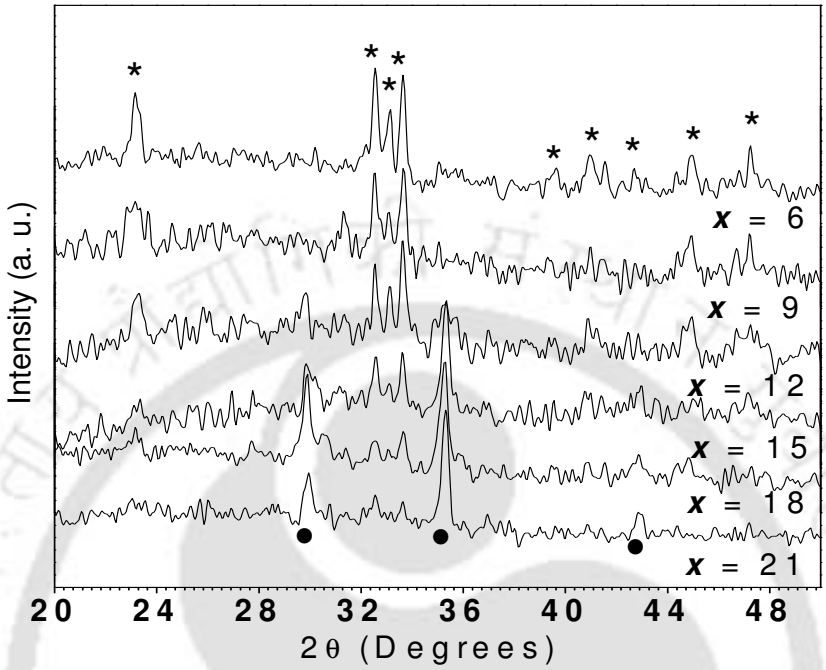

Fig. 5.3.1.1: XRD patterns of glass-ceramic samples. $NaCaPO_4$ (stars) and $ZnFe_2O_4$ (filled circles) crystallites were identified in all samples.

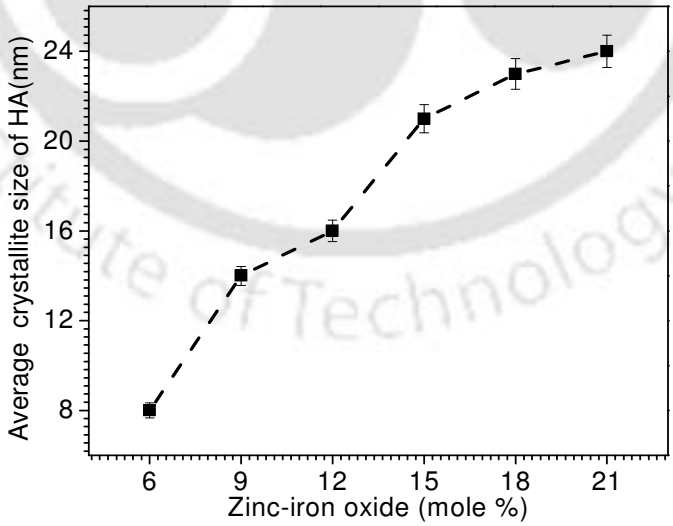

Fig. 5.3.1.2: Variation of average zinc ferrite crystallite size as a function of zinc-iron oxide concentration.

5.3.2. Microhardness studies of glass-ceramics samples

Microhardness of glass-ceramics was measured by applying a uniform load of 100 gm for a duration of 15 s. The measured microhardness values are tabulated in Table 5.3.4. Fig. 5.3.2 shows the variation of hardness value with the zinc-iron oxide mole % content in the x(ZnO, Fe_2O_3) (65-x)SiO_2 20(CaO, P_2O_5) 15Na_2O ($6 \leq x \leq 21$ mole %) glass-ceramics. The glass-ceramics samples show a higher VHN as compared to the corresponding parent glasses. VHN of the glass-ceramics samples increases linearly with zinc-iron oxide content as shown in Fig. 5.3.2 and Table 5.3.4. The presence of crystalline phases increases the VHN of the glass-ceramics. An increase in the VHN can then be interpreted as due to the increase in the percentage of the crystalline phases in the glass-ceramics as a function of zinc-iron oxide content. Thus addition of zinc-iron oxide increases the hardness of this series of samples.

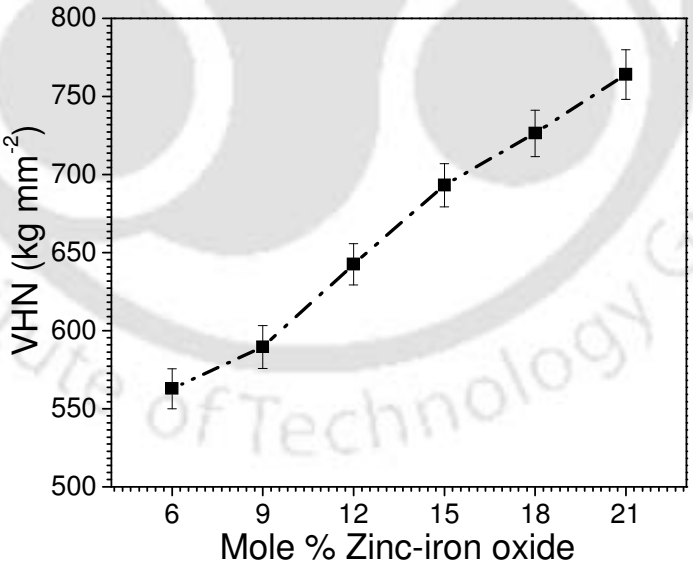

Fig. 5.3.2: Composition dependence of VHN of x(ZnO, Fe_2O_3) (65-x)SiO_2 20(CaO, P_2O_5) 15Na_2O glass-ceramics.

5.3.3. EPR studies of glass-ceramics samples

EPR absorption spectra of x(ZnO, Fe_2O_3) (65-x)SiO_2 20(CaO, P_2O_5) 15Na_2O ($6 \leq x \leq 21$ mole %) glass ceramics samples recorded at room temperature are shown in Fig. 5.3.3.1. It can be seen from Fig. 5.3.3.1 that there is a strong dependence of the structure of the absorption spectra of Fe^{3+} ($3d^5$, $^6S_{5/2}$) ions as a function of zinc-iron oxide content in the sample.

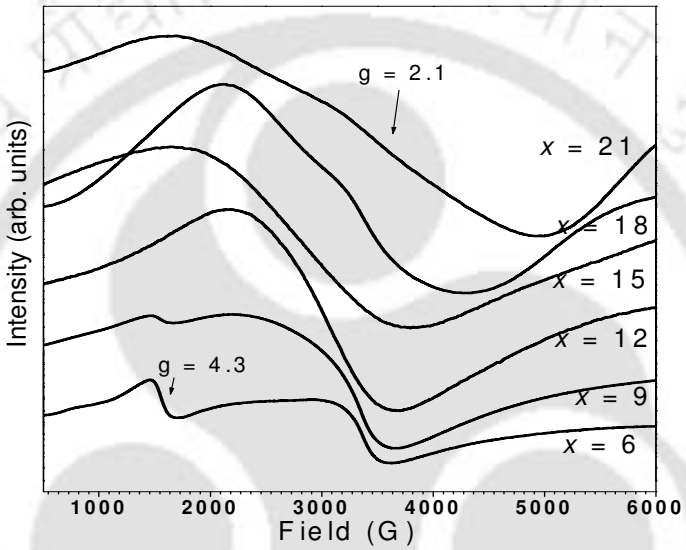

Fig. 5.3.3.1: EPR absorption spectra of x(ZnO, Fe_2O_3) (65-x)SiO_2 20(CaO, P_2O_5) 15Na_2O glass-ceramic samples.

The EPR parameters, *viz*., the line width (ΔH) and the intensity of absorption line J, corresponding to various glass-ceramics compositions were determined from the curves depicted in Fig. 5.3.3.2. It is apparent from Fig. 5.3.3.2 that the intensity [$J_{(g \approx 2.1)}$] and line width [$\Delta H_{(g \approx 2.1)}$] of the $g \approx 2.1$ absorption line increase as a function of x. The absorption line centred at $g \approx 2.1$ is due to the isolated Fe^{3+} in a slightly distorted structural unit in samples with low zinc-iron oxide content and to the clustered formations

of zinc-iron oxide for higher concentrations. The nonlinear increase of $J_{(g=2.1)}$ and $\Delta H_{(g=2.1)}$ with zinc-iron oxide concentration depicted in Fig. 5.3.3.2 shows that iron irons are present as Fe^{3+} as well as Fe^{2+} in the samples. The line width of the g ≈ 2.1 resonance absorption depends also on the zinc-iron oxide concentration.

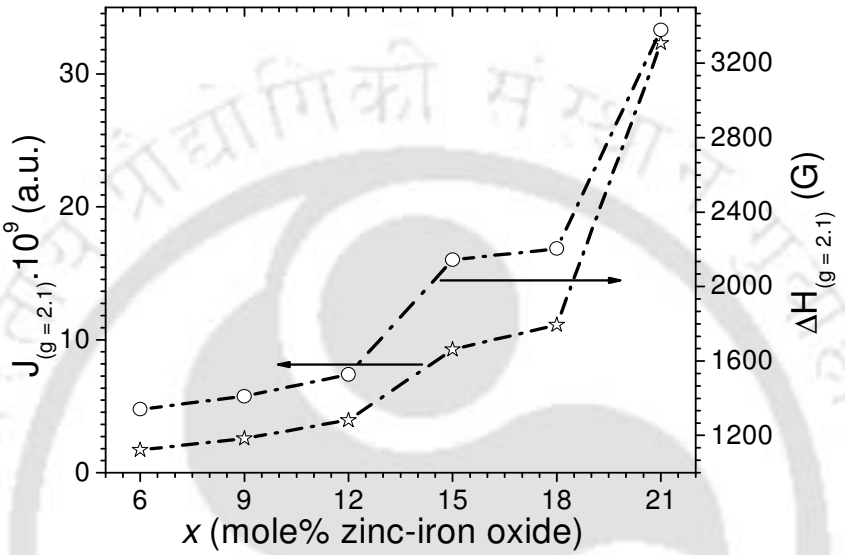

Fig. 5.3.3.2: Composition dependence of intensity and linewidth for g ≈ 2.1 absorption line of $x(ZnO, Fe_2O_3)$ $(65-x)SiO_2$ $20(CaO, P_2O_5)15Na_2O$ glass-ceramic samples.

The g ≈ 2.1 resonance arises due to the formation of iron clusters which give rise to superexchange type interaction between iron ions. The increase in $J_{(g=2.1)}$ as a function of zinc-iron oxide content indicates an increase in the ferrimagnetically coupled superexchange type interactions in the glass-ceramic samples. Superexchange mechanisms tend to narrow the absorption line. On the other hand, interactions between Fe^{3+} and Fe^{2+} ions tend to broaden the linewidth. The final linewidth depends on the relative strengths of the two mechanisms influencing the linewidth. The increase in the linewidth of the g ≈ 2.1 resonance with zinc-iron oxide concentrations shows the

dominance of the broadening mechanisms which in turns indicates a larger increase in Fe^{2+} ion concentration as zinc-iron oxide concentration is increased in the glass-ceramics. It is worthy to point out that the saturation magnetization increases in the samples as a function of x (*cf*. Fig. 5.3.4.5).

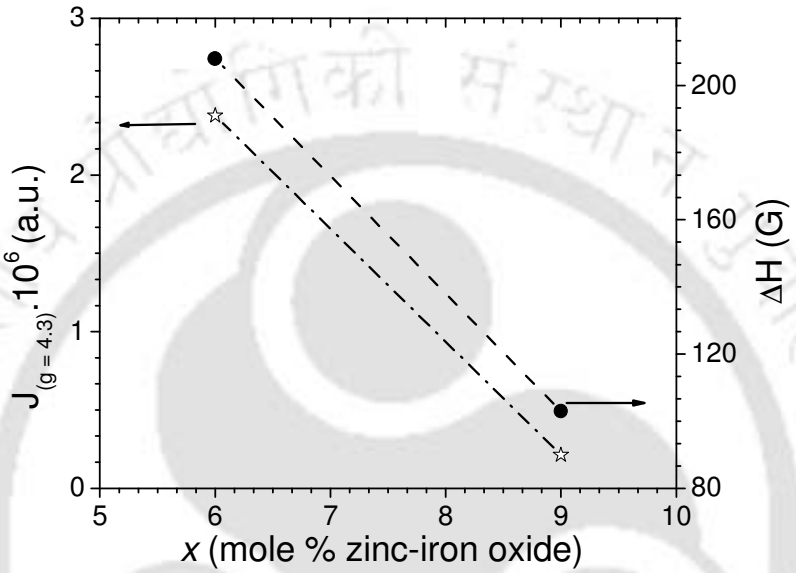

Fig. 5.3.3.3: Composition dependence of intensity and linewidth for g ≈ 4.3 absorption line of $x(ZnO, Fe_2O_3)$ $(65-x)SiO_2$ $20(CaO, P_2O_5)$ $15Na_2O$ glass-ceramic samples.

Fig. 5.3.3.1 shows that the EPR absorption line at g ≈ 4.3 is observed only in samples with x = 6 and 9 mole % zinc-iron oxide. The concentration dependence of the EPR parameters of the absorption line centered at g ≈ 4.3 is plotted as a function of composition in Fig. 5.3.3.3. The intensity ($J_{(g=4.3)}$) and linewidth ($\Delta H_{(g=4.3)}$) of the g ≈ 4.3 absorption line decreases as x is increased. Since the g ≈ 4.3 line arises from Fe^{3+} ions in low symmetry sites, the disappearance of the g ≈ 4.3 line signifies a decrease of low symmetry sites at Fe^{3+} ions and a corresponding increase in Fe^{3+} sites of higher symmetry

in the crystallization process. As already pointed out, XRD studies have confirmed that zinc-iron oxide ($Fd\bar{3}m$) crystallizes when the glasses are heat-treated at elevated temperatures.

5.3.4. Magnetic properties of glass-ceramics samples

Fig. 5.3.4.1 depicts the room temperature magnetic hysteresis (M-H) loops of glass-ceramics samples with different zinc-iron oxide concentration. Magnetic saturation is reached with an applied magnetic field of ± 20 kOe, Coercivity (H_C) and remanence (M_r) magnetization are individuated in the inset in the bottom corner of Fig. 5.3.4.1, where an enlarged view of the central part of the hysteresis cycles is shown.

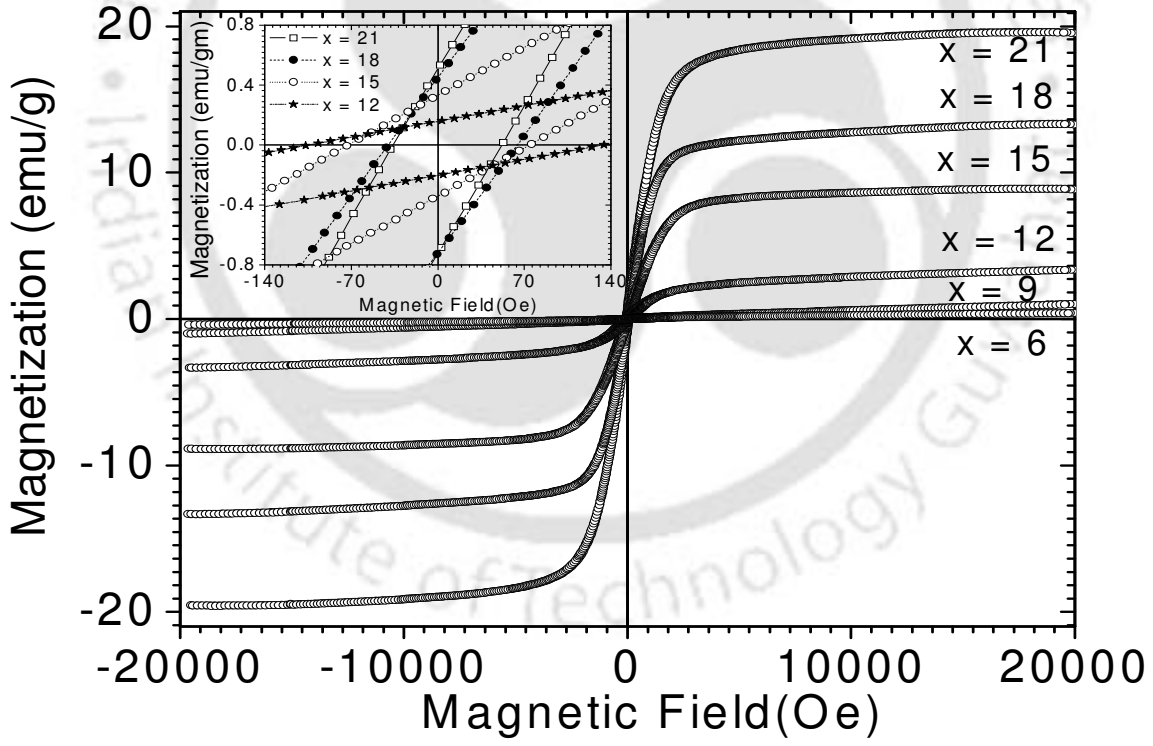

Fig. 5.3.4.1: Room temperature magnetic hysteresis loops of glass-ceramics with different zinc-iron oxide concentration under ± 20 kOe field sweep. Inset shows an expanded view of hysteresis loops close to the origin.

Table 5.3.4: Magnetic and structural parameters of the glass-ceramics samples.

Magnetic and structural parameters	**Sample (x) (mole % zinc-iron oxide)**					
	$x = 6$	$x = 9$	$x = 12$	$x = 15$	$x = 18$	$x = 21$
Average crystallite size d (nm)	8.18	13.91	15.81	20.99	22.89	23.34
Saturation magnetization M_s (emu/g)	0.41	1.10	3.33	8.89	13.33	19.60
Coercive force, H_C (Oe)	204	149	120	75	52	44
Remanence magnetization M_r (10^{-2} emu/g)	1.37	1.94	18.16	33.82	58.92	61.81
Hysteresis area ± 20 kOe (erg/g)	446	1063	2195	5414	7347	9631
Hysteresis area ± 500 Oe (erg/g)	6.4	13.6	127	287	501	656
Vickers hardness number (kg mm^{-2})	563	589	642	693	726	764

The magnetic field necessary to saturate the samples increases with increasing mole % of zinc-iron oxide. The coercive field varies from 44 to 204 Oe while saturation magnetization varies from 19.603 to 0.406 emu/g, the reported results are summarized in Table 5.3.4. The saturation magnetization (M_s) increases with the amount of magnetic phase in the sample. The highest amount of magnetite phase is obtained in the sample with $x = 20$, which also has the highest M_s. The M_s increases with the amount of $ZnFe_2O_4$ phases crystallized in the sample. Fig. 5.3.4.2 displays the saturation magnetization, coercivity, remanence magnetization and area under the hysteresis loop) obtained from M-H loops for samples with different mole % of zinc-iron oxide. The M_S (Fig. 5.3.4.2a)

increased with increasing zinc-iron oxide concentration from x = 6 to 21 mole % and showed a trend to saturate for x = 21 with the maximum value of about 19.603 emu / g. The increase of saturation magnetization with an increase in zinc-iron oxide concentration could be attributed to the development of $ZnFe_2O_4$ phase in the samples, as observed in Fig. 5.3.1.1. The coercivity of the samples (Fig. 5.3.4.2b) decreases with increasing zinc-iron oxide content from 6 to 21 mole %. As shown in Table 5.3.4, the coercive field slowly decreases with an increase in average crystallite size of $ZnFe_2O_4$. Remanence signifies the nature of the magnetic material to be spontaneously magnetized, even in the absence of external magnetic field.

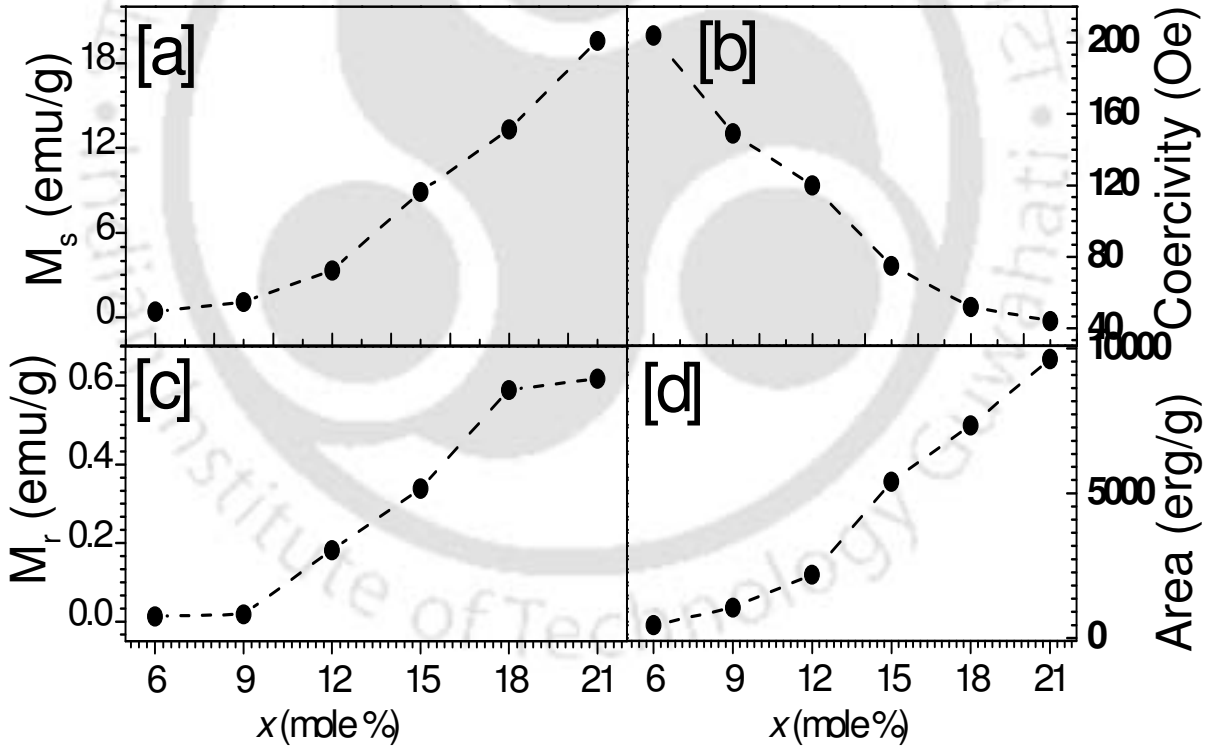

Fig. 5.3.4.2: Variation of (a) saturation magnetization, (b) coercivity, (c) remanent magnetization, and (d) area under the hystersis loop under ± 20 kOe of glass-ceramics as a function of zinc-iron oxide content.

With zinc-iron oxide increasing saturation magnetization and hysteresis area increases and coercivity decrease, this behaviour is probably depend on the size of $ZnFe_2O_4$ crystallite in glass-ceramics samples. Area of hysteresis cycle, calculated for each glass-ceramics sample, is presented in Table 5.3.4. The highest area is obtained for x = 21 mole % sample, which exhibits the highest saturation magnetization and lowest coercivity among all the samples in this series. The area under the hysteresis loop increased with increasing zinc-iron oxide content. Since the area under the loop is proportional to the energy loss and hence the heat generated by a sample under an alternating field, samples with higher zinc-iron oxide concentration are capable of generating more heat. The large variation in the area under the loops for samples with x = 6 to 21 mole % provides a means for controlled heat generation by appropriate choice of sample.

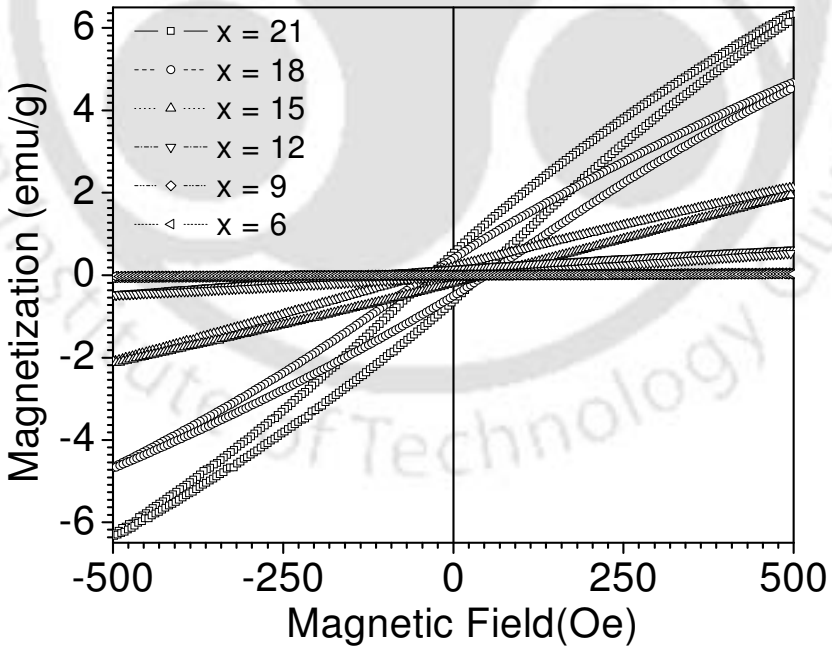

Fig. 5.3.4.3: Room temperature magnetic hysteresis loops of glass-ceramics with different zinc-iron oxide concentration under ± 500 Oe field sweep.

Such high magnetic field (± 20 kOe) is rather difficult to realise in a clinical laboratory due to technical reasons. Therefore, room temperature hysteresis cycles were measured at much lower field amplitude. Hysteresis curves were measured using a magnetic field 40 times smaller (± 500 Oe). The corresponding M-H loops are shown in Fig. 5.3.4.3. The calculated values of the hysteresis loops area for an applied field of ± 20 kOe and ± 500 Oe are listed in Table 5.3.4. It can be seen that the loop area is drastically reduced when the magnetic field is reduced. Again, the highest hysteresis loop area for ± 500 Oe field sweep is obtained for sample with 21 mole % zinc-iron oxide. The calculated values of hysteresis loop area for an applied field of ± 20 kOe and ± 500 Oe reported in Table 5.3.4 are plotted in Fig. 5.3.4.4. For an applied magnetic field of ± 500 Oe, magnetic saturation is not reached; the magnetic loss / cycle for sample with 21 mole % zinc-iron oxide is the highest. This shows that the properties of these glass-ceramics are preserved even at clinically amenable low magnetic fields.

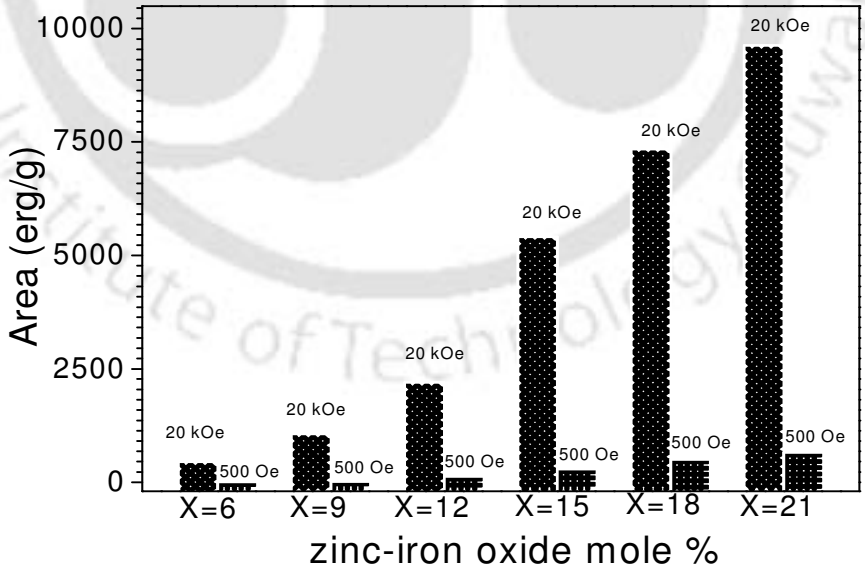

Fig. 5.3.4.4: Variation of hysteresis loop area as a function of zinc-iron oxide content, for applied fields of ± 20 kOe and ± 500 Oe.

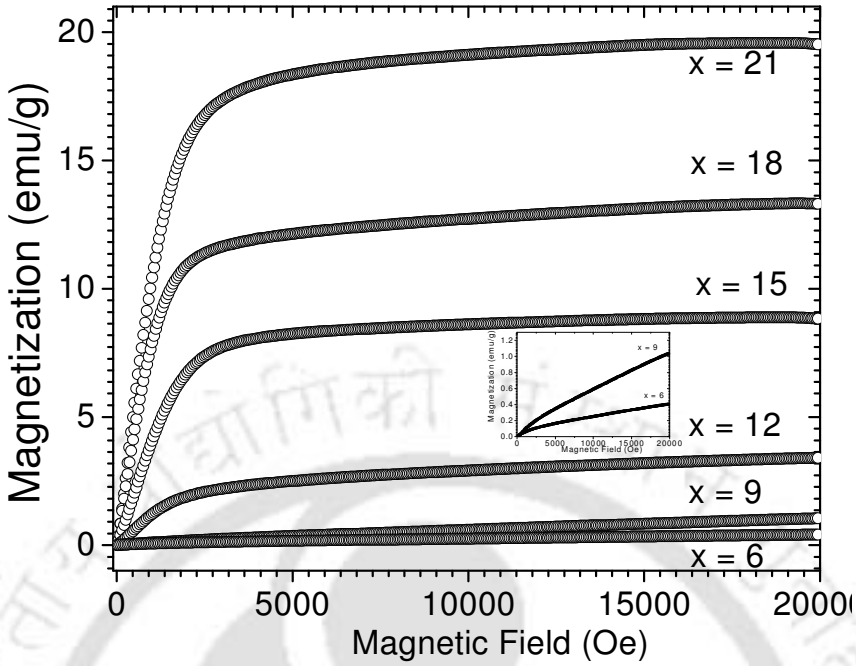

Fig. 5.3.4.5: Room temperature initial magnetization curves of the glass-ceramic samples. In-set highlights the data of x = 6 and 9 mole % samples.

Fig. 5.3.4.5 shows the initial magnetization curves for all samples measured at room temperature. The magnetization curves of the samples with x = 6 and 9 did not saturate at an applied magnetic field of 1592 kA/m (20 kOe) as revealed by the in-set in Fig. 5.3.4.5. It can be inferred from the nature of the curves that the samples with x = 6 and 9 mole % zinc-iron oxide exhibit a combination of paramagnetic and ferrimagnetic behaviour. The EPR absorptions at g ≈ 4.3 and g ≈ 2.1 are observed only in samples with x = 6 and 9 mole % zinc-iron oxide. These samples exhibit a combination of paramagnetic and ferrimagnetic behaviour. In this case too, a comparison with the EPR spectra of these samples would clarify that both these techniques yield results that support and complement each other. The magnetization curves of samples with x = 12, 15, 18 and 21 mole % saturate at a magnetic field of 20 kOe. These compositions exhibit

only ferrimagnetic behavior. EPR spectra of these compositions show only one absorption line at g ≈ 2.1, which is an indication of enhanced magnetic superexchange interaction between the iron ions.

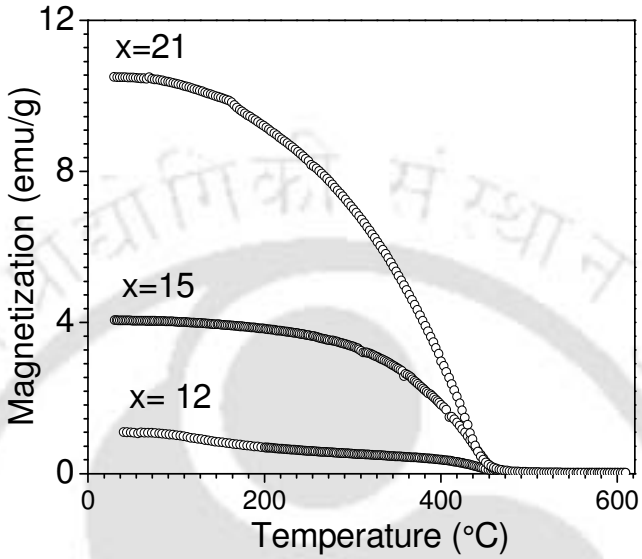

Fig. 5.3.4.6: Variation of magnetization as a function of temperature of $x(ZnO, Fe_2O_3)$ $(65\text{-}x)SiO_2$ $20(CaO, P_2O_5)15Na_2O$ glass-ceramics samples.

Fig. 5.3.4.6 shows that plot M-T curve under a constant magnetic field of 1 kOe for the glass-ceramics samples (x = 12, 15 and 21 mole %). During heating, a steady decrease in magnetization is observed. The ferrimagnetic behavior of the investigated samples is obvious from the nature of the M-T curves. Magnetic susceptibility (χ) measurements reveal the type of interactions between iron ions and the nature of magnetism in the sample. Variation of inverse magnetic susceptibility (χ^{-1}) with temperature over the range of 350 ºC to 620 ºC is shown in Fig. 5.3.4.7. The χ^{-1} - T plots which are nearly linear above 500 ºC show a downward drop at low temperatures. The deviation from linearity and the systematic downward drop of χ^{-1} - T curves indicate the

onset of short-range order just above the ferrimagnetic Neel temperature (T_N). The Neel temperature (T_N) of the glass-ceramic samples increases from 420 to 440 ºC as *x* is varied from 12 to 21 mole %. The Neel temperature increase with increase in zinc-iron oxide concentration may be correlated with the corresponding increase in the intensity of the g ≈ 2.1 resonance line [Fig. 5.3.3.2]. χ^{-1} tends to zero at $T = T_N$, which shows that the samples are entirely ferrimagnetic.

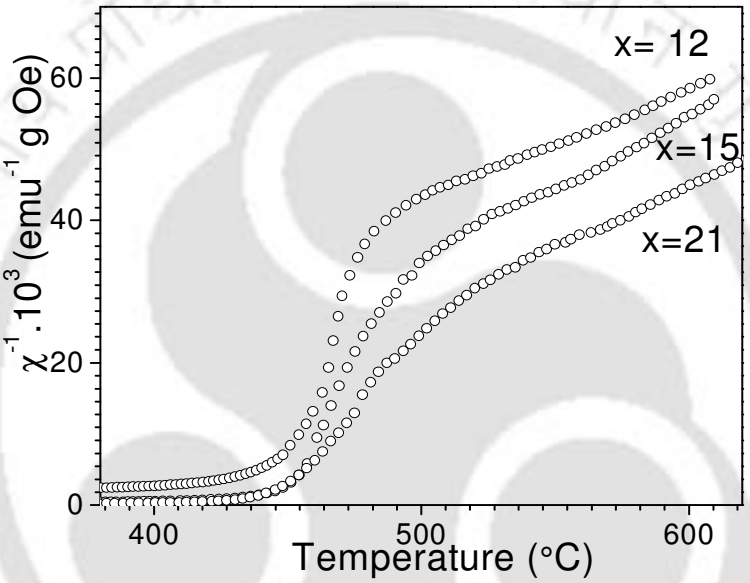

Fig. 5.3.4.7: Plots of χ^{-1} versus T for *x*(ZnO, Fe_2O_3) (65-*x*)SiO_2 20(CaO, P_2O_5)15Na_2O glass-ceramic samples.

5.3.5. *In vitro* bioactivity test of glass-ceramics samples

Glass-ceramics samples *x*(ZnO, Fe_2O_3) (65-*x*)SiO_2 20(CaO, P_2O_5)15Na_2O immersed in SBF were taken out after 1, 3, 7, 10, 20 and 30 days and lightly washed with acetone. Surface structural changes of the glass-ceramics samples treated in SBF were analyzed by GI-XRD, FT-IR spectroscopy and SEM techniques. The surface chemical analysis was carried out by SEM-EDS analysis.

5.3.5.1. GI-XRD studies of the glass-ceramics samples soaked in SBF

Fig. 5.3.5.1(a) shows the typical GI-XRD patterns obtained from the surfaces of glass-ceramics before and after soaking in SBF for various time periods. XRD analysis results of the untreated (fresh) sample [designated as 0 d in Fig. 5.3.5.1(a)] is shown in Fig. 5.3.1.1. On immersion in SBF for a day or more, new crystalline peaks appear in the GI-XRD patterns, indicating the formation of apatite crystalline layer on the surface of the glass-ceramics. Broad crystalline peaks develop in samples treated with SBF for 3 days and more. Two HA peaks develop at 2θ values of ~26° (002) and ~32° (211) after 3 days of soaking in SBF.

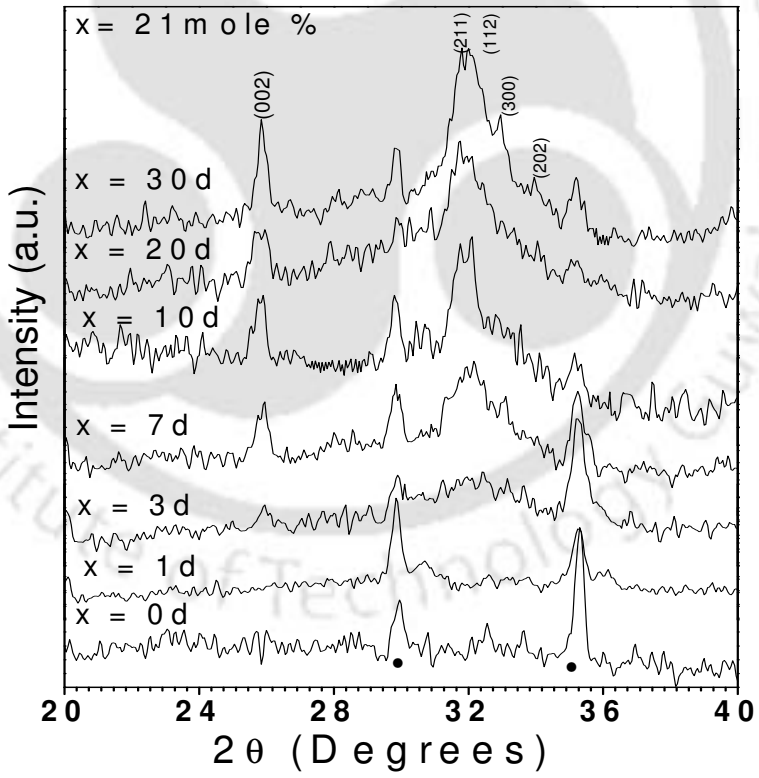

Fig. 5.3.5.1(a): GI-XRD patterns of the sample with x = 21 mole % soaked in SBF for different days.

The wide diffraction peak at 2θ ranging from 30˚ to 34˚ corresponds to the overlap of (112), (300) and (202) reflection of the well-crystallized HA. The GI-XRD patterns depicted in Fig. 5.3.5.1(a) show the preferential growth mechanism of the surface apatite layer. Apatite formation on the surface of the glass-ceramics in the SBF is governed by chemical reaction of the surface of the matrix with the fluid. Formation of the apatite layer over the glass-ceramics surface shows that the glass-ceramics samples are bioactive. The gradual growth in the intensity of the individual reflection, appearance of other low intensity apatite reflections and the narrowing of the peak width clearly show the evolution of the crystalline HA surface layer as a function of immersion time in SBF. The intensity of two major reflections, *viz*., (002) and (211), increases [*cf*. Fig. 5.3.5.1(b)] with an increase in the concentration of Ca^{2+} and PO_4^{3-} ions on the surface of the glass-ceramics immersed in SBF for various days. The average size (d) of HA crystallized was calculated from the (002) reflection peak using Scherrer`s equation (2.1).

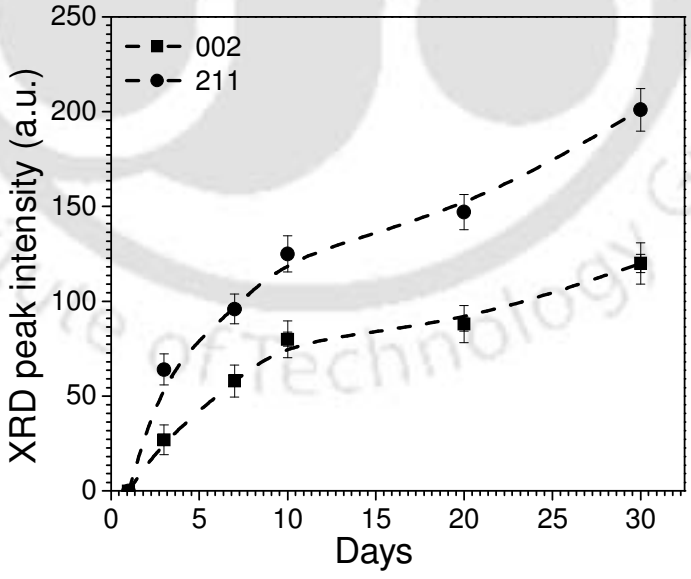

Fig. 5.3.5.1(b): GI-XRD intensity of glass sample x = 21 mole % corresponds to the (002) and (211) reflection peak for soaked in SBF for 1, 3, 7, 10, 20 and 30 days.

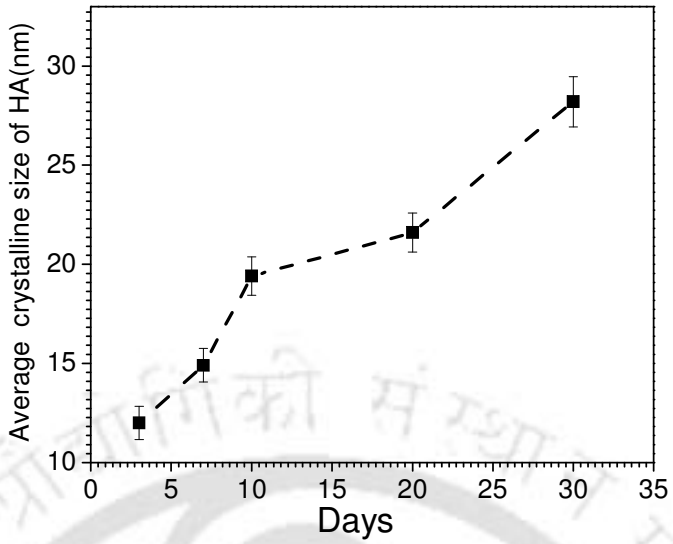

Fig. 5.3.5.1(c): The averages size of HA crystalline (nm) corresponds to the (002) reflection peak for sample x = 21 mole % soaked in SBF for 3, 7, 10, 20 and 30 days.

Fig. 5.3.5.1(c) reveals an increase in the average particle size with raise Ca^{2+} and PO_4^{3-}, on the surface layer on the glass-ceramics immersed in SBF for various days, which is consistent with results obtained on the other two glass-ceramic systems and those reported earlier [184, 200]. The crystallite size increases from about 12 ± 0.45 nm to 28.2 ± 0.68 nm in samples immersed for 3 days to 30 days. The size of HA crystalline depends on the rate of crystalline growth on the surface of the glass-ceramics in the SBF in various days. The variation of the crystallite size with immersion time shows a sharp increase in crystallite size in samples treated in SBF for 10 days, followed by a slower increase in crystallite size in samples treated in SBF for longer periods.

Fig. 5.3.5.1(d) shows the GI-XRD patterns obtained from the surfaces of glass-ceramics with x = 6, 9, 12, 15, 18 and 21 mole % zinc-iron oxide after treatment in SBF for 30 days. HA peaks appearing between 2θ values of 30° to 34° sharpen in samples

with higher *x*. The relative intensity and peak width of the characteristic apatite reflections show considerable composition dependence. It is interesting to observe the growth in the intensity and reduction in the width of the apatite reflections as a function of increasing zinc-iron oxide content in this series of glass-ceramics too.

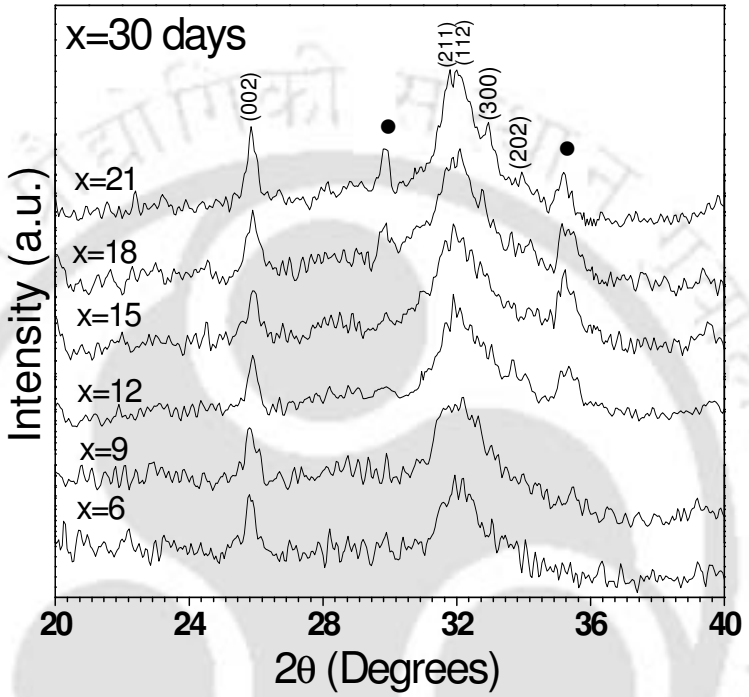

Fig. 5.3.5.1(d): GI-XRD patterns of glass-ceramics with different compositions soaked in SBF for 30 days.

Since the broad peaks signify the presence of small sized crystallites, one can infer that on immersion in SBF, the HA formation gradually improves from small sized crystalline aggregates to a well-crystallized HA phase as the amount of zinc-iron oxide is increased in the system. As mentioned earlier in this chapter, Balamurugan *et al*. [77] studied the bioactivity SiO_2–CaO–P_2O_5-ZnO system in vitro and in vivo and reported that incorporation of Zn into a bioglass does not diminish the bioactivity of such materials.

Better apatite formation in this series of glasses when the zinc-iron oxide content is increased. This might be due to the fact that in this series of glass-ceramics, ZnO-Fe_2O_3 replaces SiO_2, leaving the amount of CaO and P_2O_5 undisturbed molar ratio of Ca/P = 1.67. Such compositional variation seems to aid the apatite forming ability on the surface of these glass-ceramics. Formation of the HA layer over the glass-ceramics surface shows that the glass-ceramics samples are bioactive.

5.3.5.2. FT-IR studies of the glass-ceramics samples soaked in SBF

Fig. 5.3.5.2(a) shows the infrared reflection spectra of the glass-ceramics sample with x = 21 mole % zinc-iron oxide before and after the immersion in the simulated body fluid for 0, 1, 3, 7, 10, 20 and 30 days.

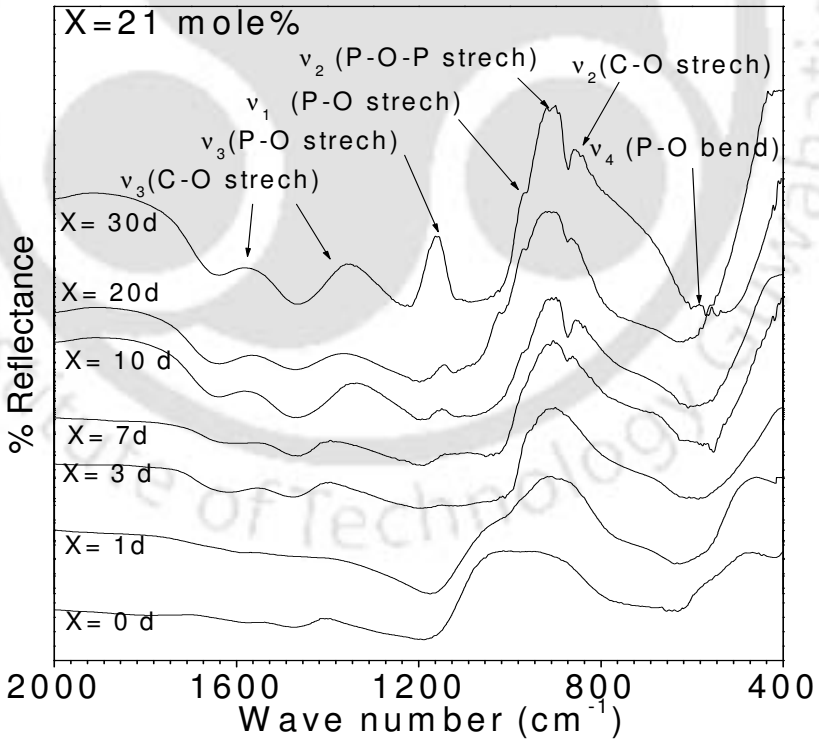

Fig. 5.3.5.2(a): FT-IR spectra of samples with x = 21 mole % soaked in SBF for different days.

The spectrum before the immersion reveals bands at 1040, 925, 773, 600 and 480 cm^{-1}. The peaks at 1040, 925, 773, 600 and 480 cm^{-1} correspond [188-190] to ν_3 Si-O stretching [with one non bridging oxygen (NBO)], Si-O stretching [with 2 NBO], Si-O-Si stretching, v_4 P-O bending and v_4 Si-O-Si bending frequencies, respectively. After 1 day of immersion in SBF, new peaks appear at 860, 905, 1350 and 1566 cm^{-1}. The peak at 905 cm^{-1} corresponds to v_1 P-O-P stretching frequency, respectively. The band located at 860 cm^{-1} and the large bands at 1350 and 1566 cm^{-1} can be assigned to C-O vibration mode of CO_3^{2-}. These bands signify the incorporation of carbonate anions from the SBF in the apatite crystal lattice. After 3 days of immersion in SBF, the appearance of the band at 960 cm^{-1}, which is related to calcium phosphate (hydroxyapatite) surface layer is observed. The peak at 960 cm^{-1} corresponds to the v_1 P-O symmetric stretching frequency. It indicates the obviation of phosphate ions from the ideal tetrahedral structure. After 7 days of immersion in SBF, the disappearance of the band at 1040 cm^{-1} is related to ν_3 Si-O stretching surface layer. After7 days of immersion in SBF, the appearance of the peak at 1158 cm^{-1} reflects the v_3 P-O stretching vibration of PO_4 unit. These bands (1158 and 905cm^{-1}) sharpen and their relative intensities increase with increase in longer immersion times. These peaks are characteristic of apatite crystals. With further increase in immersion time, the intensity of the bands related to the CO_3^{2-} group increases. Carbonate ions occupy two different sites in carbonated apatite as indicated by peaks in the region of 1650 to 1300 cm^{-1} which are due to v_3 vibration mode, whereas the peak at 860 cm^{-1} is due to the v_2 vibration mode of carbonate ion [190]. The v_3 band splits into two peaks centered at 1350 and 1566 cm^{-1}, respectively, with the distribution of the carbonate v_3 sites depending on the maturation and formation of apatite

crystals. Occupancy of the v_2 sites is considered to occur competitively between the OH^{-1} and carbonate groups at the interface of growing crystal, whereas, occupancy of the v_3 sites depends on competition between the phosphate and carbonate ions [190]. Presence of v_2 and v_3 vibration modes of carbonate is the signature of the development of HCA layer on the surface of the sample.

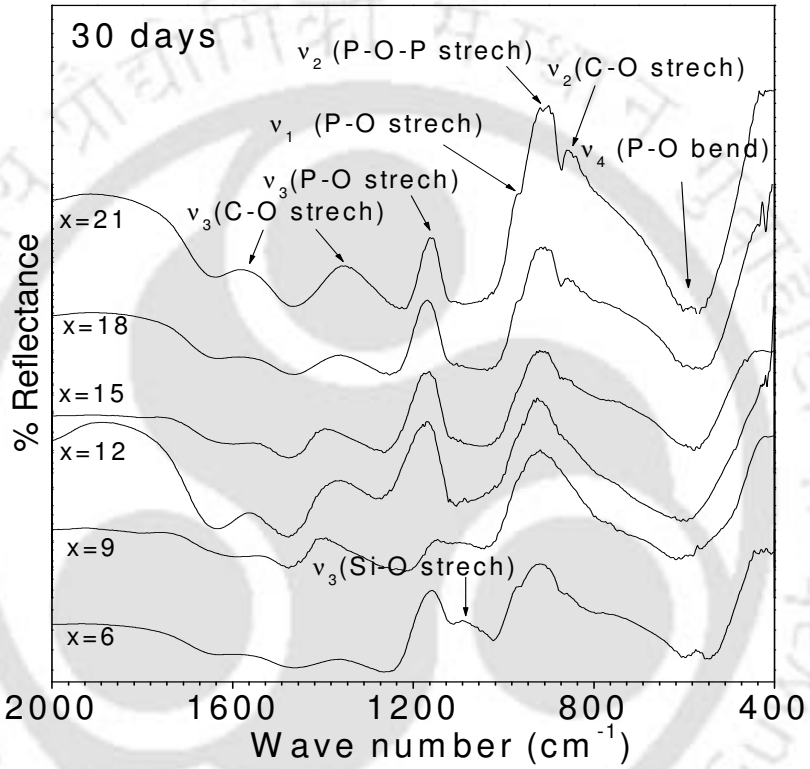

Fig. 5.3.5.2(b): FT-IR reflection spectra of surfaces of various glass-ceramics (x = 6, 9, 12, 15, 18 and 21 mole %) soaked in SBF for 30 days.

Fig. 5.3.5.2(b) shows the infrared reflection spectra of glass-ceramics samples with x = 6, 9, 12, 15, 18 and 21 mole % zinc-iron oxide after the immersion in SBF for 30 days. Spectral bands of HA assigned to PO_4^{3-} groups (ν_3–1158 cm^{-1}, ν_1–960 cm^{-1}, ν_1–905 cm^{-1} and ν_2–600 cm^{-1}) and CO_3^{2-} functional groups (v_2–860 cm^{-1}, ν_3–1350 $cm^{-1}$and ν_3–

1566 cm^{-1}) appear in the spectra. The band at 1040 cm^{-1} ν_3 Si-O stretch disappears in the samples with x = 15, 18 and 21 mole %. The peak at 905 cm^{-1} reflects the ν_1 P-O-P stretching mode. These bands (1158, 860 and 905 cm^{-1}) sharpen and their relative intensities increase with increase in zinc-iron oxide content signifying the formation of a well crystallized HCA layer in these samples. The FT-IR studies thus clearly show an increased bioactivity in these glass-ceramics as the zinc-iron oxide content is increased in the composition range studied.

5.3.5.3. SEM-EDS studies of the glass-ceramics samples soaked in SBF

Fig. 5.3.5.3(a) shows the SEM micrographs of the glass-ceramic sample with x = 21 mole % after immersion in SBF for 1, 3, 7, 10, 20 and 30 days, respectively. The micrographs provide visual evidence of the formation of a surface layer on the bioglass-ceramics, which can now be presumed to be an apatite layer.

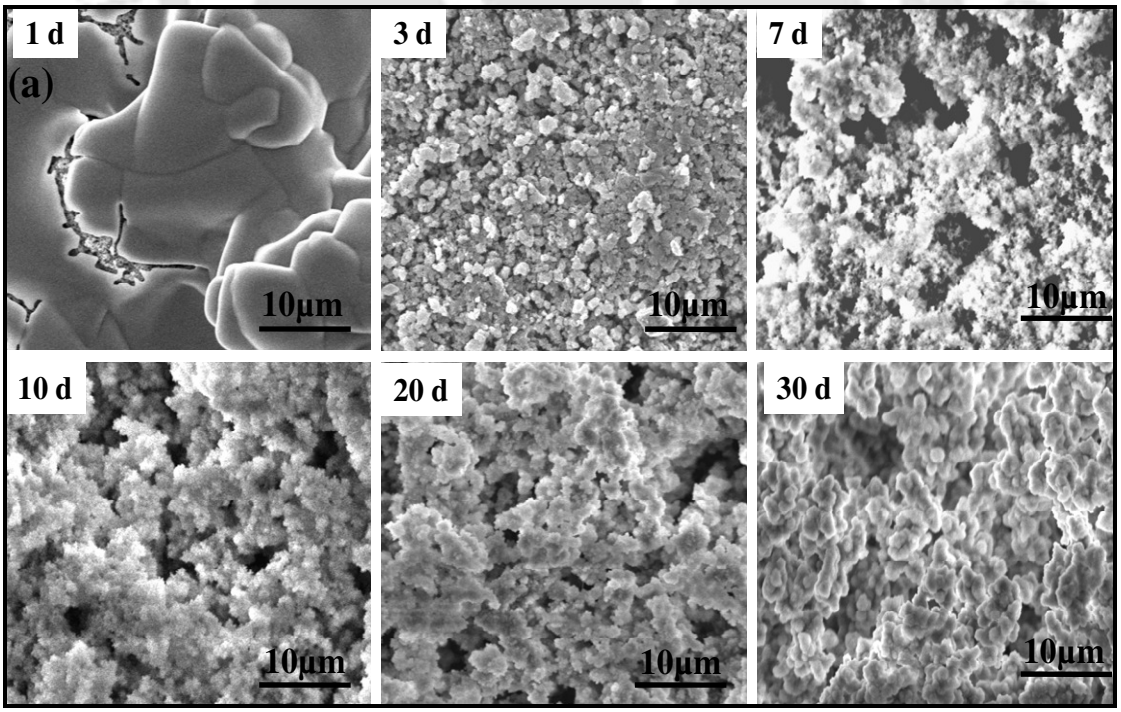

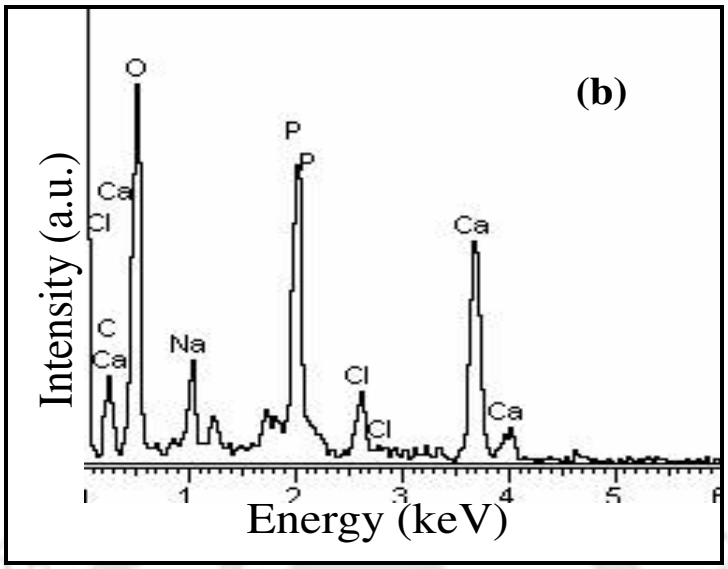

Fig. 5.3.5.3: (a) SEM micrographs of glass-ceramics with x = 21 mole % soaked in SBF (Magnification: 1000×) and (b) EDS spectra of sample soaked in SBF for 30 days.

After 30 days of immersion, the whole surface of the specimen is covered with spherical Ca-P particulate apatite layer. Results from EDS analysis reveal the gradual development of apatite on the surface of glass-ceramics samples after immersion for various time periods in SBF. The spherical particles in the sample treated in SBF for 30 days are made up of calcium and phosphorus and the Ca/P molar ratio (calculated from EDS analysis) was of ~1.67, corresponding to the value in HA. Microanalysis of the precipitates reveals the presence of small quantities of Na and Cl as shown in the EDS spectra in Fig. 5.3.5.3(b). This finding is in agreement with reports which claim that the growth of HA in SBF is accompanied by the incorporation of sodium and chlorine ions [192] as well. It may thus be concluded that the surface layer contains carbonate, sodium and chlorine substituted hydroxyapatite [193].

5.4. Summary

The salient features of the studies on $x(ZnO, Fe_2O_3)$ $(65-x)SiO_2 20(CaO, P_2O_5)$ $15Na_2O$ glasses are

1. Good quality glasses could be obtained in $x(ZnO, Fe_2O_3)$ $(65-x)SiO_2 20(CaO, P_2O_5)$ $15Na_2O$ system with x up to 21 mole %.

2. Calcium sodium phosphate and zinc ferrite crystallized in all glass compositions when heated to 800 °C.

3. Composition dependence of T_g shows a decrease in the depolarization of the glass skeleton with increasing zinc-iron oxide content.

4. Addition of zinc-iron oxide increased the density and VHN of the glasses.

5. In compositions with low x, the iron sites are populated randomly in the glass, whereas in glasses $x > 9$ mole%, the site population deviates from randomness and results in the formation of clusters. These result in superexchange type magnetic interactions between the iron ions in these glasses which are predominantly anti-ferromagnetically coupled.

6. While x_1 (mole % Fe^{3+}) and x_2 (mole % Fe^{2+}) values show an increasing trend up to 9 mole % zinc-iron oxide, x_1 decreases in glasses with $x > 9$ mole % zinc-iron oxide. All glasses were paramagnetic at room temperature.

7. Bioactivity of this series of glasses increases as the zinc-iron oxide content is increased.

8. GI-XRD and FT-IRS studies on SBF surfaces reveal the evolution of the HCA layer on the surface of the glass treated with SBF. EDS analysis showed that the Ca / P ratio of samples immersed in SBF for 30 days reach the value of 1.67 (value in HA).

The salient features of the studies on glass-ceramics derived from the parent glass compositons $x(ZnO, Fe_2O_3)$ $(65-x)SiO_2 20(CaO, P_2O_5)$ $15Na_2O$ are highlighted below.

1. Calcium sodium phosphate is the major biocompatible crystalline phases developed in all the glass-ceramics samples. Nanocrystalline zinc ferrite was present as the second crystalline phase in all the glass-ceramic samples containing zinc-iron oxide.

2. VHN increased with increase in zinc-iron oxide content.

3. An increase in ferrimagnetically coupled superexchange type interactions with increase in zinc-iron oxide content has been inferred from EPR studies on the glass-ceramic samples. Samples with x = 6 and 9 mole % zinc-iron oxide exhibit a combination of paramagnetic and ferrimagnetic behaviour.

4. Samples exhibited narrow hysteresis loop and low coercivity. The area under the hysteresis loop increased with increasing zinc-iron oxide content. This showed that these bio-glass ceramics could be useful in the localized hyperthermia treatment of cancer.

5. Bioactivity of the glass-ceramics samples increases with increase in zinc-iron oxide content. Thus, compositions with higher zinc-iron oxide content contain higher amounts of bone mineral phases as well as the magnetic phase in this series of glass-ceramics.

6. GI-XRD and FT-IRS studies on SBF treated surfaces reveal the evolution of the HCA layer on the surface of the glass-ceramic samples treated with SBF. EDS analysis showed that the Ca/P ratio of samples immersed in SBF for 30 days reach the value of 1.67 (value in HA).

7. These studies show that these ferrimagnetic bioglass-ceramics can be used in hyperthermia applications.

Chapter 6

Conclusion and scope for future work

6.1. Conclusion

In this chapter, the work done in this thesis work would be summarized and an attempt would be made to highlight the common and uncommon features observed in the studies on the three series of glasses and glass-ceramics. This work showed that the preparation and characterization of $41CaO(52\text{-}x)SiO_2 4P_2O_5 xFe_2O_3 3Na_2O$, ($x$ = 0, 2, 4, 6, 8 and 10 mole %), $4.5MgO(45\text{-}x)$ CaO $34SiO_2$ $16P_2O_5 0.5CaF_2 xFe_2O_3$ (x = 0, 5, 10, 15 and 20 wt.%) and $x(ZnO,Fe_2O_3)(65\text{-}x)SiO_2$ $20(CaO,P_2O_5)$ $15Na_2O$ (x = 6, 9, 12, 15, 18 and 21 mole %) with Ca/P = 1.67 and Fe/Zn = 6.5 bioactive glasses and magnetic bioactive glass-ceramics derived from them. *In vitro* bioactivity test was performed on all the samples to evaluate their biocompatibility. Magnetic properties relevant to thermoseed applications were also carried out. The salient features observed from these studies are compiled below.

The three series of bioactive materials studied have the following common ingredients, *viz*., SiO_2, CaO, P_2O_5 and Na_2O (or CaF_2). The choice of these basic ingredients is essential for biocompatibility of the end product. Fe_2O_3 was added as the additional element to these three materials and its concentration was also varied. This variation resulted in changes in the structure of the glass and the concentration of crystalline phases in the glass-ceramics obtained from them. The basic intention was to incorporate large amounts of iron oxide within the glass forming region of these systems. Homogenous glasses with a well-connected glassy network were obtained in the entire range of compositions prepared by melt quenching technique.

The studies on the first system [41CaO(52-*x*)$SiO_2$4P_2O_5*x*$Fe_2O_3$3Na_2O] was to understand the influence of Fe_2O_3 addition at the cost of SiO_2. As mentioned earlier in the thesis, this attempt was made amidst reports in the literature mentioning reduction in bioactivity on the addition of Fe_2O_3 in systems with similar constituents. Since, the Ca/P ratio was not disturbed in this procedure, addition of Fe_2O_3 actually ended up improving the bioactivity of this series of samples, which is a positive result towards the application of these materials as thermoseeds. In the second series [4.5MgO(45-*x*)CaO 34SiO_2 16$P_2O_5$0.5CaF_2*x*Fe_2O_3], CaO was replaced with Fe_2O_3 in wt.% without changing the percentage of other constituents. In this system too, better bioactivity resulted with the addition of Fe_2O_3. In the third system [*x*(ZnO,Fe_2O_3)(65-*x*)SiO_2 20(CaO,P_2O_5)15Na_2O], ZnO+Fe_2O_3 replaced SiO_2. By maintaining Ca/P ratio at the bone mineral value and Fe/Zn ratio at 6.5, up to 21 mole % of (ZnO+Fe_2O_3) could be added to the system, which enhanced the magnetic properties and bioactivity of these materials. The choice of the compositions and the manner in Fe_2O_3 was added to the system resulted in the

enhancement of bioactivity and magnetic properties obtained in these systems with higher Fe_2O_3 content. Unlike reports which stressed on the importance of maintaining the ratio of Fe^{2+} and Fe^{3+} ions in some glasses, the present studies show that iron in both the ionic forms contributed towards better bioactivity.

The physical properties of the three glass and glass-ceramics systems showed behaviour typical of their constituents. Hydroxyapatite, wollastonite and magnetite are the major crystalline phases which developed in all the heat treated CaO and MgO based glasses. The percentage of hydroxyapatite increased in the CaO and MgO samples with an increase in iron oxide concentration. Akermanite developed in the MgO glass-ceramics with higher Fe_2O_3 content. Calcium sodium phosphate and zinc ferrite are the major crystalline phases present in all heat treated ZnO based samples. The magnetic properties of these glass-ceramics systems were due to nanocrystalline magnetic (magnetite or zinc ferrite) present in them.

A brief comparison of some physical properties of the three glasses is made below. The glass transition and crystallisation temperatures of the ZnO glasses were lower than that of CaO and MgO glasses. T_g and T_c decreased as a function of increasing x (zinc-iron oxide content) in all three series of glasses. The density of the ZnO glasses was lower than the CaO and MgO glasses. The density values of the three glass systems followed the same trend. The same trend was shown by microhardness (VHN) indicating that the number of non-bridging oxygens in a glass decreases, the elastic moduli of the glass increase. The VHN of the MgO glasses was higher than the CaO and ZnO glasses. This suggests that the MgO system could yield high strength of glasses and glass ceramics suitable for applications involving implants with better load bearing capability.

All the glasses are paramagnetic at room temperature. Superexchange type magnetic interactions exist between the iron ions in the glasses which are predominantly anti-ferromagnetic in nature. The Fe^{2+} / Fe_{total} ion ratio increased with an increase in iron oxide content in all the glasses. *In vitro* bioactivity studies showed that the apatite forming ability in glasses increased as a function of iron and zinc-iron oxide content. As discussed above, the specific manner in which the composition is varied while adding more iron (or zinc-iron) oxide in these systems seems to aid the apatite forming ability on the surface of these glasses.

A comparative study of the three glass-ceramic systems shows that the crystallized phases determine their individual physical properties. All glass-ceramic samples exhibited higher microhardness when compared to the respective parent glass samples. MgO based glass-ceramic samples exhibited higher microhardness when compared to the CaO and ZnO based glass-ceramics samples. This feature can be attributed to the presence of akermanite ($Ca_2MgSi_2O_7$) in these glass-ceramics, which increases the strength of these glass ceramics. This MgO system could offer high strength magnetic bioglass and glass-ceramics suitable for load-bearing applications. Magnetization, coercivity, area of hysteresis loop and magnetite crystallite size varied as a function of iron oxide (or zinc-iron oxide) concentration in all the CaO, MgO and ZnO glass-ceramic samples. The magnetic parameters of the three glass systems followed the same trend, because, in all the three glass-ceramics systems, the amount and size of the nanocrsytalline phase increased with increasing iron (zinc-iron) oxide content. ZnO based glass-ceramics samples exhibited higher magnetic hysteresis loop area as compared to the CaO and MgO glass-ceramics samples. Since the area under the loop is proportional to

the energy loss and hence the heat generated by a sample under an alternating magnetic field, samples with higher zinc-iron oxide concentration are capable of generating more heat for the same magnitude of applied field. All the glass-ceramic samples were ferrimagnetic with some with low iron concentration exhibiting a small amount of paramagnetic character as well. *In vitro* bioactivity studies showed an increased apatite forming ability in glass-ceramics when the (zinc-) iron oxide content is increased.

These investigations provide a means to assess the applicability of these ferrimagnetic bioactive glass-ceramics as thermo seeds for hyperthermia treatment of cancer apart from providing an insight to the structure and properties of these new materials.

6.2 Scope for future work

The intention of this thesis was to try and obtain bioactive glasses and glass-ceramics suitable for medical applications. These studies have given a lot of insight on the base glasses and the glass-ceramics *vis-à-vis* their constituents, structure, etc. Let us look at the materials aspect first. The studies on ZnO based bioglass-ceramics show that maintaining Ca/P ratio at 1.67 yields glasses and glass-ceramics with better bioactivity. It is worth exploring other oxide systems with Ca/P ratio of 1.67. The crystallization of the mineral and magnetic phases was performed at a fixed temperature and time after initial optimization based on DTA studies. Careful variation of both the temperature and time could yield better heat treatment conditions to obtain glass-ceramics with enhanced properties. Since, the magnetic phase is responsible for the magnetic properties, means of increased loading of iron oxide in the glass-ceramics would be rewarding. Development

of bioactive glass-ceramic coatings on substrates with good mechanical properties would pave way to the development of implant materials with desired shape and properties.

Anther area worth concentrating is the bioactivity test. Surface chemistry techniques could be of great help in understanding the interactions between bioactive glasses and glass-ceramics, and proteins contained in body fluids. For example, the sites specific for protein interaction could be studied by allowing selected probe molecules on the surface of bioactive glasses and glass-ceramics before and after the interaction with proteins. Study of the presence of proteins on the morphology of layers deposited on bioactive glass and glass-ceramics surface could be a fascinating area of research. This could be done with SEM and TEM, but other spectroscopic techniques such as nuclear magnetic resonance, Raman and X-ray photo-electron spectroscopy could help understanding some differences in the 'environment' of Fe-containing structures formed upon reaction of bioactive glasses and glass-ceramics in solutions containing different types of proteins. The study concerning proteins could be a first step towards the analysis of bioactive glass and glass-ceramics reactivity in cell-containing solutions, since it is well-known that some of the interactions between cells and foreign materials are often mediated by proteins. Although, this goes out of the arena a physicist or materials scientist, *in vivo* studies on these bioactive glasses and glass-ceramics would bring out the true capability of these materials for medical applications.

REFERENCES

[1] T. Kokubo, S. Ito, M. Shigematsu, S. Sakka and T. Yamamuro, J. Mater. Sci. **20** (1985) 2001.

[2] T. Kokubo, S. Ito, M. Shigematsu, S. Sakka and T. Yamamuro, J. Mater. Sci. **22** (1987) 4067.

[3] L. L. Hench, J. Am. Ceram. Soc. **74** (1991) 1487.

[4] K. Ohura, M. Ikenaga, T. Nakamura, T. Yamamuro, Y. Ebisawa, T. Kokubo, Y. Kotoura and M. Oka, J. Appl. Biomater. **2** (1991) 153.

[5] Y. Ebisawa, Y. Sugimoto, T. Hayashi, T. Kokubo, K. Ohura and T. Yamamuro, J. Ceram. Soc. Jpn. **99** (1991) 7.

[6] M. Ikenaga, K. Ohura, T. Yamamuro, Y. Kotoura, M. Oka and T. Kokubo, J. Orthop. Res. **11** (1993) 849.

[7] Y. Ebisawa, F. Miyaji, T. Kokubo, K. Ohura and T. Nakamura, J. Ceram. Soc. Jpn. **105** (1997) 947.

[8] D. F. Williams, Ed., Elsevier, Amsterdam, 1987, pp 72.

[9] L. L. Hench and E.C. Ethridge, Biomaterials: An Interfacial Approach, Academic Press, New York (1982).

[10] L. L. Hench, Bioceramics, Butterworth-Heinemann, Oxford **7** (1994) 3.

[11] S. F. Hulbert, J. C. Bokros, L.L. Hench, J. Wilson and G. Heimke, High Tech Ceramics, Elsevier, Amsterdam, The Netherlands (1987) 189.

References

[12] K. de Groot, In: Bioceramics of Calcium Phosphate, CRC Press, Boca Raton, FL (1983) 1.

[13] L. L. Hench, Bioceramics:Materials Characteristics Versus In vivo Behavior, Annals of New York Academy of Sciences, New York, **523** (1988) 54.

[14] L. L. Hench, R. J. Splinter, W. C. Allen and T. K. Greenlee, J. Biomed. Mater. Res. **2** (1972) 117.

[15] U. Gross, R. Kinne, H. J. Schmit and V. Strunz, CRC Crit. Res. Biocompat. **4** (1988) 2.

[16] J. Wilson, A. E. Clark, E. Douek, J. Kriegger, W. K. Smith and J. S. Zamet, Bioceramics, Butterworth-Heinemann, Oxford **7** (1994) 415.

[17] U. Gross and V. Strunz, J. Biomed. Mater. Res. **19** (1985) 251.

[18] W. Holand, W. Vogel, K. Naumann and J. Gummel, J. Biomed. Mater. Res. **19** (1985) 303.

[19] J. Wilson, G. H. Pigott, F. J. Schoen and L. L. Hench, J. Biomed. Mater. Res. **15** (1981) 805.

[20] J. Wilson, D. Nolletti. In handbook of bioactive ceramics, CRC press, Boca Raton, FL. **1** (1990) 283.

[21] L. L. Hench, Annals of New York Acad. Sci. New York **54** (1998) 523

[22] K. A. Athanasiou, C. F. Zhu, D. R. Lanctot, C. M. Agrawal, C. M. and X. Wang, Tissue Engg. **6** (2000) 361.

[23] H. Lodish, Molecular Cell Biology, Scientific American Books, New York, 1995.

[24] J. L. Ong and D. C. N. Chan, Critical Reviews in Biomedical Engg. **28** (1999) 667.

[25] A. Guyton, Textbook of Medical Physilogy, Saunders, Philadelphia, 1991.

[26] R. Z. LeGeros, Prog. Crystal. Growth Charact. **4** (1981) 1.

[27] M. J. Glimcher, Phil. Trans. Roy. Soc. Lond. **B304** (1984) 479.

[28] R. Z. LeGeros, Monographys in Oral Science Vol. 15, S. Karger, Basel, Switzerland (1991).

[29] L. Hench and J. Wilson, an introduction to bioceramics, World Scientific, 1993.

[30] T. Kokubo, S. Ito, S. Sakka and T. Yamamuro, J. Mater. Sci. **21** (1986) 536.

[31] U. M. Gross, C. Muller-Mai and C. Voigt, An Introduction to Bioceramics, World Scientific, London (1993) 105.

[32] L. L. hench and T. Kokubo, Handbook of biomaterial properties by Chapman & Hall, London (1998) 359.

[33] J. D. Preston, Proceedings of the IV Int. Symp. on Dental Materials, Quintessa Pub. CO, Chicago, 1988.

[34] P. Boutin. Rev. Chir.Orthop. **58** (1972) 229.

[35] H. Bromer, E. Pfeil, H. H. Kas, German Patent 2,326,100 (1973).

[36] M. Jarcho, J. Mater. Sci. **11** (1976) 2027.

[37] H. Denissen, Dental root implants of apatite ceramics, Ph. D. Thesis, Vrije Unversiteit te Amsterdam, 1979.

[38] H. Aoki, K. Kato, M. Ogiso and T. Tabata, J. Dent. Outlook **49** (1977) 567.

[39] K. Koster, H. Heide and R. Konig, Langenbecks Arch. Chir. **343** (1977) 174.

[40] T. Kokubo, M. Shigematsu, Y. Nagashima, M. Tashiro, T. Yamamuro and S. Higashi, Bull. Inst. Chem. Res. Kyoto Univ. **60** (1982) 260.

[41] M. Ogino, F. Ohuchi and L. L. Hench, J. Biomed. Mater. Res. **14** (1980) 55.

[42] T. Kitsugi, T. Nakamura, T. Yamamuro, T. Kokubo, T. Shibuya and M. Takagi, J. Biomed. Mater. Res. **21** (1987) 1255.

[43] T. Kokubo, C. Ohtsuki, S. Kotani, T. Kitsugi and T. Yamamuro, Bioceramics, German Ceramic Society, Cologne **2** (1990) 113.

[44] T. Kokubo, H. Kushitani, S. Sakka, T. Kitsugi and T. Yamamuro, J. Biomed. Mater. Res. **24** (1990) 721.

[45] T. Kokubo, S. Ito, T. Huang, T. Hayashi, S. Sakka and T. Kitsugi and T. Yamamuro, J. Biomed. Mater. Res. **24** (1990) 331.

[46] M. R. Filgueiras, G. L. Torre and L. L. Hench, J. Biomed. Mater. Res. **27** (1993) 445.

[47] C. Ohtsuki, Y. Aoki, T. Kokubo, Y. Bando, M. Neo and T. Nakamura, J. Ceram. Soc. Jpn **103** (1995) 449.

[48] T. Kitsugi, T. Yamamuro, T. Nakamura and T. Kokubo, Int Orthop. **13** (1989) 199.

[49] T. Kokubo, Biomater. **12** (1991) 155.

[50] J. E. Gamble, Chemical anatomy, physiology and pathology of extra-cellular fluid, Harvard University Press, Cambridge, MA (1967) 1.

[51] C. Ohtsuki, H. Kushitani, T. Kokubo, S. Kotani and T. Yamamuro, J. Biomed. Mater. Res. **25** (1991) 1363.

[52] W. Neuman and M. Neuman, The chemical dynamics of bone mineral, University of Chicago, IL (1958) 34.

[53] S. Cho, K. Nakanishi, T. Kokubo, N. Soga, C. Ohtsuki and T. Nakamura, J. Am. Ceram. Soc. **78** (1995) 1769.

[54] A. Oyane, H. M. Kim, T. Furuya, T. Kokubo, T. Miyazaki and T. Nakamura, J. Biomed. Mater. Res. **65A** (2003) 188.

[55] A. Oyane, K. Onuma, A. Ito, H. M. Kim, T. Kokubo and T. Nakamura, J. Biomed. Mater. Res. **64A** (2003) 339.

[56] H. Takadama, M. Hashimoto, M. Mizuno and T. Kokubo, Phos. Res. Bull. **17** (2004) 119.

[57] C. Ohtsuki, T. Kokubo, K. Takatsuka and T.Yamamuro, J. Ceram. Soc. Jpn. **99** (1991) 357.

[58] K. Ohura, T. Nakamura, T. Yamamuro, T. Kokubo, Y. Ebisawa, Y. Kotoura and M. Oka, J. Biomed. Mater. Res. **25** (1991) 357.

[59] A. E. Clark, L. L. Hench, J. Biomed. Mater. Res. **10** (1976) 161.

[60] Y. Ebisawa, T. Kokubo, K. Ohura and T. Yamamuro, J. Mater. Sci., Mater. Med. **1** (1990) 239.

[61] M.W.G. Lockyer, D. Holland and R. Dupree, J. Non-Cryst. Solids **188** (1995) 207.

[62] C. Ohtsuki, T. Kokubo and T. Yamamura, J. Non-Cryst. Solids **143** (1992) 84.

[63] F. Branda, R. Fresa, A. Costantini and A. Buri, Biomater. **17** (1996) 2247.

[64] A. Martinez, I. Izquierdo-Baeba and M. Vallet-Regi, Chem. Mater. **12**(2000) 3080.

[65] C. Ohtsuki, T.Kokubo and T. Yamamuro, J. Mater. Sci. Mater. Med. **3** (1992) 119.

[66] K. Ohura, T. Nakamura, T. Yamamuro, Y. Ebisawa, T. Kokubo, Y. Kotoura and M. Oka, J. Mater. Sci., Mater. Med. **3** (1992) 95.

[67] E. Fujii, K. Kawabata, H. Yoshimatsu, S. Hayakawa, K. Tsuru and A. Osaka, J. Cerami. Soc. Jpn. **111** (2003) 762.

[68] K. Franks, I. Abrahams, G. Georgiou and J. C. Knowles, Biomater. **22** (2001) 497.

[69] D. Cacaina, H. ylanen, S. Simon and M. Hupa, J. Mater. Sci. Mater. Med. DOI 10.1007/s10856-007-3163-x 2007.

[70] Y. K. Lee, K. N Kim, S. Y Shoi and C. S Kim, J. Mater. Sci. Mater. Med. **11** (2000) 511.

[71] J. Roman, A. J. Salinas, M. Vallet-Regi, J. M. Oliveira, R. N. Correia and M. H. Fernandes, Biomater. **22** (2001) 2013.

[72] D. M. Liu, Mater. Chem. phys. **36** (1994) 294.

[73] M. Oliveira, R. N. Correia and M. H. Fernandes, Biomater. **16** (1995) 849.

[74] A. J. Salinas, J. Roman, M. Vallet-Regi, J. M. Oliveira, R. N. Correia and M. H. Fernandes, Biomater. **21** (2000) 251.

[75] J. Serra , P. González, S. Liste, C. Serra, S. Chiussi, B. León, M. Pérez-Amor, H. O. Ylänen and M. Hupa, J. Non-Cryst. Solids **332** (2003) 20.

[76] M. Kamitakahara, C. Ohtsuki, H. Inada, M. tanihara and T. Miyazaki, acta Biomater. **2** (2006) 467.

[77] A. Balamurugan, G. Balossier, S. Kannan, J. Michel, A. H. S. Rebelo and J. M. F. Ferreira, Acta Biomater. **3** (2007) 255.

[78] D. B. Jaroch, D. C. Clupper, J. Biomed. Mater. Res. **82A** (2007) 575.

[79] Y. Ivanova, E. Spassova, Y. Dimitriev, B. Samuneva and E. Kashchieva, J. Sol-gel Sci. Tech. **2** (1994) 819.

[80] R. L. Du, J. Chang, S. Y. Ni, W. Y. Zhai and J. Y. Wang, J. Biomater. Applica. **20** (2006) 341.

[81] R. Li, Sol-gel processing of bioactive glass powders. Ph.D. dissertation, University of Florida, 1991.

[82] R. Li, A. E. Clark and L. L. Hench, J. Appl. Biomater. **2** (1991) 231.

[83] L. L. Hench, Biomater. **19** (1998) 1419.

[84] H. Oonishi, S. Kutrshitani, E. Yasukawa, H. Iwaki, L. L. Hench, J. Wilson, E. Tsuji and T. Sugihara, J. Clin. Orthop. Related Res. **334** (1997) 316.

[85] D. L. Wheeler, K. E. Stokes, Trans 23rd Annual Meeting of the Soc. Biomater., New Orleans, LA, 1997.

[86] A. Martinez, I. I. Barba and M. V. Regi, Chem. Mater. **12** (2000) 3080.

[87] I. I. Barba, A. J. Salinas and M. V. Regí, J. Biomed. Mater. Res. **47** (1999) 243.

[88] M. V. Regı, A. M. Romero, C. V. Ragel and R. Z. LeGeros, J. Biomed. Mater. Res. **44** (1999) 416.

[89] M. V. Regı, I. I. Barba and A. J. Salinas, J. Biomed. Mater. Res. **46** (1999) 560.

[90] T. Peltola, M. Jokinen, H. Rahiala, E. Levanen, J. B. Rosenhold, I. Kangasniemi and A. Yli-Urpo, J. Biomed. Mater. Res. **44** (1999) 12.

[91] M. V. Regı and A. Ramila, Chem. Mater. **12** (2000) 961.

[92] J. P. Pariente, F. Balas, J. Roman, A. J. Salinas and M. V. Regi, J. Biomed. Mater. Res. **47** (1999) 170.

[93] J. P. Pariente, F. Balas, M. V. Regi, Chem. Mater. **12** (2000) 750.

[94] P. Li, C. Ohtsuki, T. Kokubo, K. Nakanishi, N. Soga, T. Kanamura and T. Yamamuro, J. Am. Ceram. Soc. **75** (1992) 2094.

[95] P. Li, C. Ohtsuki, T. Kokubo, K. Nakanishi, N. Soga, T. Nakamura and T. Yamamuro, J. Mater. Sci., Mater. Med. **4** (1993) 127.

[96] P. Li, T. Kokubo, K. Nakanishi and K. D. Groot, Biomater. **14** (1993) 963.

[97] T. Kokubo, S. B. Cho, K. Nakanishi, N. Soga, C. Ohtsuki, T. Kitsugi, T. Yamamuro and T. Nakamura, Biocerami. **7** (1994) 49.

[98] W. R. Lacefield, An Introduction to Bioceramics, World Sci., London (1993) 223.

[99] J. G. C. Wolke, K. Van Dijk, H. G. Schaeken, K. de Groot and J. A. Jansen, J. Biomed. Mater. Res. **28** (1994) 1477.

[100] J. L. Ong, C.W. Prince and L. C. Lucas, J. Biomed. Mater. Res. **29** (1995) 165.

[101] K. Van Dijk, H. G. Schaeken, J. C. G. Wolke, C. H. M. Maree, F. H. P. M. Habraken, J. Verhoeven and J. A. Jansen, J. Biomed. Mater. Res. **29** (1995) 269.

[102] E. Gyorgy, S. Grigorescu, G. Socol, I. N. Mihailescu, D. Janackovic, A. Dindune, Z. Kanepe, E. Palcevskis, E. L. Zdrentu and S. M. Petrescu, Appli. Surface Sci. **253** (2007) 7981.

[103] V. Cannillo, F. Pierli, S. Sampath and C. Siligardi, J. Euro. Cerami. Soc. **29(4)** (2009) 611.

[104] Y. Zhao, M. Song, C. Chen and J. Liu, J. Non-Cryst. Solids **354(33)** (2008) 4000.

[105] T. Onoki, X. Wang, S. Zhu, Y. Hoshikawa, N. Sugiyama, M. Akao, E. Yasuda, M. Yoshimura and A. Inoue, J. Ceram. Soc. Jpn. **116** (2008) 115.

[106] J. P. Borrajo, P. Gonzalez, S. Liste, J. Serra, S. Chiussi, B. Leon and M. Perez-Amor, Mater. Sci. Engg. C: Biomi. Supramol. Systems **C25(2)** (2005) 187.

[107] E. Verne, C. F. Valles, C. V. Brovarone, S. Spriano and C. Moisescu, J. Euro. Ceram. Soc. **24(9)** (2004) 2699.

[108] C. C. Mardare, A. I. Mardare, J. R. F. Fernandes, E. Joanni, S. C. A. Pina, M. H. V. Fernandes and R. N. Correia, J. Euro. Ceram. Soc. **23(7)** (2003) 1027.

[109] H. Ishizawa and M. Ogino, J. Biomed. Mater. Res. **29** (1995) 65.

[110] C. Gruttner, S. Rudershausen and J. Teller, J. Magn. Magn. Mater. **225** (2001) 1.

[111] O. Mykhaylyk, A. Cherchenko, A. Ilkin, N. Dudchenko, V. Ruditsa, M. Novoseletz and Y. Zozulya, J. Magn. Magn. Mater. **225** (2001) 241.

[112] D. K. Kim, Y.Zhang, J. Kehr, T. Klason, B. Bjelke and M. Muhammed, J. Magn. Magn. Mater. **225** (2001) 256.

[113] M. Koneracka, P. Kopcansky, M. Antalik, M. Timko, C. N. Ramchand, D. Lobo, R. V. Mehta and R. V. Upadhyay, J. Magn. Magn. Mater. **201** (1999) 427–430

[114] C. Poeckley-Schoeniger, J. Koepke, F. Gueckel, J. Sturm and M. Georgi, Magn. Reson. Imag. **17** (1999) 383.

[115] U. O. Hafeli, In: Magnetism in medicine (eds) W. Andra, H. Novak (Berlin: John Wiley and Sons)

[116] J.Chatterjee, Y. Haik and C. Ching-Jen, J. Magn. Magn. Mater. **225** (2001) 21.

[117] C. Del Gratta, S. Della Penna, P. Battista, L. Di Donato, P. Vitullo, G. L. Romani and S. Di Luzio, Phys. Med. Biol. **40** (1995) 671.

[118] P. A. Liberti, C. G. Rao and L. W. M. M. Terstappen, J. Magn. Magn. Mater. **225** (2001) 301.

[119] M. Shinkai, M. Yanase, M. Suzuki, H. Honda, T. Wakabayashi, J. Yoshida and T. Kobayashi, J. Magn. Magn. Mater. **194** (1999) 176.

[120] A. Jordan, P. Wust, R. Scholz, B. Tesche, H. Fahling, T. Mitrovics, T. Vogl, J. Cervos- Navarro and R. Felix, Int. J. Hyperthermia **12** (1996) 705–722.

[121] S. Golui, D. Datta and D. Bahadur, Proc. 8th Int. Conf. on ferrites (ICF 8) Kyoto, Japan (2000) 105.

[122] http://www.geocities.com/HotSprings/Villa/5443/alts/hytherm.html.

[123] O. S. Nielsen, M. Horsman and J. Overgaard, European J. Cancer **37** (2001) 1587.

[124] R. V. Ramanujan, Proc. First Intl. Bioengg. Conf. Singapur (2004) 174.

[125] M. H. Falk and R. D. Issels, International J. Hyperther. **17(1)** (2001) 1.

[126] O. Bretcanu, E. Verne, M. Coisson, P. Tiberto and P. Allia, J. Mag. Mag. Mater. **300** (2006) 412.

[127] M. Kawashita, M. Tanaka, T. Kokubo, Y. Inoue, T. Yao, S. Hamada and T. Shinjo, Biomater. **26** (2005) 2231.

[128] O. Bretcanu, S. Spriano, E. Verne, M. Coisson, P. Tiberto and P. Allia, acta Biomater. **1** (2005) 421.

[129] K. Singh and D. Bahadur, J. Mater. Sci., Mater. Med. **10** (1999) 481.

[130] O. Bretcanu, S. Spriano, C. B. Vitale and E. Verne, J. Mater. Sci. **41** (2006) 1029.

[131] Th. Leventouri, A. C. Kis, J. R. Thompson and I. M. Anderson, Biomater. **26** (2005) 4924.

[132] Y. Ebisawa, F. Miyaji, T. Kokubo, K. Ohura and T. Nakamura, Biomater. **18** (1997) 1277.

[133] M. Kawashita, Y. Iwahashi, T. Kokubo, T. Yao, S. Hamada and T. Shinjo, J. Ceram. Soc. Jpn. **112** (2004) 373.

[134] D.Eniu, D. Cacaina, M. Coldea, M. Valeanu and S. Simon, J. Magn. Magn. Mater. **293** (2005) 310.

[135] Y. K. Lee, S. B. Lee, Y. -U. Kim, K. N. Kim, S. -Y. Choi, K. H. Lee, I. B. Shim and C. -S. Kim, J. Mater. Sci. **38** (2003) 4221.

[136] M. Kawashita, S. Domi, Y. Saito, M. Aoki, Y. Ebisawa, T. Kokubo, T. Saito, M. Takano, N. Araki and M. Hiraoka, J. Mater. Sci., Mater. Med. **19** (2008) 1897.

[137] E. W. Gorter, Nature **165** (1950) 798.

[138] B. Jeyadevan, K. Tohji and K. Nakatsuka, J. Appl. Phys. **76** (1994) 6325.

[139] B. D. Cullity and S. R. Stock, Elements of X-ray Diffractions, third ed., Prentice Hall, Upper Saddle River, N J (2001) 170.

[140] E. S. Watson, M. J. O'Neil, J. Justin and N. Brener, Anal. Chem. **36** (1964) 1233.

[141] H. Farouk, F. M. Ezz Eldin, H. Farhan, H. A. El-Batal and I. Kashif, Phys. Chem. Glasses **35** (1994) 207.

[142] D. Sudhakar Rao and P.P. Karat, Phys. Chem. Glasses **35** (1994) 124.

[143] B. Vaidhyanathan, S. Murugavel, S. Asokan and K. J. Rao, J. Phys. Chem. B **101** (1997) 9717.

[144] M. Yamane and J.D. Mackenzie, J. Non-Cryst. Solids **15** (1974) 153.

[145] J. E. Shelby, Introduction to Glass Science and Technology, RSC, 1997.

[146] A. Petzold, F.G. Withsmann and H. Von Kampiz, Glasteck Ber. **43** (1961) 56.

[147] S. Foner, Rev. Sci. Inst. **30** (1959) 548.

[148] R. D. Cullity, Introduction to Mag. Mater. (Addison-Wesley, Reading, 1972).

[149] T. Nishida and T. Takashima, Bull. Chem. Soc. Jpn. **60** (1987) 941.

[150] I. Kashif, H. Farouk, S.H. Salah, A. A. A. Rahman and A. M. Sanad, J. mater. Sci.: Mater. Electr. **2** (1991) 220.

[151] T. Komatsu and N. Soga, J. Chem. Phys. **73**(3) (1980) 1781.

[152] D. W. Moon, J. M. Aitken, R. K. MacCrone and G. S. Cieloszyk, Phys. Chem. Glasses **16** (1975) 91.

[153] E. Burzo and I. Ardelean, Phys. Status Solidi (b) **87** (1978) K137.

[154] M. Nofz, R. Stosser and F. G. Wihsmann. Phys. Chem. Glasses **31** (1990) 57.

[155] A. S. Rao, R. R. Reddy, T. V. R. Rao and J. L. Rao. Solid State Commun. **96** (1995) 701.

[156] J. Kliava, R. Berger, Y. Servant, J. Emery, J. M. Greneche and J. Trokss, J. Non-Cryst. Solids **202** (1996) 205.

[157] E. Burzo and I. Ardelean, Phys. Chem. Glasses **20** (1979) 15.

[158] J. L. Rao, A. Murali and E.D. Rao, J. Non-Cryst. Solids **202** (1996) 215.

[159] J. Dumas, J. L. Tholence, M.Continentio, J. C. Fernandes and R. B. Guimaraes, J. Magn. Magn. Mater, **226-230** (2001) 468.

[160] R. P. Sreekanth Chakradhar, A. Murali and J. Lakshmana Rao, Opt. Mater. **10** (1998) 109.

[161] I. Ardelean, Gh. Ilonca, O. Cozar, V. Simon and S. Filip. Mater. Lett. **21** (1994) 321.

[162] I. Ardelean, M. Peteanu, V. Simon, S. Filip, F.Ciorcas and I. Todor, J. Magn. Magn. Mater, **196&197** (1999) 257.

[163] I. Ardelean, M. Peteanu, S. Filip, V. Simon and G. Györffy, Solid State Commun. **102** (1997) 341.

[164] I. Ardelean, H. H. Qiu and H. Sakata, Mater. Lett. **32** (1997) 335.

[165] A. K. Bandyopadhyay, J. Zarzycki, P. Auric and J. Chappert, J. Non-Cryst. Solids **40** (1980) 353.

[166] D. Loveridge and S. Parke, Phys. Chem. Glasses **12** (1971) 19.

[167] S. P. Chaudhuri and S. K. Patra, J. Mater. Sci. **35** (2000) 4735.

[168] B. Bleaney and K. W. H. Stevens, Rep. Prog. Phys. **16** (1953) 108.

[169] T. Castner, Jr., G. S. Newell, W. C. Holton, and C. P. Slichter, J. Chem. Phys. **32** (1960) 668.

[170] H. H. Wickman, M. P. Klein, and D. A. Shirly, J. Chem. Phys. **42** (1965) 2113.

[171] B. Kumar and C. H. Chen. J. Appl. Phys. **75** (1994) 6760.

[172] M. Peteanu, L. Cociu and I. Ardelean, J. Mat. Technol. **10** (1994) 97

[173] E. Burzo, I. Ursu, D. Ungur and I. Ardelean, Mat. Res. Bull. **15** (1980) 1273.

[174] I. Ardelean, P. Pascuta and M. Peteanu, J. Mod. Phys. Lett. **B 16 (7)** (2002) 231.

[175] A. Mekki and K. Ziq, J. Magn. Magn. Mater. **189** (1998) 207.

[176] C. M. Hurd. Contemp. Phys. **23** (1982) 469.

[177] I. Ardelean, P. Pascuta and V. Ioncu, J. Mod. Phys. Lett. B **15** (30) (2001) 1445.

[178] I. Ardelean, C. Andronache, C. Cimpean and P. Pascuta, J. Optoelectron. Adv. Mater. **8** (2006) 1372.

[179] F. A. Wegwood and A. C. Wright, J. Non-Cryst. Solids **21** (1976) 95.

[180] Gh. Ilonca, I. Ardelean and O. Cozar. J. Phys. **49** (1988) C8.

[181] T. Kitsugi, T. Yamamuro, T. Nakamura and T. Kokubo, J. Biomed. Mater. Res. **23** (1989) 631.

[182] K.H. Karlsson, K. Froberg and T. Ringbom, J. Non-Cryst. Solids **112** (1989) 69.

[183] C. Ohtsuki, H. Kushitani, T. Kokubo, S. Kotani and T. Yamamuro, J. Biomed. Mater. Res. **95** (1991) 1363.

[184] Li-yun, Z. Chuan-bo and H. Jian-feng, Mater. Lett. **59** (2005) 1902.

[185] Y. Ebisawa, T. Kokubo, K. Ohura and T. Yamamuro, J. Mater. Sci., Mater. Med. **4** (1992) 225.

[186] T. W. Wang, H. C. Wu, W. R. Wang, F. H. Lin, P. J. Lou, M. J. Shieh, T. H. Young, J. Biomed. Mater. Res. Part A **83A** (2007) 828.

[187] O. Bretcanu, E. Verne, M. Coisson, P. Tiberto and P. Allia, J. Magn. Magn. Mater. **305** (2006) 529.

[188] C. Y. Kim, A. E. Clark and L. L. Hench, J. Non-Cryst. Solids **113** (1989) 195.

[189] C. C. Silva, M. A. Valente, M. P. F. Graca and A. S. B. Sombra, Solid State Sci. **6** (2004) 1365.

[190] I. Rehman and W. Bonfield, J. Mater. Sci., Mater. Med. **8** (1997) 1.

[191] W. L. Konijnendijk, Phillips Res. Rep. Suppl. **1** (1975) 243.

[192] S. V. Dorozhkin, E. I. Dorozhkina and M. Epple, J. Appl. Biomate. & Biomecha. **1** (2003) 200.

[193] J. Barralet, S. Best and W. Bonefield, J. Biomed. Mater. Res. **41** (1998) 79.

[194] K. Tanaka, N. Soga, R. Ota and K. Hirao, Bull. Chem. Soc. Jpn. **59** (1986) 1079.

[195] S. Simon, D. Eniu, A. Pasca, D. Dadarlat and V. Simon, Mod. Phys. Lett. **B15** (2001) 921.

[196] S. Woltz, R. Hiergeist, P. Gornert and C. Russel, J. Magn. Magn. Mater, **298** (2006) 7.

[197] P. Auric, N. V. Dang, A. K. Bandyopadhyay and J. Zarzycki, J. Non-Cryst. Solids **50** (1982) 97.

[198] J. A. Kerr, in: D.R. Lide (Ed.), CRC Handbook of Chem. Phys., 81st ed, CRC Press, Boca Raton USA, 2000.

[199] R. K. Singh, G. P. Kothiyal and A. Srinivasan, J. Non-Cryst. Solids **354** (2008) 3166.

[200] R. K. Singh, G. P. Kothiyal and A. Srinivasan, Appl. Surface Sci. DOI doi:10.1016/j.apsusc.2009. 02.089 (2009).

[201] R. K. Singh, G. P. Kothiyal and A. Srinivasan, Solid State Commun. **146** (2008) 25.

PUBLICATIONS

IN JOURNALS:

1. Magnetic and structural properties of $CaO\text{-}SiO_2\text{-}P_2O_5\text{-}Na_2O\text{-}Fe_2O_3$ glass ceramics, **R. K. Singh**, G. P. Kothiyal and A. Srinivasan, *J. Magn. Magn. Mater*. **320** (2008) 1352.

2. Electron Spin Resonance and magnetic studies on $CaO\text{-}SiO_2\text{-}P_2O_5\text{-}Na_2O\text{-}Fe_2O_3$ glasses, **R. K. Singh**, G. P. Kothiyal and A. Srinivasan, *J. Non-Cryst. Solids* **354** (2008) 3166.

3. Influence of iron ions on magnetic properties of $CaO\text{-}SiO_2\text{-}P_2O_5\text{-}Na_2O$ Fe_2O_3 glass-ceramics, **R. K. Singh**, G. P. Kothiyal and A. Srinivasan, *Solid State Commun.* **146** (2008) 25.

4. Evolution of magnetism in $CaO\text{-}SiO_2\text{-}P_2O_5\text{-}Na_2O\text{-}Fe_2O_3$ bioglass ceramics, **R. K. Singh**, A. Perumal, G.P. Kothiyal and A. Srinivasan, *Mater. Sci. Forum* **587** (2008) 171.

5. Evaluation of $CaO\text{-}SiO_2\text{-}P_2O_5\text{-}Na_2O\text{-}Fe_2O_3$ bioglass-ceramics for hyperthermia application, **R. K. Singh**, G. P. Kothiyal and A. Srinivasan, *J. Mat. Sci: Materials in Medicine* DOI 10.1007/s10856-008-3497-z (2008).

6. Bioactivity of $CaO\text{-}SiO_2\text{-}P_2O_5\text{-}Na_2O\text{-}Fe_2O_3$ glass-ceramics: In vitro evaluation, **R. K. Singh**, G. P. Kothiyal and A. Srinivasan, *Arch. BioCeram. Res.* **8** (2008) 89.

7. In vitro evaluation of bioactivity of $CaO\text{-}SiO_2\text{-}P_2O_5\text{-}Na_2O\text{-}Fe_2O_3$ glasses, **R. K. Singh,** G. P. Kothiyal and A. Srinivasan, *Appl. Surf. Sci.* DOI doi:10.1016/j.apsusc. 2009.02.089 (2009).

8. EPR and magnetic properties of $MgO\text{-}CaO\text{-}SiO_2\text{-}P_2O_5\text{-}CaF_2\text{-}Fe_2O_3$ glass-ceramics, **R. K. Singh** and A. Srinivasan, *J. Magn. Magn. Mater*. **321** (2009) 2749.

9. Bioactivity of ferrimagnetic $MgO\text{-}CaO\text{-}SiO_2\text{-}P_2O_5\text{-}Fe_2O_3$ glass-ceramics, **R. K. Singh** and A. Srinivasan, *Ceram. Inter.,* (2009), doi:10.1016/j.ceramint.2009.07.028**.**

10. Bioactivity of $SiO_2\text{-}CaO\text{-}P_2O_5\text{-}Na_2O$ glasses containing zinc-iron oxide, **R. K. Singh** and A. Srinivasan, *Appl. Surf. Sci.,* (2009) doi:10.1016/j.apsusc. 2009.09.102.

11. Structural and magnetic properties of $MgO\text{-}CaO\text{-}SiO_2\text{-}P_2O_5\text{-}CaF_2\text{-}Fe_2O_3$ glasses, **R. K. Singh** and A. Srinivasan, (under review in *Phy. Chem. Glasses*).

12. Structure and magnetic properties of glass-ceramics containing nanocrystalline zinc-ferrite, **R. K. Singh** and A. Srinivasan, under communication to *Curr. Appl. Phys*. (2009).

13. Bioactivity of MgO-CaO-SiO_2-P_2O_5-CaF_2 glasses – An in vitro evaluation, **R. K. Singh** and A. Srinivasan, under communication to *J. Phys. Chem. Solids* (2009).

14. EPR and magnetic properties of ZnO-Fe_2O_3-CaO-P_2O_5-SiO_2-Na_2O glasses, **R. K. Singh** and A. Srinivasan, under communication to *J. Magn. Magn. Mater*. (2009).

15. Evaluation of bioactive glass-ceramics containing calcium sodium phosphate and zinc ferrite nanocrystals for hyperthermia application, **R. K. Singh** and A. Srinivasan, under communication to *Mater. Phys. Chem*., (2009).

16. Effect of heat treatment on the structure and magnetic properties of ferrimagnetic bioactive glass-ceramics, **R. K. Singh** and A. Srinivasan, (to be communicated).

IN CONFERENCES:

1. Electron Spin Resonance and magnetic susceptibility of CaO-SiO_2-P_2O_5-Na_2O-Fe_2O_3 glasses and glass – ceramic, **R. K. Singh**, G.P.Kothiyal and A. Srinivasan, Proc. DAE-SSP Symp. India, 52 (2007) 533.

2. Studies on new bioglasses and bioglass-ceramics containing Fe_3O_4**, R. K. Singh**, G. P. Kothiyal and A. Srinivasan**,** Proc. DAE-SSP Symp. india, 51 (2006) 411.

3. Effect of Fe_2O_3 addition on the properties of CaO-SiO_2-P_2O_5-Na_2O glasses, **R. K. Singh**, G. P. Kothiyal and A. Srinivasan, Proc. DAE-SSP Symp. India, 53 (2008) 621.

4. In Vitro evaluation of bioactivity of CaO-SiO_2-P_2O_5-Na_2O-Fe_2O_3 ferrimagnetic Bioglass- ceramics, **R. K. Singh**, K. Sharma, G.P. Kothiyal and A. Srinivasan, Nat. Conf. Adv. Mater.,Devices & Technol. ,Tirupati, india, Feb.20-22,2008,IT-5pp.11.

5. Synthesis & preliminary characterization of a new class of glassceramics for hyperthermia treatment application, **R. K. Singh**, A. Dixit, S. Sarma, P.S. Robi, K. Sharma, G.P. Kothiyal and A. Srinivasan, Natl. Symp. Sci. & Tech. Glass/Glass-Ceramics, Mumbai, india,Sept.15-16,2006,p.p.123.

6. Magnetic properties of MgO-CaO-SiO_2-P_2O_5-CaF_2-Fe_2O_3 bioglass-ceramics, **R. K. Singh**, G. P. Kothiyal and A. Srinivasan, Proc. Natl. Symp. Sci. & Tech. Glass/Glass-Ceramics, Mumbai, India, Oct.15-17, 2008, pp.180.

7. Assessment of CaO-SiO_2-P_2O_5-Na_2O-Fe_2O_3 glass-ceramics for hyperthermia application, **R. K. Singh**, G. P. Kothiyal and A. Srinivasan, Proc. Natl. Symp. Sci. & Tech. Glass/Glass-Ceramics, Mumbai, India, Oct.15-17, 2008, pp.10.

8. Effect of Fe_2O_3 addition on the properties of MgO-CaO-SiO_2-P_2O_5-CaF_2 glasses and in vitro evaluation, **R. K. Singh** and A. Srinivasan, 23rd Inter. Conf. on Amorphous and Nanocrystalline Semiconductors (ICANS23) Netherland, Aug. 23-28**,** 2009, abstract ID 318, pp. 256.

9. Evaluation of ZnO-Fe_2O_3-SiO_2-CaO-P_2O_5-Na_2O glass-ceramics for hyperthermia application, **R. K. Singh** and A. Srinivasan, Asian Bioceram. Symp. Japan, Dec. 9-11**,** 2008 (accepted for oral presentation O20).

****